

Combining Electron and Optical Spectroscopy to Study the Diamond Surface for NV Centre Applications



This **Thesis** is submitted to
Aberystwyth University

by

Johnathan Ash BSc MSc

in candidature for the degree

Doctor of Philosophy (PhD)

This thesis is dedicated to my parents, Robert and Diane
for everything you do

ACKNOWLEDGEMENTS

This work would not have been possible without the help and support of so many incredible people. Therefore, I would like to take the opportunity to show my appreciation and gratitude.

First and foremost, I would like to thank my supervisor Professor Andrew Evans - not only for the opportunity to undertake this work, but for the knowledge, patience, and guidance which you have provided. It has been truly invaluable.

I would also like to express my sincerest gratitude to Dr Simon Cooil. Whilst he has not been my official supervisor, he is someone from whom I have learnt a great deal. His support and friendship throughout this work cannot be understated.

I would also like to thank the staff I have worked with from the Department of Physics at Aberystwyth University, who have made my time here a true pleasure. I would especially like to thank Mr Joseph Durk, Dr Benjamin Reed and Dr Simon Astley for your help, discussions, and entertainment during the times we were all stuck in the lab. Thanks also to Dr Dave Langstaff, Dr Thomas Knight and Dr Matt Gunn for technical and coding support, as well as helpful advice and interesting conversations throughout my PhD.

I would also like to thank my parents for their unwavering support and love, without which I would not have made this far. I have also been lucky to have the support of the rest of my family and some incredible friends: Kelly, Emma, Morgan, Rose, Zoe, Nicola, John, and Marly - thank you all for being there for me. To anyone else who has offered support, advice or even just a motivational speech, I thank you also.

A special thanks also goes to my girlfriend, Beth. Words cannot describe how thankful I am to have found someone who can provide such constant love and support.

Finally, I would like to acknowledge the EPSRC Diamond Science and Technology Centre for Doctoral training for the funding which made this project possible.

"I drink and I know things."

Tyrion Lannister.

ABSTRACT

This thesis presents a study of chemical and electronic properties of the (100) oxygen terminated surface of diamond as a basis for quantum applications revolving around near surface nitrogen-vacancy centres. A combination of X-ray Photoelectron Spectroscopy (XPS) Ultraviolet Photoelectron Spectroscopy (UPS), Real-time Electron Energy Spectroscopy (REES) and Near-Ambient Pressure XPS (NAP-XPS) have been implemented. A computational model has also been developed to describe the surface photovoltage generated during these measurements and its dependency on temperature. A (001) moderately boron doped diamond was oxygen terminated by two methods and monitored in real time during a series of annealing cycles up to 1000°C. The desorption mechanisms, chemical species stoichiometry and the electronic band structures will be present herein. During this work a work function of 2.42 eV from a plasma treated surface was found, the highest reported for an oxygen terminated diamond surface.

In conjunction, the design, construction, calibration and initial measurement of the OptiXS instrument will be presented. Whilst the use of optical and electron spectroscopy is commonplace in materials science, they are rarely, if ever performed together. The OptiXS (Optical and X-ray Spectroscopy) instrument has been developed to provide the ability to perform these techniques simultaneously and *in-situ*, opening possible avenues for real-time, parallel optical and electron spectroscopic studies during sample processing techniques, such as thin film deposition, heating or cooling cycles or ion bombardment. Within this thesis the manipulator design process, calibration experiments, and initial attempts at nitrogen implantation will be given.

All XPS and REES taken in this work has been fitted using the newly developed Materials Characterisation Suite, an analysis package which currently specialises in photoemission core level fitting and REES fit propagation. The background theory, analysis procedures, and user interfaces will also be presented in this work.

GLOSSARY OF ABBREVIATIONS

Acronym	Abbreviation
ARPES	Angle-Resolved Photoelectron Spectroscopy
AFM	Atomic Force Microscopy
BG	Bandgap
BN	Boron Nitride
CEM	Channel Electron Multiplier
CCD	Charge-Coupled Device
CVD	Chemical Vapour Deposition
CBM	Conduction Band Minimum
CF	Conflat
EELS	Electron Energy Loss Spectroscopy
FAT	Fixed Analyser Transmission
FRR	Fixed Retard Ratio
FTIR	Fourier-Transform Infrared
FWHM	Full-Width at Half-Maximum
HA	Hemispherical Analyser
HPHT	High-Pressure High-Temperature
IMFP	Inelastic Mean-Free-Path
IR	Infrared
LASER	Light Amplification by Stimulated Emission of Radiation
LEED	Low Energy Electron Diffraction
LV/MV/HV/VHV/XHV	Low/Medium/High/Very-High/Extreme Ultra-high Vacuum
MCS	Material Characterisation Suite
MFP	Mean-Free-Path
MCP	Microchannel Plate
ML	Monolayer

NCD	Nanocrystalline Diamond
NAP-XPS	Near-Ambient Pressure X-ray Photoelectron Spectroscopy
Nd:YAG	Neodymium-doped Yttrium Aluminium Garnet
NV	Nitrogen-Vacancy
NV ⁻ /NV ⁰	Negatively-Charged/Neutral Nitrogen-Vacancy
OptiXS	Optical and X-ray Spectroscopy
PSB	Phonon Sideband
PEEM	Photoelectron Emission Microscopy
PES	Photoelectron Spectroscopy
PL	Photoluminescence
PTFE	Polytetrafluoroethylene
PEA/NEA	Positive/Negative Electron Affinity
RF	Radio Frequency
REES	Realtime Electron Energy Spectroscopy
RMS	Root-Mean-Square
SVSC	Shirley-Vegh-Salvi-Castle
SNR	Signal-to-Noise Ratio
SCD	Single-Crystal Diamond
SPV	Surface Photovoltage
TPA	<i>trans</i> -Polyacetylene
UHV	Ultra-High Vacuum
UV	Ultraviolet
UPS	Ultraviolet Photoelectron Spectroscopy
VBM	Valence Band Maximum
WF	Work Function
XEOLS	X-ray Excited Optical Luminescence Spectroscopy
XPS	X-ray Photoelectron Spectroscopy
ZPL	Zero Phonon Line

Chapter 1 – INTRODUCTION	8
1.1 INTRODUCTION	8
1.2 THESIS LAYOUT AND CONTRIBUTION	10
Chapter 2 – THEORY AND TECHNIQUES	13
2.1 PHOTOELECTRON SPECTROSCOPY	14
2.1.1 PRINCIPLES OF PHOTOELECTRON SPECTROSCOPY	14
2.1.2 PHOTOEMISSION SPECTRAL FEATURES	17
2.1.2.1 CORE LEVEL PHOTOEMISSION	19
2.1.2.2 SPIN-ORBIT COUPLING	19
2.1.2.3 AUGER ELECTRON EMISSION	20
2.1.2.4 PLASMON LOSS, SATELLITE PEAKS AND OTHER FEATURES	22
2.1.2.5 UPS FEATURES	25
2.1.3 PHOTOIONISATION CROSS SECTION	25
2.1.4 ELECTRON MEAN FREE PATH	27
2.1.5 REAL-TIME ELECTRON ENERGY SPECTROSCOPY (REES)	29
2.2 QUANTIFICATION OF XPS AND THE DEVELOPMENT OF THE MATERIALS CHARACTERISATION SUITE	31
2.2.1 THE PHOTOELECTRON PEAK LINE-SHAPE	32
2.2.1.1 THE VOIGT AND PSEUDO-VOIGT FUNCTIONS	32
2.2.1.2 ASYMMETRY	37
2.2.1.3 XPS BACKGROUND	41
2.2.2 THE MATERIALS CHARACTERISATION SUITE USER INTERFACE	43
2.2.2.1 XPS ANALYSIS PANEL	44
2.2.2.2 REES ANALYSIS PANEL	51
2.2.2.3 PERIODIC TABLE PANEL	54
2.2.3 THE MCS SUMMARY	54
2.3 OPTICAL SPECTROSCOPY	57
2.3.1 LUMINESCENCE	57
2.3.1.1 THE PRINCIPLES OF LUMINESCENCE	57
2.3.1.2 PHOTOLUMINESCENCE SPECTROSCOPY	60
2.3.2 RAMAN SPECTROSCOPY	61
2.3.3 OPTICAL SPECTROSCOPY FEATURES	63
Chapter 3 – INSTRUMENTATION	66
3.1 ULTRA-HIGH VACUUM	66
3.2 PHOTON SOURCES	70
3.2.1 TWIN ANODE X-RAY SOURCE	70
3.2.2 ULTRAVIOLET DISCHARGE SOURCE	72
3.2.3 SYNCHROTRON RADIATION	73
3.2.3.1. SYNCHROTRON OPERATION	73
3.2.3.2 SYNCHROTRON RADIATION THEORY	76
3.2.4 OPTICAL LASER SOURCES	78
3.3 IN-SITU SURFACE MODIFICATION	80
3.3.1 LOW ENEGERY ION SOURCE	80
3.3.2. THIN FILM DEPOSITION	81
3.3.3. PLASMA TREATMENT	82
3.4 SAMPLE STAGES, MOUNTING AND MANIPULATION	84
3.5 OPTICAL SPECTROMETER	87
3.6 THE HEMISPHERICAL ANALYSER	89

3.7 THE DEVELOPMENT OF THE OPTICAL AND X-RAY SPECTROSCOPY INSTRUMENT (OPTIXS)	98
3.7.1 OVERVIEW	98
3.7.2. THE OPTIXS MANIPULATOR	104
3.7.3 CALIBRATION AND CHARECTERISATION	108
3.7.3.1 HA50 HEMISPHERICAL ANALYSER CALIBRATION	109
3.7.3.2 SIMULTANEUOUS STUDY OF IRON DEPOSITION ON DIAMOND AND BORON NITRIDE WITH IN-SITU, REAL-TIME RAMAN AND XPS	112
3.7.4 OTHER WORK	122
3.7.5 OPTIXS SUMMARY	124
<i>Chapter 4 – MATERIALS</i>	125
4.1 DIAMOND	125
4.1.1 THE PROPERTIES OF DIAMOND	126
4.1.2 THE SYNTHESIS OF DIAMOND	127
4.1.3 DOPANTS AND DEFECTS IN DIAMOND	134
4.1.4 THE NITROGEN-VACANCY CENTRE	136
4.1.5 THE DIAMOND SURFACE	144
4.1.6 NANOCRYSTALLINE DIAMOND FILMS	151
<i>Chapter 5 – OXYGEN TERMINATED (001) DIAMOND SURFACE</i>	155
5.1 COMPARISON OF OXYGEN SPECIES FORMED BY OXIDATION TECHNIQUES	156
5.1.1 EXPERIMENTAL OVERVIEW	156
5.1.2 RESULTS	157
5.1.2.1 ACID-ETCHED DIAMOND SURFACE	157
5.1.2.2 PLASMA TREATED DIAMOND SURFACE	171
5.2 BAND DIAGRAMS AND SURFACE PHOTOVOLTAGE	181
5.3 FURTHER WORK	196
<i>Chapter 6 – NITROGEN IMPLANTATION IN DIAMOND</i>	198
6.1 EXPERIMENTAL OVERVIEW	199
6.1.1 THE SAMPLES	199
6.1.2 EXPERIMENTAL PROCEDURE	201
6.2 RESULTS	203
6.2.1 HPHT DIAMONDS	203
6.2.2 NANOCRYSTALLINE DIAMOND FILMS	209
<i>Chapter 7 – SUMMARY</i>	221
<i>Chapter 8 – APPENDIX</i>	225
8.1 MCS/IGOR CURVE FITING	225
8.2 INSTRUMENTAL ERRORS AND TYPICAL ERROR VALUES	229
<i>Chapter 9 – REFERENCES</i>	232

Chapter 1 – INTRODUCTION

1.1 INTRODUCTION

The NV centre is a point defect in diamond consisting of a neighbouring nitrogen atom and a vacancy centre. The electronic, optical and spin properties, as well as the superlative properties of its host material, diamond, have placed it at the forefront of candidates for quantum-based applications [1]. Since it was first observed as a single point defect in 1997, there has been a plethora of studies based around the NV centre for a wide range of applications, including quantum cryptography, nanoscale magnetic/electric field sensing, and spintronics, to name a few. Many of these applications require the NV centres to be located within nanometres of the surface. Recent studies have shown the NV centre will readily interact with surface states which can lead to the degradation of the desirable properties [2], highlighting the importance of surface preparation and leading to an influx of research based around near-surface NV centres. This is highlighted further by Figure 1.1, which shows total yearly publications pertaining to the Nitrogen Vacancy centre, as well as the proportion of which mention the diamond surface.

One of the most insightful techniques with regards to the chemical and electronic properties of surfaces is photoemission spectroscopy. Through this work, three main variants of photoemission spectroscopies are used in tandem to provide an in-depth study of the oxygen terminated diamond surface. XPS probe core level electrons and provide information on the chemical species present as well as the

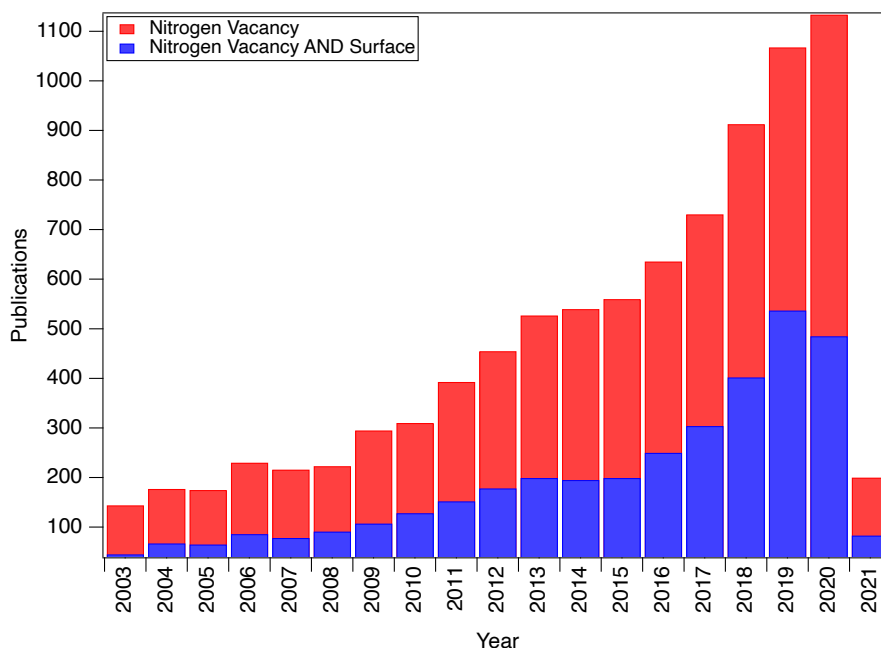


Figure 1.1: The number of publications regarding nitrogen vacancies centres (Red) and the proportion of those papers which mention the diamond surface (blue).

stoichiometry of said species. UPS probes the valence band electronic states and is used to determine the surface electronic properties, such as work function or electron affinity. Finally, Real-time photoelectron spectroscopy (REES) was utilised to measure the desorption temperature, desorption rates and temperature-induced band-bending to provide insight into the surface photovoltage generated when measuring doped diamond.

Analysis of photoemission core levels revolves around using Voigt profile components to fit to the measured data. Voigt profiles are a convolution of Gaussian and Lorentzian profiles and the contribution for each can be, in most cases, physically justified. The Lorentzian contribution is associated with core-hole lifetimes or anode-based X-ray sources, whereas Gaussian contributions come from instrumentation aspects such as focusing, CCD measurement or sample roughness. The resultant convolution profile exhibits Gaussian or Lorentzian properties, depending on the ratio of the G/L widths. Commonly, to avoid the computational effort of convolutions,

a mathematical approximation to the Voigt is used instead; this is the Pseudo-Voigt profile. This function is a weighted sum of a Gaussian and Lorentzian, where the weighting is determined by a mixing factor, μ . Whilst a very good approximation, the G and L width parameters are often lost or become meaningless in many fittings, with the nature of the output function dependant on only the pseudo-Voigt width and the mixing factor. To attempt to rectify this, the Material Characterisation Suite, presented in this work, was developed. The goal of this was to provide an easy-to-use fitting software which provides Voigt and pseudo-Voigt capabilities whilst maintaining physical accuracy. Historically, REES fitting has been very limited using commercially available software, such as CasaXPS, which requires binning the number of measurements cycles to a maximum of 300, severely reducing the time acquisition rate. The MCS was designed to be able to handle REES fit propagation as well, without having to bin data prior to analysis in order to maintain the temporal resolution.

1.2 THESIS LAYOUT AND CONTRIBUTION

This thesis contains 7 chapters, including this introductory chapter. The layout and contributors for each are as follows:

Chapter 2 focusses on the background theory of the numerous techniques used throughout this work. Sections on photoelectron spectroscopy and optical spectroscopies will present the fundamental theories of the measurement methods as well as review typical features found in measured spectra. The first of the research work will also be presented in this chapter with the **Materials Characterisation Suite (MCS)** (see **section 2.2.2**) and the underpinning functions used throughout

photoemission spectroscopy analysis presented in **section 2.2**. The MCS was developed in a collaborative effort between the author, Dr Simon Cooil (University of Oslo, formerly Aberystwyth University), and Mr Joseph Durk (Aberystwyth University). The initial iterative fitting function was also produced by Dr Thomas Knight (Aberystwyth University).

Chapter 3 presents the range of instrumentation which has been utilised during this work. The need for Ultra-High Vacuum, the various excitation sources and detection methods, as well as sample modification, preparation, mounting and manipulation will be detailed. The second research section will also be presented in this chapter. The development, calibration and review of the **OptiXS system** is given in **section 3.7**, which includes the design and construction of the OptiXS system manipulator (**section 3.7.2**) as well as testing, calibration and some initial research measurements. Design and Construction of the OptiXS system was undertaken by the author and Dr Simon Cooil (University of Oslo).

Chapter 4 provides a review of the materials studied in this work. The properties, synthesis and control of dopants in diamond is reviewed. This is followed by an overview of the NV centre which reviews some of its properties, how the centre is created and manipulated, and some of the known or future applications. The diamond surface is presented next, which focusses on the (001) surface, its properties, terminations and morphology. The chapter is concluded with a brief introduction to nanocrystalline diamond (NCD) films which are used in chapter 7. The NCD films were grown by collaborators Professor Oliver Williams and Dr Soumen Mandel (Cardiff University)

Chapter 5 presents the results from photoemission studies of the oxygen terminated (001) diamond surfaces formed by two acid treatments during a series of annealing cycles up to 1000°C. Some results, which were taken at the VerSoX (B07) beamline at the Diamond Light Source, of the acid etched diamond surface under different conditions and different excitation energies are also presented. This chapter finishes with a presentation of a surface photovoltage model for the (001) diamond surface. An automated version of this model was developed in collaboration with Dr Thomas Knight (Aberystwyth University). At the time of writing, various aspects of this chapter are currently in preparation to be published.

Chapter 6 presents initial measurements performed on the OptiXS system which aimed to test the nitrogen implantation and newly installed plasma treatment capabilities.

Chapter 7 summarises the thesis and discusses future work.

Chapter 2 – THEORY AND TECHNIQUES

The following chapter presents the essential theory underlying the techniques used in this work. There are two main groups of techniques used throughout this work. These are electron spectroscopies, which primarily rely on the photoelectric effect, and optical-based methods, which rely on the interactions between materials and light. Photoelectron Spectroscopy (PES) is well known as one of the most informative methods for studying the chemical and electronic properties of surfaces. It is routine for surface scientists to combine PES with a range of other electron-based techniques which together can provide a vast amount of information on the surface properties of materials. Optical-based spectroscopic methods are also widely used in material characterisation and can provide complimentary information to electron-based methods. Luminescence based techniques can garner information on the electronic structure, the defects and dopants in a material, and are frequently used in material identification. Other optical spectroscopies, such as Raman spectroscopy or Fourier transform infrared (FTIR) spectroscopy can probe vibrational states in materials, provide information about chemical species present in the solid or liquid sample, as well as provide insight into the isotropic composition or internal stress of materials. Combining these techniques can provide a vast wealth of information, crucial to material science research.

2.1 PHOTOELECTRON SPECTROSCOPY

2.1.1 PRINCIPLES OF PHOTOELECTRON SPECTROSCOPY

The photoelectric effect, as first discovered by Heinrich Hertz in 1887, is the ejection of electrons from a material when irradiated by light [3]. It was later explained by Albert Einstein in his quantised theory of light [4]. This provided a gateway to one of the most insightful techniques for studying the surface chemistry, composition and electronic structure of materials.

The principle of photoelectron involves electrons of a material interacting with an incident light source. Many models have been put forward to describe the photoemission process, which are discussed in detail by *S. Hüfner* [5]. However, to a simple approximation, the photoemission process can be described using a three-step model:

1. An incident photon with energy greater than an electron binding energy (E_B) is absorbed by an electron, exciting it to a higher energy state.
2. The excited electron travels through the material, possibly undergoing inelastic scattering events, until the vacuum/surface interface is reached.
3. The electron is ejected into the vacuum. The remaining energy of the electron as it reaches the surfaces is the kinetic energy (E_k) of the electron in the vacuum.

Therefore, the kinetic energy of the electrons in the vacuum, E_k is defined by:

$$E_k = h\nu - E_B - \phi_S$$

Equation 2.1

where $h\nu$ is the energy of the incident photon, h being Planck's constant and ν is the photon frequency, ϕ_S is the work function and E_B is the electron binding energy in the material.

The Fermi level of a material is defined as the energy level at which an electron has a binding energy of 0 eV. In this case, equation. 2.1 can be simplified to:

$$E_k = h\nu - \phi_S$$

Equation 2.2

As the electron analyser has a work function of its own (ϕ_A), which is different to the sample (ϕ_S), this must be corrected for in order for accurate measurement. This can be achieved by forming a contact potential at the detector equal to $\phi_S - \phi_A$ thereby offsetting the electron kinetic energy. Applying this correction to equation. 2.1 gives:

$$E_k = h\nu - E_B - \phi_S + (\phi_S - \phi_A)$$

Equation 2.3

Which can be simplified to

$$E_k = h\nu - E_B - \phi_A$$

Equation 2.4

which is the measured kinetic energy in the electron analyser. The energy levels involved in the photoemission process are depicted in Figure 2.1.

Some electrons undergo inelastic collisions whilst passing through the crystal. The electrons which scatter in this manner and still make it to the surface form a low energy continuum known as the secondary electron tail. Other photoemission techniques can also measure the momentum of the electron, rather than just the kinetic energy, in order to image electronic structures, but these will not be discussed in this work.

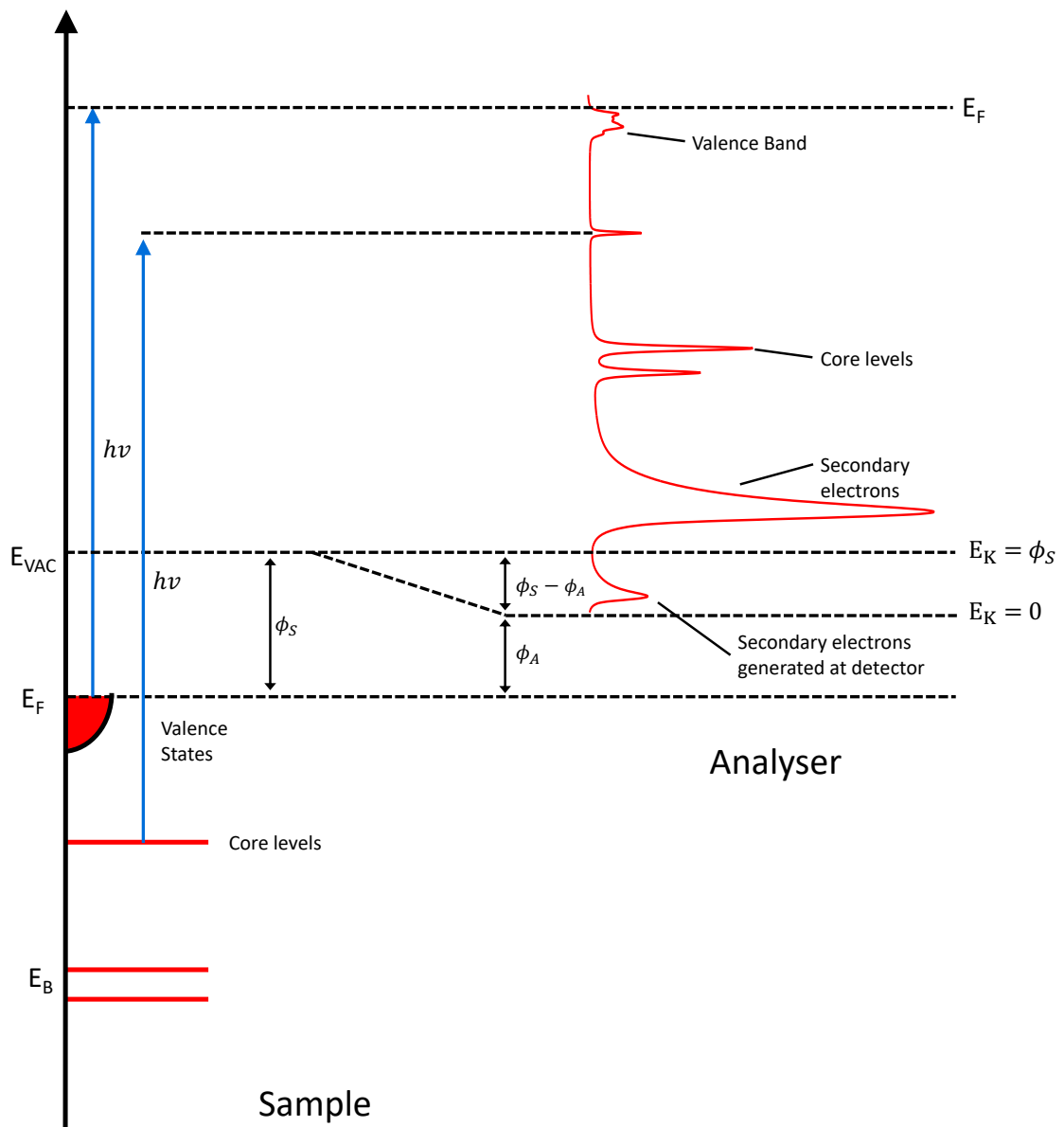


Figure 2.1: The relationship between the sample's electron energy states and the measured spectrum at the analyser. The energy band alignment between the sample and the analyser is shown by the dashed lines in the centre of the figure. The offset of the analyser spectra from the sample states is the excitation photon energy.

2.1.2 PHOTOEMISSION SPECTRAL FEATURES

There are many variants of photoelectron spectroscopy which can be used to probe different characteristics of materials. The two main types used in this work are XPS and UPS. Since its first use in the late 50s, XPS has become into one of the most versatile techniques in surface analysis. XPS utilises the high energy of X-ray photons (of the order of 1 keV) to excite deep core level electrons and thus determine their binding energy. Elemental composition then becomes readily available due to the uniqueness of core level binding energies for various elements [6].

Conversely, UPS uses lower excitation energies (generally <50 eV) and probes much lower binding energy electrons known as valence band electrons. The valence band electrons are of importance as they govern a wide range of surface properties. For example, the surface atoms are what define the surface energy when bulk coordination is lost thus the charge distribution of the surface defines the work function. UPS can also probe the electronic structure of adsorbates, giving the ability to measure bonding strength to the surface, as well as distinguishing what surfactants or surface termination is present [7]. Whilst X-ray photons are of sufficient energy to excite the valence band electrons, the photoionisation cross-section of valence band electrons is extremely low. This is overcome through the use of ultraviolet radiation, which dramatically increases the number of photon-electron interactions in this energy range, increasing the measured signal and leading to a higher energy resolution. Both techniques gain surface sensitivity due to the MFP of photoelectrons being of the order of nanometres. The lower kinetic energy photoelectrons emitted during UPS have an approximate mean free path of 0.5 nm, whereas the XPS

photoelectron MFP can be estimated as ~ 3 nm, leading to an enhanced surface sensitivity from UPS.

XPS and UPS spectra are affected by various mechanics which produce notable features in the data. Figure 2.2a shows an example XPS survey scan of a diamond surface, 2.2b shows a high resolution XPS spectrum of a sputtered silver sample, and a UPS scan of a diamond sample is given in 2.2c, all with the main features annotated.

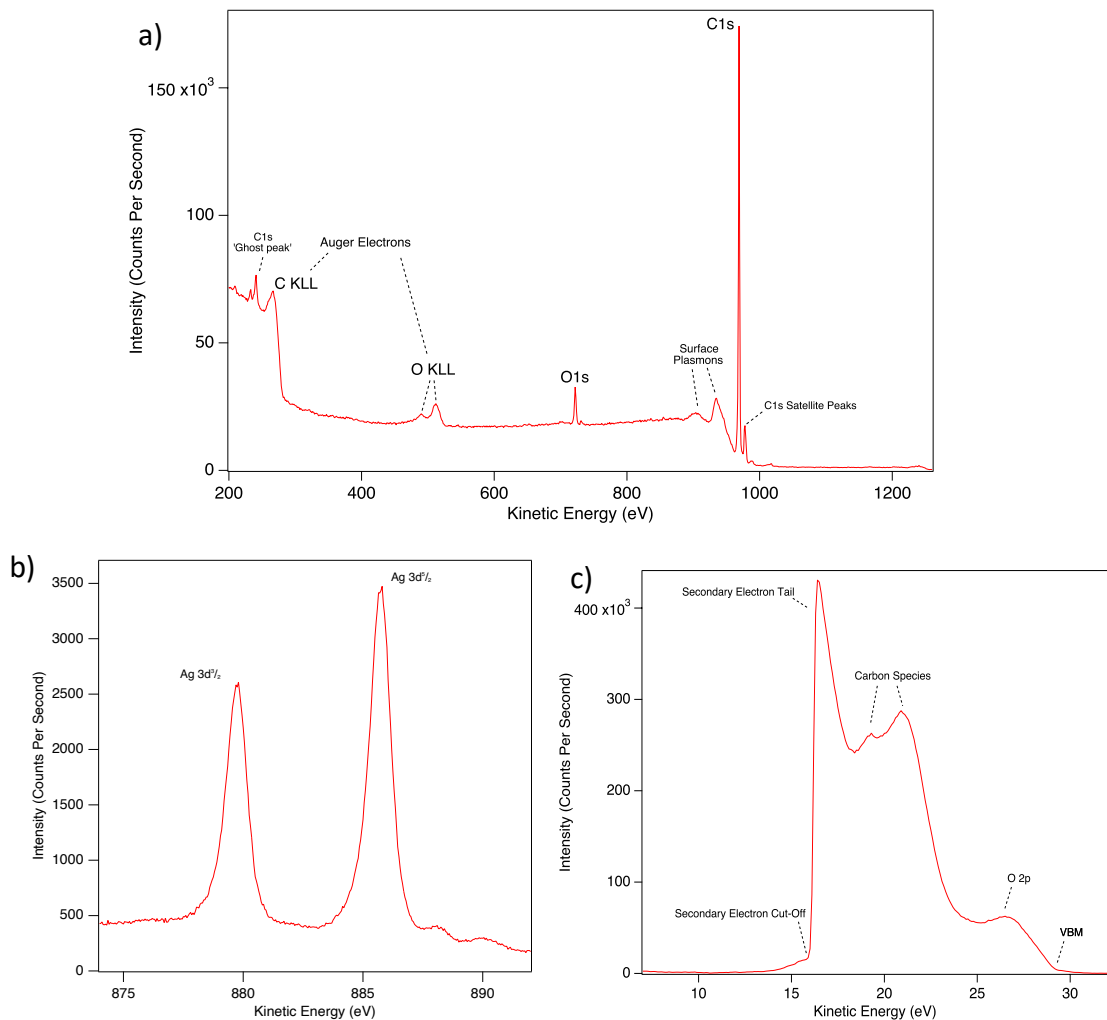


Figure 2.2: (a) An example XPS widescan of a diamond sample with prominent features labelled. (b) An example XPS core-level spectrum taken of the silver 3d peak showing the effect of spin-orbit coupling. (c) An example UPS widescan with main features labelled.

2.1.2.1 CORE LEVEL PHOTOEMISSION

As seen in the XPS widescan in Figure 2.2a there are two main core level peaks present (labelled C1s and O1s). These are conceptually the simplest features in XPS as they correspond to core level electrons which have been excited out of the sample and directly into the vacuum. Although core levels have an 'exact' binding energy, it is impossible to get delta-function like features in an XPS (or UPS) spectra due to peak broadening induced by the X-ray source and core-hole lifetimes. These will be discussed further in the XPS quantification and instrumentation sections.

2.1.2.2 SPIN-ORBIT COUPLING

Spin-orbit coupling is a crucial concept in photoemission. It arises due to angular momentum and spin properties of electrons in certain electron shells. Electrons possess both an orbital angular momentum, l , and a spin magnetic dipole moment, s . The interaction between these properties causes a splitting in electron energy levels due to the total angular momentum j , given by:

$$j = |l \pm s|, \text{ where } s = \frac{1}{2}$$

Equation 2.5

The behaviour of the spin-orbit coupling depends on the electron orbital shell as this determines the value for l . Table 2.1 shows the l and j values for s , p , d and f orbitals. For orbitals which have more than one value for j , spin-orbit coupling will be present; an example Ag 3d core-level spectrum is given in Figure 2.2b, where two peaks, which are present due to spin-orbit coupling, can be clearly seen. The degeneracy of energy levels also dictates the number of electrons which will be photoemitted from each given state. Therefore, by calculating the degeneracy the area ratios of split peaks can be determined. Degeneracy can be calculated by using

equation 2.6 and is shown in Table 2.1 with the area ratios which will be measured by XPS.

$$\text{Degeneracy} = 2j + 1$$

Equation 2.6

Table 2.1: The l values for various sub-shells and the calculated j values, degeneracy and area ratios.

Sub-shell	l value	j value(s)	Degeneracy ($2j + 1$)	Area Ratio
s	0	$1/2$	2	n/a
p	1	$3/2, 1/2$	4, 2	2 : 1
d	2	$5/2, 3/2$	6, 4	3 : 2
f	3	$7/2, 5/2$	8, 6	4 : 3

2.1.2.3 AUGER ELECTRON EMISSION

Another prominent spectral feature is due to a process known as the Auger effect. The photoelectrons emitted via this process are therefore commonly called ‘Auger electrons’. The Auger effect, depicted in Figure 2.3, is a secondary emission process whereby a photoelectron is emitted from an atom due to the de-excitation required to fill a core-hole left by an initial photoemission process. During the filling of a core-hole the electron must lose energy equal to the difference in the initial and final energy states. This relaxation process can either result in the creation of a photon or the emission of a second electron, providing the energy loss in the relaxation is sufficient to overcome the binding energy of the secondary electron. The nomenclature of Auger electrons is determined by the three shells involved in the process, using the X-ray notation K, L, M, (N, O) or V for electrons in the s , p , d , (f , g) shell or the valence band, respectively. Shown in Figure 2.3 are three examples of Auger emission processes. Figure 2.3a shows a KLL (KL_1L_2) transition, where a K core-level electron is emitted, causing an L electron to relax and the emission of an L

electron. Figure 2.3b shows an LVV (L_3VV) Auger process where an L core-level electron is emitted, causing an electron to relax from the valence band (VB) and then the emission of a second valence band electron. Figure 2.3c shows an LLM ($L_1L_2M_1$) Auger emission where an L core-level electron is emitted, causing an L electron to relax and the emission of an M electron. This is a special case of Auger emission, where the hole is filled by an electron from the same shell, but different sub-shells, known as a Coster-Kronig transition [8]. A super Coster-Kronig transition is where the initial photoelectron, relaxing electron and Auger emitted electron all come from sub-shells in the same electron shell. Coster-Kronig transitions are important as they can cause large screening effects due to doubly positive orbitals which can form. This can lead to changes in core-level lines shapes, especially in higher shells ($p, d, f...$), which will be discussed in the XPS quantification section.

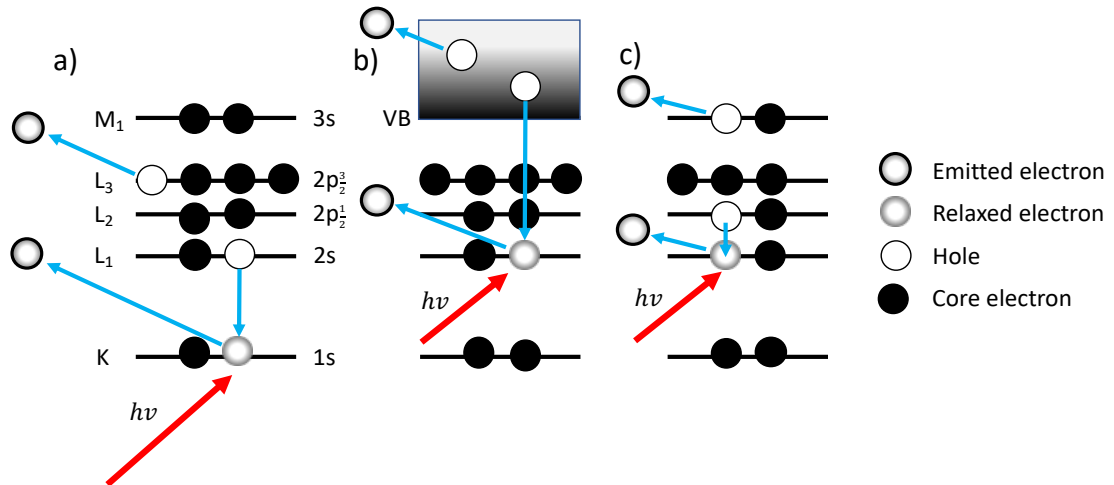


Figure 2.3: a) A KLL Auger emission process, b) an LVV Auger emission process and c) a LLM Auger emission process. Blue arrows indicate electron processes (emission, relaxation) and the red arrows ($h\nu$) indicates the incident photon.

The kinetic energy $E_{k(XYZ)}$ of an Auger electron for any three core level transition XYZ can be calculated from the binding energies E_X, E_Y, E_Z using equation.

2.7.

$$E_{k(XYZ)} = E_X - E_Y - E_Z$$

Equation 2.7

where E_X is the primary electron binding energy, E_Y is the relaxing electron binding energy and E_Z is the emitted Auger electron binding energy. A useful quality of Auger electrons is their kinetic energy is constant, regardless of the excitation energy used. Because of this, many home labs utilise 2 excitation sources which can be used to offset core level features away from Auger emission features, or identify unknown features as Auger electrons by checking for a constant kinetic energy for both excitation energies.

2.1.2.4 PLASMON LOSS, SATELLITE PEAKS AND OTHER FEATURES

During photoemission the emitted electron may undergo a number of interactions as it propagates through its host material. These interactions or ‘many-body effects’ include, but are not limited to, electron-electron interactions, electron-phonon coupling, or electron-defect scattering. One such process is plasmon creation. Peaks associated with plasmon formation arise due to interactions between the photoelectron and quantised vibrations in the valence band or the free electron sea in metals. During the creation of plasmons, the photoelectron loses energy equal to that of the created plasmon energy, creating ‘plasmon loss’ features [9]. There are two main types of plasmons, depending on how they are created: intrinsic and extrinsic.

Extrinsic plasmons occur as the electron travels through the material and incurs losses in energy due to coupling between the valence band electrons and the electric field of the photoelectron. Intrinsic plasmons occur simultaneously with the photoemission process in an area localised to the atom. As the electron is ejected the

positively charged core-hole produced may couple with oscillations in the valence band, causing the electron to be emitted with a lower energy [10], [11].

In both cases the energy loss is proportional to the frequency, or a multiple of, the coupled vibrations ω_p . This vibrational frequency is different for bulk and surface oscillations. The plasmon energy loss will therefore be $n\hbar\omega_{pb}$ or $n\hbar\omega_{ps}$ for bulk and surface plasmons, respectively, where \hbar is the reduced Planck's constant, n is an integer value and ω_{pb} and ω_{ps} are the bulk and surface oscillation frequencies, respectively [12]. Other features in XPS spectra can be linked to the instrumentation used, namely the X-ray source. These are satellite peaks, ghost peaks and crosstalk peaks.

Satellite peaks occur when a non-monochromatic light source is used meaning multiple incident photon energies are present. As the photoelectrons' kinetic energy depends on the excitation energy, electrons with a range of kinetic energies are produced from each core-level. Satellite peaks for commonly used lab-based X-ray sources can be well described from the precalibrated X-ray emission profile of the sources. Table 2.2 shows the emission profile properties of two commonly used X-ray sources, magnesium and aluminium X-ray anodes. Shown are the principal emission photon energy, the emission lines with the relative photon

Table 2.2 The emission properties of two commonly used lab-based X-ray sources; magnesium and aluminium anode sources.

Source	Principle Photon Energy (eV)	Property	$k\alpha_{1,2}$	$k\alpha_3$	$k\alpha_4$	$k\alpha_5$	$k\alpha_6$	$k\alpha_7$	$k\alpha_8$	$k\beta$
Mg	1253.6	Displacement (eV)	0	8.4	10.2	17.5	20.0	19.2	15.7	48.5
		Relative Height (%)	100	8.0	4.1	0.55	0.45	0.3	0.1	0.5
Al	1468.3	Displacement (eV)	0	9.8	11.8	20.1	23.4	21.8	18.5	69.7
		Relative Height (%)	100	6.4	3.2	0.4	0.3	0.1	0.1	0.55

energy and their relative intensity. As the relative intensities and energies are known, a simple procedure can be implemented to remove these features from the measured spectra. This information is used in the software developed in this work to remove satellite peaks from data which is described in more detail in the XPS quantification section. These features can be seen at a slightly higher kinetic energy than the C1s and Ag3d core levels in Figures 2.2a and 2.2b, respectively.

Ghost peaks arise from contaminants, such as oxides, present on the X-ray anode which produce secondary X-rays with varying photon energies, depending on the contaminating element. Oxygen ghost peaks are very common in lab based XPS due to the difficulty of cleaning the anodes once installed. Copper is another possible signal as Mg or Al is usually deposited onto copper, but this is less common with more modern X-ray sources employing a barrier layer of Ag to negate this effect. Oxygen produces a primary emission line $K\alpha$ at 525 eV, sufficient to excite the C1s core level electrons. The ghost peak produced can be seen in Figure 2.2a at approximately 250 eV.

A final source-based feature which may be present is from a process known as 'cross-talk'. Commonly, magnesium and aluminium anodes are present in one X-ray gun (seen in section 3.2.1) called a twin-anode source. Based on the geometry of the system, electrons which are accelerated towards one anode can leak across to impinge onto the second anode, leading to a small amount of X-ray emission from the non-desired source. These unwanted X-rays can lead to puzzling photoemission peaks. A typical twin anode gun produces <1% of crosstalk during use, but this may be sufficient to be a concern when analysing XPS spectra.

2.1.2.5 UPS FEATURES

UPS spectra provide information on the valence band structure and electronic properties with high surface sensitivity. As with XPS some low binding energy core-levels can be measured; in the example UPS spectrum shown in Figure 2.2c the oxygen 2p core level as well as some carbon-containing features can be seen. Other useful features are; the secondary electron tail, and secondary cut-off, which are at the low kinetic energy side of the spectrum, the valence band maximum, which can be seen on the high kinetic energy edge, and in some measurements the Fermi edge, which can be used to calibrate the energy scale to the Fermi level. The energy of these features can be used to calculate properties such as the work function and the electron affinity of the sample. States beyond the secondary cut-off point, as seen by the small feature which extends beyond 15 eV on Figure 2.2c, may be induced by; regions of differing work function, instrumental effects, such as secondary electron generation at the detector or through the analyser, surface states, or thermionic emission processes from within the bandgap [13].

2.1.3 PHOTOIONISATION CROSS SECTION

When analysing XPS spectra it is vital to consider the photoionisation cross-section σ for a true quantification. The photoionisation cross-section is the parameter which describes the likelihood of an electron containing system to produce a photoelectron. It is defined as the sum of the probabilities for photoionisation for a given photon energy $h\nu$ from all possible excitation paths of all electron orbitals per unit area, per unit time.

The probability P for an electron to transition from an initial state i to final state f is given by Fermi's golden rule.

$$P_{i \rightarrow f} = \frac{2\pi}{\hbar} |\langle \psi_f | \Delta | \psi_i \rangle|^2 \rho$$

Equation 2.8

where ψ_f and ψ_i are the wavefunctions of the final and initial states, Δ is the perturbation Hamiltonian between the two states, and ρ is the density of states in the material. Fermi's golden rule applies to initial states that have not been depleted due to previous photoionisation events.

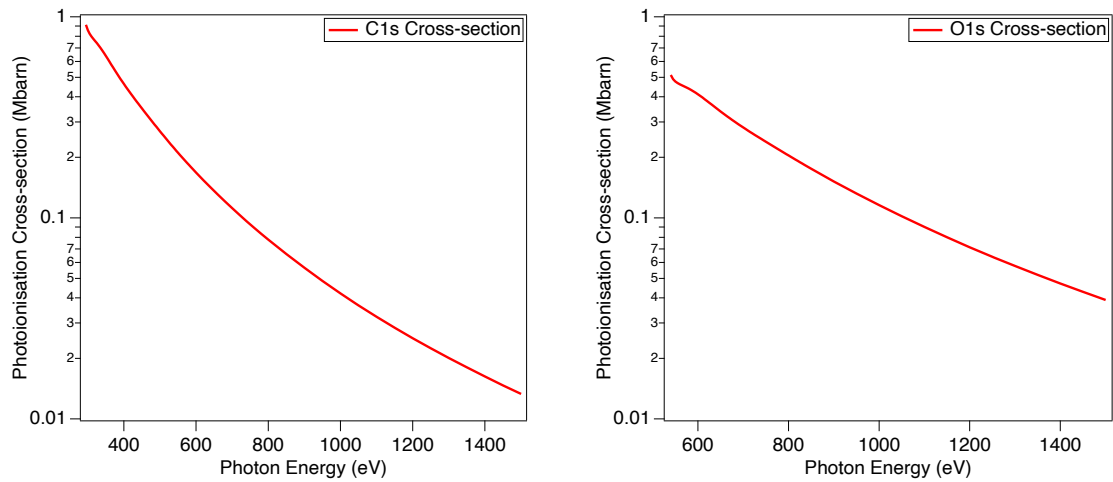


Figure 2.4: (left) The photoionisation cross-section for the carbon 1s and (right) the photoionisation cross-section for the oxygen 1s core level.

The photoionisation cross-section as a function of photon energy has been calculated for many elements and can be used to normalise peak areas on XPS spectra when performing a quantitative analysis. Example photoionisation cross-section values for photon energies up to 1500 eV are shown for C1s and O1s core levels in Figure 2.4. The C1s and O1s cross-sections are plotted on the same logarithmic scales to highlight the effect of photon energy as well as how drastically the cross-section can vary between elements. The trend in photoionisation cross-section with increasing photon energy is due to the overlap between the wave functions of the incident photon and the core level decreasing. This property can be very beneficial when using variable energy photon sources. By selecting photon energies near the

measured core level's binding energy, the signal intensity can be increased by multiple orders of magnitude, when compared to lab-based sources.

2.1.4 ELECTRON MEAN FREE PATH

Most photoelectrons generated are not immediately emitted into vacuum. They must first travel through the sample some distance before reaching the surface. It is therefore imperative to consider the electron MFP (sometimes referred to as the electron attenuation length). As mentioned previously, as an electron propagates through a medium, it may undergo inelastic scattering events, which will cause kinetic energy of the electron to be lost. The average distance which an electron will travel before undergoing some scattering event is known as the electron Inelastic Mean Free Path (IMFP). The IMFP is dependent on the kinetic energy of the photoelectron, as well as the propagation media. The IMFP λ as a function of kinetic energy E_k can be approximated by equation 2.9 and is shown in Figure 2.5 [14].

$$\lambda = \frac{143}{E_k} + 0.054\sqrt{E_k}$$

Equation 2.9

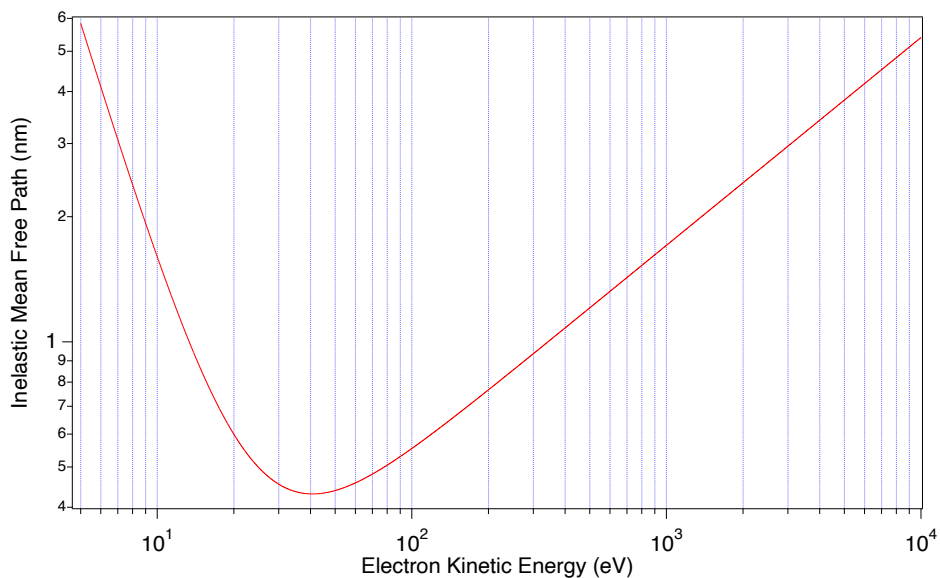


Figure 2.5: The inelastic mean free path approximate function for electrons travelling through any material. The actual IMFP values are scattered around this function.

The electron IMFP is important as it dictates the intensity of the measured signal as a function of the depth that the photoelectron was generated. It is also what is responsible for the large secondary electron tail mentioned earlier. If the intensity of emitted electrons from a clean bulk sample is known, the measured intensity, and normal emission can be calculated by using the Beer-Lambert law, shown in equation 2.10.

$$I = I_0 e^{-\frac{x}{\lambda}}$$

Equation 2.10

where I is the measured intensity, I_0 is intensity from the bulk material, x is the depth at which the photoelectron is generated, and λ is the electrons IMFP.

As the IMFP is on the scale of nanometres, any photoemission based techniques are also surface sensitive within the nanometre range, even though X-ray penetration is generally orders of magnitude larger. For example, if measuring electrons with a kinetic energy of 40 eV (the minimum on the IMFP curve), 3 electrons from a depth of 2 nm or more into the sample will have a 99% chance of scattering and not being emitted into vacuum, leading to a very high surface sensitivity.

Surface sensitivity can also be tuned by changing the detection angle with respect to the sample surface. A simple depiction of this is shown in Figure 2.6, where on the left is a measurement at normal emission and on the right the measurement angle θ is 45 degrees from the surface normal. The highlighted areas would be the relative depth d from which photoelectrons are emitted. The depth is related to the cosine of the measurement angle. The measurement depth at 45 degrees is approximately 70% of the depth when measuring normal to the surface.

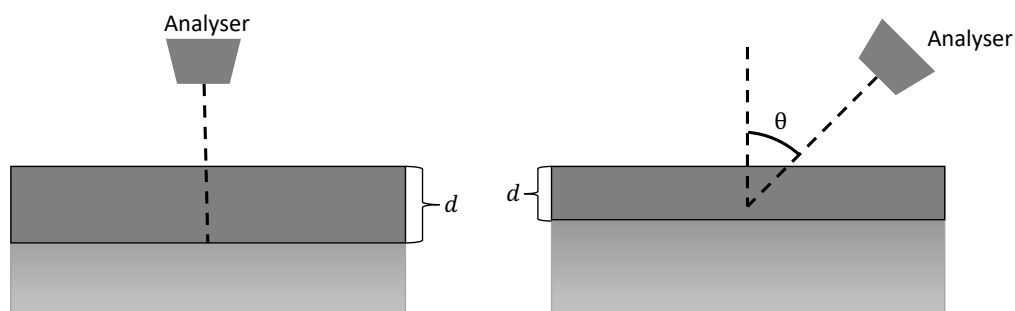


Figure 2.6: A simple schematic showing how the measurement angle affects the surface sensitivity of the technique. The dark grey areas show the relative depth for which signal will be measured.

Therefore, being able to tune the photon energy, as well as the measurement angle provides control over the measurement depth, which can be utilised to provide insight into the chemical profile through a material.

2.1.5 REAL-TIME ELECTRON ENERGY SPECTROSCOPY (REES)

Traditionally, XPS or UPS is a measurement of a thermally and/or chemically 'static' system where, in the simplest case, one kinetic energy is measured at any one time and voltages in the hemispherical analyser (detailed in section 3.6) are swept step-by-step in order to build up a spectrum. However, with the availability of Charge-Coupled Devices (CCDs) and multi-channel electron multipliers it is possible to simultaneously collect data for a range of kinetic energies, whilst still maintaining a reasonable signal-to-noise ratio (SNR). This opens the possibility of taking time-resolved XPS as entire core-levels can be measured in a single acquisition. REES has predominantly found use in studying the effect of temperature, deposition or other surface processing techniques which can be performed *in-situ*. Previous applications of REES include, but are not limited to; the study of the growth of epitaxial graphene on diamond-iron substrates [12], [15], monitoring binding energy shifts induced by surface photovoltage [16], measuring band alignments of organic-inorganic

interfaces [17], directly observing Schottky to ohmic contact transitions [18], as well as detecting molecular organization in organic semiconductor thin films [19].

2.2 QUANTIFICATION OF XPS AND THE DEVELOPMENT OF THE MATERIALS CHARACTERISATION SUITE

Quantification of XPS is a crucial aspect of the technique and is necessary to garner the most information about the sample's surface properties. Widescans can be used to calculate the stoichiometry of a material, and higher resolution scans can determine the bonding type, charge states or spin-orbit splitting. Further properties such as core-hole lifetimes, structural features or the presence of electron shielding may also be measured. The quantification of XPS, however, requires fitting of generated line-shapes to the measured data, and for trustworthy quantification, this method must be rigorous and controlled. During this work a bespoke analysis program for XPS and REES, dubbed the Materials Characterisation Suite (MCS), has been developed by a number of members of the materials group at Aberystwyth University, namely Dr Simon Coolil, Mr Joseph Durk and Dr Thomas Knight. However, the main bulk of the coding was implemented by the author. MCS is written in IgorPro8 with the hope of producing a tool which, can not only provide robust fitting capabilities, but also give the control over all fitting parameters needed by the user, whilst maintaining a user-friendly interface. Whilst other commercial fitting software exists, certain functionalities which would be beneficial have been slow to be implemented. Some of the ambitions of the MCS are as follows:

- Increase the throughput of spectra being analysed whilst maintaining physical accuracy.
- Provide the ability to fit with true Voigt convolutions, with asymmetry
- Active background fitting capabilities

- Expediate the process of fit propagation through multiple spectra (REES analysis)
- Bring in other analysis packages to create a multidisciplinary analysis software suite.

This section will present and compare the functions used to model XPS core-levels. As well as detail the post-acquisition steps required for a quantitative analysis and describe how these were implemented in the aforementioned MCS program during this work.

2.2.1 THE PHOTOELECTRON PEAK LINE-SHAPE

2.2.1.1 THE VOIGT AND PSEUDO-VOIGT FUNCTIONS

As mentioned previously, the signals attributed to photoemission from core-levels are not perfect delta functions, unless one were to measure a core level with an infinitely long core-hole lifetime, using a spectrometer with infinite resolution, and a perfectly monochromatic X-ray source [20]. However, with this not being the case, a convolution of the delta function and broadening effects must be used to describe the core-level shape. Because of these factors, the shape of the peak can provide insight into the materials properties, more than just the intensity and the peak position can alone. The photoelectron peak line shape arises from the convolution of imperfect instrumentation and material based effects which together produce a Voigt function. A Voigt function is the convolution of a normalised Gaussian and a normalised Lorentzian function. The normalised Gaussian $G(E)$ and Lorentzian $L(E)$ functions are shown in eq. 2.11 and 2.12, respectively.

$$G(E) = \sqrt{\frac{4 \ln 2}{\pi \omega_G^2}} e^{-\left(\frac{4 \ln 2}{\omega_G^2}\right)(E-E_0)^2}$$

Equation 2.11

$$L(E) = \frac{1}{2\pi} \cdot \frac{\omega_L}{\left(\frac{\omega_L}{2}\right)^2 + (E - E_0)^2}$$

Equation 2.12

where ω_G and ω_L are the Gaussian and Lorentzian Full-Width at Half-Maximum (FWHM), respectively and E_0 is the peak central energy.

Typical contributors to Gaussian broadening are instrumental effects such as; entrance/exit slit widths, electron and X-ray focussing elements, X-ray energy distribution from monochromators and synchrotron undulators, and surface roughness. Typical Lorentzian contributions arise from; anode X-ray sources and the measured element core-hole lifetimes.

The Voigt convolution is mathematically shown in equation 2.13 and is numerically calculated during the fitting of data using the IgorPro8 convolve function, expressed in equation 2.14.

$$V(E) = G(E) \otimes L(E)$$

Equation 2.13

$$V[p] = \sum_{m=0}^{N-1} G[m] \cdot L[p - m]$$

Equation 2.14

where \otimes is the convolution integral, N is the number of data points in the input datasets, and p and m correspond to elements in the output and the input datasets, respectively. It can be described as the sum of the point-by-point product of the overlapped datapoint as a reversed copy of the Gaussian dataset is swept across the

Lorentzian dataset. Finally, the FWHM of the Voigt profile can be approximated using the Gaussian and Lorentzian widths by equation 2.15. Equation 2.15 is exact for a pure Gaussian and gives an error of 0.0003% for a pure Lorentzian.

$$\omega_V \approx 0.5346 \omega_L + \sqrt{0.2166 \omega_L^2 + \omega_G^2}$$

Equation 2.15

In theory, a Voigt function provides the best fit possible, but has traditionally been considered computationally expensive, due to the need for a convolution [21]. For the most part with modern day computers, this is negligible, however when it is necessary to fit core levels with many components, or a large number of core levels require fitting, such as in REES analysis which can consist of 1000s of spectra, the computational effort saved by using less ‘intense’ fit functions becomes prevalent.

The pseudo-Voigt function is a numerical approximation to the true Voigt convolution and is considerably less computationally expensive. There are two main methods for forming a pseudo-Voigt profile; the product method, which involves the multiplication of Gaussian and Lorentzian functions, and the sum method, where the addition of a Lorentzian and Gaussian function is calculated. In both cases, a mixing factor μ is used as a measure of the Lorentzian-Gaussian ratio [22]. The sum form of the pseudo-Voigt $pV(x)$ is given in equation 2.16 using the Gaussian and Lorentzian equations given in 2.13 and 2.14. The product form has been consistently shown to produce inferior fitting results, and so will not be used in this work [21].

$$pV(E) = A \cdot \{(1 - \mu) \cdot G(E, \omega_p) + \mu \cdot L(E, \omega_p)\}$$

Equation 2.16

where A is the area of the pseudo-Voigt, and ω_p is the FWHM of the pseudo-Voigt. Note the same width parameter is used in both the Gaussian and Lorentzian

contributions, this is due to the linear approximation of the pseudo-Voigt profile. A height parameter is commonly stated in place of area, depending on whether the pseudo-Voigt is normalised by height or by area. ω_p can be estimated from given Gaussian and Lorentzian FWHM contributions by equation 2.17 [23], [24].

$$\omega_p \approx \left[\omega_g^5 + 2.69269\omega_g^4\omega_L + 2.42843\omega_g^3\omega_L^2 + 4.47163\omega_g^2\omega_L^3 + 0.007842\omega_g\omega_L^4 + \omega_L^5 \right]^{\frac{1}{5}}$$

Equation 2.17

This can then be used to calculate the mixing factor μ , required to produce the respective Voigt profile with an accuracy of 1% using the equation:

$$\mu \approx 1.36603 \frac{\omega_L}{\omega_p} - 0.47719 \left(\frac{\omega_L}{\omega_p} \right)^2 + 0.11116 \left(\frac{\omega_L}{\omega_p} \right)^3$$

Equation 2.18

Commonly, the mixing factor is a fit parameter which is allowed to float, due to the computational inefficiency required for the above calculation during fitting. This means extra care is required if quoting Gaussian and Lorentzian contributions from a pseudo-Voigt fit. Once the pseudo-Voigt width is generated and the mixing factor is adjusted, the parameters which initially defined the Lorentzian and Gaussian contributions are rendered obsolete. When fitting XPS it is beneficial to know the true Gaussian and Lorentzian values, as well as the FWHM of the Voigt function. For example, when taking XPS measurements at a synchrotron, the Gaussian width contribution should correspond to the spectral bandwidth of the undulator and monochromator, combined with the analyser resolution. All of these should have known values.

This is shown in Figure 2.7, which contains 2 sets of peaks. The 8 peaks on the left are Voigt profiles centred on $x = 0$ and calculated from varying Gaussian and

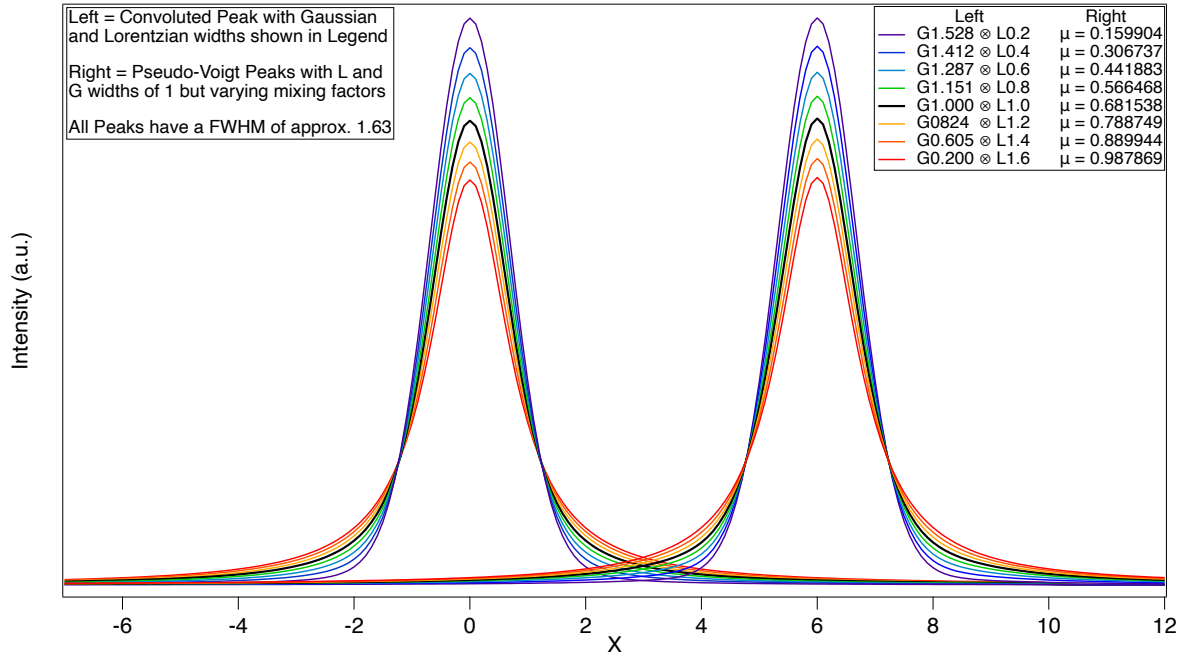


Figure 2.7: (left) A set of Voigt profiles calculated using a range of Lorentzian and Gaussian width contributions, shown in the figure legend. (right) A set of pseudo-Voigt functions which are calculated using Gaussian and Lorentzian contributions of 1, but varying mixing factors. All profiles have a FWHM of approximately 1.63.

Lorentzian contributions, but all of which provide a Voigt FWHM of approximately 1.63. The 8 peaks on the right of the graph are a series of pseudo-Voigt profiles, centred around $x = 6$, also with a FWHM of approximately 1.63, and **all** of which had an input value for ω_G and ω_L of 1, whilst only the mixing factor μ value was varied. The values for μ were selected to mimic the Voigt counterparts shown.

Figure 2.7 highlights the impact that the mixing factor can have when calculating a pseudo-Voigt function. Although this may seem detrimental to the use of pseudo-Voigt profiles, it is far from the case. By adjusting a single variable, rather than calculating it using equation 2.18, the fitting procedure remains quick and efficient. When the fit is complete, the Lorentzian and Gaussian widths which would produce an identical Voigt profile are calculated, within an error of <1%, using equations 2.18 and 2.15.

2.2.1.2 ASYMMETRY

So far, only symmetric peak profiles have been discussed, however these only describe the profiles of core-level emission from semiconductors. Asymmetry in photoemission signals is caused by a number of effects; overlapping sub-signals due to the presence of extended satellites or multiple chemical states, vibrational excitations caused by the photoemission process and multi-electron excitations, and photoelectron energy loss via hole-pair formation as the photoelectron travels through the large density of states near the Fermi-level in metals. The majority of these effects can be modelled using a sum of many symmetric components. However, the asymmetry caused by the electron energy loss mechanism in metals cannot. Thus, an asymmetric peak function is required to produce a reliable analysis.

There is a plethora of asymmetric functions which have been formulated over the past 5 decades and it is still heavily debated today as to which is the 'best' one to use. Some profiles are derived from a theoretical standpoint, whereas some models approach analysis from a more heuristic point-of-view.

Probably the most prominent theoretical approaches are the Doniach-Šunjić and Mahan profiles [25], [26]. Both methods attempt to mathematically describe the many electron effects seen in metals. While application of both these methods are possible and theoretically valid, there are certain cons to using each. The Mahan profile, for example, would require two convolutions per peak to implement. As mentioned before, this is possible with modern day computers, but can still cause issues when fitting many components or REES data. The Doniach-Šunjić method suffers from complications during fitting due to assumptions made for the model. The D-S profile requires energy losses for photoemitted electrons by many-body effects

to be smaller than the material valence band. This leads to the possibility of non-physical effects in the peak tail for areas which are far away from the peak centre. It is also impossible to truly integrate the area under a DS curve as the asymmetric tail never converges to 0, therefore a cut-off for integration must be used.

Less commonly used asymmetric curves, such as the Gelius curve or the exponential asymmetric blend curve, involve adjusting or ‘blending’ the symmetric peak profile with a secondary function. The secondary function is usually only applied to the lower kinetic energy side of the peak in order to produce the asymmetry.

Another style of approaching asymmetry is by substituting energy-dependant functions in place for the width parameter ω into the pseudo-Voigt function itself. There are a number of suggested functions for the width parameter. *Kojima, 1987* proposed the use of a linear function [27], *Evans 1991* put forward the idea of defining an asymmetry parameter based on the separate half-width at half-maximum parameters for either side of the peak. However, a 2-parameter sigmoidal function shown in ref. [20] has been shown to give some of the best fits for complex asymmetric profiles without introducing non-physical artefacts. The asymmetric-pseudo-Voigt function denoted by pV_A is shown in full in equation 2.19 and 2.20.

$$pV_A(E) = A \left\{ (1 - \mu) \left[\sqrt{\frac{4 \ln 2}{\pi \omega(E)^2}} e^{\frac{-4 \ln 2 (E - E_0)^2}{\omega(E)^2}} \right] + \mu \frac{1}{2\pi} \left[\frac{\omega(E)}{\left(\frac{\omega(E)}{2}\right)^2 + (E - E_0)^2} \right] \right\}$$

Equation 2.19

where:

$$\omega(E) = \frac{2\omega_0}{1 + e^{-a(E - E_0 - b)}}$$

Equation 2.20

where a is the asymmetry factor and b is the shift of the sigmodal function relative to the peak position.

Equation 2.20 dictates the asymmetric nature of the resultant profile. By substituting a function in place of the width parameter, a profile with a varying width is formed. In other words, if one took a small section of the asymmetric profile for some value x it would look like a similar section from a symmetric peak made using the value $\omega(x)$. When the asymmetry value $a = 0$ a symmetric peak is produced. However, when a is non-zero, equation 2.9 results in an asymmetric profile with a FWHM ranging from 0 to $2\omega_0$, where the tail eventually converges to a symmetric peak profile of width $2\omega_0$. Figure 2.8 shows one symmetric peak (2.8a) and two asymmetric peaks (2.8b, c) with their corresponding width functions showing how $\omega(x)$ distorts the peak shape. All three pseudo-Voigts in Figure 2.8 have a width parameter ω_0 value of 1.63, an area parameter of 1, a peak centre of 0 and a mixing factor μ of 0.5. Figure 2.8a has a value for a and b of 0, Figure 2.8b has a value of -1 for a and 0 for b and Figure 2.8c has a value of -1 for a and b .

It should be noted that this function (as with all asymmetric functions) can cause discrepancies between the generated peak's properties, and the parameters used in the model. For example, there is a noticeable change in the peak FWHM, peak centre (or maximum) and peak area (intensity) for the 3 curves shown in Figure 2.7. Therefore, care should again be taken when using asymmetric line shapes, and some of the mentioned properties may need to be calculated numerically, post analysis.

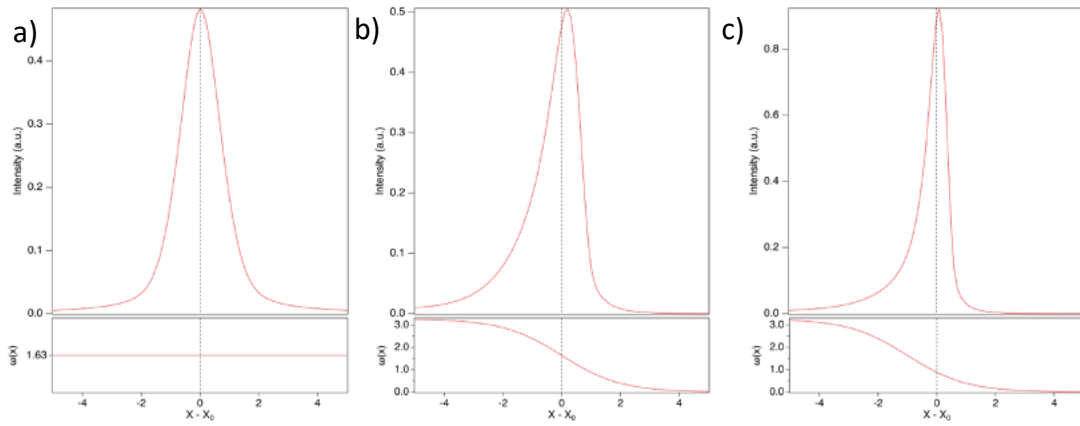


Figure 2.8: a) A symmetric pseudo-Voigt function and the width function associated with it below. Note the function is constant, resulting in a constant width. b) The same peak but with a value given for a in equation 2.20 of -1. Note on the RHS of the peak, the FWHM appears smaller than that on the LHS which converges towards a symmetric peak profile with a width of $2\omega_0$. c) The same peak, but with a value of -1 for both a and b in equation 2.20. Note the sigmoidal is shifted so the majority of the peak area is on the lower end of the possible values of FWHM, resulting in a much narrower peak, but that still converges towards a width of $2\omega_0$.

For the MCS, asymmetry was also required for the Voigt convolutions. As mentioned before, there are some methods which can be applied in order for an asymmetric convolution, such as the Mahan profile, but a less computational expensive method would be preferred. For this, the same idea of using a function in place of the width parameter has been implemented. When using the asymmetry function in the convolution, it is more physically justified [25], as well as computationally simpler, to apply it to the Lorentzian contribution only. This is due to most Gaussian broadening contributions being instrumentation-based and therefore not susceptible to the asymmetry-causing effects. This however should not deter the function's fitting ability. In fact, during testing of this idea, the addition of asymmetry appeared to have less impact on the peak properties, when compared to the input parameters. The peak position stayed more constant, the FWHM still differed in extreme cases but was also less affected, and the peak area remained very close to the initial value.

2.2.1.3 XPS BACKGROUND

The final contribution to the shape of XPS spectra is the background. So far, the examples given for the line shapes have been free of any background contributions. However, the Ag3d data given in Figure 2.2b clearly shows that the peaks are not sitting on a flat background. The background in XPS arises from the inelastic scattering of electrons as described in section 2.1.4, and there are various practical background models to choose from. The Tougaard background, for example, is one of the most well described backgrounds, and its physical origins are very well known, however implementation can be quite complex. Another background model was proposed by *D.A. Shirley* [28] originally in 1972 and developed further by *A. Proctor* and *P. M. Sherwood* [29]. Shirley type backgrounds assume the background due to energy losses can be related to the integral of the measured signal. Shirley steps are commonly approximated by a sigmoidal-like function. On top of the aforementioned background types, simple background shapes such as linear, quadratic or exponential functions can help when fitting a complex background but may provide no physical description to the system. In practice, the general approach is to use combinations of multiple background types to produce the most accurate fit.

There are also two approaches to implementing background removal. The most common method is to identify the background type, select two data points which define the fitting region, and then calculate and remove the background contribution prior to any parameter optimisation. This is the static approach. The less common, but more reliable and accurate approach is to include the background model in the parameter optimisation (fitting) process. This *active* approach has

repeatedly been shown to produce better fits, and provide advantages with regards to data requirements [30]–[32].

A thorough review of the plethora of background types and implementation methods is given in [31]. However, in the MCS program, two main background types are included currently, with a third in testing:

- 1) The Shirley-Vegh-Salvi-Castle (SVSC) background [30].**
- 2) The slope background [32] (in testing).**
- 3) Linear background**

The SVSC background is an active background procedure. It is a development on the Shirley-Proctor-Sherwood function and uses a scaled integral of each normalised Voigt (or pseudo-Voigt) component as its own background. It is shown mathematically in equation 2.21.

$$B_{SVSC,i}(E) = k_i \int V_i(E) dE$$

Equation 2.21

where k_i is the scaling factor or ‘step height’ of the i th Voigt peak, $V_i(E)$.

The slope background is a Tougaard-type background which again can be calculated actively during the fitting procedure. It is given by the scaled integral of the sum of the SVSC backgrounds and is given in equation 2.22.

$$B_{\text{slope}}(E) = k_{\text{slope}} \int \sum_{i=1}^{i=N} B_{SVSC,i}(E)$$

Equation 2.22

The linear background has been chosen to simply try to improve the robustness of the fitting procedure, if there is a particularly complex spectra to be fit. Plasmon loss peaks and satellite shake-up features can also pose a problem to fitting,

when they overlap with regions of interest. If these are known features and/or are far enough away from the areas of interest, Voigts/pseudo-Voigts can be applied to fitting background shapes themselves, in order to provide the highest fitting accuracy in the regions of interest.

2.2.2 THE MATERIALS CHARACTERISATION SUITE USER INTERFACE

The Materials Characterisation Suite is a program based in IgorPro8, originally developed to help expediate the photoemission fitting procedures used in IgorPro by members in the Aberystwyth surface science group. Currently, the software specialises on XPS and REES analysis, however it has been used in some form to analyse data from optical-based methods such as Raman and photoluminescence (see section 2.3). Future plans are to improve on, and add to, the analysis capability for non-photoemission based techniques.

XPS core-level and REES analysis are approached in different manners. Core level analysis aims to accurately quantify the multiple components which may be present. This requires a controlled, detailed, and robust fitting procedure in order to avoid misinterpretation. REES analysis employs a coarser approach to fitting, but it is necessary to propagate the fit through a large number of spectra in a controlled manner. Generally, only one or two components can be resolved in REES analysis due to the higher SNR and lower energy resolution. This is a result of the shorter acquisition times and higher pass energies required for REES measurements. Resolving and controlling components during the fit propagation, becomes increasingly more challenging the more components are present. However, REES analysis can measure very subtle changes in peak position, area and widths over time, useful for studying surface treatments or chemical transitions.

The MCS currently consists of 3 interface windows containing the workplaces for XPS analysis, REES analysis and an interactive periodic table, respectively. The interactive table is adapted from an Igor procedure developed in Aarhus University. The purpose of this is for looking up core level energies for each element, as well as the respective photoionisation cross sections. These three interfaces and the workflows for using each are discussed below.

2.2.2.1 XPS ANALYSIS PANEL

As mentioned previously, there are numerous factors which affect XPS core level signals. The number of components measured, spin-orbit splitting, photoionisation cross-sections, the excitation energy, satellites, and the instrument sensitivity all play a role in the final signal. This means an ideal XPS analysis software requires the ability to deal with a varying number of components, as well as perform a range of post-acquisition data processes. The simplified workflow implemented in MCS is shown in Figure 2.9, and an image the XPS panel is shown in Figure 2.10, with some of the important features highlighted.

Once the data are loaded into the software, normalisation and satellite subtraction can be performed before any fitting commences. These steps can be skipped or implemented at any point, if required. The normalisation deals with the photoionisation cross-section, as well as the transmission efficiency of the electron analyser, which varies with kinetic energy. Dealing with the cross-section is fairly simple as it is analogous to a 'relative sensitivity'. To do this, each data point is divided by the input cross section value (found on the periodic table panel, see section 2.2.2.3). Dealing with the sensitivity of the electron analyser is less trivial. As the analyser efficiency depends on the kinetic energy of the electron measured, a

correction function must be applied to the data. These correction functions are known as transmission functions, and vary between analyser, as well as between different modes on the same analyser. Transmission functions $T(E)$ can be exported alongside data on some acquisition software, however if this option is not available, they can be approximated by equation 2.23.

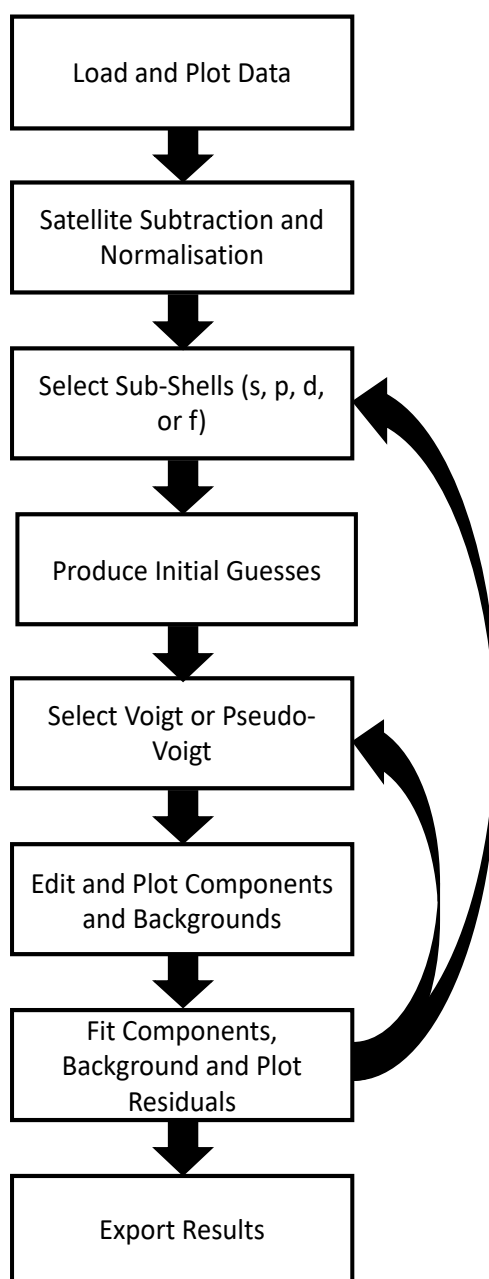


Figure 2.9 : The workflow used by the MCS program.

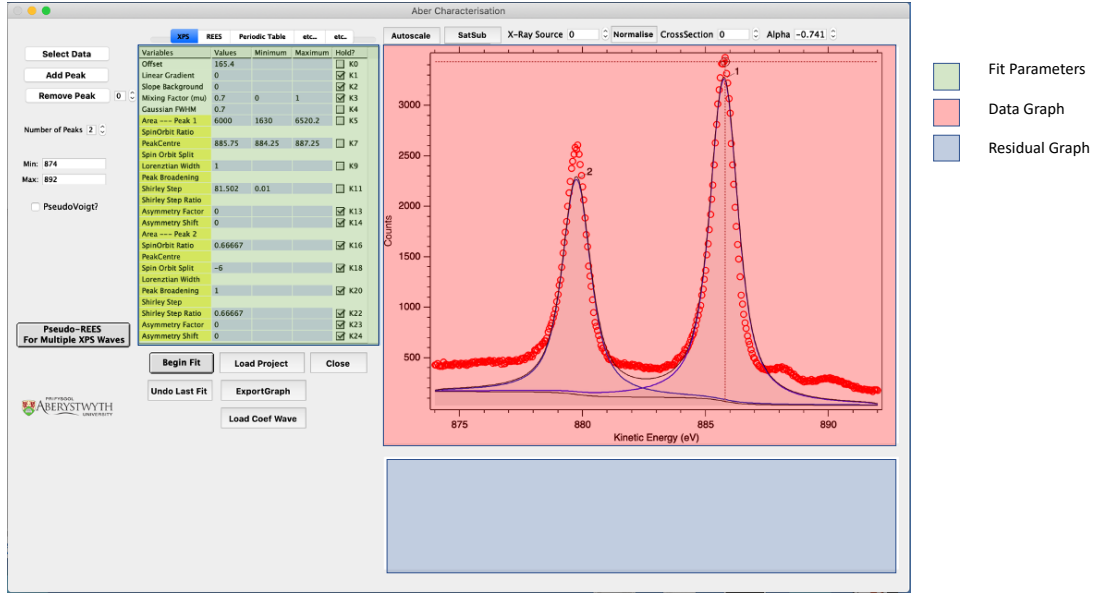


Figure 2.10 The MCS XPS panel in use with important areas highlighted as shown in the legend. Example data of an Ag3d core level with a d-peak added is given. The data has not yet been fitted.

$$T(E) \sim \frac{S}{\sqrt{E_k}}$$

Equation 2.23

where S is dependent on the analyser or analyser mode.

Currently, the MCS can use the transmission function for data loaded in from *SPECS Labs* software, if the transmission function was exported with the data. If a transmission function is not available, the data are corrected using equation 2.22 and a value for $S = 1$ used.

The final detail that should be accounted for during normalisation is the energy dependence of the MFP, detailed in section 2.1.4. In 1982, *W. Hanke, et al.*, proposed a model to approximate the MFP's λ dependency of the kinetic energy of the electron E_k , in the form of

$$\lambda(E_k) = aE_k^p$$

Equation 2.24

where α is a material-dependant term. The use of the energy-dependant exponential has no physical justification, but has been shown to approximate the IMFP for a large number of elements for photoelectrons with kinetic energy >300 eV [33]–[35]. The p parameter in equation 2.23 has been shown to be both a material and energy-dependant term. Values between 0.54 and 0.892 have been quoted in literature, for various materials and an extensive discussion on this parameter is given by *Powell* [36] and *Ebel* [37]. However, *Jablonski* [38] calculated an average value for p for three main material groups; elements, inorganic compounds and organic compounds, as well an average value for all materials. These are given in Table 2.3. The p values given produce an IMFP function with a deviation of 2-3% between a kinetic energy range of 500 and 1500 eV. However, it is suggested that at energies lower than this, the model will deviate, with an error of 20% reached at 200 eV. For most lab-based photoemission experiments, the large majority of core levels will not be affected too much by this deviation. However, for example, if one used an Al anode source (1486 eV) and measured two core-levels; one with a low binding energy (<300 eV), and one with a very high binding energy (>1300 eV), elemental ratio calculations may have errors > 20%. This may seem drastic but can still be considered an acceptable analysis in some cases.

Table 2.3: The average p values calculated for different groups of materials.

Material Class	Exponent Value p
Elements	0.7283
Inorganic Compounds	0.7234
Organic Compounds	0.7665
All Materials	0.7414

Synchrotron based experiments overcome this issue by adjusting the incident photon energy to ~ 100 eV above the measured core level binding energy, resulting in the emission of only low energy electrons. This not only increases the sensitivity of the measurement, but the measured electrons will also have a constant kinetic energy between core levels, leading to a constant IMFP. Therefore, it is only experiments with a constant excitation energy, and core levels at energies far from each other, where the exponent model for the IMFP may not be viable.

As well as normalisation, MCS provides the option for satellite subtraction to be applied to data. As with normalisation, this is generally done before fitting, but it is possible to do at any stage of the fitting process. The satellite subtraction can currently be performed on data taken using a magnesium or aluminium anode X-ray source. The subtraction procedure estimates contributions to the measured signal from the satellite emission lines produced by these sources, as detailed in section 3.2.1. To perform the subtraction, datasets are created using the raw data as a template. Then values for the energy difference from the main emission line, and the relative intensity for each (shown in Table 2.2) is used to shift and scale each copied dataset. These are then subtracted from the raw data to calculate the satellite-subtracted data. Figure 2.11 shows the effect of satellite subtraction on tin 3d core level data taken using a Mg anode. Figure 2.11a shows the raw data as well as the untrimmed datasets for each of the satellite contributions from $k\alpha_3 - k\alpha_8$. These are displayed on a logarithmic scale for clarity. 2.11b shows the raw data (red), the resultant sum of the satellites (blue) and the satellite subtracted data (black).

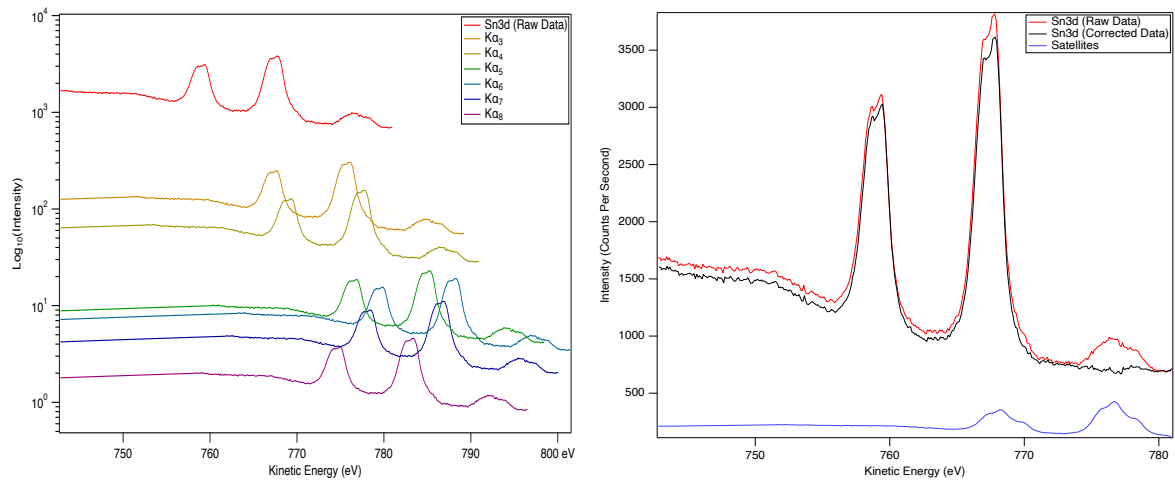


Figure 2.11: (left) The raw data (red line) and the satellite contributions calculated for a magnesium anode source. A logarithmic scale is used on the intensity axis for clarity. (right) The same example raw data (red), the satellite-subtracted data (black), and the total sum of the satellite contributions which was subtracted (Blue).

It is clear that the subtraction function provides a spectrum that is free from any major satellite contributions. Although some features around the satellite's region remain, these will be near-negligible when attempting to fit the regions of interest. This residual noise around the removed satellites is caused by a number of reasons, which relate to both the complexity of the emission profiles from the anode itself and a number of assumptions made for the satellite subtraction protocol. The two main assumptions are:

- The anode source is **perfectly** clean and oxygen free. The presence of an oxide layer (MgO or Al₂O₃) on the anode will cause the addition of other satellites as well as variations in intensity of already present satellites [39].
- The spectral width of all of satellite emission lines are the same. Every satellite dataset is simply scaled and shifted. No expansion or contraction, which would account for FWHM variations, has been performed.

After the data have been corrected accordingly, the fit process began. When developing MCS, one of the main aims was keep this process as simple as possible, whilst avoiding a 'black box' type of program. Transparency and control are given to

the user whilst maintaining a high degree of accuracy to the physics of the photoemission process.

Addition of components is simply done by dragging the cursor to the desired location and clicking add peak. The user can select the peak type (*s*, *p*, *d* or *f*), depending on the sub-shell(s) present in the spectra, and an initial guess profile will be plotted and with all fit parameters presented to the user. This is shown in the example interface in Figure 2.10, where the fit parameters are highlighted by a green region, the graph window is highlighted by a red region. The raw data (red circles) and the calculated components (blue lines) are shown on the graph window. The example data are of a Ag3d core level, and a '*d*' peak profile has been added, giving two components.

As mentioned previously, *p*, *d* and *f* subshells undergo spin-orbit coupling, which causes a splitting of the energy level. As well as this, degeneracy in these split levels leads to a difference in the resultant components' areas. MCS takes this into account during the peak addition process with the components being formed in such a way that the ratio and splitting values can be input in place of absolute values. For example, in Figure 2.10, 'peak 2' has four parameters linking it to 'peak 1'; the Spin Orbit Ratio, which has a value of 0.66667 to account for the 2:3 degeneracy ratio seen in *d* orbitals; the Spin Orbit Splitting, with a default value of -6, putting it at a kinetic energy 6 eV lower than peak 1; peak broadening, which is by default 1, which provides no peak broadening, but can be floated to account for broadening between split components due to Coster-Kronig transitions or crystal field effects; and Shirley Step Ratio, which again is 0.6667 as the step height should also related to degeneracy, similarly to the signal area. An important feature to note about the model is the

implementation of the Gaussian and Lorentzian contributions. Each peak has its own Lorentzian width parameter, because this is linked to sample properties so may vary between components. However, a single Gaussian width parameter is applied to all peaks, as Gaussian broadening is mostly instrumental based so all components should share this value. This is useful when fitting Voigt profiles, and the mixing factor value is ignored, but will need to be checked if pseudo-Voigts are used.

Once the components are made, parameters are altered until the model is matched, within reason to the data. Once reasonable initial guesses are found, parameter optimisation can begin. The fitting procedure applies the Levenberg–Marquardt least squares method in order to find the best fit. In short, the algorithm aims to minimise the sum of the squares of the difference between the raw data and the fit data. It should be noted the L-M algorithm, as with many fitting algorithms, only finds the local minima of the sum of the residual squares. This means the initial guess has to be somewhat representative of the true model in order to find the correct fit. Once the fit is complete, the parameters and displayed model are updated accordingly and can once again be edited for further fitting, if needed. At this point a residual is also calculated and displayed in the residual graph box. χ -squared and Abbe’s criterion are also calculated to provide statistical values on the ‘goodness-of-fit’. These, along with fitting errors, and good fitting practices implemented throughout this work are discussed further in section 8.1 in the Appendix.

2.2.2.2 REES ANALYSIS PANEL

REES analysis requires a slightly expanded procedure in order to fit multiple spectra quickly and effectively. The workflow of REES analysis is shown in Figure 2.12 and the REES panel with example data already fitted is shown in Figure 2.13. Unlike XPS

analysis, REES data can be analysed with a coarser fit, but involves a much larger number of spectra to be analysed, usually in the order of a few thousand. Fitting such a large number of spectra can indicate trends with a very fine resolution, even with a coarse fit. Previously, when using other fitting software such as CasaXPS, the procedure was to bin the data to give 300 spectra before analysis due to the loading limit of CasaXPS. Binning is an important feature to have as it can drastically increase SNR, however it does reduce time resolution. Technically, MCS has no upper limit to the number of spectra which can be analysed. The limiting factor would be the RAM of the PC on which the analysis was performed, due to IgorPro's handling of data.

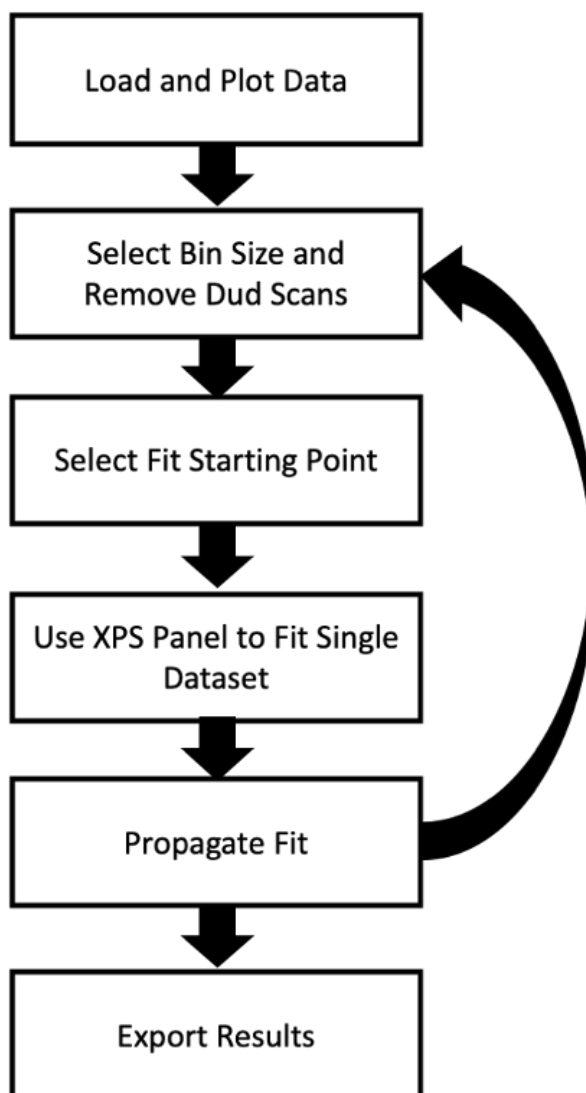


Figure 2.12: The workflow used in REES Analysis.

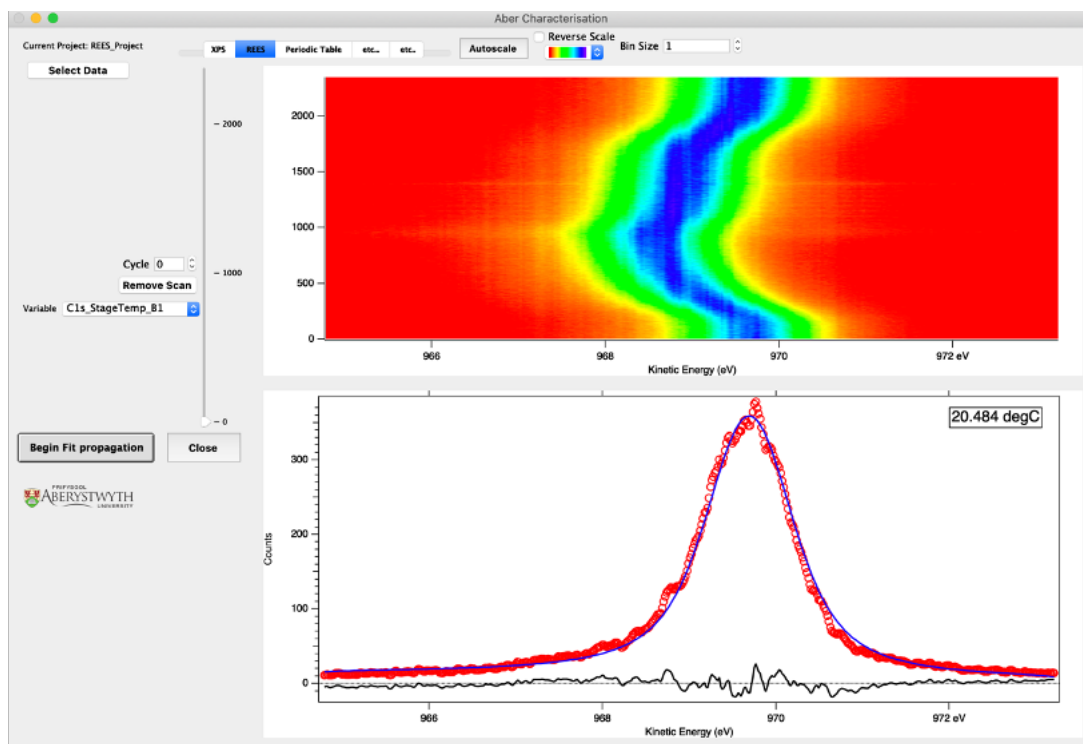


Figure 2.13 : The MCS REES panel with example data already fitted. The top graph is C1s spectra measured during a temperature cycle. The bottom graph shows the data from the selected cycle (red circles), the fitted data (blue line) and the residual from the fit (black line).

Once imported and loaded into MCS, the user selects the starting spectrum to independently fit. Once this single core level has been fit, the propagation can begin. The fit propagation uses the fit results from first cycle as the initial guesses for the second cycle, and so on. The fit can be propagated through the experimental cycles in ascending or descending order, depending on the dataset. For example, fit propagation is much more stable when following the expulsion of a signal, rather than fitting from a flat background initially. One such example of this is when analysing a REES deposition experiment. This type of data is much more readily fit in reverse order to how the data were taken. Once the fit is complete, certain information is exported. The area, peak position, Lorentzian and Gaussian FWHM contributions, and the Voigt FWHM, are all automatically plotted against cycle number, with the full fit parameter list for all cycles being concatenated together and stored. With the MCS package, a data loader has been developed for files output from SPECTRA and

SPECSlab acquisition software, in order to import and format the data in a suitable manner for MCS use.

2.2.2.3 PERIODIC TABLE PANEL

The third panel in the MCS contains an interactive periodic table, which can be used to look up the binding energy and cross-sections for the majority of elemental core-levels, required for data normalisation. The original binding energy lookup table was developed in Aarhus University. This was modified to include the photoionisation cross-section data, and then integrated into the MCS package. The periodic table panel is shown in Figure 2.14, showing the information displayed for iron, with an X-ray energy of 1253.6 eV input (Mg anode source energy), as an example.

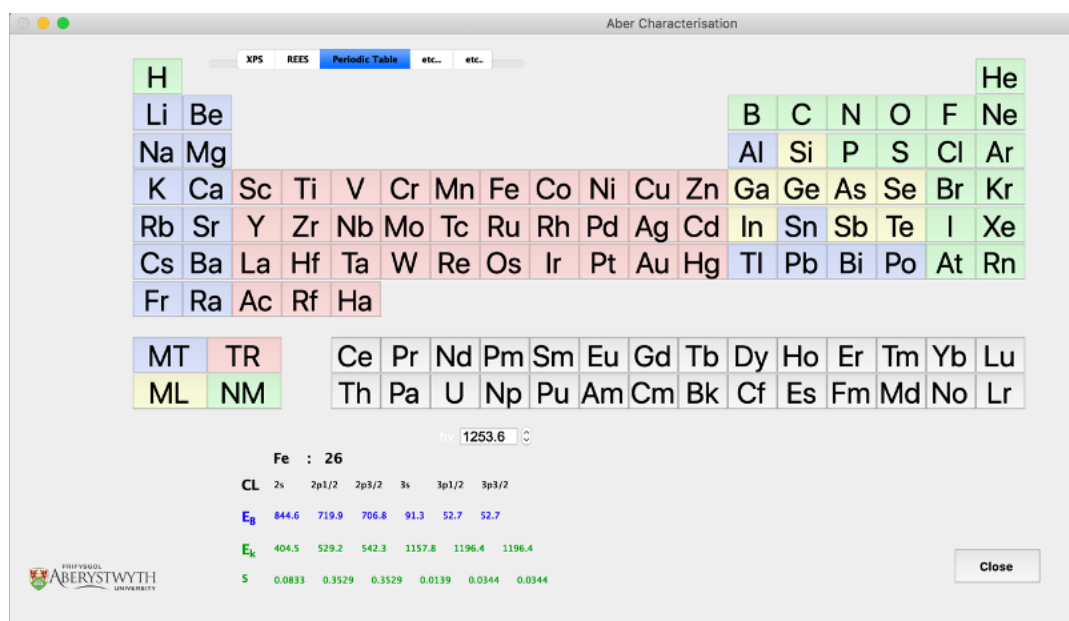


Figure 2.14: The periodic table panel implemented in the MCS program. The user can input a photon energy below the table (or on the XPS panel) and select an element. The core levels, binding energies, kinetic energies and the photoionisation cross-sections for the selected element are then displayed.

2.2.3 THE MCS SUMMARY

The material characterisation suite has been developed to help assist with the analysis of XPS and REES data, and a number of the main goals have been met. Firstly,

the fitting functions provided include an active background procedure, as well as the ability to utilise either asymmetric true Voigt convolution, or pseudo-Voigt functions. With regards to the expediting of fitting spectra, this has been seen in feedback from the users in the Aberystwyth Research group, with a number of papers currently in preparation containing photoemission data solely analysed with the MCS software. On top of this, all spectra in this work have been analysed using this program. This includes large REES datasets, which did not require binning to 300 cycles. Currently the largest number of spectra fit during a single propagation is approximately 3600, with an analysis time of around 5 minutes.

Whilst the MCS is being used successfully for photoemission analysis, there are a number of future plans for the software, some of which are already in development. Some of these plans are listed below.

- Removal of some of the current limitations on the REES fitting procedure. At the time of writing, fitting propagation can only be performed on all measured cycles, either in ascending or descending order. To improve on this the addition of cycle limits will give the ability to fit selected cycle regions, saving computational time and/or having to slice out datasets manually.
- Fully implement the Toougaard-like 'slope' background into the MCS. The functionality of this has been tested in a fitting function, but implementation into the MCS requires adapting a large number of the functions.
- Automation of lookup-tables would expediate analysis further. Currently, an idea for this somewhere for the user to 'search' for core levels, for example "C1s" would find the cross section for carbon 1s. Other methods discussed for

this include buttons, or a drop down menu, filled with the cross section values when searched, rather than textbox as is currently used.

- Integration of further analysis procedures for other experimental techniques such as:
 - Photoelectron Emission Microscopy (PEEM), for which an analysis package has already been developed, which provides various functions useful for PEEM analysis such as drift correction, image masking, line analysis, area stack integration and more.
 - Raman/Photoluminescence Spectroscopy which would require the ability to analyse 2D spectra as well as hyperspectral maps which require more complex image processing techniques, many of which already exist as built-in functions inside Igor. A basic Raman analysis software package is in development, but further work is required before this can be integrated fully.
 - Atomic Force Microscopy (AFM) is another technique commonly used in the Aberystwyth research group, so it may be beneficial to add AFM image analysis functionality as well. Whilst very good AFM analysis software does exist, such as Gwyddion, the overall goal of the MCS was to bring analysis of many techniques together into one program, to reduce possible license costs, learning time and overall analysis time.

2.3 OPTICAL SPECTROSCOPY

Optical Spectroscopy is the study of the interaction of visible light with matter as a function of wavelength. These light-matter interactions can be used to determine many material properties. There are five main mechanisms by which light can interact with matter. These are; elastic scattering (scattering without a change in photon energy), inelastic scattering (scattering with a change in photon energy), reflection, absorption and emission [40]. In this work the main optical techniques used are based around the absorption, emission and inelastic scattering effects. These are luminescence and Raman spectroscopy.

2.3.1 LUMINESCENCE

2.3.1.1 THE PRINCIPLES OF LUMINESCENCE

Luminescence was first observed in 1845 when quinine was seen to possess a blue glow whilst illuminated [41]. Since then, many developments have led to a much greater understanding of luminescence, as well as a multitude of techniques which depend on the luminescence of materials. Luminescence occurs when an electron in an excited (electronic) state relaxes into a lower energy state via emission of a photon. However, there are two main paths that an electron may take to reach the ground state whilst emitting a photon. These are known by fluorescence and phosphorescence.

Fluorescence is the more direct, and thereby much quicker relaxation route, although some internal non-radiative transitions between vibrational states may occur. Phosphorescence, however, doesn't immediately re-emit the absorbed radiation. Instead, the excited electron undergoes intersystem crossing usually to a state of different spin multiplicity, commonly a triplet state. In order to return to the original ground state, the electron must undergo a 'forbidden' transition from the high spin multiplicity state. Although these transitions are possible, the unfavorability of them cause the electron to become trapped, leading to a much slower relaxation time. Fluorescence typically occurs on timescales of the order of 10's of nanoseconds, whereas phosphorescence can have lifetimes between milliseconds and hours. A Jablonski diagram shows the electronic and vibrational energy levels involved in fluorescence and phosphorescence in Figure 2.15.

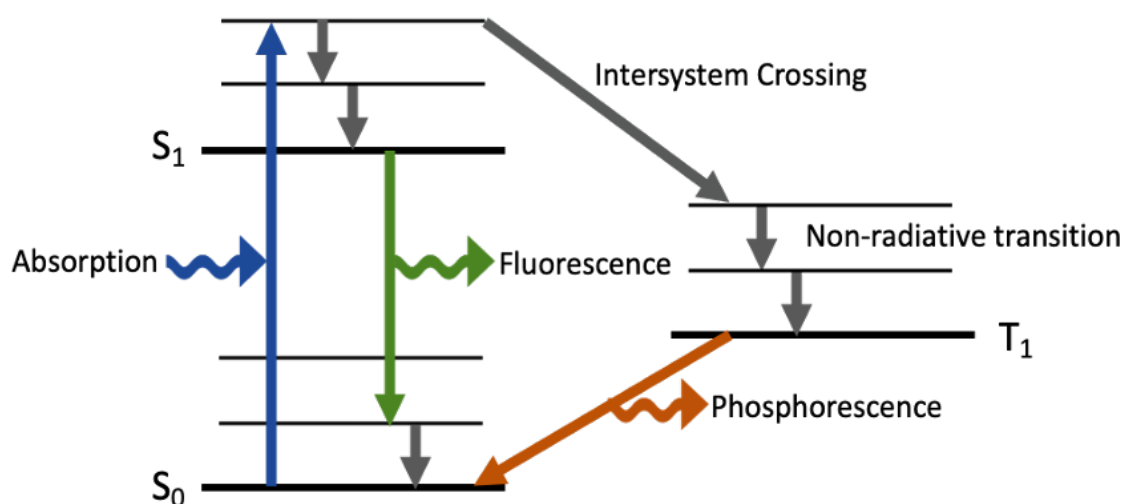


Figure 2.15: A Jablonski diagram which demonstrates the processes of fluorescence and phosphorescence. Coloured arrows indicate an absorption or emission process, wavy arrows indicate incident or emitted photons and grey arrows indicate non-radiative transitions.

A transition where an electron is excited into a higher electronic and vibrational state is known as a vibronic transition. As the electronic transitions are much quicker than the change in the position of atomic nuclei, the Frank-Condon

principle applies. The Frank-Condon principle governs the intensity of vibronic transitions. The principle states a vibrational transition is more likely to occur in tandem with an electronic transition, when the overlap between the two vibrational states' wave functions is greater. Figure 2.16 depicts the Frank-Condon principle. As stated before, the electronic transitions occur instantaneously in comparison to any nuclei movements, so these transitions are shown as vertical lines on the diagram. The non-vertical lines are relaxations between vibrational levels, where the electron gives energy to its surroundings, usually non-radiatively by producing a phonon.

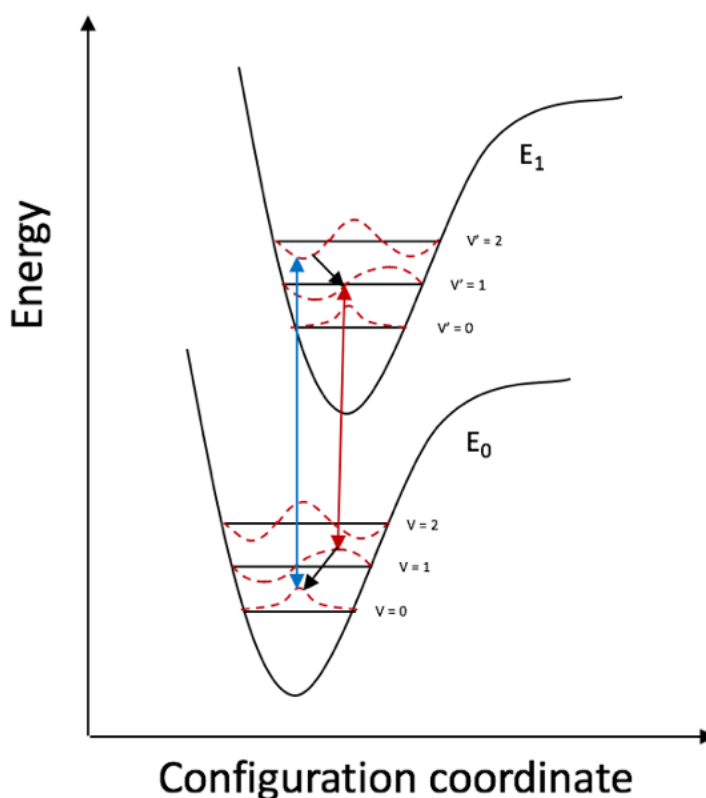


Figure 2.16: A simple example of configuration coordinate diagram, which is used to depict the Franck-Condon principle. Radiative transitions are shown by the coloured arrows. Non-radiative transitions are shown by black arrows. The dashed lines indicate the wavefunction of each energy level. The translation of the excited in the x -axis indicates an increase bond lengths between neighbouring atoms.

There is a plethora of luminescence based techniques that are used in a wide variety of fields including physics, chemistry, medicine, materials science and geology. Luminescence describes the spontaneous emission of light when an electron

relaxes from an excited state, however the techniques based on luminescence are described also by the excitation source. Some examples of luminescence are given in Table 2.4, along with the excitation sources of each, and a possible advantage to using each method. During this work, the main technique used was photoluminescence, however cathodoluminescence has been tested during the development of the OptiXS (Optical and X-ray Spectroscopy) instrument, described in chapter 3.

Table 2.4 A number of the different types of luminescence as well the excitation sources and an advantage for each technique.

Technique	Excitation Source	Advantage
Photoluminescence	Light absorption	Quick, non-destructive
Bioluminescence	Biological Reactions	Useful for genetic engineering
Electrochemiluminescence	Electrochemical Reaction	Sensitive chemical analysis
Cathodoluminescence	Electrons	Surface sensitivity
Sonoluminescence	Bubbles excited by sound	Can detect ions in acid

2.3.1.2 PHOTOLUMINESCENCE SPECTROSCOPY

Photoluminescence (PL) spectroscopy is the measurement of the spontaneous emission due to an electron undergoing relaxation, after a material has been optically excited. As with photoelectron spectroscopy, PL can be used to provide in-depth information about the electronic energy level structure of a system in a non-destructive manner. Unlike electron based spectroscopy, photoluminescence does not require a lot of sample preparation or ultra-high vacuum conditions. On top on this, it can provide complementary information not provided by electron spectroscopy alone.

For example, the excitation source for photoluminescence is relatively low energy (compared to the X-ray sources used in photoemission), and in some cases can be varied readily in order to probe different energy level structures in a material. Excitation via infrared can readily probe vibrational or rotational levels, whereas UV

light probes transitions in valence electron bands. The intensity of photon emission can provide information on surface quality, and other features can determine impurity types/levels, as well as gauging disorder on a surface or interface [42].

2.3.2 RAMAN SPECTROSCOPY

As mentioned, light which impinges on a sample may undergo a scattering event. Optical scattering in general is the process of photons being forced to deviate from their current path by non-uniformities in the medium through which they travel [43]. Even with the absence of any classical absorption or emission processes, it is convenient to conceptualise virtual energy levels in which scattering events occur. Scattering events are divided into two types; elastic and inelastic scattering. Elastic photon scattering (or Rayleigh scattering) is the process where the scattered photon has the same energy as the incident photon. This commonly occurs on smaller molecules or through the electronic structure of the media of travel. Inelastic scattering, or Raman scattering, is the process whereby the scattered photon will have a different energy than the incident photon. Raman scattering was first observed in 1928 by C. V. Raman, after whom the process is named. He noticed that when certain substances were illuminated by monochromatic light emitted light of slightly higher and slightly lower energy than the excitation source [44].

The Raman effect is caused by the interaction between an incident photon and a rovibrational (rotational and vibrational) energy level, and there are two types of Raman scattering, differentiated by the increase or decrease in photon energy. These are called Stokes Raman and Anti-Stokes Raman scattering. Stokes scattering can be thought of as the absorption of a photon by an atom or molecule in the ground state to a virtual energy state, followed immediately by the emission of a lower

energy photon as the molecule relaxes into a higher rovibrational state than it was initially. Anti-Stokes shift requires the atom/molecule to exist in an excited rovibrational state already. The process is similar to Stokes, where the atom/molecule is excited into a virtual state, but instead of returning to the excited rovibrational state, the atom/molecule relaxes into the lower ground state. These changes in the rovibrational states are actually the creation or destruction of a phonon in the material being probed. The change in energy during Stokes or anti-Stokes shift is then equal to the energy of phonon's created or dissipated, $h\nu$. The Raman effect only occurs for approximately 1 in 10 million photons, however with modern day lasers and photon detectors, Raman spectroscopy is a very viable spectroscopic method. A simple depiction of elastic scattering and both forms of Raman scattering is given in Figure 2.17.

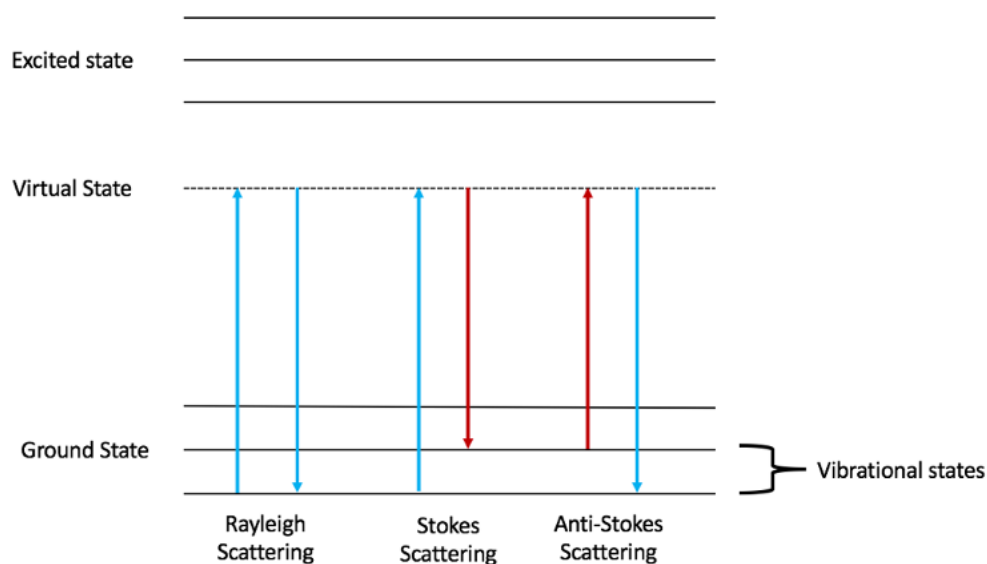


Figure 2.17: The process of Rayleigh scattering, Stokes scatter and Anti-Stokes scattering. The use of energy levels although not physically accurate, helps depict the processes described.

In practice, as there is no emission present, Raman spectroscopy measures the shift in energy from the excitation source. Raman shift $\Delta\nu$ is usually given in the form of wavenumber (cm^{-1}), as it is independent of the excitation source. The

wavenumber is calculated by taking the difference in the inverse of wavelengths of the excitation source λ_0 and the scattered photon λ_v , shown in equation 2.24.

$$\Delta\nu = \frac{1}{\lambda_0} - \frac{1}{\lambda_v}$$

Equation 2.25

Due to the uniqueness of vibrational modes in samples, Raman spectroscopy can be used to identify chemical composition. Changes in the local atomic environment also alter the rovibrational modes available. These environmental effects can be measured via changes in position, shape or number of Raman peaks. Raman spectroscopy can be applied to measure properties such as strain, structure, molecular orientation, and the isotopic composition in materials. In this work, real-time Raman spectroscopy has also been used to calibrate temperature measurements of diamond samples, (see chapter 3 and 5).

2.3.3 OPTICAL SPECTROSCOPY FEATURES

Photoluminescence and Raman spectroscopy commonly occur simultaneously in materials. Therefore, they can easily be measured together, and must be differentiated in order to avoid mis-characterisation. On top of this, there are many processes/optical transitions which occur together that can add to the complexity of PL and Raman. For example, Figure 2.17 shows just one possible route that can be taken by an electron during photoluminescence. The actual number of different excitation and relaxation paths result in more than just a single emission line.

The emission produced by an electron relaxing from the lowest vibrational state of the excited electronic state, to the lowest vibrational state of the ground electronic state, is known as the Zero Phonon Line (ZPL). Emission from all other

possible transitions make up what is known as the Phonon Side Band (PSB), and both are very useful in explaining the luminescent properties of materials and colour centres [45]. An example of both a zero phonon line and a phonon side band are shown in Figure 2.18a, which is an optical spectrum taken between 550 – 900 nm, using a 532 nm excitation source. The sample was a nitrogen-containing diamond which produces emission at 575 nm, and 638 nm due to the presence of neutral and negatively charged NV centres, respectively. The negatively charged NV centre is also responsible for the PSB in the spectrum.

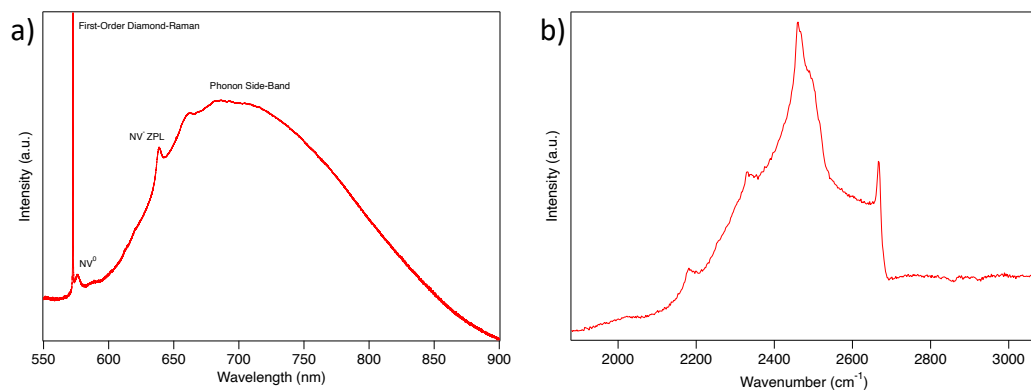


Figure 2.18 a) An extended optical spectrum of a nitrogen-containing diamond showing Raman, emission and phonon-based features. b) The second-order Raman spectrum from an intrinsic single crystal diamond indicating the complexity of second-order processes. Each peak can be linked to a specific multi-phonon process.

The intensity of phonon sidebands and anti-Stokes Raman features are highly temperature dependant. This is because the presence of phonons in a material is also temperature dependant. The energy of vibrational transitions in most materials is around the order of $k_B T$, where k_B is Boltzmann's constant and T is the temperature. This means thermal excitation between vibrational modes is possible, leading to a temperature-dependent phonon population. The phonon population of vibrational states can be seen when measuring anti-Stokes features (as the intensity will be exponentially dependant on the wavenumber) and is also responsible for a large

decrease in signal when compared to Stokes-shifted signals. Throughout this work, only Stokes-shifted Raman Spectroscopy will be used.

The phonon population also has a profound effect on the PSB, and this can be exploited. Low temperature photoluminescence is commonly performed, as this reduces exciton-phonon interactions leading to; a reduced PSB, sharpening of PL peaks, and increasing the detail that can be resolved in a spectrum. This will be discussed further in chapter 4 when presenting the Stokes centre.

So far, only first-order Raman processes, which involves a single phonon, have been discussed. However, there are many Raman features that arise from multi-phonon processes and can provide further information about the probed material. Figure 2.18 shows the second-order diamond Raman structure which can be used to determine information on the phonon dispersion curves and crystal quality [46].

Chapter 3 – INSTRUMENTATION

So far, a range of techniques have been presented. However, none of these would be possible without proper instrumentation. This chapter will present an overview of the instrumentation required for the previously discussed techniques. Also included in this chapter is the development of the Optical and X-ray Spectroscopy instrument (OptiXS) which includes; the design and construction of a new sample manipulator, addition and calibration of relevant components, as well as some ‘proof-of-concept’ experiments. The latter of these has led to the performing of optical and electron spectroscopy simultaneously, during surface processing routines, such as deposition.

3.1 ULTRA-HIGH VACUUM

The application of vacuum-like condition is possibly one of the most important aspects of many surface-science experiments. As a true vacuum is never experimentally possible, a number of ranges to describe the level of vacuum have been defined, these are shown in Table 3.1. For the surface-science experiments used in this work Ultra-High Vacuum (UHV) is a necessity, for two main reasons; the increase in the electron MFP, and surface cleanliness.

Table 3.1: The 6 main categories of vacuum.

Vacuum Level	Pressure Range (mbar)
Low (LV)	$10^3 - 3.3 \times 10^1$
Medium (MV)	$3.3 \times 10^1 - 10^{-3}$
High (HV)	$10^{-3} - 10^{-6}$
Very High (VHV)	$10^{-6} - 10^{-9}$
Ultra High (UHV)	$10^{-9} - 10^{-12}$
Extreme Ultrahigh (XHV)	$< 10^{-12}$

The electron MFP regarding electron propagation through solids has already been discussed briefly, however for various aspects of the utilised techniques in this work, particles (including electrons) are required to travel relatively large distances through space. For example, in order to make it to the detector of the hemispherical electron analyser for XPS, the electrons have to travel distances of the order of 1 m. Particles are scattered in the gas phase via collisions, and the probability of scattering events occurring is based on the number of particles per unit volume, highlighting the importance of the working pressure. The MFP λ for a neutral particle travelling through gas can be calculated using the equation

$$\lambda = \frac{k_B T}{\sqrt{2} A P}$$

Equation 3.1

where k_B is Boltzmann constant, T is the temperature, P is the pressure and A is the collision cross-section. The mean-free paths for an argon atom ($A = 188$ pm) for each pressure range is given in Table 3.2. For many applications, a mean-free path in the order of metres is required, therefore experimental systems should be pumped down to pressures $<10^{-4}$ mbar [47].

Table 3.2: The calculated lower limit of MFP for each vacuum range.

Vacuum Level	Mean-Free-Path (m)
Low (10^3)	2.28×10^{-7}
Medium (10^1)	2.28×10^{-5}
High (10^{-3})	0.228
Very High (10^{-6})	228
Ultra High (10^{-9})	2.28×10^5
Extreme Ultrahigh (10^{-12})	2.28×10^8

Another benefit of UHV is the clean environment it provides. In order to perform an accurate surface analysis, the surface of a sample must stay constant during measurement. Considering a complete XPS dataset may take a number of hours to acquire, surface contamination over time is important. The rate at which a surface becomes contaminated depends on the rate of adsorption and desorption. In order to understand this process further, one must consider the molecular flux on the surface.

Kinetic theory states that the incident particle flux Γ from an ideal gas on a unit surface is given by the equation

$$\Gamma = \frac{1}{4} n \bar{v}$$

Equation 3.2

where n is the number of particles and \bar{v} is the average particle velocity.

The root-mean-square of the particle velocities v_{rms}^2 can be derived from the kinetic energy of a particle and its mass m by the equation

$$v_{\text{rms}}^2 = \frac{3k_{\text{B}}T}{m}$$

Equation 3.3

The average velocity \bar{v} can then be calculated from v_{rms}^2 and this means the average velocity can also be related to the mass and kinetic energy of particles by

$$\bar{v} = \sqrt{\frac{8}{3\pi}} v_{\text{rms}} = 2 \sqrt{\frac{6}{\pi}} \frac{k_{\text{B}}T}{m}$$

Equation 3.4

Then by using the equation for the number of particles in the system

$$n = \frac{k_{\text{B}}T}{P}$$

Equation 3.5

and substituting equation 3.4 and 3.5 into equation 3.2, the relationship between particle flux, pressure, temperature and particle mass can be given by

$$\Gamma = \frac{P}{\sqrt{2\pi m k_B T}}$$

Equation 3.6

Equation 3.6 determines the number of particles which impinge on a surface per unit area per unit time. The number of particles which actually adsorb onto the surface, will be a fraction the particle flux. This fraction is known as the sticking coefficient ξ and has limits of 0 and 1. A sticking coefficient of 1 will produce a system where every incident particle sticks to the surface, and the sticking coefficient will be 0 when the system is at equilibrium. The sticking coefficient takes into consideration the rate of desorption, as well as adsorption, to calculate a net rate.

The Langmuir unit L can be used as a simple approximation for predicting monolayer formation times. The Langmuir unit is a dosage unit and can be calculated using the equation

$$L = Pt \times 10^6$$

Equation 3.7

where P is the pressure in Torr (or \sim mbar) and t is the time exposed. A factor of 10^6 is required as, by definition 1 Langmuir is defined as the exposure to $\sim 10^{-6}$ mbar for 1 second. If one assumes a sticking coefficient of unity a Langmuir is approximately the required dosage for a monolayer to form [48]. Using this approximation, the monolayer formation time has been calculated for each pressure range, shown in Table

3.3. This leads to the common use of working pressures of 10^{-10} - 10^{-11} mbar where the monolayer formation time is of the order of hours, suitable for XPS experiments.

Table 3.3: The monolayer formation time for each of the pressure ranges.

Vacuum Level	Monolayer Formation
Low (10^3)	1 ns
Medium (10^1)	10 μ s
High (10^{-3})	1 ms
Very High (10^{-6})	1 s
Ultra High (10^{-9})	~17 mins
Extreme Ultrahigh (10^{-12})	~277 hours

3.2 PHOTON SOURCES

3.2.1 TWIN ANODE X-RAY SOURCE

All XPS experiments in this work that were performed in the home laboratory utilise a twin-anode X-ray gun to supply excitation photons. A modern twin-anode source, shown in Figure 3.1 (with the shroud cap removed), is fairly simple in principle. Firstly, a current (~ 5 A) is run through a thoriated tungsten filament to generate electrons via thermionic emission. These electrons are accelerated towards a magnesium or aluminium anode at a high voltage, typically 15 kV. Upon impact, electrons in the anode material are excited, and via subsequent relaxation or *bremsstrahlung*, X-rays are produced. The emission current of the anode sources in the home lab are 20/26mA for the Mg anodes and 24/32mA for the Al anodes, for the OptiXS/REES systems, respectively.

For both magnesium and aluminium sources, there are multiple emission lines produced. The primary emission lines $k\alpha_{1,2}$ for the magnesium and aluminium sources are 1253.6 and 1486.6 eV, respectively, and correspond to the $2p_{3/2}^3, 2p_{3/2}^1 \rightarrow 1s$

transitions. The X-rays pass through an aluminium window to attenuate undesired emission lines, as well as the *bremsstrahlung* background emission. The emission spectrum for the K-transitions in a magnesium anode is given in Figure 3.2, taken from [39].

The filament, common ground and filament pins shown in Figure 3.1 are set up in such a way that the current can be passed around each side independently, leading to the twin source capability. This geometry is what leads to a small amount of cross talk, as electrons may make it to the undesired anode, especially from near the common ground pin. A central bar not shown in 3.1 is commonly in place in the centre of the anode to reduce cross-talk. The system is also water cooled through the central copper column. The cooling water must be deionised as it is used as the delivery mechanism for the 15 kV.

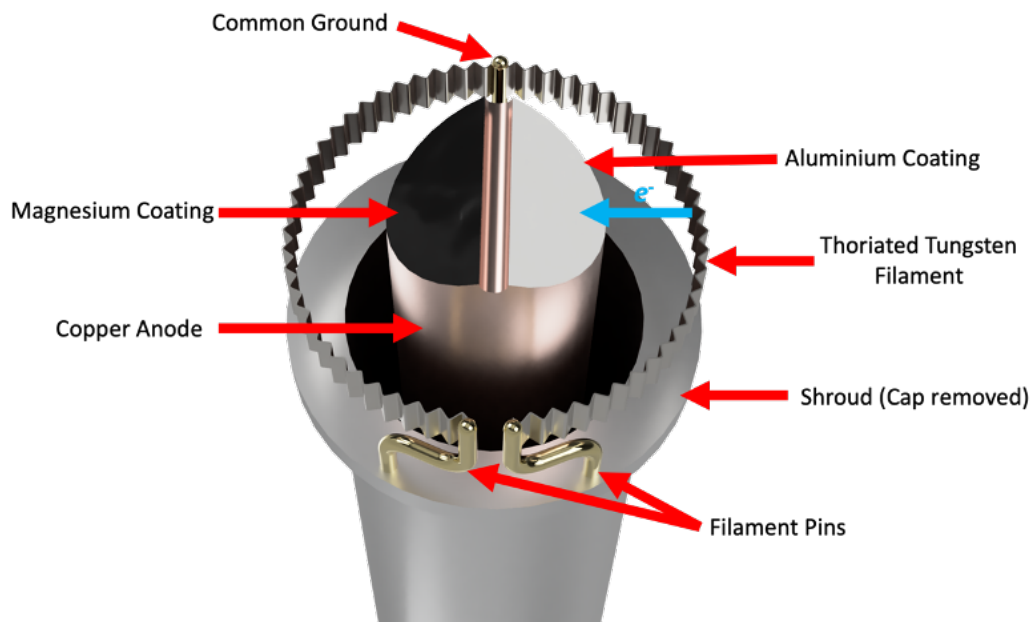


Figure 3.1: The components of a modern day twin-anode X-ray source with aluminium and magnesium coatings. The 3D model was based on the current X-ray source used in the REES system and provided by Dr Simon Cooil.

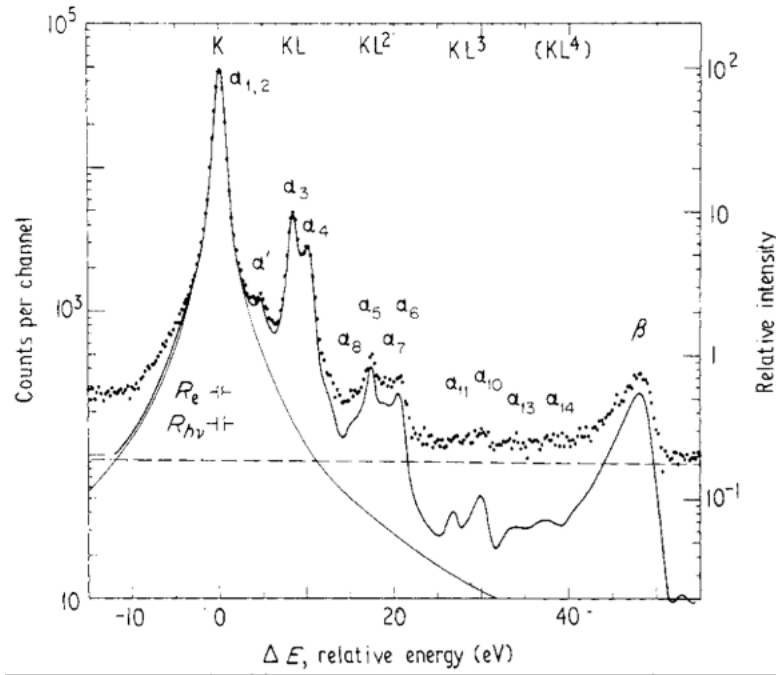


Figure 3.2: The K emission spectrum of a magnesium anode. The dots indicate the measured spectrum, the solid lines show the theoretical emission line shapes, and the dashed lines shows the average background. Figure taken from [38].

3.2.2 ULTRAVIOLET DISCHARGE SOURCE

Due to the extremely low photoionisation cross section of valence state electrons when using high photon energies, it is difficult to resolve many of the valence band structures. For this, an ultraviolet light source is required. Two sources are used in the home laboratory; The *SPECS UVS 300* is used on the REES system and the *SPECS UV 10/35* on the OptiXS system, however both instruments have the same basic principle.

Electrons are first generated thermionically at a cathode and accelerated by an inhomogeneous magnetic field into a discharge chamber. High purity, inert gases are then leaked into the discharge chamber where the accelerated electrons collide with the gas atoms, leading to ionisation and the ignition of a stable plasma. The relaxation of these ionised gas atoms is the source of the high intensity ultraviolet radiation. The most frequently used gas for plasma ignition is helium, which produces

two emission lines at 21.2 eV (He I) and 40.8 eV (He II). The ratio of He I and He II emission is dependent on the pressure in the discharge chamber and in the case of the UVS 300, the discharge current, meaning the sources can be ‘tuned’ between the two emission lines. The UV light is delivered into the analysis chamber via a quartz glass capillary. The capillary is differentially pumped by a rotary and turbomolecular pump in order to maintain a low chamber pressure ($<10^{-9}$ mbar for the UVS300, and $<10^{-7}$ mbar for the UVS 10/35). The UVS 300 is a much more complex instrument but can provide UV radiation with the same brilliance as some 3rd generation synchrotrons. The UVS 10/35 is a much smaller instrument but can be ignited using a number of gases (He, Ne, Ar, Kr, Xe) for a range of UV photon energies.

3.2.3 SYNCHROTRON RADIATION

Some data presented in this work were taken at synchrotron beamlines. Synchrotrons are central facilities that provide a tuneable and high brilliance photon source, used in a multitude of research fields. For some of the data in this study, tunability of the photon source was required to increase the surface sensitivity of photoemission experiments.

3.2.3.1. SYNCHROTRON OPERATION

Synchrotron radiation is produced by changing the momentum of relativistic charged particles, usually electrons, through the use of magnetic fields. Synchrotron radiation was initially observed by accident in 1947 by *Elder et al.* where they noticed that “high energy electrons subjected to large radial accelerations radiate considerable energy in the optical spectrum” [49]. Synchrotron radiation was initially regarded as a loss in the electron kinetic energy. The first generation of synchrotrons were predominately used in the study of nuclear and high energy physics, with the synchrotron radiation

considered a by-product, utilised by a small number of parasitic beamlines. The second generation synchrotrons were specifically made for the production of radiation, with the first opening in Daresbury in 1981. In second generation synchrotrons, radiation was only produced by bending magnets at the 'corners' of the radial path. Nowadays, in third generation synchrotrons, insertion devices such as wigglers and undulators are used to further increase the brilliance, as well as provide more control of the emitted radiation [50].

A diagram of a third generation synchrotron taken from [51] is shown in Figure 3.3. The process of X-ray production in third generation synchrotrons generally has 5 steps:

An approximation of the electron beam energy during each step is provided, based on data from the Diamond Light Source, Didcot, UK.

- 1) Electrons are produced via thermionic emission by heating a high voltage cathode, usually a tungsten filament. These liberated electrons are initially accelerated to around 90 keV.
- 2) Bunches of electrons then enter a linear accelerator (linac) which uses a series of radio frequency cavities to progressively accelerate the electrons (100 MeV).
- 3) A booster synchrotron then further accelerates the electrons to near the speed of light until the electrons reach the energy of the main, larger storage ring (3 GeV). The bunches at this stage are confined to an oval shape by a magnetic lattice, approximately 0.25 mm wide and 0.02 mm in height.
- 4) The electrons are inserted into the main storage ring. Insertion is not a trivial process as the periodicity of electron bunches as they travel around the

storage ring can be critical to certain measurements. Most notably, these are time resolved measurements which utilizes the bunch frequencies.

- 5) The electron bunches now propagate around the storage ring through bending magnets, wigglers and undulators. A radio frequency cavity is used to maintain the electron bunch size as well as boost the electrons kinetic energy every lap to account for energy loss from collisions and radiation emission.
- 6) Some synchrotrons operate in a 'top-up' mode. This is where new electron bunches are added to the ring intermittently (approx. every 10 minutes) to account for lost electrons. This mode helps maintain a constant electron beam current, and in turn radiation of a constant brilliance.

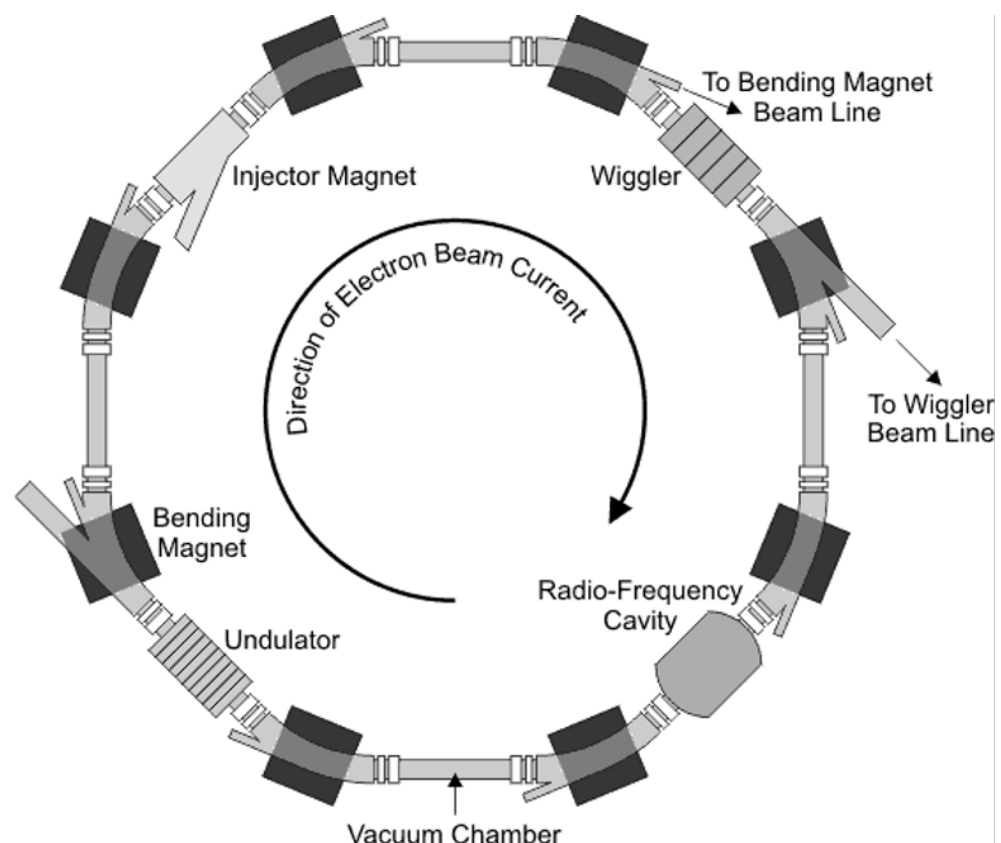


Figure 3.3: The main components in the storage ring of a synchrotron. The booster ring and linac mentioned would be located in the inner space of the storage ring. Figure taken from (Dinnebier and Billinge, 2008) [35].

3.2.3.2 SYNCHROTRON RADIATION THEORY

As mentioned, electrons emit light as their momentum is changed. However, the features of the emitted light can vary greatly, depending on the electron velocity, as well as the frequency of angular changes the electron undergoes. The energy E of electrons moving at velocity v_e can be calculated using the equation

$$E = \frac{m_e c^2}{\sqrt{1 - \frac{v_e^2}{c^2}}}$$

Equation 3.8

where m_e is the mass of the electron (9.11×10^{-31} kg) and c is the speed of light (299792458 m s⁻¹). The term $1/\sqrt{1 - \frac{v_e^2}{c^2}}$ in equation 3.7 is known as the Lorentz factor γ , and it is the proportionality by which the mass of an electron increases as its velocity increases. Continuously accelerating electrons in a circular path results in the constant radiation of electromagnetic waves. The angular dispersion of this emitted light also varies greatly with the electron velocity. As shown in Figure 3.4, an electron travelling at speeds much lower than the speed of light $v_e \ll c$ will emit light homogeneously in all directions. In contrast, as the electron approaches the speed of light $v_e \sim c$, the light emitted will form a narrow cone with an angular dispersion of approximately $1/\gamma$ radians.

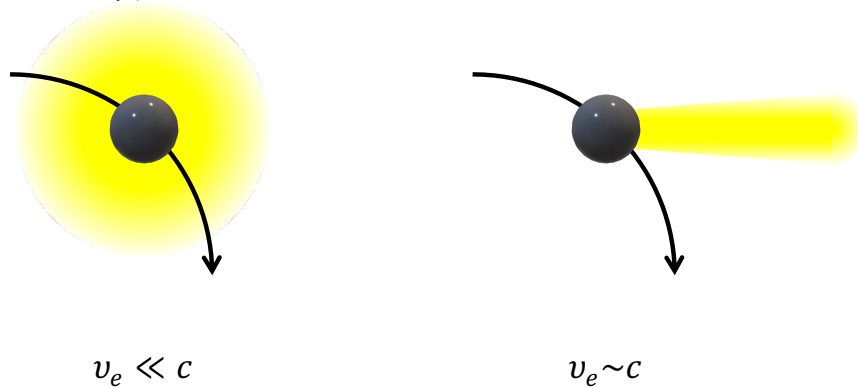


Figure 3.4: The difference in the radiation angular distributions emitted by electrons travelling at velocities much lower than the speed of light and electrons travelling at velocities comparable to the speed of light.

The X-ray generation shown in Figure 3.4 can be achieved solely by bending magnets. However, through the addition of insertion devices a higher brilliance and higher maximum photon energy can be achieved. The two types of insertion devices are wigglers and undulators. Both work by instigating a sinusoidal oscillation on the electron bunches tangential to their direction of travel, through a series of opposing magnetic dipoles. Any electron undergoing such oscillations will radiate at the times where the displacement from the central path is at a maximum. However, the difference between wigglers and undulators is the size and frequency of the magnets used, and in turn the oscillations the electrons undergo.

Wigglers oscillate the electron in a sinusoidal manner with a large enough amplitude such that the angular deviation of the electron from its trajectory is greater than the angular dispersion of the radiated light. This means there is no overlap in the emitted radiation between successive dipoles, and therefore no interference. Wigglers can therefore produce higher energy X-ray beams with wide spectral ranges. Conversely, undulators oscillate the electron bunches with amplitude comparable to the divergence of the radiated beam. This leads to overlaps in the radiation produced between dipoles, and in turn constructive interference between certain wavelengths of light. This interference has the advantage of greatly reducing the spectral range but drastically increasing the flux. In practice, undulators require a larger number of smaller magnets than wigglers, as solely reducing the field strength in order to induce smaller oscillations would result in a large drop in X-ray intensity. The separation between dipoles in undulators can also play a part in the coherence and spectral width of the *bremsstrahlung*.

3.2.4 OPTICAL LASER SOURCES

A laser is a device that produces spatially coherent and monochromatic light through the process of Light Amplification by Stimulated Emission of Radiation (LASER), from which the devices get their name. It is common practice to use a number of lasers with different wavelengths as the excitation energy can have profound effects on the structures seen in the measured optical spectra, both in terms of luminescence and Raman spectroscopy. The home laboratory currently has three lasers. A 532 nm (green) Diode-Pumped Solid-State (DPSS) laser, a 488 nm argon ion laser and a 632.8 nm He-Ne laser. These three lasers produce light with a power of approximately, 80 mW, 30 mW and 40 mW, at source, respectively. These powers may drop when measured at the sample, depending on losses occur during travel through the optical systems.

To describe the general working principles of lasers there are three main steps; pumping, population inversion, and stimulated emission. Firstly, the use of some energy source is utilised to cause the continuous excitation of electrons in the lasing (or gain) media. This process is known as pumping. The pumping can be performed by a basic light source, electric field, or in the case of DPSS lasers, other lasers. This continuous excitation eventually leads to a higher number of electrons in the excited state, known as population inversion, which is necessary for stimulated emission to begin. As electrons relax, spontaneous emission will occur, in exactly the same manner as the luminescence process described in section 2.3.1. However, as emitted photons propagate through the gain medium, they may interact with other electrons in the excited state. As the emitted photons are of the same energy as the transition energy between the relaxed and excited states, it may cause the electron

to drop to the ground state, producing more photons of the same energy. This interaction is the process of stimulated emission. Stimulated emission occurs in most media under regular conditions, but it is outweighed by the process of absorption. However, when a population inversion is present, the process of stimulated emission becomes much more common, leading to a net amplification of the emitted photon. It is common to place the gain medium in a cavity to further increase the lasing power. A cavity is a set of mirrors which acts as a standing wave resonator. Light confined in the cavity reflects multiple times, producing standing waves for certain resonant frequencies. The multiple reflections mean the photons performing the stimulated emission pass through the gain medium multiple times, further increasing the amount of stimulated emission. The light exits the cavity through a small exit hole on the output mirror, or the use of a partially reflective material where between 80-99% of the light is reflected, depending on the efficiency of the gain material.

The home lab's 532 nm green laser utilises an 808 nm GaAlAs laser diode to pump a neodymium-doped yttrium aluminium garnet (Nd: YAG), which produces emission at 1064 nm. This light is then frequency doubled to produce 532 nm light.

The 632.8 nm laser is a helium-neon laser. The gain material in this laser is a He-Ne gas mixture in an approximate 9:1 ratio. A high voltage electrical discharge tube is used to produce energetic electrons which collide with the He atoms in a gas reservoir, exciting electrons from the helium ground state into the 2s orbital. Collisions between the excited helium atoms and ground state neon atoms occur, and thanks to the fortuitous similarity between the energy of He 2s state and the Ne 4s and 5s states, energy can be transferred between the two atoms. This leads to excitations in the Ne atoms from the ground state to these 4s/5s states. Eventually

there is a population inversion in the Ne atoms. The neon atoms relax through a number of relaxation routes; however, the dominant emission line is at 632.8nm. The gas container is then placed in an optical cavity for amplification of the 632.8nm stimulated emission.

The 488 nm laser is an Ar-ion laser. Similarly, to the He-Ne laser, a noble gas is used as the gain medium. However, the gas particles are now ionised, rather than just pumped into an excited state. Because of this, the pumping energy required is much higher, and therefore must be actively cooled to avoid device degradation. This results in a very low efficiency for argon lasers of around 1%. Typically, the laser is pumped by a high current density discharge and the ionic plasma is confined using a magnetic field. Argon ion plasmas produce a number of emission lines between 351.1 nm and 1092.3 nm. Many of these unwanted emission lines are removed in the lab source by a 488 nm notch filter.

3.3 IN-SITU SURFACE MODIFICATION

3.3.1 LOW ENERGY ION SOURCE

In the home laboratory, both the REES and OptiXS system are equipped with an ion source. The main use of ion sources in surface science is sputtering samples to produce a clean surface. Sputtering usually involves accelerating argon ions into the sample at low energy (<1 keV), which collide with the surface atoms, breaking the surface bonds, and removing them. The ion sources work by flowing a relatively small current (<3 A) through a filament. The chosen gas is then leaked into the chamber at a pressure level around $10^{-5}/10^{-6}$ mbar, depending on the source. As the gas atoms flow near the filament, they are ionised by the combination of thermionic electrons

and the heat from the filament. A voltage is then applied by the anode, which is located between the filament and the sample, causing the ions to be accelerated towards the sample. The ISIS3000 ion source in the OptiXS chamber can provide ions up to 3 keV, and this higher energy increases the penetration depth of the produced ions [52]. This capability has led the source to be used with nitrogen gas for *in-situ* near-surface implantation, see chapter 6.

3.3.2. THIN FILM DEPOSITION

Thin film deposition is achieved through the use of home-made Knudsen effusion cells. The Knudsen cells consist of an alumina (Al_2O_3) ceramic crucible surrounded by a set of flat, twin-bore ceramics (also alumina) which are lashed around the main crucible using heat-resistant wire. Tantalum wire is fed through the twin-bore ceramics in order to surround the crucible uniformly. This is important as the uniformity of heating can play a part in deposition rate and purity. One of the twin-bore ceramics is sometimes used for a type R (Rhodium-Platinum) thermocouple. The crucible structure is then wrapped by tantalum heat shields and mounted on a support attached to a conflat (CF) flange. The tantalum wiring is then welded to the copper feedthroughs for the delivery of current. The Knudsen cells are then mounted behind gate valves and pumped independently in order to not affect the main chamber's working pressure. This also provides the ability to remove, repair and swap deposition material freely without needing to vent the entire system. This will be shown further in the OptiXS sections as this was taken into consideration when designing major components. 3D models of a typical K-cell are shown in Figure 3.5.

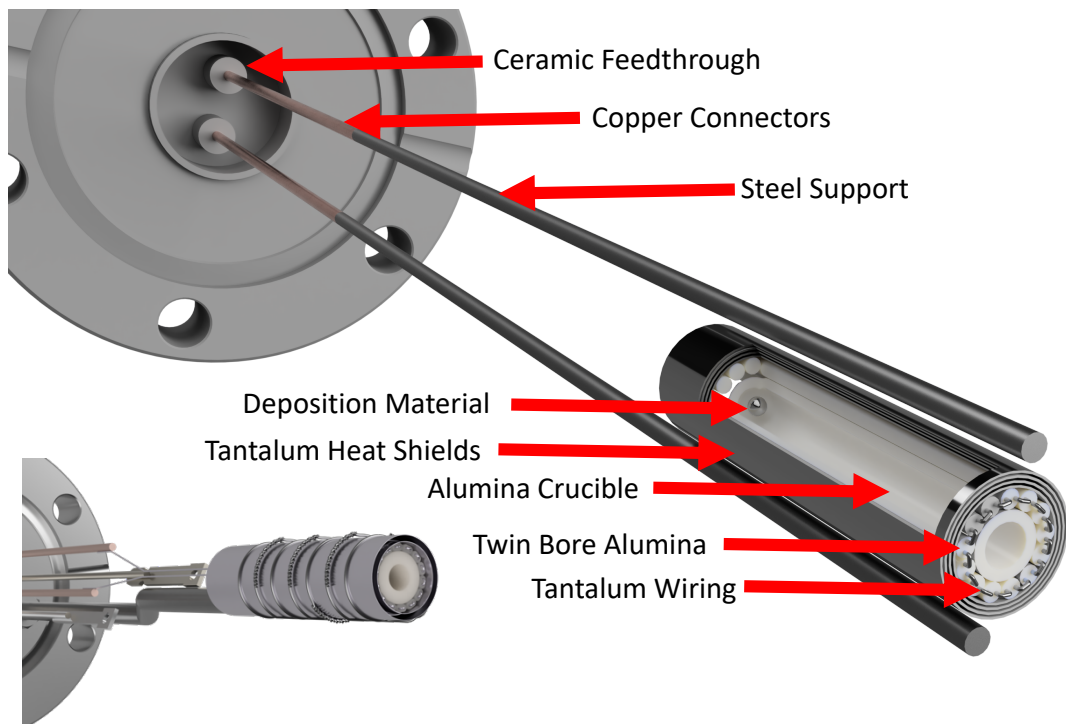


Figure 3.5: A 3D model of the home-built K-cell used for deposition. The lashing, wiring and supporting structure is shown in more detail in the inset figure.

3.3.3. PLASMA TREATMENT

Plasma treatment for modifying surface termination has been implemented using a custom built microwave assisted plasma source. The plasma system, originally designed for the REES system by Dr Gruffydd Williams and Dr Simon Cooil (Section 4.4.1, [6]), was modified during this work in order to be suitable for the OptiXS system. It is also designed in such a manner that the plasma sources are interchangeable between the two systems, and may be transportable to beamlines and other facilities, if required. On the REES system the plasma source is located on its own chamber, on the OptiXS system it is attached to the load lock.

The plasma source consists of a brass microwave cavity, surrounding a quartz glass tube, attached to a support structure. The support structure is built around the conflat flanges required for gas delivery (CF16) and mounting (CF40) onto the main system. The glass quartz is fed through specially made flanges with central compression fittings (Swagelok) which are sealed using polytetrafluoroethylene (PTFE) ferrules. The brass cavity position around the glass tube can be adjusted by a set of orthogonal micromanipulators, clamped to the CF40 flange via a Thorlabs clamp. A pin is located on the top of the cavity which enables adjustment of the cavity size, required for tuning to RF resonance. A needle valve is attached the back-end of the quartz tube for gas delivery, which is attached to the bespoke gas delivery systems on the REES or OptiXS instruments. A 3D model of the plasma system used on both systems is shown in Figure 3.6, one of the supporting legs has been removed for visual clarity.

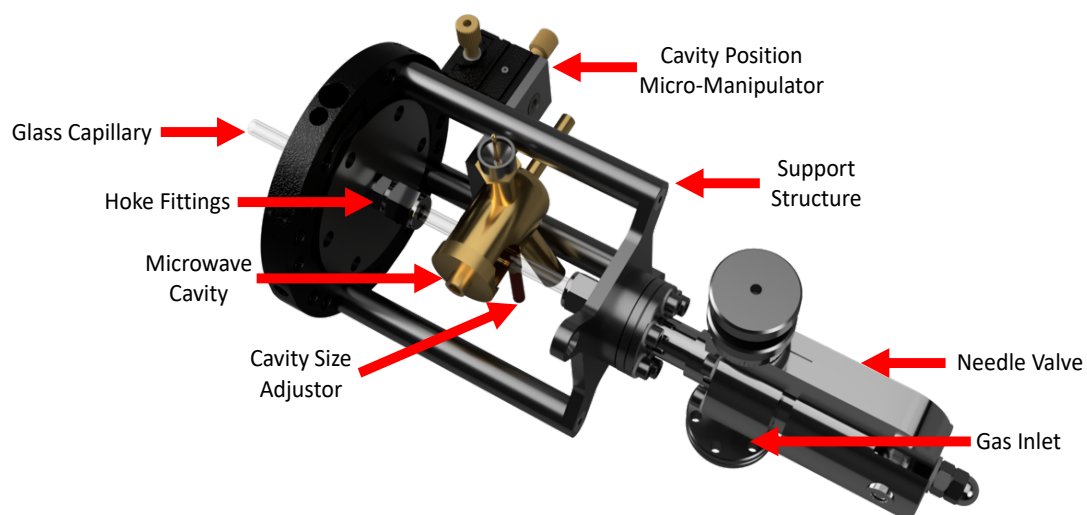


Figure 3.6: The bespoke, plasma source system in use on both the REES and OptiXS systems. The gas inlet leads to a manifold which allows for multiple gases to be flowed through. The design for both systems is identical and on smaller chambers allowing for interchanging between systems should repairs/maintenance be required.

Microwaves are generated by a 2.4 GHz EMS 200 MK II microtron coupled to a reflected microwave power meter. The generated microwave power during operation is 100 W, and a reflected power of <5 W is required for ignition. The cavity is mounted approximately 100 mm from the sample position and the quartz glass tube is positioned such that the end is approximately 20 mm away from the sample. Currently 2 gas mixtures have been used to generate plasmas in these systems; A nitrous oxide/argon (50/50) gas mixtures which predominately generates oxygen radicals used for oxygen termination (see chapter 5), and a hydrogen/argon (50/50) gas used for hydrogen termination. For the hydrogen termination process a filament heats the sample to 400°C from the rear, but this has not been required in this work as oxygen termination can be performed at room temperature [6], [53].

3.4 SAMPLE STAGES, MOUNTING AND MANIPULATION

Due to the necessity to preserve vacuum in the analysis chambers of photoemission systems, the common procedure is to load a sample into a smaller chamber, known as a load lock. Load locks are connected to the main system and can be vented independently for introducing the sample to the system. They can then be pumped down to a reasonable vacuum level before transferring the sample. This means a mechanism for moving samples between chambers, as well as secure sample stages to hold them, is required. The sample stages in REES and OptiXS are of similar design so that sample mounting for all systems is identical.

Samples are mounted on a tantalum plate, shown in Figure 3.7 (left). The tantalum plate is shaped such that the front end can be guided into the sample holder, and a cross-piece on the back-end can be locked into fittings on the mag-arms

used to transfer the samples. Tantalum is chosen for the sample plate because of its high melting point and chemical stability at high temperatures. A 3D model showing the locking structure is also given in Figure 3.7 (right). The cross piece can be located into the initial cut, the magnetic arm is then rotated 90° and the final section of the groove is for 'locking' the sample holder in place.

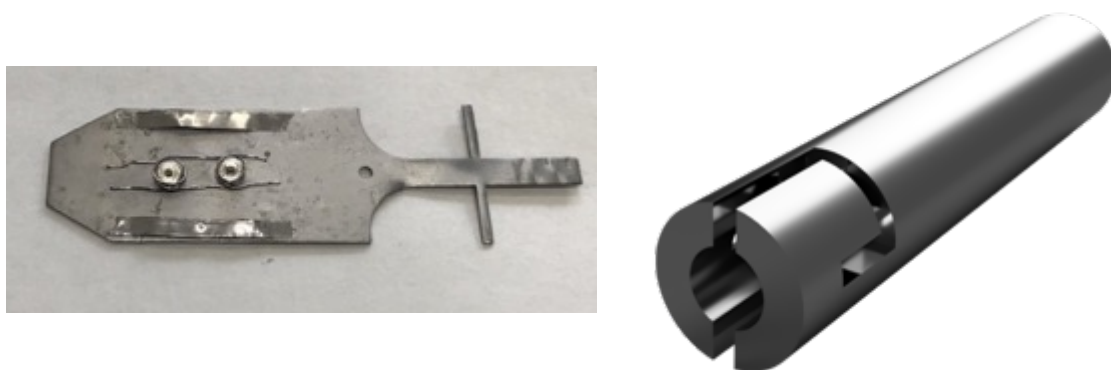


Figure 3.7: (left) The tantalum sample plate design used in the Aberystwyth University materials lab. Shown are two small diamond samples, mounted in platinum and held in place by tantalum wire which is spot welded to the plate. The cross piece is required for locking in the magnetic arm and strips of tantalum help create a good thermal contact with the heater stage. (right) The design of the locking mechanism on the magnetic arms used in sample transfer.

Throughout the two systems, all sample stages are designed in a manner to hold the sample plates, however there are some differences in the design and construction. The REES sample stage, shown in Figure 3.8, has a single space and is made from a Boralectric heater with a tantalum faceplate mounted 1 mm off the heater surface. The Boralectric heater comprises a graphitic track set within a hexagonal boron nitride plate and can reach temperatures off $\sim 1100^{\circ}\text{C}$. Graphite washers located at two of the corners are used for delivery of current to the heater. The heater is mounted onto a stainless steel plate by two insulating support rods in opposing corners. Two shorter bolts are attached to the other two corners for current delivery. Tantalum foil is mounted on the tantalum rods behind the heater for heat

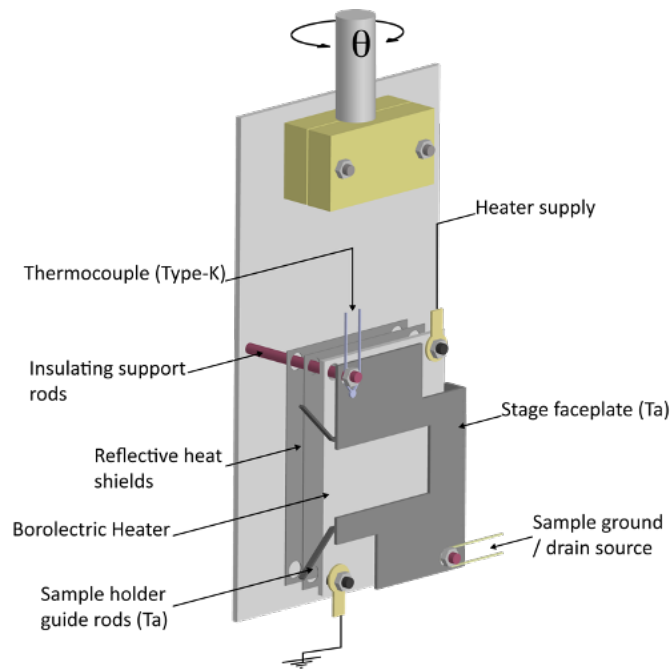


Figure 3.8: The REES system sample stage design. Taken with permission from Dr Simon Cool's thesis. [6]

shielding; this not only protects the steel plate at high temperature, but reflects radiative heat back towards the sample, increasing the maximum achievable temperature. A K-type thermocouple is attached to one of the non-electrical tantalum mounting rods for temperature measurement. 1 mm tantalum wires are used for guide rods and define the sample's mounting location. A wider opening assists with locating the sample plate into the stage. 1 mm Ta wire is also used as a washer on the two non-electrical rods on top of the Borolelectric in order to keep the faceplate raised and level. The sample stages are connected to an Omniax *xy* table with a built in *z*-drive and bellows for *xyz* manipulation. A rotary stage is mounted on the top of the manipulator for sample rotation. As the stage is also electrically isolated from the system, a connection for biasing the sample is attached. This is most commonly used for UPS were shifting the valence band information away from the high-intense secondary tail is necessary to avoid damaging the detector.

A similar heating stage design is implemented in the preparation chamber of the REES system (see section 3.8). However, a secondary stage is mounted beneath the Boralectric heater with a grid cover installed. This can be used for sample storage or for patterning of deposited films. The design of both these sample stages inspired the OptiXS manipulator design, which will be presented in section 3.5.

3.5 OPTICAL SPECTROMETER

In order to perform the optical spectroscopies described in chapter 2, an instrument capable of collecting, and dispersing light based on its wavelength is required. This purpose is fulfilled by optical spectrometers. Optical spectrometers specifically designed for Raman and Photoluminescence exist, however the basic working principle is the same, so both techniques can usually be performed on the same device. The majority of the optical data in this work has been taken on the Horiba LabRam. Although the name suggests it is solely for Raman, it is also used frequently for photoluminescence. Figure 3.9 shows a very simple schematic of the spectrometer used in the home laboratory. Strictly speaking, a spectrometer is an instrument which collects light and passes it through a diffraction grating which is dispersed onto a photon detector, usually a CCD. Each capacitor, or pixel, in the CCD generates a charge of magnitude relative to the incident photon intensity. These charge packets are collected and measured. The software then maps the pixel number to the wavelength/wavenumber. The components used in collection and measurement of light are marked by the dashed area in Figure 3.9. Portable spectrometers, such as the *OceanOptics Flame* spectrometer can contain only these components. However, in practice the majority of spectrometers are more complex.

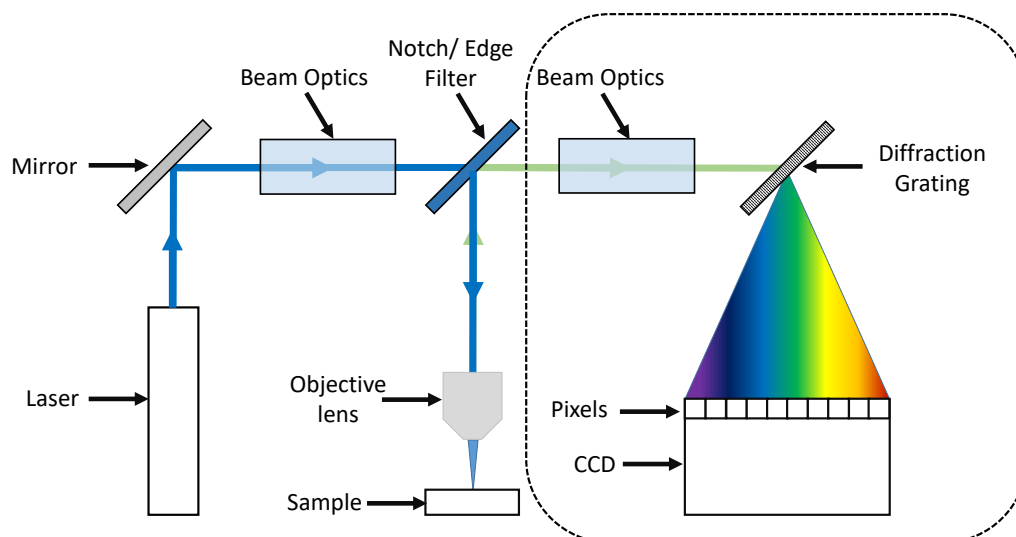


Figure 3.9: A simple schematic of an optical spectrometer. The dashed area is technically the spectrometer, however in practice, spectrometers include a number of additional components such as the light source, sample area and beam optics.

The Horiba LabRam spectrometer in the home lab can utilise the three lasers described in section 3.2.3. These lasers then pass through a series of ‘beam optic’ components before being reflected towards the sample by an edge or notch filter. The light is focussed onto the sample surface by a high numerical aperture objective lens with a 10x, 50x or 100x magnification. The spectrometer described is a reflection mode spectrometer, meaning light from the sample is collected using the same objective lens which is then passed through the notch/edge filter. After this, the light is again passed through a series of beam optics, before hitting a diffraction grating and dispersing onto the CCD (Charge-Coupled device).

The development of the CCD was a crucial milestone for a number of spectroscopic methods, including optical and photoemission methods. First developed in 1970 by Boyle and Smith, the CCD is an array of photosensitive, metal-oxide-semiconductor capacitors which produce a charge when light impinges onto them via the formation of electron-hole pairs. The magnitude of the charge induced will be proportional to the intensity of the incoming photons. The charge packets

induced are then 'marched' along the capacitor rows by a varying potential well height, until they arrive at an amplifier at the end of the row, where the charge is converted into a digital signal. This is synced with a transfer clock to maintain the order and integrity of the charge packets. The process of charge transfer, also known as the bucket brigade process, continues until the complete charge registry of the 2D array has been measured. This can then be converted into a 2D image.

The sections labelled 'beam optics' may contain a range of components, depending on the measurements required. These include; beam choppers for reducing the laser power, or in some cases provide a periodic light source, pinholes or irises for narrowing the beam size to improve spatial resolution or confocal (depth-resolved) microscopy, or optical filters for 'cleaning' the beam profile. Additionally, mirrors can be introduced into the beam optic sections before and after the sample. These mirrors either guide the beam towards a camera to provide a live video of the sample, or towards a set of fibre optics, which leads to the superhead lens system for *in-situ* measurements. This will be described in the OptiXS sections of this chapter.

3.6 THE HEMISPHERICAL ANALYSER

As discussed, XPS is based upon the ability to measure the kinetic energy of emitted photoelectrons from the sample material. There are a number of different effects which can be used to measure this; these include resonant collision phenomena, time of flight analysis, dispersion via an electric field, or retardation caused by a potential barrier [54]. A number of designs exist which apply the dispersion and retardation principles in the energy analysis of electrons. The designs apply a number of geometric shapes to trace a path which under known conditions only electrons of a

certain kinetic energy will travel. Toroidal, plane and cylindrical analysers are some of the geometries which exist, however, the most common analyser, and the one used for all of the photoemission experiments in this work, is the hemispherical analyser. There are two hemispherical analysers in the home lab which will be described. The REES system uses a *SPECS Phoibos 100* analyser, whereas the OptiXS systems uses a smaller, *HA50* analyser. Both analysers have the same working principles but have some distinct differences. The *Phoibos 100* is a more modern analyser, provide a number of lens modes which can be applied to the photoelectrons as they travel through it.

A schematic of a modern electron analyser, such as the *Phoibos 100*, is shown in Figure 3.10. The process of photoelectron detection begins when the electrons are collected by the nose-cone of the analyser. A series of electrostatic lenses then manipulate these electrons in a controlled manner, eventually focusing them onto the entrance slit of the hemispherical section. This ‘electron manipulation’ performed by the electrostatic lenses plays an important part in the photoelectron analysis. The different styles of manipulation by the electrostatic lenses are known as lens modes.

The *Phoibos 100* analyser possesses four groups of lens modes; transmission modes, angular dispersion modes, magnification modes and acceleration modes [55]. These modes have separate applications for which they are suited. The lens mode chosen defines the measured area on the sample, or the acceptance angle of the nose-cone. They can also manipulate the electrons in such a way that the directional information of the electron trajectory from the sample is preserved, projecting real-space imaging onto the detector. From this, angular information can be determined and converted into k-space measurements for Angle-Resolved Photoelectron

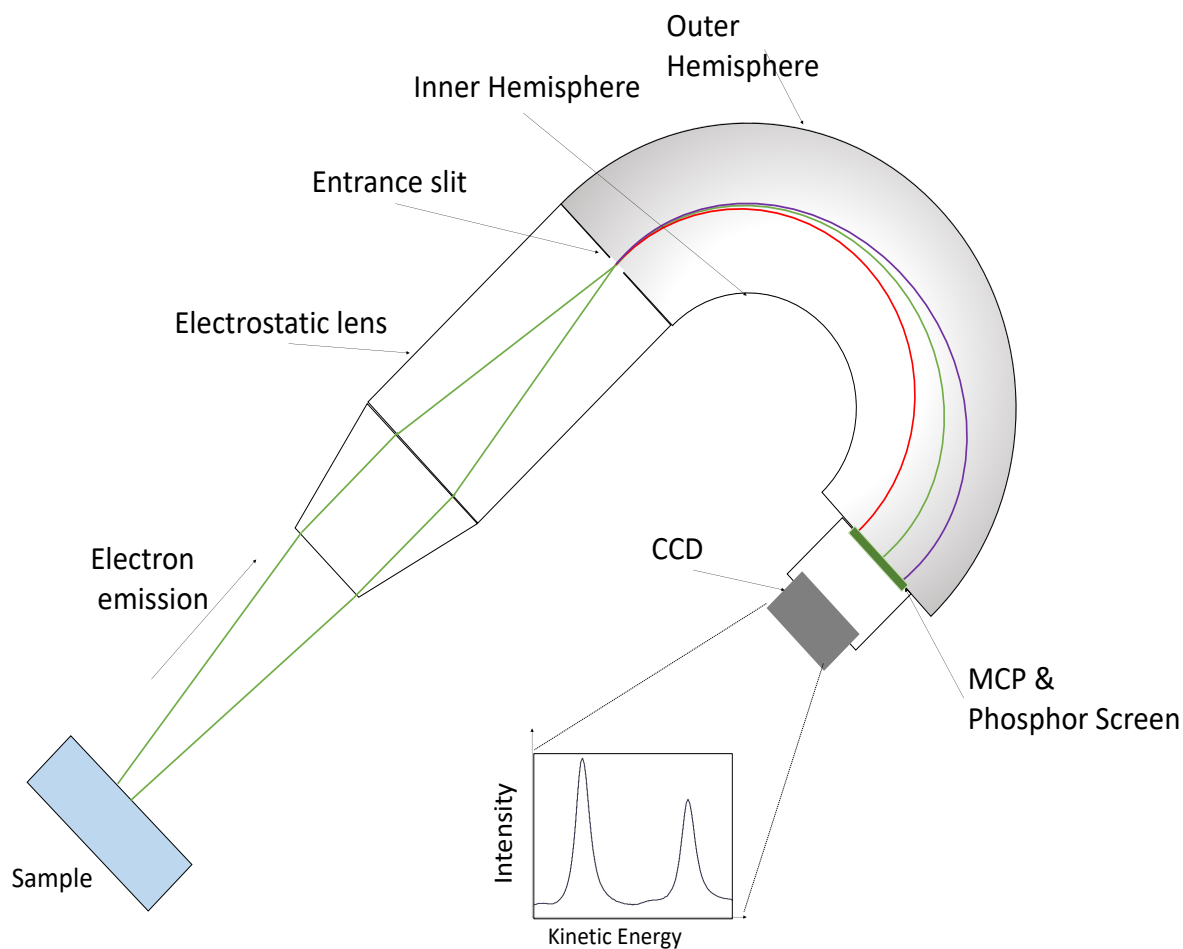


Figure 3.10: A simple schematic of the major components in an XPS system.

Spectroscopy (ARPES). The lenses are also responsible for applying a decelerating/accelerating voltage on the photoelectrons before they enter the hemispherical lens system.

An electric field is formed across two concentric hemispheres by applying two different negative potentials to each of them. Electrons which enter this field are deflected upon a radial path, for which the radius depends on the kinetic energy of the electron, dispersing the electrons along the radial plane. Higher energy electrons will take a wider radial path, and lower energy electrons will travel with a smaller radius. The 'spread' of electron energies, as well as the central kinetic energy (shown by the green path of on Figure 3.10), is defined by the difference in voltages applied

across the hemispheres. This energy spread is known as the pass energy E_p and can be calculated by the equation

$$E_p = -\Delta V \frac{e R_1 R_2}{R_2^2 - R_1^2}$$

Equation 3.9

where ΔV is the voltage difference between the hemispheres, R_1 and R_2 are the radii of the inner and outer hemispheres, respectively, and e is the value for the elementary charge, given as $1.602176... \times 10^{19}$ C.

In practice, the retarding voltages applied by the lenses define the kinetic energy of the electrons measured, and the voltages on the hemispheres are kept constant, this is known as Fixed Analyser Transmission (or FAT). During measurements, the lens voltages are swept in order to scan through a range of kinetic energies. The efficiency of electron delivery to the focal plane of the analyser is dependent on the kinetic energy of the electron. It is also dependant on the lens mode used. The efficiency dependency is what defines the transmission function described earlier. The transmission function must be taken into account in order to provide a true XPS quantification.

For some applications a second analyser mode may be used. The Fixed Retard Ratio (FRR) mode utilises a variable pass energy to maintain a constant deceleration/acceleration factor which is defined by

$$R = \frac{E_k}{E_p}$$

Equation 3.10

Although FRR can be used for any measurement, it is less commonly applied. The FRR mode can provide more detail in certain measurements, which do not

require a rigorous quantification. When using FRR for scans of wide kinetic energy ranges, it almost mimics the normalisation process. This is due to the reduction of the pass energy as the kinetic energy reduces.

The pass energy is one of the most important variables to consider when performing any photoemission measurements. The pass energy affects both the resolution and the measurement intensity. A larger pass energy results in a larger number of electrons at the detector, as well as a greater energy range of electrons that are ‘allowed’ to pass through the hemispheres. The overall intensity depends on the square of the pass energy. Therefore, doubling the pass energy will result in approximately $1.414 \times (\sqrt{2})$ greater signal. The larger pass energy also results in a larger spread of electron energies being mapped onto the detector, resulting in a decrease in the resolution. This intensity-resolution trade-off results in a larger pass energy being used in survey scans, where only rudimentary quantification is performed. However, for the detail needed in core level scans, a lower pass energy is required because of the increased resolution. The lower signal intensity results in a higher SNR, requiring a larger number of acquisition sweeps to rectify. The resolution is also affected by the widths of the entrance and exit slits. Intuitively, the wider the slit widths, the lower the resolution. The analyser resolution ΔE can then be calculated using the equation

$$\Delta E = E_p \left(\frac{W_{\text{ent}} + W_{\text{exit}}}{2R_0} + \frac{\alpha^2}{4} \right)$$

Equation 3.11

where W_{ent} and W_{exit} are the entrance and exit slits, respectively, R_0 is the central radius of the hemispherical analyser (the green path on Figure 3.10) and α is the half angular dispersion at the entrance slit plane.

As the photoelectrons arrive at the detection side of the analyser, there is an energy dispersion present. Electrons with a kinetic energy equal to the pass energy will arrive in the central of the exit slit/detector. The variation in photoelectron energies will transpose to a physical deviation from the central path such that

$$\Delta E_k = D \Delta x$$

Equation 3.12

where D is the dispersion factor, presented in eV mm^{-1} or eV pixel^{-1} for CCD detectors. There are two electron detection methods used in the two hemispherical analysers in the home laboratory. The *HA50* utilises a Channel Electron Multiplier (CEM), whereas the *Phoibos 100* as depicted in Figure 3.10, uses a more modern phosphor screen, in tandem with a microchannel plate (MCP) and CCD combination. Even with the more modern technology, a CEM is still a feasible form of electron detection with a number of benefits.

The CEM in the *HA50* is a single channel, high-gain electron multiplier [56]. The main structure is a spiral shaped piece of glass coated in a high-resistance, semiconducting material, shown in Figure 3.11. As a voltage is applied to this structure, it becomes a continuous dynode. A continuous dynode is analogous in principle to a discrete dynode, but the spiral structure facilitates collection for a larger range of electron trajectories. As electrons enter the CEM and impinge on the inner surface, it can cause secondary electron emission from the semiconducting material. One electron may induced roughly 1-3 secondary electrons. After the secondary

emission, these electrons are accelerated, due to the negative voltage applied to the CEM, leading to further collisions between the electrons and the CEM walls. The final result is a series of further secondary emissions which leads to an avalanche effect, and ultimately a large gain of electrons. Typically, if a single electron enters a CEM of this sort, 10^8 electrons will arrive at the analyser exit. The current gain can be controlled by the voltage applied on the CEM.

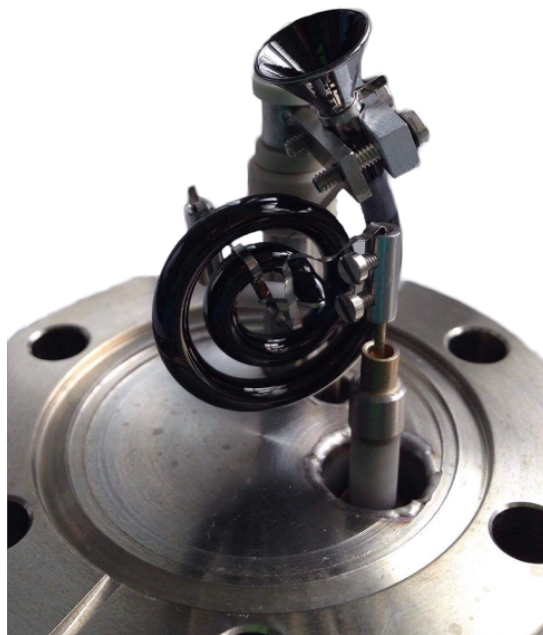


Figure 3.11: The CEM detector used in the HA50 analyser.

One can find the working (multiplier) voltage of a CEM by slowly ramping the applied voltage whilst plotting the measured signal. The signal will increase in a sigmoidal like manner, until a plateau is reached. The start of the plateau is where the working voltage resides. This voltage will be increased during the lifetime of the device due to general wear-and-tear. There is also a maximum multiplier voltage which can be applied. This means the working voltage can be a good indication of the device lifetime. A lock-in amplifier, and the use of threshold detection values provide signal with a very low SNR. Whilst CEM can provide a highly sensitive signal with very

low noise contributions, it is limited in its capabilities. Limitations include; only one electron energy can be measured at one time, and a single CEM has a relatively small angular acceptance (approx. 3°). This means many electrons with trajectories that deviate greatly from the central analyser path do not contribute to the measured signal, both of which lead to increased measurement times.

Modern day electron analysers now utilise a series of channels in order to provide a wider angular acceptance, a higher measurement resolution, as well as providing the ability to produce photoemission images. The first development away from single channel detectors, was to simply add exit slits and extra CEMs either side of the central detector, in order to capture a wider angular range of photoelectron energy dispersion. Devices of this type are still available today, with *SPECS* offering 5- and 9-channel detectors for 'extremely high count rate' applications. Further development aimed to increase the number of channels, to produce detecting units capable of collecting a large amount of the electron dispersion area, whilst maintaining a high energy resolution. This led to the development of position-sensitive detectors, which use an array of channels, rather than a single row. Channels parallel to the electrical field allow for energy-resolved measurements, and the orthogonal channels provide a spatial resolution in the non-energy-dispersive plane. An array containing a large number of channels may result in some issues regarding cross-talk between channels and hardware geometry. Nevertheless, there are 2D CEM detectors with 1526 channels that have been developed which overcome these issues [57]–[59]. However, because of the complexity of these detectors, the *Phoibos* 100 implements a simpler detection set-up, made up of a phosphorescent screen and a CCD to image the electron dispersion optically.

The phosphorescent screen glows when impinged by the photoelectrons, and the intensity of the 'glow' is proportional to the number of electrons which have collided with the screen. It is this emission that is imaged by the 2D CCD. The CCD used on the home lab *Phoibos* analyser is the *PixelFly* CCD. The *PixelFly* contains a 500x500 array of pixels (capacitors) and works in an identical manner as the CCD on the *Horiba LabRam*, described in the previous section. The large dynamic range of the *PixelFly* detector results in the ability to readily measure weak and strong signals on the same 2D array simultaneously. Amplification of the CCD signal post-detection is generally avoided as this will increase the noise on the signal. To account for this, electron amplification is performed before the electrons impinge on the phosphor screen via a micro-channel plate. This is essentially an array of tunnels through a highly resistive material, effectively producing an array of multiplier tubes. Each of these tubes work in a similar fashion to a CEM, but thanks to the array's shape, the electron position at the detection array can be maintained.

Further benefits associated with the use of a CCD detector array is the information which can be acquired perpendicular to the energy dispersion axis. As mentioned, the pass energy also describes the energy range of the electrons that are 'allowed' to pass through the hemispheres. For a normal transmission mode, the perpendicular axis therefore provides real-space information of the *z*-axis of the sample. This is ideal for sample alignment, where one would strive to minimise the photoemission contribution of other materials around the sample *i.e.* the sample stage and holder. In angular modes, which are not used in this work, the azimuthal angle between the sample and the path of the photoelectron is preserved, leading to mapping of the band structure onto the CCD.

3.7 THE DEVELOPMENT OF THE OPTICAL AND X-RAY SPECTROSCOPY INSTRUMENT (OPTIXS)

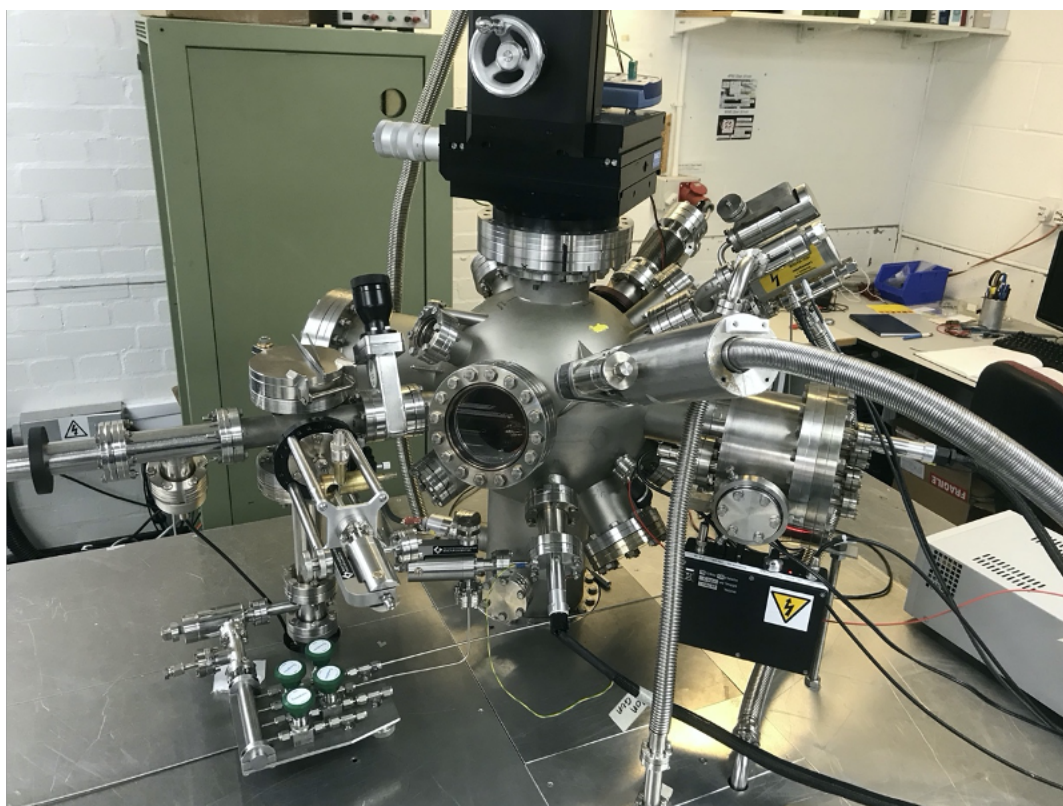


Figure 3.12: The OptiXS system at the Aberystwyth University materials lab.

3.7.1 OVERVIEW

As outlined in previous chapters, a large amount of information can be gained by photoemission and optical spectroscopies. This information may be improved upon when these techniques are utilised simultaneously during real-time experiments. The main goals of this work were to develop an instrument capable of; treating diamond surfaces to adjust and control the surface termination, perform implantation of nitrogen into the near-surface region of diamond, and also provide heating/cooling capabilities in tandem with real-time optical and electron spectroscopies. However, the instrument is also designed to be a high-throughput, multifunctional, user-friendly system for a wide range of materials and applications. This led to the Optical

and X-ray Spectroscopy (OptiXS) system. An image of OptiXS is given in Figure 3.12 and a 3D model showing the majority of components in the main chamber is shown in Figure 3.13.

At the time of writing, OptiXS has been used in studies of photovoltaic materials, organic and inorganic compounds, and ion implantation in diamond. There are also plans for further use in a number of projects from a range of fields.

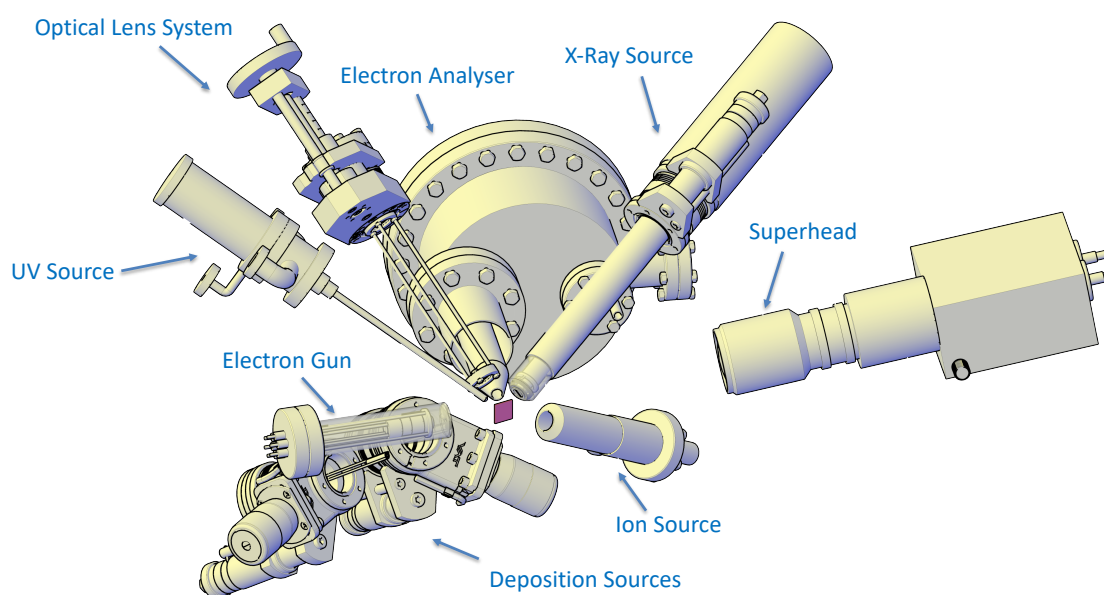


Figure 3.13: The OptiXS analysis chamber components. The purple square in the centre indicates the sample position.

During this project the main developments of the OptiXS system included the following.

1. The development of a multi-technique analysis chamber that includes *in-situ* capabilities for Raman spectroscopy, XPS/UPS, PL, cathodoluminescence, XEOLS (X-ray Excited Optical Luminescence Spectroscopy), and rudimentary EELS (Electron Energy Loss Spectroscopy).
2. The development of a plasma source for surface termination.
3. The development of a variable temperature (-177 to +1000 °C) manipulator.

4. The addition of a quick change deposition source that doesn't require system venting.

5. The development of a gas delivery system for the delivery of high purity gas to the various instruments.

6. Calibration of the hemispherical electron analyser, increasing signal from the Raman superhead for *in-situ* Raman measurements, and performing the initial testing of the instrument capabilities.

For clarity and simplicity, the instrument components have been split into three sections; the **analysis chamber**, **Load lock/Plasma Chamber**, and the **gas lines**.

Analysis Chamber: This is the chamber used for sample characterisation. It consists of a 300 mm diameter mu-metal spherical chamber with a number of portholes, focussed on the chamber centre. Figure 3.13 shows a 3D model of the components used in the analysis chamber. A PSP HA50 hemispherical analyser is installed on the chamber equator, coupled to a VG XR3E2 twin-anode X-ray source, with magnesium and aluminium anodes, utilised for XPS. A SPECS 10/35 source provides the ultraviolet light required for UPS. Both the UV source and X-ray gun are mounted at an angle of 54.7° with respect to the sample normal (and the nosecone of the analyser). A PSP ISIS3000 ion source, capable of ion acceleration up to 3 keV, is installed on a low angle flange for sample sputtering and near-surface ion deposition. A Prevac ES40 electron gun, also on an equatorial flange, can provide up to 30 mA electron exposure with a maximum kinetic energy of 5 keV. Focussing elements provide a minimum spot size of approximately 2mm², also allowing the spot to be translated on the sample. Automated controls provide a mapping function to allow controlled dosage over a given area.

Optical spectroscopy capabilities can be performed via two ports, depending on the light delivery/collection method required. One of the choices is an *in-vacuo* lens mounted onto a z-drive and coupled to a fibreoptic feedthrough flange which can be connected to a fibre outside of the vacuum. An *Ocean Optics flame* spectrometer can also be mounted directly onto the flange output for direct light collection and minimal losses. The other choice is the superhead device which can deliver and collect a laser light ex-vacuo through a flange window.

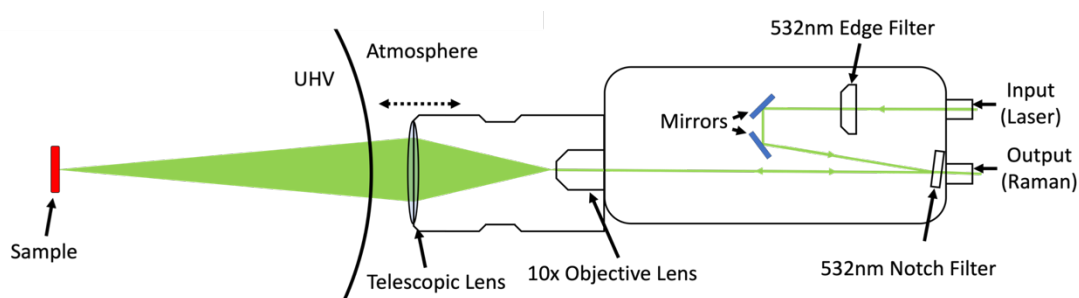


Figure 3.14: The superhead instrument which can be mounted on a number of chamber windows and used for light delivery and collection for in-situ optical spectroscopy.

The superhead, shown in Figure 3.14, consists of; a fibre input/output, a series of mirrors and filters which deliver light through a x10 microscope objective lens, and a telescopic lens with a focal length range of the order of the chamber radius (approx. 250-400 mm). The input and output of the superhead are connected to optical fibres. The input fibre is fed from lasers on the Horiba LabRam optical table and the output fibres feed to the spectrometer itself. The input fibre is a single mode, 100 μm bore fibre, in order to deliver sufficient laser power whilst maintaining a small spot size at the sample. The output fibre is a 400 μm bore fibre with extra cladding. The wider bore increased the measured signal significantly, and the cladding was necessary due to unwanted light penetrating the previous fibre and disrupting measurements.

Deposition sources are also installed on the analysis chamber. A quick-change K-cell port utilising a gate valve, and a dedicated pumping path provides the ability to

swap deposition sources, without the need to vent the main chamber. This reduces down-time during K-cell transitions to a few hours, taking into account time for pumping, and a short bake.

The final instrument, not shown in Figure 3.13, in the main chamber is the sample stage and manipulator, which protrudes into the chamber vertically through the top flange. The design and development of the OptiXS system is described in section 3.7.2.

Load Lock/Plasma Chamber: The load lock is the route of access for introducing samples into the system. It is connected to the analysis chamber, separated by a gate valve to preserve the working pressure in the main chamber during venting of the load lock. The load lock can be brought to atmospheric pressure through a vent valve located under the OptiXS table. A magnetic arm is connected to the load lock on the opposing side from the analysis chamber, on which samples are mounted and transferred. Perpendicular to the magnetic arm is the plasma source described previously. During plasma treatment the sample is held by the magnetic arm. The chamber and plasma unit are pumped from atmosphere by a two stage rotary pump to a pressure of 10^{-3} mbar, and a Leybold TW70 turbomolecular is used to pump the chamber further to a base pressure of approximately 3×10^{-8} mbar. During roughing, a pirani gauge is used to monitor the pressure, and a cold cathode is used when the pressure drops below 10^{-3} mbar. Plasma treatment is performed at pressures ranging between 10^{-4} and 10^{-5} mbar, with ignition sometimes requiring pressures of the order of 10^{-3} mbar. The load lock is also connected to the gas lines via an all-metal valve. The load lock pumping path is used for pump-purging of the gas line system.

The Gas Lines: Gas delivery to a number of components around OptiXS is required. The UV source, ion gun and plasma source all require the controlled delivery of high purity gas for their applications. The main component of the gas line is a small cylindrical volume welded to a CF16 flange, with four 0.25" gas lines along its length. The CF16 side is attached to an all metal valve on the load lock for pump/purging capabilities. The four pipe fittings are attached to Swagelok valves that lead into four T-pieces. The T-pieces are aligned vertically, with the lower piping route leading to the gas bottles, and the side opposite the valves lead to the corresponding instrument on OptiXS. A schematic of the gas lines is shown in Figure 3.15.

The gas piping system is designed in such a way that each pipe between the bottle and instrument can be isolated. Isolation of the narrow piping drastically reduces the volume of gas stored between the bottle and instrument. This helps maintain a high purity of gas during operation. Connecting the pipes to the larger volumes allows for

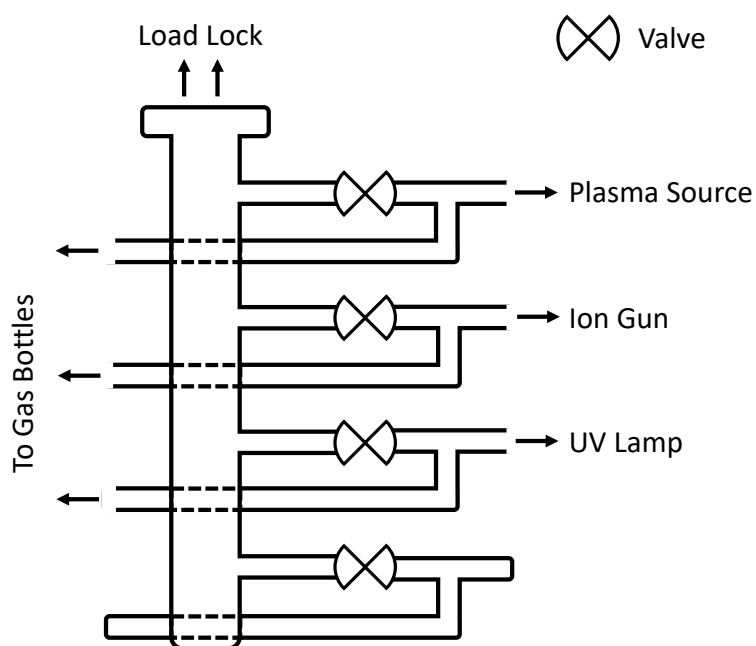


Figure 3.15 : A schematic of the OptiXS gas line system. The pipes leading to the gas bottles are connected directly onto the gas bottle regulators. All pipes to the instruments lead to needle valves for controlled gas flow into the system. The dashed line indicates piping going underneath the volume which leads to the load lock.

quick pump/purging to the load lock, as well as quick gas changes between instruments, and even provides the ability to produce gas mixtures, if required.

3.7.2. THE OPTIXS MANIPULATOR

The OptiXS manipulator has been designed and constructed during this work. The general design has taken inspiration from the REES system sample stages. However, the design process has attempted to implement certain improvements for a more versatile manipulator, which is also easier to maintain. There are five main components to the OptiXS manipulator; the liquid nitrogen inlet, the electrical feedthrough adapter, the rotary drive, the *xyz* manipulation unit and the *in-vacuo* stage itself. The manipulator (excluding the *xyz* and rotary stages) is shown in Figure 3.16.

The OptiXS manipulator has two sample stages, a ‘hot stage’ and a ‘cold stage’. These were designed in AutoCAD, with the majority of the pieces being machined on site. The 3D model of both stages is shown in Figure 3.17. The hot stage has a very similar design to the REES sample stage. With a Boralectric heater mounted on tantalum rods. The tantalum heat shielding differs slightly, as it is more enveloping than the REES stage. This was to reduce of radiative dissipation being a very large source of heat loss, and the necessity to protect more components in the OptiXS chamber, including the cold stage and the steel support plate on the manipulator itself. Ceramic pieces are used to attach the hot-stage to the steel support plate in order to electrically isolate it from the system. This allows for a voltage to be applied to the stage alone, in order to bias the sample, which is necessary when measuring the secondary electron cut-off. This is especially useful for UPS where shifting the valence

band structure away from the large secondary electron tail is key for accurate quantification of electronic properties.

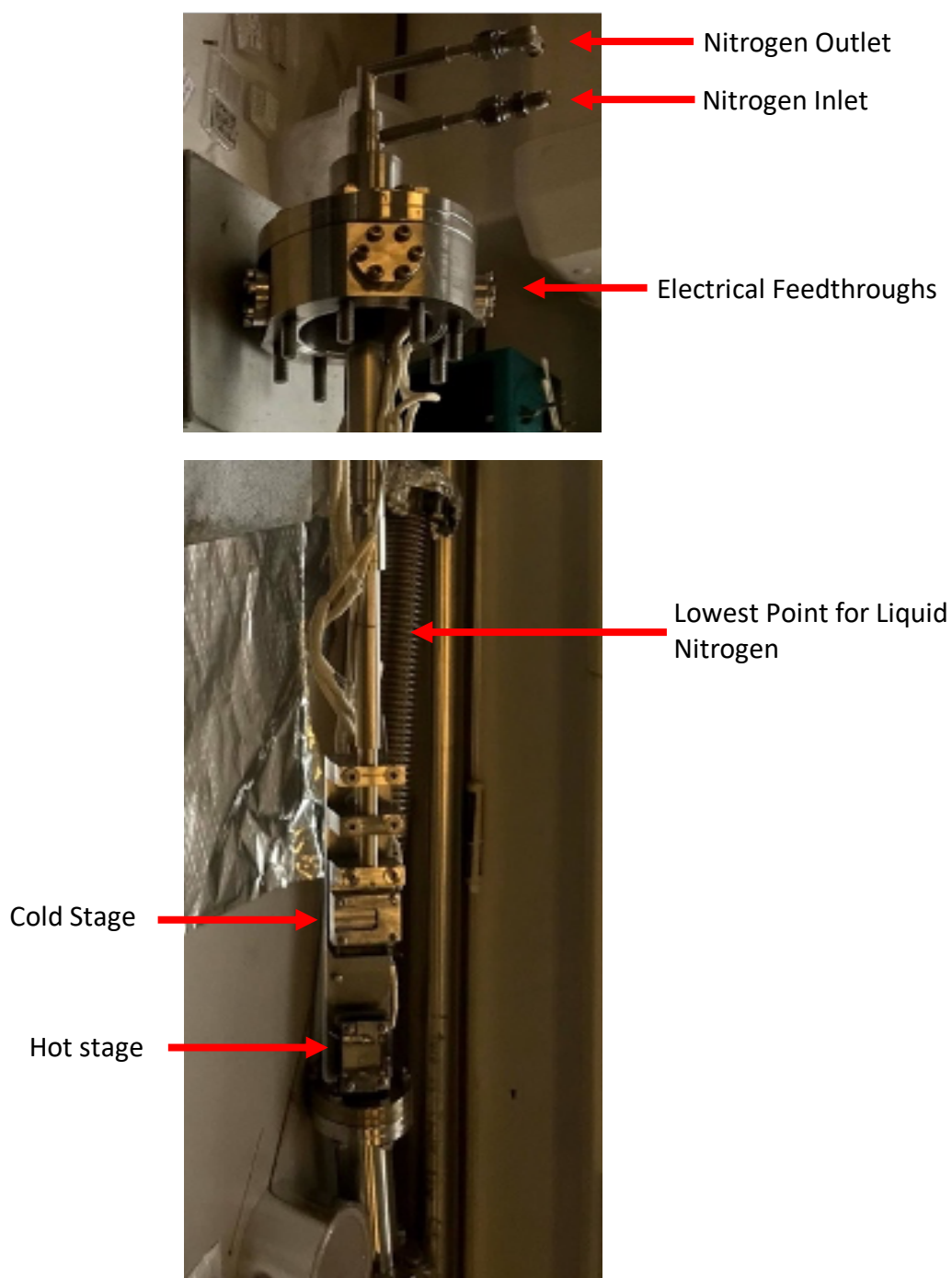


Figure 3.16 The OptiXS manipulator and sample stage with the main components labelled. This is mounted through the xyz stage on the system when in use. The images are cropped such that the manipulator arm is shortened for clarity.

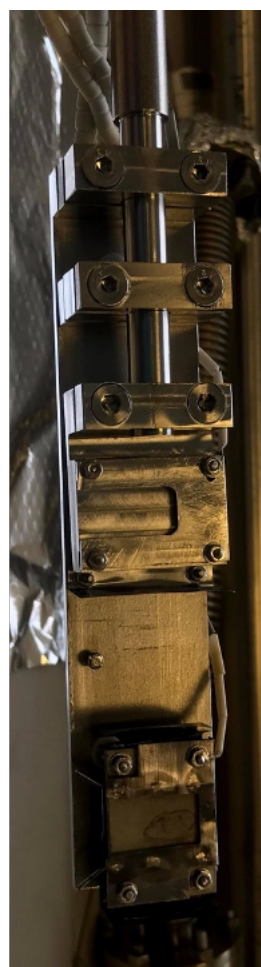
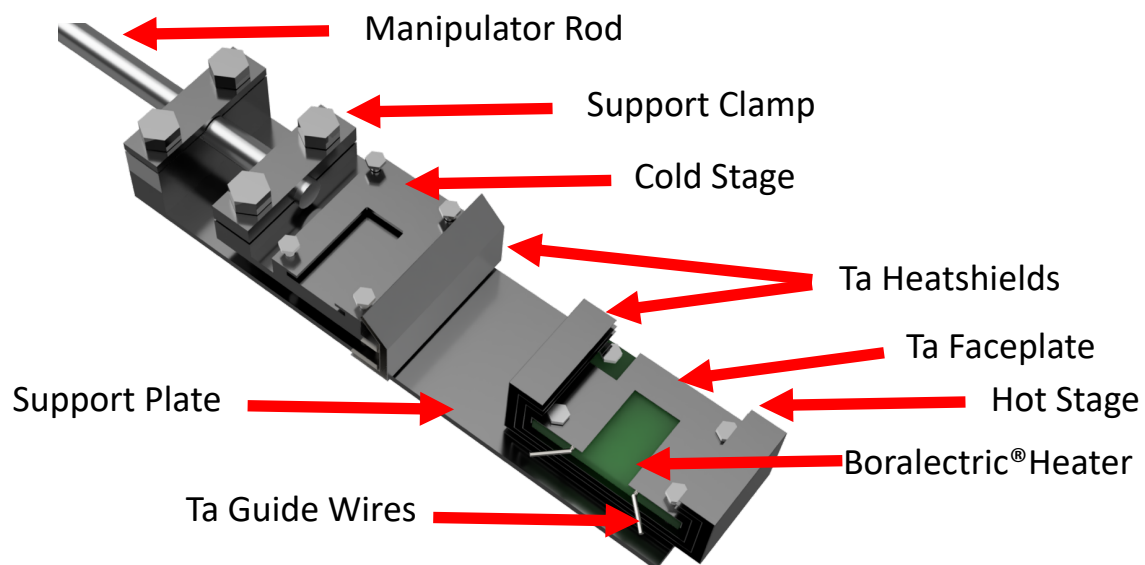


Figure 3.17: (top) The 3D design model of the OptiXS sample stage, made in AutoCAD and rendering in Autodesk Fusion. The final sample stage installed in the OptiXS system is shown below. The front and back are displayed in order to clearly show the wiring and the stages themselves.

The cold stage is machined from stainless steel and connected directly to the manipulator rod by a stainless steel clamp. This direct connection has been made in order to improve the thermal conductivity between the liquid nitrogen inlet pipe and the stage itself. The liquid nitrogen is input into the top of the manipulator and flows into a hollow section of the manipulator rod, where it evaporates and leaves via the outlet. Thermocouples are attached to both stages underneath one of the support bolt heads. This provides a good thermal contact to the faceplates whilst still being in close proximity to the sample, and not hindering experimental procedures.

Electrical connections are made through a bespoke home-made multi-flange adapter. Currently, four CF16 flanges are available for electrical feedthroughs to be mounted. However, the piece was designed in a manner that if more feedthroughs were needed, the adapter would only require a relatively small amount of machining to become an eight-flange adapter. Currently there are two CF16 electrical feedthrough installed on the manipulator: a 6-pin feedthrough specifically designed for K-type thermocouples, and a 16-pin flange for; power delivery to the heater stage, applying bias to the sample stage, or measuring resonant frequencies on quartz crystal balances, used for measuring deposition rates from K-cells.

The top component of the manipulator is the nitrogen cooling system. The cooling system consist of a coaxial hollow centre which extends down into the manipulator rod (the bottom of the hollow section is indicated by the red arrow on Figure 3.16). As mentioned, there is an input where liquid nitrogen enters into the inner section of the two layers of the manipulator rod. Once the nitrogen reaches the bottom it evaporates and proceeds to rise up the length of the manipulator through the outer section, eventually leaving through the outlet pipe.

The components shown in Figure 3.16 can then be mounted through the rotary and *xyz* stages. The manipulator was designed such that the cross-sectional area of the sample stages is smaller than the inner diameter of the wide-bore rotary stage, and the bellows on the *xyz* manipulator. The benefits of this design are two-fold; 360-degree rotation is possible due to the wiring being part of the rotating section. In some manipulator designs the wiring does not rotate, leading to the wrapping of wires around the central manipulator arm, limiting the amount of rotation possible. Usually, to overcome this, excess wiring is installed to avoid it limiting rotation too much, however with this design there is no limitation internally. The second benefit is ease of maintenance and repair. With other manipulators in the home lab, if there is an issue with the sample stage, such as wiring, wear and tear, or damage, the entire manipulator must be removed to access the necessary components. This is a very labour intensive and difficult task due to the weight of the manipulation stages. With this new design, the *xyz* and rotary drive can be left on the system, and solely the central arm can be removed through the centre of these components. The section removed is shown in Figure 3.16.

3.7.3 CALIBRATION AND CHARECTERISATION

In order to be confident in the ability and accuracy of the OptiXS system, it must be calibrated and tested. With the addition of multiple new elements, this was not a trivial task. This section will include the process of calibrating the HA50 analyser, as well as ‘proof of concept’ experiments, where the multifunctionality was tested. The ion source and the plasma system were also installed and tested during this work; however, these will be discussed in Chapter 7.

3.7.3.1 HA50 HEMISPHERICAL ANALYSER CALIBRATION

Modern day hemispherical analysers, such as the *SPECS Phoibos100* on the REES, are calibrated by taking a series of wide energy range scans of a clean calibration target with well known, consistent core level energies. Commonly for this, silver, copper or gold, are measured at different pass energies on a specific lens modes. Once these are taken, the *SPECSlab* prodigy software calculates the calibration. The *SPECS* calibration can be used to calibrate the energy axis, as well as the gains factor, which in essence is accounting for the relative sensitivity of each pixel in the detector. However, for the *HA50* analyser, it is a much more manual process.

To calibrate the energy axis using a *HA50* analyser, two digital-to-analogue conversion voltages are available to adjust the energy axis. The two voltages represent a 'shifting' of the energy axis and a 'stretching' of the energy axis. With this ability, a number of core level peaks can be measured, and the voltages adjusted until all peaks are within measurement accuracy of the known energy. The minimum number of core levels needed would obviously be two, however a 3 (or more) point calibration is more trustworthy. As the *HA50* analyser was installed before the new manipulator, it was initially calibrated using a copper sample, without degassing or sputtering, so the core levels to be used were the Cu2p doublet (to check the energy axis over a short energy range), and the C1s core level signal from adventitious carbon on the copper surface (to check the energy axis over a longer range). This calibration was also prior to the recoating of the Mg and Al anodes, this meant a large ghost peak of the C1s core level was present because of oxidation of the Mg anode. Serendipitously, this ghost peak could be used to assist in the calibration as the energy difference between Mg $K\alpha$ and O $K\alpha$ photons is 729.3 eV, so the kinetic

energy difference of the C1s core level, and its ghost should be this also. With this being a calibration on an unclean copper sample, the calibration was checked again after the sample heating stage and the ion gun was installed, using the Ag3d and LLM Auger features from a silver sample. A third calibration was performed after the anode was recoated, as this can change the spectral shape of the X-rays emitted.

Once calibrated, a number of other parameters linked to the CEM can be adjusted to optimise the performance of the *HA50* Analyser. These are the 'threshold' voltages and the multiplier supply voltage. The gains voltage is described in section 3.6 and is adjusted until a plateau in the signal intensity is reached. The threshold voltages are the parameters which a CEM uses to differentiate between a signal and noise. For simplicity, it is best to describe the threshold as, the larger the threshold voltage is, the larger the electron density at the detector side of the CEM needed in order to be registered as a signal. While fairly simple in nature, it is a very powerful tool that can provide a very high SNR if set correctly, comparable to a lot of modern day CCD's.

Finally, it is beneficial to measure the (Gaussian) broadening contribution to the measured signal from the analyser itself. As shown in equation 3.11, a theoretical resolution can be calculated, however, quick measurements can prove useful to give a baseline for expected linewidths provided by the analyser. For this characterisation, high resolution 3d core levels from the clean silver sample used in the calibration were measured at a number of pass energies (44, 22 and 10 eV), and the FWHM of the resultant peaks were calculated by fitting a Voigt profile to each one. From this, the Gaussian and Lorentzian contributions can be extracted. Figure 3.18 shows the Ag3d spectra measured using the three pass energies. The raw data are shown by the

circular markers and fit envelopes are shown by the solid lines. Table 3.4 shows the fit parameters extracted from each spectra. It should be noted that all width parameters were left to float, so the consistent Lorentzian contribution is solely from the fit as this was not constrained.

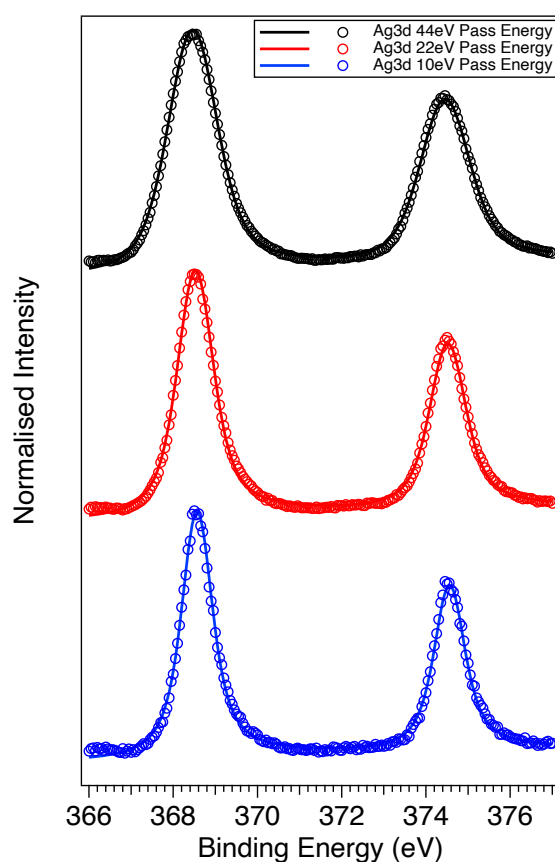


Figure 3.18: Ag3d spectra taken at three pass energies, 44 eV (black), 22 eV (red) and 10 eV (blue). The intensities are normalised, so the width variation is more clearly shown.

Table 3.4: Width parameters calculated from the fitting of Ag3d spectra taken at different pass energies.

Pass Energy (eV)	FWHM (eV)	Lorentzian width, from fit (eV)	Gaussian width, from fit (eV)
44	1.43	0.64	1.01
22	1.04	0.64	0.63
10	0.87	0.63	0.47

3.7.3.2 SIMULTANEOUS STUDY OF IRON DEPOSITION ON DIAMOND AND BORON NITRIDE WITH *IN-SITU*, REAL-TIME RAMAN AND XPS

One of the main benefits to developing the OptiXS system was the ability to perform *in-situ* optical and electron spectroscopies simultaneously. With the equipment in place, a series of experiments were undertaken to test the capability of the system. The first experiment expands upon previous works in the materials group in Aberystwyth which utilises iron overlayers on single crystal diamonds. This experiment involved using the iron K-cell installed on OptiXS to slowly deposit clean iron onto a diamond substrate and to monitor the effect this has on the first-order diamond Raman and the XPS signal. XPS is commonly implemented to monitor film growth due to its surface sensitivity, and by using a Beer-Lambert law it is relatively easy to calculate an overlayer thickness from the attenuation of the signal from the substrate core levels, in this case, C1s. As this was the initial test experiment for the multifunctionality, an expendable sample was created using 50 μm diamond grit pressed into copper. The growth of Fe onto a sample was successfully measured with the results showing a non-uniform growth model, most likely due to the sample roughness. The roughness of the sample also induces difficulty for a full statistical analysis because of shadowing effects, however growth rates can still be deduced. The last experiment used the results from the boron nitride deposition to monitor the Raman attenuation in real-time of a single crystal (100) diamond and to use this to determine when a 2 nm iron film is grown. This sample would then be used in other experiments within the materials research group at Aberystwyth.

During the diamond grit experiment, the goal was to test the feasibility of performing deposition, optical and electrical measurements in tandem. It was also the first use of an iron deposition source used on this system, so it would double as a calibration run for the K-cell too. All in all, three deposition runs were performed at increasing K-cell currents. These were a 90 minute run at 1.35 A, a 60 minute run at 1.5 A and another 60 minute run at 1.75 A. Figure 3.19 shows the results obtained. The XPS widescans alone are given to show that, as expected, there was a steady increase in the iron signal, and an attenuation of the copper/diamond substrate signal. However, the quantitative analysis gave results which suggested extremely low deposition rates of $< 1 \text{ \AA}$ per hour. The unexpected value was put down to the size of the diamond grit used, and the resultant roughness of the surface formed when pressed into copper. With the grit size being $50 \text{ }\mu\text{m}$, if an almost perfect packing of the grit into the copper sample is assumed, the root-mean-square roughness would be of the order of $25 \text{ }\mu\text{m}$. This value, and the fact the K-cell is mounted low on the chamber, results in a shadowing of a large portion of the surface, which makes the quantitative side of this experiment unreliable. However, a number of useful points were found from this. The Raman signal did progressively attenuate to a measurable degree, and it could be measured simultaneously with XPS. To do this, the sample was rotated away from normal to the photoelectron analyser towards the objective lens of the superhead, until a good compromise of signal intensities was found. This was found to be a fairly small rotation of approx. 20° off normal as optical spectroscopy is much less sensitive to measurement angle than XPS.

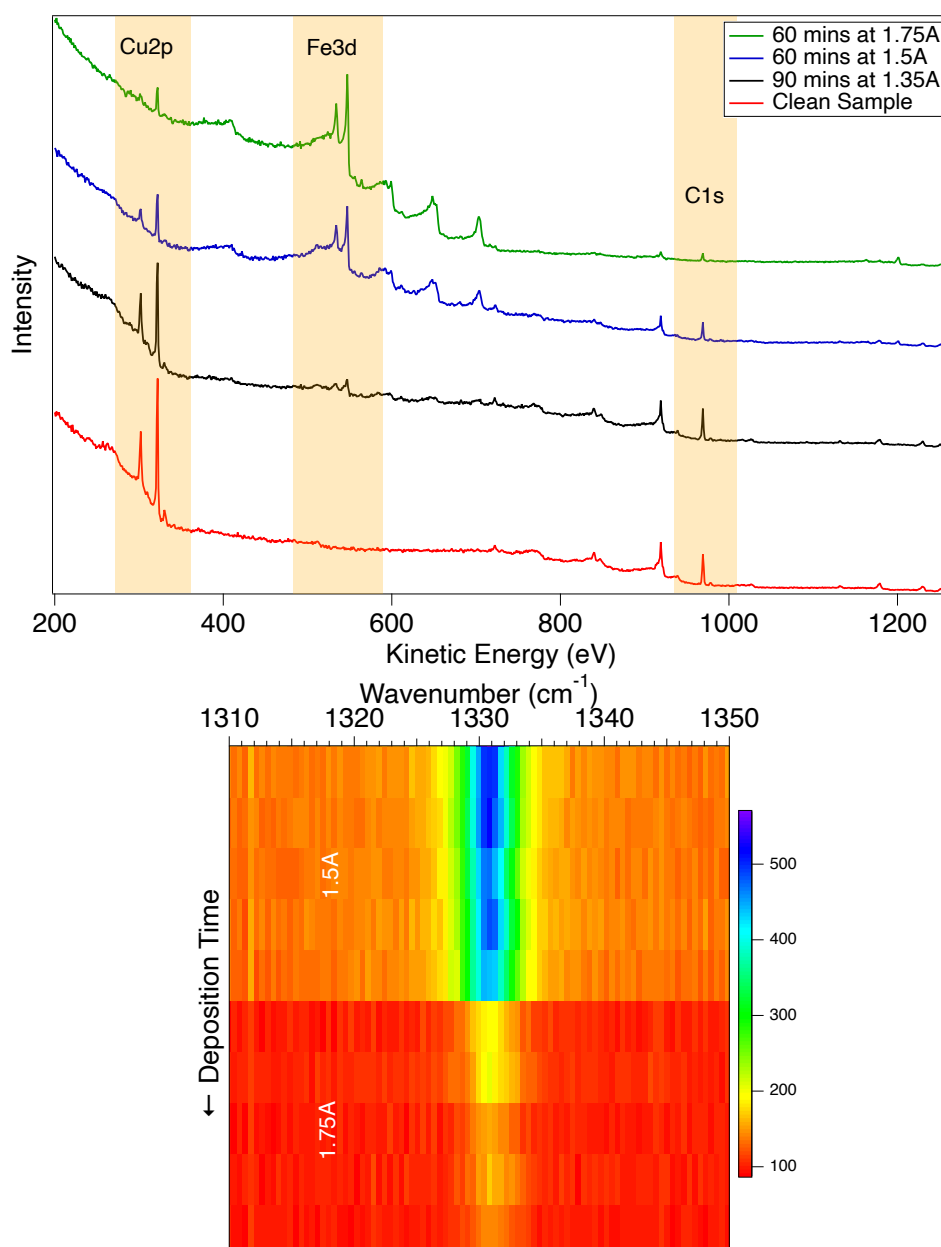


Figure 3.19: (top) A series of widescans of diamond grits pressed into copper taken after iron deposition runs at various deposition currents. The regions highlighted show the copper, iron and carbon signal which were used in the quantitative analysis. (bottom) The Raman spectra taken at different stages during the final two deposition runs. The 1.35 A run is not shown as the change in the Raman signal was negligible. A colour scale is given to indicate the intensity (counts) associated with each colour.

The next experiment, in collaboration with Joseph Durk from Aberystwyth and using single crystal, polished boron nitride samples from Element Six Ltd, was similar in nature, where the first-order Raman, and the photoelectron signals were used to monitor the iron deposition. Further development with the XPS and Raman acquisition software allowed the ability to perform these techniques in real-time and

simultaneously with the deposition. REES has been a highly valuable technique in previous work from the Aberystwyth group, where a CCD is used to measure energy regions in a static scan. However, with the OptiXS utilising a single-channel detector a 'pseudo-REES' style of XPS is taken, in which the kinetic energy is swept quickly by the analyser over the specified core level. This results in scans taken every 10+ seconds, depending on the core level measured, rather than 2 to 4 seconds, as is the case in true snapshot mode REES. The optical spectroscopy side of the experiment, however, can still take spectra in the timescale of a few seconds, provided the laser intensity and/or measured signal intensity is high enough, which is the case for single crystal boron nitride and diamond samples.

Cubic boron nitride is very similar to diamond in terms of crystal structure and mechanical properties. Its main application is found in cutting tools, specifically the cutting of ferrous metals, such as steel, which would readily dissolve diamond at high temperatures, meaning a quick degradation in the cutting tool itself. It may also find application in the production of its 2-dimensional allotrope, borene, in a similar manner that diamond has already been shown to do with graphene, where a thin layer of iron was deposited onto the diamond surface and the sample was heated [15]. Carbon atoms from the diamond substrate then dissolve into the iron and permeate through to the vacuum exposed side of the iron overlayer. The carbon then recrystallises as graphene layers, enabling the controlled growth of single or multi-layered graphene. This process has been well studied on both diamond and boron nitride by electron-based spectroscopies, such as XPS, LEED (Low Energy Electron Diffraction) and PEEM (Photoemission Electron Microscopy), however optical

measurements of the sample during growth of the iron overlayer has not yet been possible.

In this experiment, measurements were performed during exposure to a K-cell at two different emission currents, 1.5 A for a total of 135 minutes and 1.75 A for 165 minutes. The time at each emission current differed based on the changes (or stability) in the real time results. During each run, three measurements were taken. On the optical side, Raman spectra ranging from 950-1410 cm^{-1} were taken every 3 seconds using the 532 nm excitation source. This encompassed the 2 first-order boron nitride Raman peaks present at 1056 and 1306 cm^{-1} . Also, during deposition, two XPS core levels were to be measured, N1s and Fe2p using a magnesium anode source with a photon energy of 1253.6 eV. The scan parameters for these regions were as follows;

N1s: Kinetic energy Range 845 to 862 eV with 0.2 eV steps, a dwell time of 0.1 s and a pass energy of 44 eV

Fe2p: Kinetic energy Range 520 to 550 eV with 0.2 eV steps, a dwell time of 0.1 s and a pass energy of 44 eV

These parameters meant an overall acquisition time of approximately 10 seconds and 20 seconds for the N1s and Fe2p regions, respectively and accounting for small amounts of 'dead time' between scans or voltage adjustments. Figure 3.20 shows the raw XPS, and Raman data taken during the 1.5 A deposition. The spectra again have been stitched into a 2D image to clearly see the change in signal over time. There is a very clear reduction in the N1s intensity and an appearance of Fe3d peaks during this deposition. The position of the Fe2p $\frac{3}{2}$ peak (lower binding energy peak) at 710 eV suggests, as previous experiments have shown, the deposited material is iron

oxide, Fe_2O_3 . This is common when the deposition is too slow for the base pressure of the system and the monolayer formation time of the deposited material is similar to that of the monolayer formation from other molecules left in the chamber. The Raman 2D dataset as well does show significant attenuation over time, although a large oscillation in the signal with a periodicity of approximately 10 minutes was seen. This strange oscillation was found to be due to the air conditioning system in the lab, with one of the fans located above the photodetector on the optical spectrometer. As the air-con cooled the lab, the photodetector became slightly more efficient, increasing the measured signal, and *vice versa*.

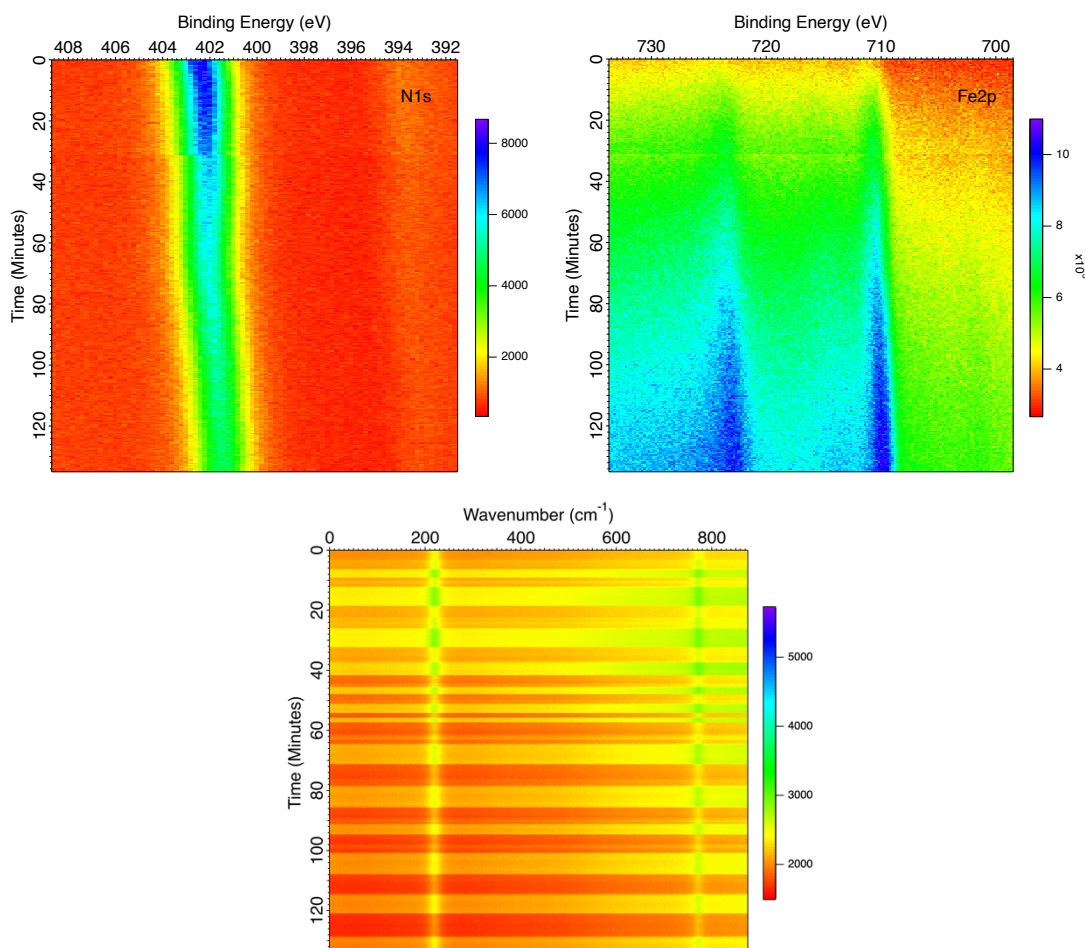


Figure 3.20: (top, left) The raw N1s core level data against deposition time for the 1.5A deposition current. (top, right) the Fe2p dataset from the same deposition run. (bottom) The Raman 2D data also during the same 1.5 A deposition run.

All the data were then analysed using the REES fit propagation developed in the MCS software. The Raman data was fitted using this software too but needed converting post fit from pixel number to wavenumber as it was only possible to fit using an x -axis with a regular, constant step between datapoints, which is not always the case when taking measurements. Once fitted, the peak area and position were extracted, and for the Raman data, the background could be removed, to some extent. After extraction of the peak area of the N1s core level, this can then be smoothed and converted to a relative intensity (relative to the intensity of the first data point). This gives a profile of I/I_0 which, by using equation 2.10 and the IMFP of an N1s core level electron emitted by a 1253.6 eV photon, can be converted to an overlayer thickness. Once calculated, the thickness of the iron layer can be plotted against the relative intensity, or attenuation of the Raman signal. In Figure 3.21 the calculated thickness of iron deposited through the run is shown, as is the attenuation of the Raman signal. The red data in both plots are the raw data and the black data are a 3rd order polynomial fit intended to provide a smoother data set. Smoothing is very commonly performed on REES data due to the high level of noise which is unavoidable when taking quicker measurements. As shown in Figure 3.21, from this initial run a final overlayer thickness of 1.36 nm was deposited which caused a 16% drop in the intensity of the Raman signal. The oscillation in the Raman intensity was again due to the cooling of the photodetector by the air conditioning unit during

measurements. Smoothing of the data was performed to remove this unwanted oscillation.

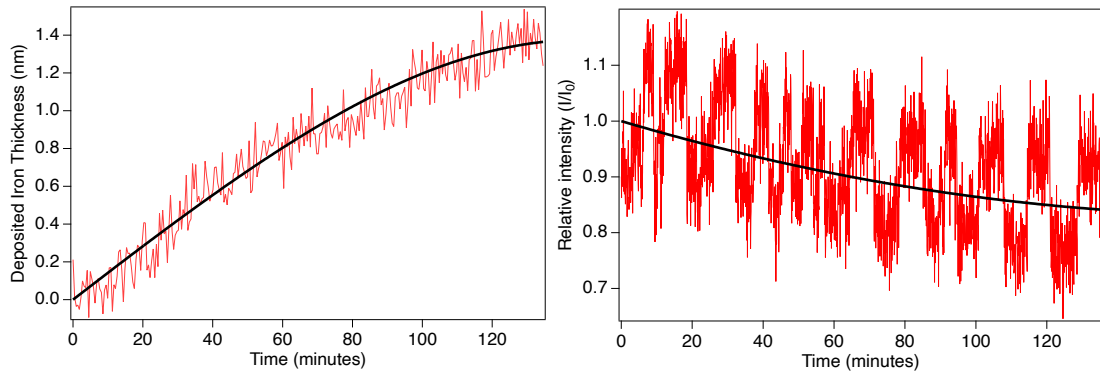


Figure 3.21: (left) The thickness of iron deposition during a 135 minute deposition at a K-Cell current of 1.5A and (right) the relative intensity of the measured Raman signal of the boron nitride substrate during the same deposition.

After a 1.5 A deposition, the K-cell current was increased to 1.75 A then the experiment and analysis were repeated. Peak fit propagation was once again performed, and the areas were extracted. In a similar fashion to previous runs, the attenuation of the Raman and thickness of deposited material were calculated. These are shown in Figure 3.22. The raw data extracted from the fit propagation are shown in red, and a polynomial fit for smoothing of the data are shown in black.

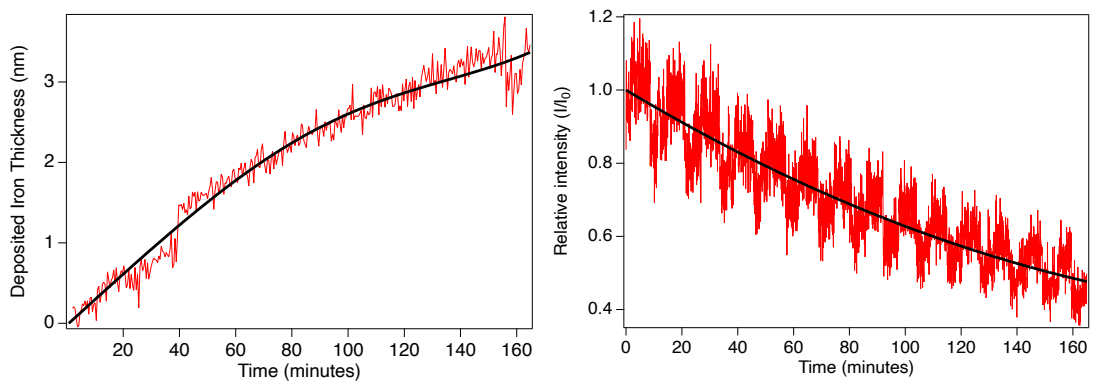


Figure 3.22: (left) The thickness of iron deposition during a 165 minute deposition at a K-cell current of 1.75 A and (right) the relative intensity of the measured Raman signal of the boron nitride substrate during the same deposition.

During the 1.75 A deposition, a total of 3.37 nm of iron was deposited, which resulted in the further 53% reduction in the measured Raman signal. The final step for this experimental analysis was to combine the information from both deposition runs to provide the complete picture on how the epitaxial iron layer thickness affects the attenuation of the Raman signal. With the nature of the experiment, this can be performed by simply scaling the normalised relative intensity of the 1.75 A run, by the final value of the 1.5 A run. The total deposited thickness of iron would also simply be the sum of the thickness deposited through both runs. Figure 3.23 shows the result of this and shows the total amount of deposited iron against the relative Raman intensity measured. The 1.5 A deposition is shown in red, and the 1.75 A deposition is shown in black.

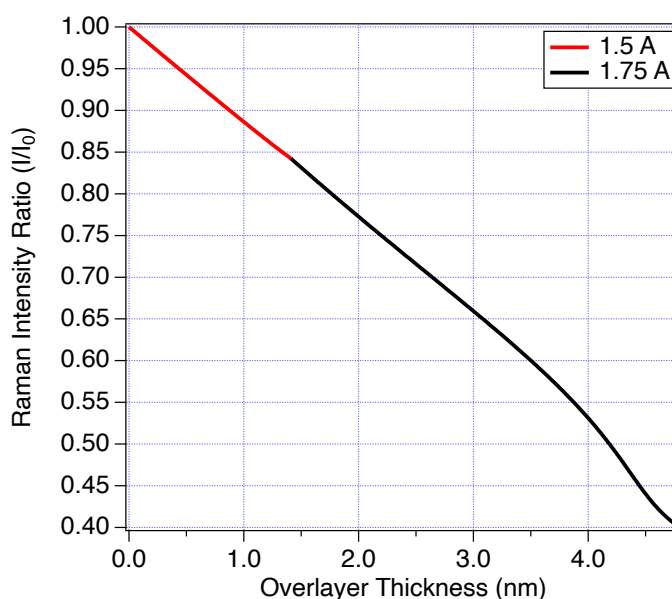


Figure 3.23: The attenuation of the measured Raman signal as a function of iron overlayer thickness. Two deposition runs are included with the K-cell currents shown.

Overall, this experiment proved the feasibility of performing *in-situ* optical and electron-based spectroscopies simultaneously in the OptiXS system as well as the ability to treat the sample during measurement. It has also shown a part of the optical properties of the iron overlayer, and importantly provided the information that even

at a thickness approaching 5 nm, the iron layer is still translucent, to the wavelengths of light measured. Another key bit of information in terms of instrumentation which can be drawn from the experiment is the deposition rates attained by the K-cell at two currents, with average values of 0.61 nm hr^{-1} and 1.22 nm hr^{-1} for the 1.5 A and 1.75 A deposition runs, respectively.

As a final test of repeatability, a single crystal (001) diamond to be used by collaborators within the Aberystwyth materials group required a film of iron on the surface. Iron on diamond films has been studied extensively already using XPS [6], [12], [15], so the aim for this experiment was to grow the thin iron film using the attenuation of the first-order diamond Raman signal, located at 1332 cm^{-1} , alone to gauge the film thickness. A 2 nm film would be required, as this is sufficiently thick to facilitate the graphene growth process, which provides around 50% attenuation of the XPS signal, and approximately 20% attenuation for the Raman signal. A k-cell current of 1.75 A was used during the deposition due to the increased growth rate. Figure 3.24 shows the raw Raman spectra and the calculated attenuation during deposition. The attenuation was again calculated by manipulating output data from

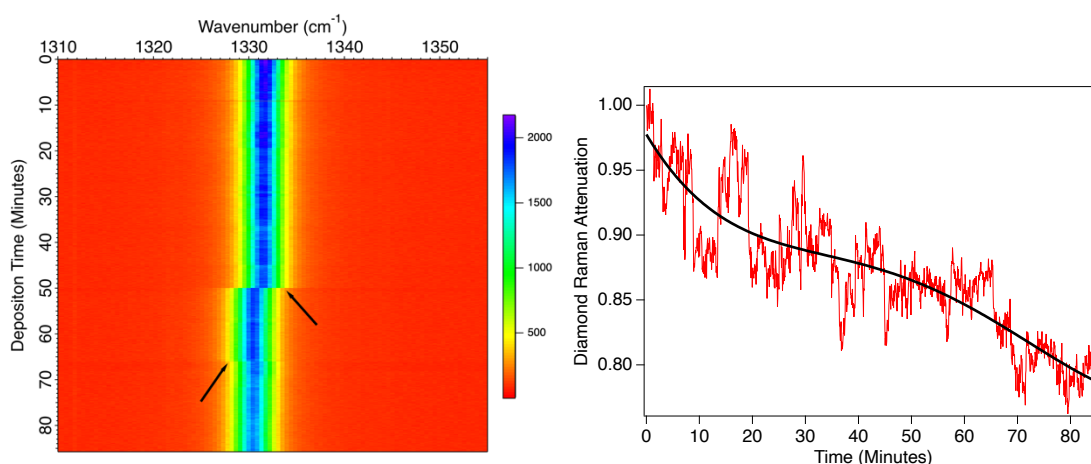


Figure 3.24: (left) The raw Raman data taken during iron deposition on a (100) single crystal diamond. The two points marked with black arrows were due to crashes in the spectrometer PC, and slight errors on the recalibration causing slight shifts in peak position. (Right) The diamond Raman attenuation (or relative area) through the deposition.

peak fit propagation in the MCS program. Again, during deposition there was a noticeable attenuation and, assuming a 2 nm film thickness grown, a deposition time of 85 minutes gives a deposition rate of approximately 1.4 nm hr^{-1} , which although slightly higher, it is still consistent with the previous deposition rate measured at 1.75 Å previously. As expected, noise on the peak area is quite large, but with the upgrade of the photodetector on the optical spectrometer, as well as its own dedicated cooling fan, the undesirable oscillations from the air conditioning unit have been removed.

3.7.4 OTHER WORK

During the course of this development project, many trial or test experiments were performed on the OptiXS system. Some of the more extended experiments have already been presented. This section will present some of the work required to get the OptiXS system to a working stage, such as testing of the heating and cooling stages, as well as present some further capabilities that have been trialled, such as cathodoluminescence and X-ray excited optical luminescence.

Figure 3.25a shows cathodoluminescence spectra taken of the polycrystalline hexagonal boron nitride Boralectric heater at three electron beam currents, and 3.25b shows XEOLS measurements of the same heater. The spectra were measured using an OceanOptics Flame portable spectrometer mounted onto the back of the superhead optics system. These measurements were taken during early stages of OptiXS' development, so a number of upgrades/components were yet to be installed.

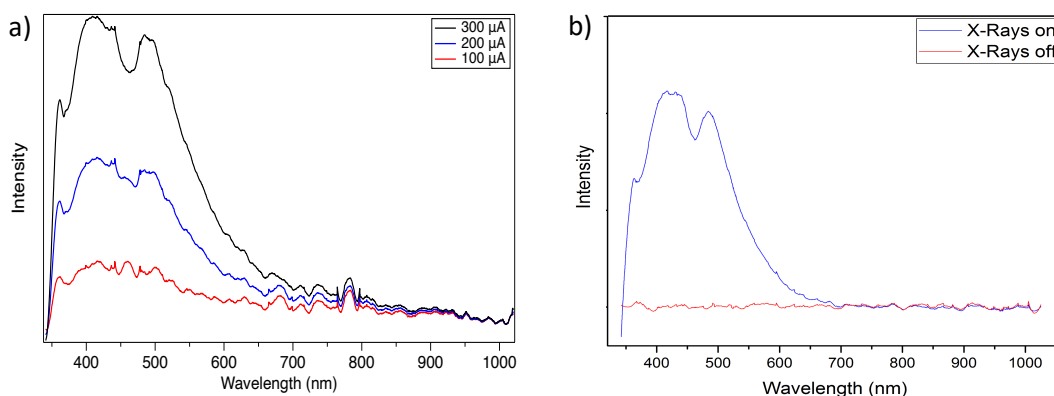


Figure 3.25: a) A series of cathodoluminescence measurements taken of a p-hBN Boralectric heater at 3 electron beam emission currents during the testing phase of the OptiXS instrument. b) X-ray Excited Optical Luminescence measurements of the same p-hBN heater.

Another aspect tested was the cold stage capability. This was performed in tandem with some early tests of the optics and heating stage, whereby Raman spectra of a single crystal diamond were taken at a range of temperatures up to 700 K and the shift in the first-order diamond Raman could be monitored. The resulting spectra are shown in Figure 3.26. The measured temperature for the ‘nitrogen cooled’ spectra was measured to be <120 K. However, at the time of measurement the electrical feedthroughs used at the top of manipulator were copper wires to which the thermocouple wires were welded. This junction acted as a second thermocouple which, at room temperature, did not affect the sample stage temperature measurement substantially, but when the liquid nitrogen was introduced into the system, it also dramatically cooled the top of the manipulator, including the electrical feedthroughs meaning it was impossible to get a reliable temperature reading. This issue has since been resolved by replacing the feedthrough with a K-type thermocouple electrical feedthrough. However, supply of liquid nitrogen for further testing has been an issue, so this experiment was not repeated.

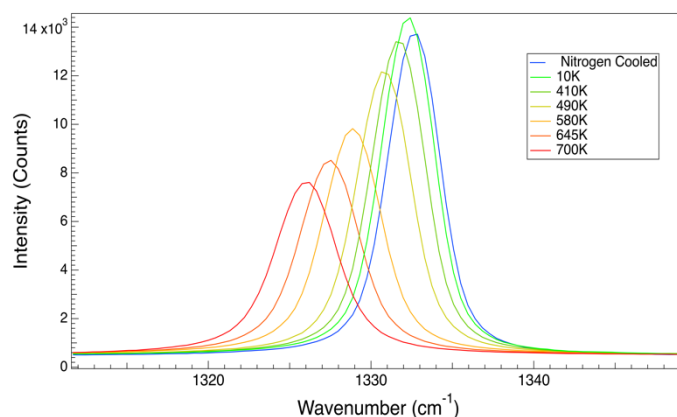


Figure 3.26: A series of first-order diamond Raman measurements taken at a range of temperatures from ~ 120 K to 700 K.

3.7.5 OPTIXS SUMMARY

To summarise, a multi-functional, UHV system for measuring simultaneous optical and electron spectroscopies, as well providing a selection of sample processing methods, has been developed. Some of the key developments are;

- testing and calibration of new components such as the electron detector, optical fibres, the deposition source and K-cell quick change port, and the X-ray gun, which during this work has been both replaced by a new gun and recoated.
- Prove the simultaneous capabilities by monitoring thin film depositions and annealing cycles with real-time Raman spectroscopy and XPS.
- Characterise the new sample manipulator's hot and cold stages, which have successfully designed and constructed within this work, with a sample temperature range between -150 and 1100°C now possible.
- Tested other techniques such as cathodoluminescence and XEOLs to help determine the full capability of the OptiXS system.

Chapter 4 – MATERIALS

This chapter will present an overview of the properties of the materials used in this work. The predominate material will be single crystal (001) diamond. The history, structure, synthesis and the electrical properties will be reviewed. In parts of this work, NanoCrystalline Diamond (NCD) films grown on silicon substrates were also used, the nature of this material will also be examined. Finally, as this work revolves around the application and production of NV centres in diamond the properties of these will also be discussed here.

4.1 DIAMOND

Diamond is a material which is superlative in nature. Whilst it is well known for its extreme hardness and thermal conductivity other properties such as transparency, X-ray hardness, biocompatibility, and chemical stability have opened avenues to a wide range of new applications such as X-ray detection [60], drug delivery [61] and photonic devices [62]. One of the most prevalent research areas is based on the use of defects or ‘colour centres’ present in diamond for quantum technology applications. One such defect is the NV centre whose desirable spins properties and ability to act as a solid state “artificial atom” have made it a promising candidate for spintronic [63], quantum information processing [64] and sensing applications [65], [66]. The majority of quantum applications require NV centres close to the diamond surface [67]–[69]. Previous studies however, have shown that as NV centres approach the diamond surface, interactions with spin and charge states present on the surface can diminish the usability of the defects [2], [70]. This coupled with the

continual decrease in size as devices approach the nano-scale mean surface preparation becomes crucial for device development.

4.1.1 THE PROPERTIES OF DIAMOND

Diamond is a metastable crystalline form of carbon under standard conditions. Unlike the thermodynamically preferred allotrope, graphite, diamond forms a tetrahedral shaped structure of sp^3 type bonds. The unit cell, shown in Figure 4.1, of such a structure is a face-centred cubic cell with a two atom basis at the lattice points $(0,0,0)$ and $(\frac{1}{4}, \frac{1}{4}, \frac{1}{4})$. Under standard conditions the lattice constant of the unit cell is 3.6 Å and a both length of 1.54 Å, which is equivalent to a quarter of the unit cell length between opposing corners. The diamond structure is the reason for many of its extreme properties. The densely packed atoms, high symmetry and strong bonds of this structure provide many of diamond's supreme properties, some of which are listed in Table 4.1 [71].

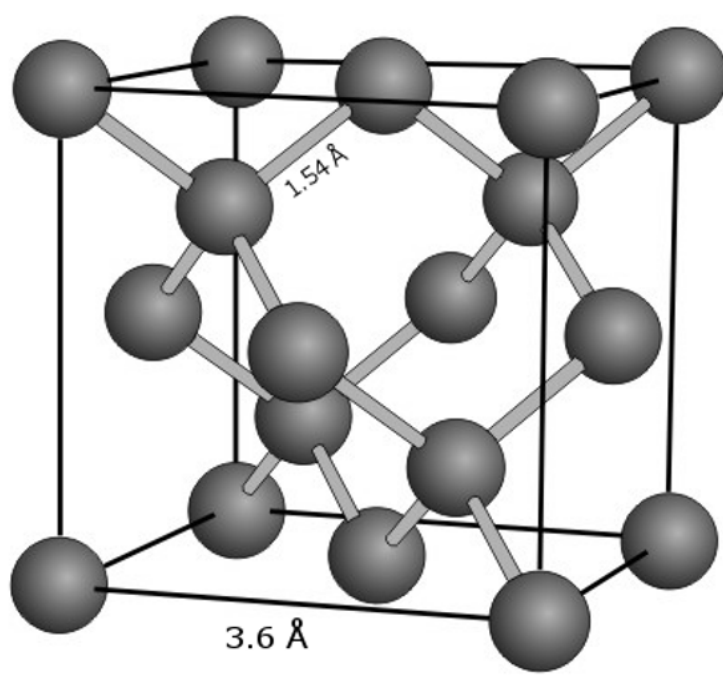


Figure 4.1: The unit cell of diamond. The bond length and lattice constant are also shown.

Table 4.1: A number of the superlative characteristics possessed by diamond.

Highest known mechanical hardness (90GPa)
Highest thermal conductivity ($2200\text{Wm}^{-1}\text{K}^{-1}$)
Low linear thermal expansion coefficient ($1 \times 10^{-6} \text{ K}^{-1}$)
Highest bulk modulus ($1.2 \times 10^{12} \text{ Nm}^{-2}$)
Lowest compressibility ($8.3 \times 10^{-13} \text{ m}^2\text{N}^{-1}$)
Highest sound propagation velocity ($17.5 \times 10^3 \text{ ms}^{-1}$)
Wide range transparency from UV to IR, and some X-Ray wavelengths
Extreme X-ray hardness
Biocompatibility and Chemical stability
Wide bandgap (5.5eV) and High Resistivity ($10 \times 10^{13} \Omega\text{m}$)
Wide electron affinity range, including a negative affinity, depending on surface termination
Metallic conductive with high boron doping ($>10^{20} \text{ cm}^{-3}$), Superconductive at low temperature ($<10\text{K}$).

Synthesis of diamond is difficult due to the high activation energy required for it to naturally form. Diamond can form naturally at the high pressure and temperatures produced at depths of around 160 km into the Earth's crust. However, with modern technology, diamonds can also be man-made. There are two main methods of diamond growth High Pressure High Temperature (HPHT) growth, or Chemical Vapour Deposition (CVD).

4.1.2 THE SYNTHESIS OF DIAMOND

Intrinsic (or pure) diamond is naturally a wide bandgap insulator with a bandgap of 5.5 eV. However, impurities and defects are commonly introduced into the diamond lattice during natural growth, which can have a wide range of effects on the diamond

properties. Because of this, guidelines into the classification of natural diamonds based on atomic impurities are used. The first classification sorted diamonds based on the absorption of infrared (IR) and ultraviolet (UV) light [72]. The majority of diamonds were found to absorb IR and UV light and were classed as Type I ('type one') and the 'transparent' diamonds that did not were Type II ('type two').

Type I diamonds are always nitrogen containing, however, due to the effect that different nitrogen defects in the diamond have on the fluorescence, further classification based on the concentration and clustering size of nitrogen was required. Type Ia diamonds contain the most nitrogen, up to 3000 parts per million (ppm) and make up around 95% of all natural diamonds. Type Ia diamonds are defined by the presence of nitrogen clusters in the diamond lattice. The size of these clusters can be classified further into type IaA diamond, where the nitrogen atoms exist in pairs alone, or type IaB diamond where larger nitrogen clusters, such as the N₂ or N₃ centre, are present. Type IaB diamonds are a yellow colour, whereas Type IaA are colourless. Type Ib is a much smaller subset of Type I diamonds, making up around 0.1% of natural diamonds. This category of diamond contains up to 500 ppm of nitrogen, with the impurities being made of single point defects, which are much more diffuse in the crystal lattice. Crystals of this type are commonly yellow in colour and are the most common form of diamond grown by High Pressure High Temperature synthesis in labs.

Type II diamonds are free from any measurable nitrogen content. This class of diamonds is also split into subsets, based initially on phosphorescence measurements [73]. A diamond is classified into the Type IIa set if it has little or no impurities in the crystal lattice, and these diamonds make up around 1-2% of all diamonds.

Diamond of this class are the closest to intrinsic diamond formed in the Earth's crust. Although usually colourless, imperfections formed by plastic deformation in the crystal lattice can sometimes exhibit a wide range of colours including brown, yellow or purple. High pressure, high temperature treatment of such samples can anneal out many of these structural defects, producing a colourless stone. Diamonds grown via CVD are most commonly Type IIa, as laboratory controlled growth allows for much higher purities than most naturally grown diamond. The final diamond type is Type IIb. These diamonds make up around 0.1% of natural diamonds. Type IIb diamonds, although free of nitrogen, contain some amount of boron in their lattice. At high enough boron concentrations, these diamonds exhibit strong phosphorescence and high conductivity. Boron doped diamonds can range from colourless to deep blue or black, depending on the concentration. As boron is an electron acceptor, boron-doped diamond is a p-type semiconductor. Diamond crystals may belong to a number of these diamond types, depending on defect concentration (or purity) which can vary throughout the crystal. This can occur in naturally grown diamonds which have been exposed to varying growth conditions.

Diamond can only form naturally in the extreme pressures and temperatures produced in the Earth's lithosphere (excluding meteorite strikes or extra-terrestrial sources). Here, pressures around 5 GPa and temperatures nearing 1000°C are present. The current growth model suggests that diamond forms from sp^2 carbon containing melts, in the presence of molten transition metals, such as iron, nickel or cobalt. The metals catalyse the conversion of the graphitic carbon to sp^3 carbon nucleation sites for diamond growth [74]. Natural diamond growth is an extremely slow process, with the entire process of formation and transportation to the surface

taking millions of years. Demand for diamond over the past few decades has outweighed the natural supply, making the synthetic growth of diamond a necessity. There are a number of methods of diamond growth used in the industry today. The two most notable methods are High Pressure High Temperature (HPHT) Synthesis and Chemical Vapour Deposition (CVD).

Some controversy surrounds the first laboratory growth of diamonds, but most sources state it was achieved in 1954 by General Electric [75] via HPHT synthesis. For HPHT synthesis, small capsules containing some form of carbon (usually graphitic but diamond seeds are sometimes used) and some mix of transition metals, again usually iron, nickel or cobalt, are placed into presses and exposed to pressures exceeding 5 GPa and temperatures of around 1350°C. A phase diagram of carbon is shown in Figure 4.2 with a green area showing the common conditions used in industrial diamond growth, a similar phase diagram can be found in [76]. The Berman-Simon line separates the regions of diamond and graphite stability (or metastability) [77]. The extreme pressures and temperatures are such that diamond is the stable form of carbon and therefore the crystallisation of diamond is possible. Nowadays, HPHT synthesis is used for a wide range of diamond materials. The most prolific use is for the growth of diamond grit used in cutting or abrasion tools. However, the largest single crystal synthetic diamonds have also been produced via HPHT synthesis, with diamonds exceeding 103 carats being grown. The growth conditions during synthesis also have a profound effect on the diamonds grown. For example, diamonds grown under higher pressures and temperatures preferentially grow octahedral crystals, whereas less extreme conditions favour cubic shaped growth. This is due to the effect pressure and temperature have on the growth rate

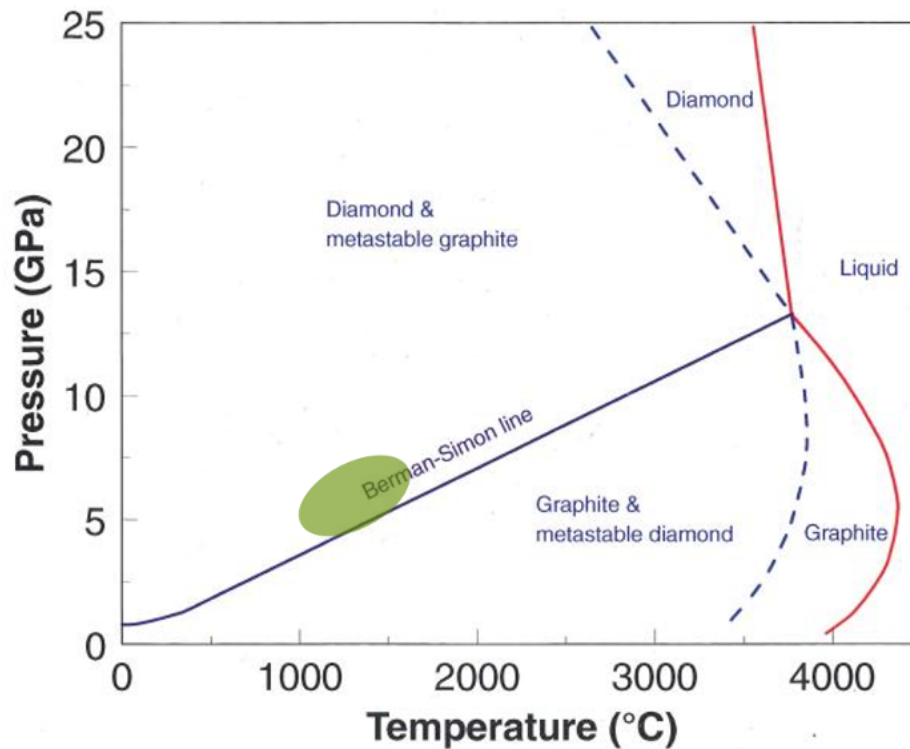


Figure 4.2: The phase diagram of carbon. The Berman-Simon line shows the transition conditions from graphite to diamond stability. The green area shown is the general conditions commonly used in industrial HPHT growth. Taken from the Diamond Science and Technology Lecture course. Lecture given by David Fisher, De Beers technologies.

of different planes of diamond, which will be described shortly. The catalytic metal mixture and addition of other precursors can also provide control over growth rate, diamond quality and doping, with boron or nitrogen doped diamonds commonly grown.

With the possibility of synthesising diamond realised, work began on attempting to grow diamond from gas-phase carbon-containing substituents. Chemical Vapour Deposition had already been used to grow other crystals during the 1950s, however the first successful diamond deposition via CVD wasn't achieved until the 1960s, and it wasn't until the 1980s that CVD diamond growth became highly studied. The simplest form of the standard model of CVD diamond growth is follows; a hydrogen(H_2): methane (CH_4) gas mixture is passed over a growth substrate, like a diamond seed, and hydrogen atoms are formed by dissociating hydrogen from the H_2

and CH₄ molecules by ion impact or thermal processes. The H atom reacts with a hydrogen atom bonded on the seed surface, reforming the H₂, but producing a free radical or dangling bond on the surface. The carbon-containing radicals (CH₃, CH₂, CH₁ ...) formed by the hydrogen abstraction in the gas mixtures may now react with the dangling bond on the surface, adding a carbon to the diamond structure. If the same process occurs at a neighbouring bond on the diamond surface, further reactions with H atoms will then allow these sites to cross bond, extending the sp³ bonding structure and the diamond crystal will grow [78], [79]. This growth process of nucleation and growth can be described by the Langmuir-Hinshelwood Growth model [80], [81], however further complications can arise when considering how CH₃ can react with bi-radical sites, surface migration of chemical species and other hydrocarbon species which are in lower concentrations but frequently ignored [82]. The quality, structure and crystallinity of the diamond grown depends highly on the gas mixtures used.

The 'Bachmann triangle', shown in Figure 4.3, was developed in the 1990s to amass the wide variety of recipes being developed into a model based on the carbon: hydrogen: oxygen gas mixture ratio [83], [84]. Typical gas mixtures used today are 99% Hydrogen: 1%CH₄ with argon added as a stabilising agent. There are two main techniques implemented today to induce the hydrogen dissociation required for CVD growth of diamond. Hot filament is the simpler, albeit less efficacious method, whereby a current is passed through a filament, usually tungsten or molybdenum, which is held above the surface of the growth seed as the gas is passed through the growth chamber. Temperatures of around 900°C near the plasma filament are achieved, with sample temperatures nearing 400°C. The more complex, but generally

more effective method is Microwave Plasma-activated CVD (MPCVD). Simply, this uses a microwave cavity as the growth chamber to induce and contain a plasma above the substrate during growth. Apparent temperatures in the plasma exceed 3200°C, although the growing diamond is either cooled or heated to maintain it at the optimal growth temperature of ~900C.

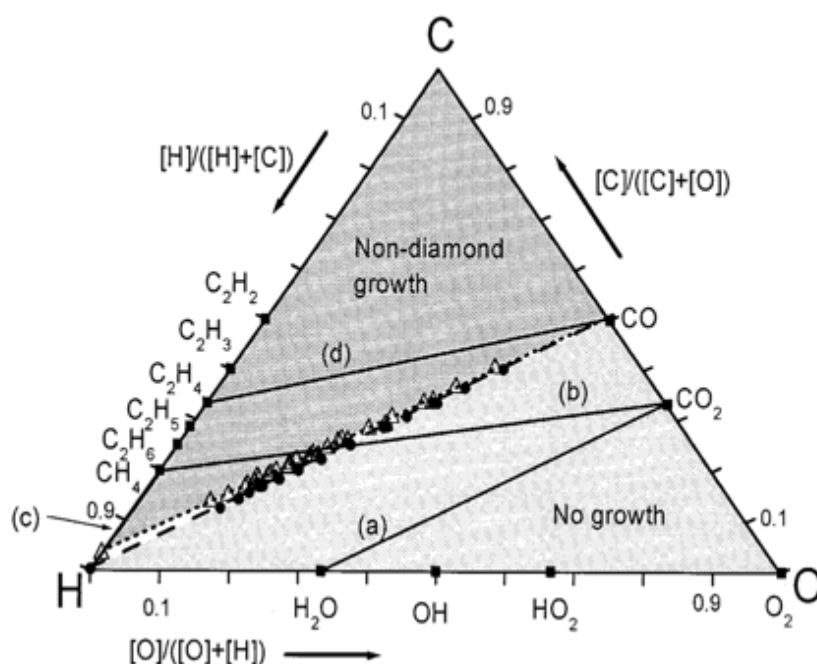


Figure 4.3: The Bachmann triangle. This diagram is formed from the results of approximately 70 growth recipes and shows the effect the ratio of C:H:O has on the CVD growth of diamond. It should be noted the type of growth is dependent on the atomic ratio present in the plasma, and independent of the input gas mixture.

Chemical Vapour Deposition is commonly the method of choice for optical grade quality diamond, as there is a much greater degree of control over the growth conditions/environment. The scalability of CVD growth is constantly being pushed, with some diamond wafers close to 10 cm in diameter being reported. Doping of diamonds is also readily possible during CVD growth through the addition of dopant gases in the precursor gas mixture. Boron doping, for example, can be achieved by the addition of diborane gas during growth. Nitrogen addition is also possible and the addition of nitrogen in the reactor has been known to increase growth rates twofold

(this is true for HPHT synthesis too). Use of multiple or many seed crystals lead to polycrystalline, microcrystalline or nanocrystalline diamond films and the growth conditions are key in favouring growth for each. Extensive modelling of the radical species population, gas mixtures and how these affect the crystallinity have been performed to better predict growth [85], [86]. The growth of nanocrystalline diamond films will be discussed further later in this chapter.

4.1.3 DOPANTS AND DEFECTS IN DIAMOND

With a bandgap of 5.48 eV, it may seem counterintuitive to consider doping single crystal diamond. However, high thermal conductivity, high hole/electron mobility carrier distances and a high electrical breakdown field threshold make the material of great interest in the field of high power or high frequency electronics. One of the most common practices in the electronic device industry to change the electrical properties of a material is doping. Doping diamond involves the replacement of carbon atoms in the crystal lattice with a different element. The effect the dopant has on electrical properties depends mainly on the number of free electrons in the dopants outer shell. Atoms with a higher number of electrons in their outer shell than carbon are known as electron donors, contrariwise, atoms with a lower number of valence electrons are electron acceptors. When electron acceptor or donors are inserted into the crystal lattice, energy levels within the bandgap are formed. Donor levels, formed by doping with electron donors, are closer to the valence band than the conduction band and provide excess electrons as charge carriers. The term 'n-type' doping is used to denote the negative charge carriers. Conversely, acceptor levels are formed usually closer to the conduction band and provide charge carriers in the form of holes. Doping to provide positive charge carriers is known as p-type

doping. For diamond, p-type doping is fairly commonplace, as boron doping of diamond provides acceptor levels approximately 370 meV above the valence band which give diamond semiconducting properties. High boron concentrations (above $4.5 \times 10^{20} \text{ cm}^{-3}$) cause a transition to metallic conductivity [87]. Metallic properties in diamond have already paved the way for a number of applications which utilise diamond's robustness and chemical stability [88]. Metallic BDD has also shown great promise for quantum scale devices, showing robustness in the electronic band structure, even when the boron doping is confined to a thickness of 1.8 nm [89], and superconductivity at temperatures of 10 K [90], [91].

In contrast, n-type doping of diamond has proven to be far more elusive. With the diamond lattice so tightly packed, significant doping of most elements is difficult simply because the of larger atomic nuclei [92]. As stated, nitrogen can substitute for carbon atoms, however it only provides a donor level 1.7 eV below the conduction band, which is useless for conductivity at room temperature [93]. Other attempts at n-type doping include doping of phosphorus and sulphur. To dope diamond with such element, gases containing the required elements are introduced during growth (usually CVD). The introduction of hydrogen sulphide, H_2S during diamond growth did indeed allow for sulphur doping, however no donor level was found [94]. Phosphorus doping by the introduction of phosphine PH_3 or trimethylphosphine, $\text{P}(\text{CH}_3)_3$ has shown a little promise, with controlled doping concentration levels of 10^{16} - 10^{19} cm^{-3} [95], being achieved and a donor level 0.57 eV below the conduction band. However, high temperatures are still required to instigate any level of conductivity [96].

However, the effect adding secondary elements to diamond stretch beyond just the realms of electrical devices. Defects in diamond are widely studied based on

the optical properties they imbue into the material. These defects, or colour centres as they are commonly called, encompass a wide range of elements and a wide range of applications and areas of research. Some of the most notable possible applications are based in quantum information technologies. These technologies rely on the quantum spin and electrical properties of point defects in diamond. There are a wide arrange of defects present in diamond which have been studied for a range of applications, defects include, but are not limited to, the silicon-vacancy, nickel-vacancy, lead-vacancy, germanium-vacancy, and the tin-vacancy. However, the defect of focus in this study is the nitrogen-vacancy, which will now be presented.

4.1.4 THE NITROGEN-VACANCY CENTRE

A colour centre in diamond which has received a huge amount of interest in recent years is the negatively charged nitrogen-vacancy (NV^-) centre. Single nitrogen vacancies centres were first observed in 1997 by scanning confocal microscopy of single crystal diamond samples [97]. Soon after this experiment, a number of properties possessed by the NV^- centre highlighted it as a candidate for a number of applications. The NV^- was soon found to be a single-photon generator, suggesting the NV^- centre's potential for quantum optical applications [98], [99]. Manipulation and optical readout of the NV^- centre's electronic spin states opened avenues to applying the centre as a qubits (quantum bits) in quantum metrology devices [100]. Since these initial demonstrations, the NV^- has been used in a vast plethora of experiments; a list of some further properties and applications of the NV^- centre are displayed in Table 4.2.

The NV centre, as the name suggests, is a point defect in diamond whereby a carbon atom has been substitutionally replaced by a nitrogen atom and this exists

next to a vacancy, where a carbon atom is missing from the tetrahedral structure. Nitrogen forms sp^3 bonds with three neighbouring carbons and leaves a ‘dangling bond’ pointing towards the vacancy. The structure of this can be seen in Figure 4.4. The centre, usually situated along a $\{111\}$ crystalline direction, exhibits C_{3v} symmetry, meaning three rotational symmetry operations with rotations of 0° , 120° , and 240° , as well as three reflectional planes of symmetry [101].

Table 4.2: Some of the properties displayed by and applications of the negatively charged NV centre in diamond.

Nanoscale Magnetometry [67], [69], [102], [103]
Bio-magnetometry [104]
Electric Field Mapping [105]
Quantum Decoherence Microscopy [106]
Testing Fundamental Condensed Matter and Quantum Theory [107]–[110]
Nanoscale Thermometry [111]–[113]
Photonic Devices
Quantum Entanglement between separate NV centres [114], [115], NV centres and photons[116], and NV centres and physical vibrations in cantilevers [117], [118]
Quantum Cryptography [119]

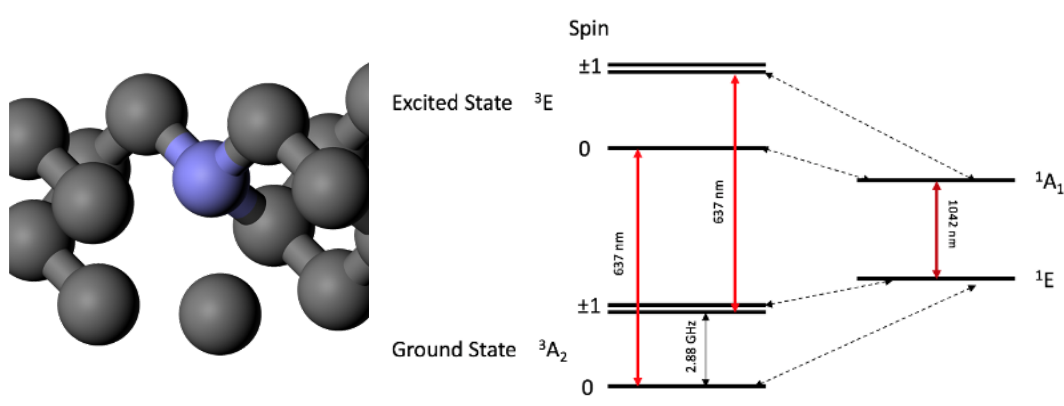


Figure 4.4: (left) The nitrogen-vacancy centre in a small diamond lattice (close to a unit cell). The nitrogen atom is represented by a blue sphere and carbon is represented by black spheres. (right) The electronic structure of the negatively charged NV centre. Important transitions are labelled. Radiative transitions are shown by red arrows and non-radiative process are shown by the black, dashed arrows.

The NV centre can exist in two charge states, neutral (NV^0) and the negatively charged state (NV^-). Differentiation between the two charge states is possible thanks to the optical emissions associated with each, with zero phonon emission lines for the NV^0 and NV^- at 2.16 eV (575 nm) and 1.94 eV (637 nm), respectively [120]. Studies into the properties of the neutral charge state of the NV centre have been undertaken and it has been shown to exhibit different properties to its negatively charged counterpart [121]. Further characterisation of the NV^- centre electronic structure has been performed via magnetic resonance measurements. The NV^- centre exhibits zero field magnetic resonance at 2.88 GHz. This resonance has been attributed to transition in the ground electronic state ($^3\text{A}_2$) between spin states of $m_s = 0$ and $m_s = \pm 1$. Optically pumping the centre, with light of wavelength equal to or shorter than the zero phonon line (637 nm) leads to further magnetic resonance. The optically detected magnetic resonance (ODMR) is observed at 1.42 GHz and this is due to similar spin state transitions but in the excited ^3E state.

A secondary optical emission of 1042 nm light is also exhibited by the NV^- centre. The relative intensity of this is dependent on the presence of the 2.88 GHz magnetic resonance. This has been attributed to a radiative transitions between intermediary singlet states $^1\text{A} \rightarrow ^1\text{E}$ which are accessible via non-radiative intersystem crossings transitions from the ^3E excited triplet state [122]. Approximately 97% of electron relaxation is via a single 637 nm (excluding phononic transitions) under normal conditions. However, with the presence of the 2.88 GHz microwaves which pump electrons into the $m_s = \pm 1$ spin state, this value drops to 70%, with the remaining 30% now relaxing via the multi-system path. With all this information the electronic structure (excluding some hyperfine structures) can be made. This is

shown in Figure 4.4. The electronic structure of the NV⁻ and its controllability via a number of external factors, such as magnetic/electric fields, strain [123], optical pumping and even temperature [124], are the main reasonings behind its desirability in the aforementioned applications.

Nitrogen-vacancy centres can be formed in diamond by a number of methods. Controlled introduction of nitrogen during CVD growth can provide some nitrogen vacancies, although other nitrogen-containing defects will be present [125] [126]. Delta doping (δ -doping) can be performed during CVD growth to provide constrained layers of nitrogen 'rich' diamond, containing the NV centres [127]. However, one of the most common methods of nitrogen-vacancy creation is through ion implantation and annealing. This process involves accelerating N⁺ ions towards a diamond sample, embedding the nitrogen into the diamond. As a nitrogen ion propagates through the crystal it will collide with carbon atoms in the lattice, this will result in one of a number of events. If the nitrogen ion is of sufficient energy, it may forcibly eject the carbon atom from its position in the lattice, leaving a vacant site. If the energy of the nitrogen ion is still high it will continue to propagate through the lattice, causing more collision events. However, if the energy is low enough, the nitrogen ion will be trapped by the vacant site, replacing the carbon atom in the lattice. This process will, in turn, lead to the production of substitutional nitrogen defect, vacancies and, if the vacancies and substitutional nitrogen happen to be neighbouring, NV centres. The ejected carbons may also form interstitial carbons and some damage to the diamond lattice in other ways will be formed. The depth profile of the defects and damage will be dependent on the initial energy of the accelerated ions.

Formation of NV centres this way is generally quite inefficient due to the randomness of collision events. Therefore, a range of 'recipes' in order to improve the improve the creation efficiency have been developed. Annealing nitrogen (and vacancy) containing diamond has been shown to be one of the most effective methods for this. High temperature annealing above 600°C is sufficient energy input to cause vacancies, carbon interstitials and other aspects of damage in the diamond, to become mobile. The mobility eventually leads to the removal of the carbon interstitials and (unwanted) vacancies by either allowing these defects to coalesce or propagate to the crystal surfaces. The mobile vacancies may also migrate to nearby substitutional nitrogen and may form NV centres, where at this temperature, they are still immobile [128].

Higher heat treatments are still viable. 900°C treatments have been shown to essentially speed up the processes that occur at 600°C and provide an even higher rate of NV centre formation [129]. At temperatures above 1200°C, other defects, such as interstitial nitrogen, now become mobile. Whilst the likelihood of these now mobile defects creating more NV centres are low, the removal of them is welcomed as the reduction of strain in the crystal lattice increases the optical qualities of the NV centre. Further increases in temperature are generally limited due to the graphitisation of diamond and the dissociation of the nitrogen vacancies themselves, which occurs at 1300°C in damaged diamond or 1600°C in undamaged diamond. It may also lead to the formation of large nitrogen-containing-complex defects in diamond such as the H3 centre (N-V-N) which are unusable for quantum technologies and very difficult to remove [125]. HPHT treatments up to 2000°C have been performed, and whilst there is a reduction in the NV centres numbers, it has been

shown to affect the charge state of the NV centres which are created with a higher NV⁻: NV⁰ ratio found after these HPHT treatments.

Annealing can also be used in conjunction with other processes to increase the NV centre yield in diamond. NV centre creation via annealing assumes the presence of single substitutional nitrogen and single vacancies without which annealing would simply be the removal of unwanted defects. However, after nitrogen incorporation, by either CVD or ion implantation, the limitation of NV centre creation is commonly through the lack of sufficient vacancies in the diamond lattice. Therefore, vacancy creation is an essential tool for NV centre production. Three main techniques are used for this; ion implantation, electron irradiation and laser ablation. The working principle of each technique is the same; input energy into the diamond lattice of sufficient level to displace carbon atoms which is approximately 30 eV [130].

As mentioned, vacancies are formed during ion implantation of nitrogen, however in order to generate solely vacancies carbon ions or helium ions are viable options. Carbon-ion implantation benefits from introducing no other elements into the system, so the process of annealing is known to very reliably remove any damage or carbon-based 'defects' which may form [131]. Helium-ion implantation benefits from helium's inert nature so will form no substantially problematic defects and He-ion beams are also highly focusable, so patterning of the vacancies is possible. Typical energies for helium implantation are around 30 keV. The high level of focussing and high energy ensures vacancy creation at the focal point, whilst also ensuring most of the He atoms come to a halt much deeper into the lattice, away from the vacancy creation sites [132]. Electron irradiation works in a very similar manner by using highly focused beams of high energy electrons (> 145 keV) to displace carbon atoms,

whereas laser ablation uses very short, high energy laser pulses to introduce damaged regions in the diamond lattice, which inherently contain vacancies. The laser writing of diamond benefits from the high dependence of energy intensity with focus of the laser pulses. This dependence of vacancy production of the focusing of electron beams and laser pulses provides the ability to tune the vacancy distribution in all three dimensions in the crystal lattice, as well as the ability to form cluster or single nitrogen vacancies, depending on the laser/electron beam spot size, ideal for device fabrication. Recent technological developments have provided the same tunability for ion implantation also, with the use of highly focussed ion beams used to produce arrays on implanted NV centres. Drawbacks in both laser writing and ion implantation are still present due to the inconsistent nature of vacancy production or nitrogen implantation, so some progress is still required to perfect NV production for device fabrication.

Once Nitrogen vacancy centres are formed in a diamond sample, the next issue to overcome is the stability of the centre themselves. As mentioned, the neutral NV centre is almost useless and so steps to convert as many NV^0 centres to stable NV^-

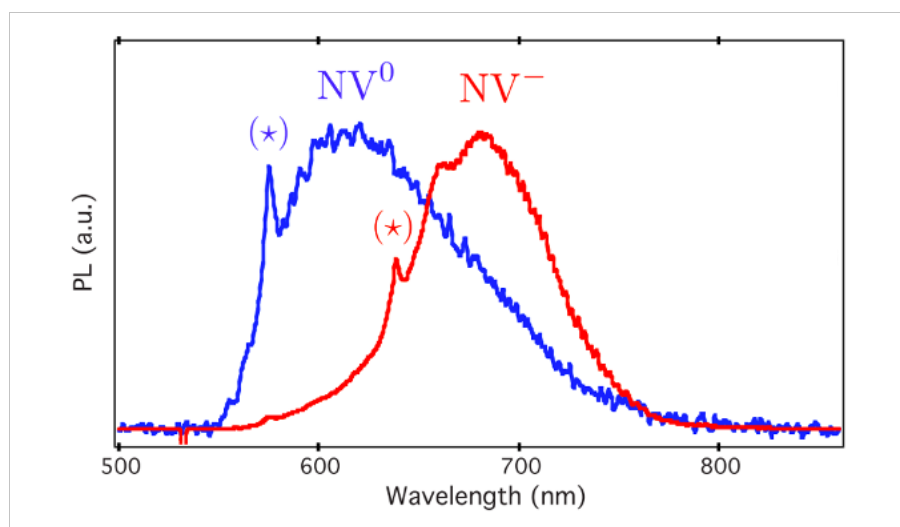


Figure 4.5: The photoluminescence spectra for the neutral NV centre (blue) and the negatively charged NV centre (red). The stars indicate the position of the ZPL for both defects [69].

centres is crucial. Probably the simplest way of differentiating between the charge states of the nitrogen vacancy is by the photoluminescence emitted by each. The neutral NV has a distinct ZPL at 575 nm whereas the negative NV ZPL is 637 nm. Figure 4.5, reprinted from [70] shows the emission spectra of both these colour centres.

Conversion and stabilisation of the negative charge state is crucial for applying the NV⁻ for any application. The main aspect which affects the nitrogen-vacancy is the surface. Interactions with spin states which are present at the diamond surface introduce noise or broadening [2], [133], [134] and charge states or the electronic structure of the surface affects the charge state of the vacancy centre [70], [135], [136]. The possibility of using NV⁻ centres which are located in the bulk diamond is also unlikely, as the deeper into the diamond, the lower the interactions NV centres will have with external signals. For example, in magnetic resonance measurements, the signal reduces proportionally to the depth of the nitrogen-vacancy cubed, meaning the sensitivity drops off extremely quickly with depth [137]. Again, a range of recipes and attempts to control the diamond surface have been made from chemical etching, annealing in controlled atmospheres and plasma treatments, however, the three main surface properties to control are as follows:

- **Surface Morphology:** - Disorder or damage in the surface has generally been associated with noise generation, reduction in coherence times for quantum applications and the instability of the negative charge state due to unwanted spin states and area of sp²/adventitious carbon present in these areas.
- **Electron Affinity:** - The electron affinity (χ) of a surface is the energy required to move an electron from the bottom of the conduction band to the vacuum level.

$$\chi = E_{vac} - E_{CBM}$$

Equation 4.1

Positive electron affinities lead to the transfer of electrons to the vacuum and an upward band bending at the diamond surface. The upward band bending leads to the transferral of electrons from the NV⁻ centres to the surface. Therefore, positive electron affinities are preferential. Positive electron affinity can be achieved by fluorine, nitrogen and oxygen terminations, the latter of which will be discussed in the next section and is the topic of study for Chapter 6.

4.1.5 THE DIAMOND SURFACE

Surfaces in a condensed matter are unavoidable. Often materials are described by bulk properties assuming an infinite periodicity in the unit cell. However, in reality the bulk material must eventually come to an end to form an interface with its surroundings, whether that be another material or free space (or vacuum). This interface is the surface of the material, and these areas can possess properties vastly different from the bulk material. The interruption of the crystal lattice results in exposed dangling bonds which are highly energetically unstable. The relaxation of surface bonds can be brought about by the reconstruction of surface atoms or the termination of the bonds by external reagents. This reordering of chemical bonding at the surface induces vast changes in the chemical, electronic and morphological properties of the surface. The surface properties will also depend on the lattice plane they are formed by. The two most commonly studied diamond surfaces are the [111] and the [001] planes, which are depicted on the unit cell in Figure 4.6. In this work

the focus will be on the [001] diamond surface so the reconstructions as well as most prevalent surface terminations will be presented henceforth.

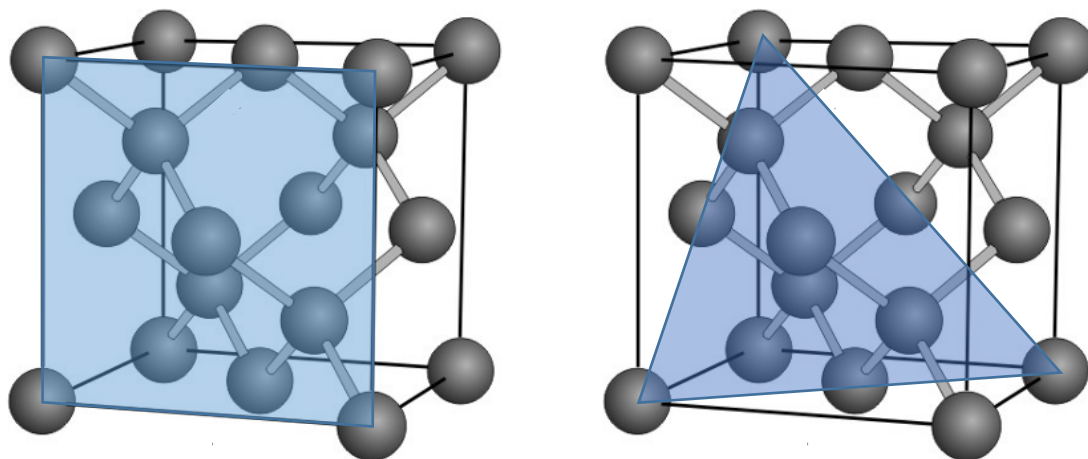


Figure 4.6: (left) The [001] diamond lattice plane and (right) the (111) diamond lattice plane.

The surface formed by cleaving along the [001] direction in diamond before any reconstruction contains two dangling bonds in a 1x1 surface geometry and an atomic spacing of 2.52 Å, shown in Figure 4.7a. This 1x1 structuring is therefore unstable unless bonded with non-carbon reagents, such as oxygen, shown in Figure 4.7b. However, without the presence of other elements to react with, the surface may undergo relaxation by forming π bonded dimers with neighbouring carbon atoms in a 2x1 surface geometry, shown in Figure 4.7c. This 2x1 reconstruction without the presence of adatoms is typically referred to as a 'clean' diamond surface, free from contaminating species. Typically, this surface is still energetically unfavourable and minimal presence of adatoms are required to remove the reconstruction. Hydrogen atoms, which are ubiquitous during the growth of CVD diamond readily react with the surface and can form a 2x1:H-termination, shown in Figure 4.7d.

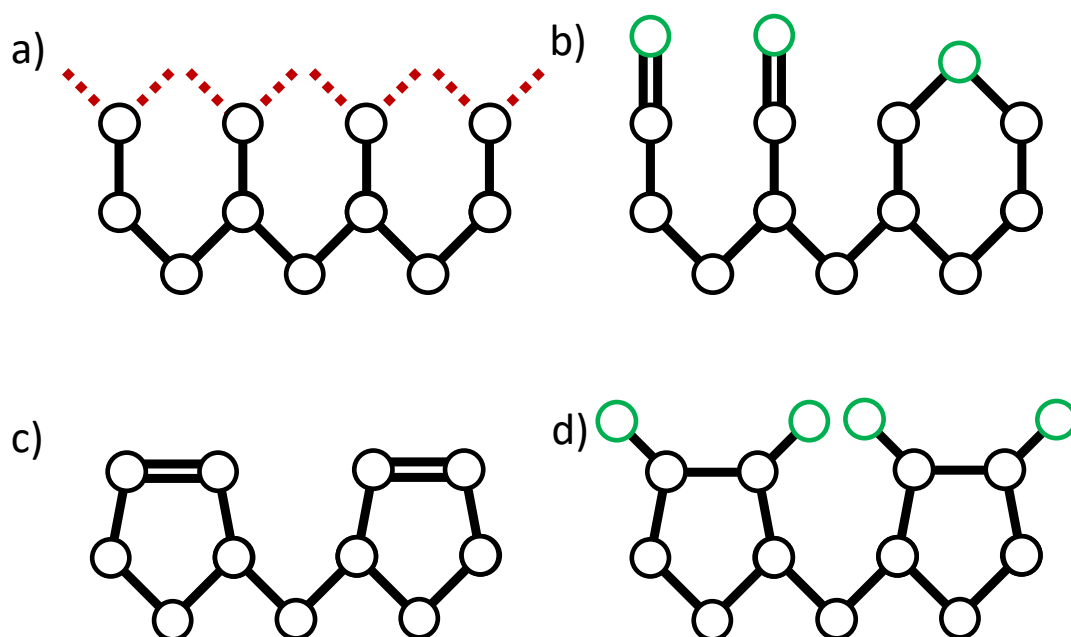


Figure 4.7: a) The freshly cleaved, unreconstructed 1x1 diamond surface with dangling bonds indicated by the red dashed lines. b) The 1x1 terminated diamond surface where the surface dangling bonds have formed a double bond with a non-carbon adatom or a bridge with a single atom between two carbons. The green atoms in this case are commonly oxygen. c) The 2x1 'clean' diamond surface structure. d) The 2x1 terminated diamond surface with single bonded adatoms, commonly hydrogen.

Bulk diamond is a very wide band gap insulator, however, the surface structures shown can form surface states which vastly modify the electronic properties at the surface. The clean 2x1 diamond surface, for example, exhibits semiconducting properties due to the formation of a 1.3 eV bandgap at the surface which arises from the broadening and splitting the π (bonding) and π^* (antibonding) states due to the maintained distance of 2.52 Å between surface dimers [138]. Beyond just reconstructions, the surface may be terminated by other elements, and the surface properties, such as electron affinity, work function and conductivity can be altered profoundly by the chemical species present on the surface. Whilst many surface terminations exist, the two most commonly studied are the hydrogen and oxygen terminations. These surfaces will be discussed briefly.

Hydrogen termination of [001] diamond, shown in Figure 4.7d, has a 2x1 surface geometry with C-H bond lengths of 1.11 Å and spacing between hydrogen

atoms of 2.49 Å. One of the most distinctive properties of this surface is its metallic-like conductivity and negative electron affinity. Initially observed in 1989, the mechanism behind the conductive properties has been debated since. Initial suggestions were based around p-type doping confined around the first 10 nm of the surface with a very low activation energy of 50 meV [139].

However, the current belief is the conductive surface arises from a combination of the negative electron affinity, which arises due to the polarity of C-H bonds induced by carbon's higher electronegativity, and surface transfer doping by surface adsorbates [140], [141]. With the negative electron affinity provided by the hydrogenated surface, and with a suitable adsorbate whose electron affinity exceeds the ionisation potential of the hydrogen terminated surface. With such an adsorbate, electron transfer from the surface to the adsorbate occurs, bending the diamond CBM and VBM bands until an equilibrium is reached and the Fermi levels of the surface and adsorbate are equal. One such example of adsorbate is buckminsterfullerene (C_{60}), although conduction in the presence of water has also been shown. The mechanism described is shown in Figure 4.8 where C_{60} is the example adsorbate. Figure 4.8a shows the band diagram before transfer doping, and 4.8b shows the band bending once chemical equilibrium has been reached. The diamond in this work has a negative electron affinity of 1.3 eV, and the Figure is reprinted from [140]. The surface conductivity dependence on the presence of surface adsorbates has also been confirmed by annealing of hydrogenated diamond surfaces within UHV chambers. The 200-450°C annealing process removed surface adsorbates, and thereby removed the surface conductivity but kept the hydrogen terminated intact [141]. It is also worth noting that this upward band bending is

present in intrinsic diamond, for p-doped diamond the surface states created by surface terminations are generally below the Fermi level of bulk p-type diamond, resulting in downward band bending [142].

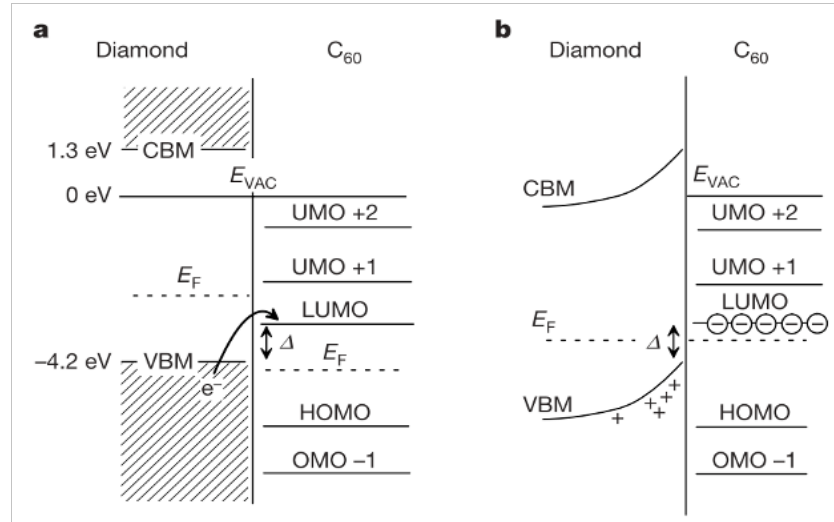


Figure 4.8 : (left) The band structure of the hydrogen terminated diamond surface with adsorbed C_{60} molecules before surface transfer doping. (right) The same surface after equilibrium has been reached via surface transfer doping.

Hydrogen termination of diamond is the most common termination of CVD grown diamond and is also one of the most stable terminations due to the high bond strength of the C-H bond. Temperatures exceeding 600°C are required to remove the hydrogen termination. The hydrogen terminated surface is also hydrophilic due to the dipoles formed at the surface by the carbon atom's higher electronegativity in the C-H bonds. It can be identified by a low contact angle with water as a simple test for surface termination. For nitrogen-vacancy applications, the hydrogen terminated surface has been dismissed due to the instability of shallow negatively charged NV centres. The electron traps on the surface facilitate electron transfer from the negative centres within the depletion width and lead to the upward band bending discussed.

Conversely to the hydrogen terminated diamond surface, oxygen termination exists in a 1x1 geometry. However due to the existence of two dangling bonds per

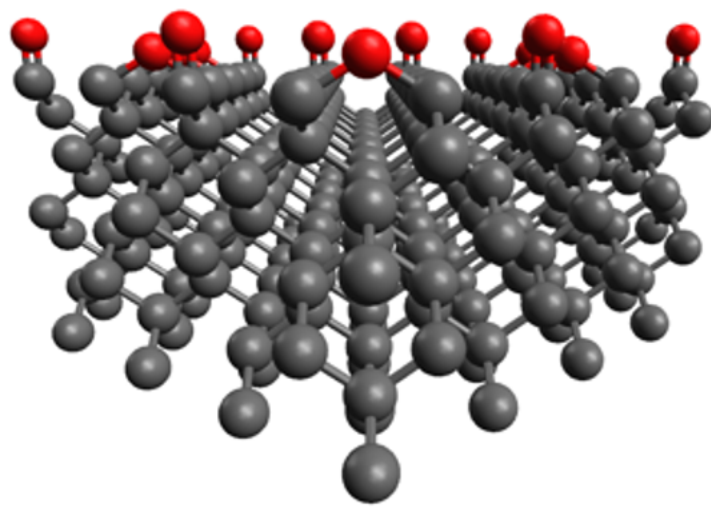


Figure 4.9: A small section of oxygen terminated [001] diamond surface with ketone and ether species present. Oxygen is shown by the red atoms.

carbon atom at the surface and the divalent nature of oxygen, a number of surface species can be formed. As shown in Figure 4.7b, oxygen atoms may form double bonds with the surface atoms, known as ketone ($\text{C}=\text{O}$) groups or ‘oxygen bridges’, known as ether ($\text{C}-\text{O}-\text{C}$) groups. Due to the nature of the double bonds, the bond length is notably shorter with a bond length of 1.19 \AA , compared to bond lengths of 1.48 \AA for $\text{C}-\text{O}$ bonds in the oxygen configuration. Figure 4.9 shows a small, modelled unit of a [100] diamond surface with the ketone and ether groups shown by the red atoms. Oxygen terminated surfaces will always contain more than just one chemical species on the surface. Full coverage by ether or ketone groups are usually hindered by further relaxations or induced strain by slight mismatches in bond lengths over longer distances on the surface.

Oxygen terminated [001] diamond induces significantly different electronic properties in comparison to its hydrogen counterpart. Oxygen terminated [001] diamond does not conduct and is (generally) known to have a positive electron affinity. As discussed, the electron affinity is dependent on the electrostatic dipoles which exist on the diamond surface. For the hydrogen, carbon’s higher

electronegativity induces a positive dipole moment (normal to the diamond surface), which leads to a reduced or negative electron affinity, whereas oxygen, the second most electronegative element behind fluorine, induces a negative dipole moment (of a larger magnitude) thereby producing an increase in the surfaces electron affinity [138]. Due to the complexity of the oxygen terminated surface, however, the electron affinity can vary significantly from sample to sample. Slightly differing methods of oxidation can also produce very different electronic properties. Some of the most common oxidation methods are acid etching, (sulphuric acid is a common reagent of choice for oxidising diamond), plasma treatments or annealing in controlled, oxygen-containing environments. The general consideration for producing the highest electron affinity values is the surface morphology. Aggressive oxidation by either high temperature treatments or highly oxidising reagents are shown to lead to disordering in the surface termination, which diminish the surface's desired properties. However, removal of the disordered or 'damaged' areas can lead to some of the largest positive electron affinities on diamond surfaces. Sangtawesin, *et al.* [2], showed oxygen annealing a [001] triacid (perchloric, nitric and sulphuric acid) cleaned diamond surface in oxygen at 400°C increased the electron affinity from 0.92 eV to 2.14 eV. This large increased was proposed to be due to the removal of disorder at the surface.

Although no surface states are formed in the bandgap by oxygen termination (the only state found is approximately 3 eV below the VBM [143]), some band bending does occur at the surface, due to the generation of a barrier potential at the diamonds surface. The magnitude of the band bending is generally of the same level as the charge neutrality level of diamond, which is the position for the Fermi level

which renders the surface without a net charge, of 1.4V. The Band bending, and band structures of oxygen terminated diamond will be discussed further in chapter 5.

Oxygen terminated diamond is also hydrophilic due to the nature of the dipoles on the surface, it is also a fairly stable surface termination requiring temperatures exceeding 400°C to remove most oxygen species. The electronic properties and ordering of the oxygen surface has meant it is one of the most widely researched surfaces with regards to NV centres and has been shown to reduce signal noise, increase conversion of shallow NV centres to the negative charge state and increase the stability of these centres [2], [135], [144].

4.1.6 NANOCRYSTALLINE DIAMOND FILMS

A section of the work presented in chapter 6 utilised nanocrystalline diamond (NCD) films as a substrate for implantation, therefore a brief introduction to this material, its growth, its applications and its properties will be presented. Nanocrystalline diamond (NCD) films are of interest as they have been shown to contain many of the superlative properties of bulk diamond; for example, a high Young's modulus (1100 GPa), a high thermal conductivity (up to 2000 W m⁻¹ K⁻¹) and a phase velocity of 12,000 m s⁻¹ [145]. NCD can also be produced at a lower cost, lower temperatures and over larger areas than single crystal diamond, thanks to the development of modern CVD technologies [146]. NCD films find possible applications dependant on predominantly it's mechanical properties, such as Surface Acoustics Wave (SAW) devices, and Micro-Electro-Mechanical Systems (MEMS), however, they can also find electronic applications due to its ability to become superconductive [147], or become a field electron emitter [148]. Other applications include X-ray windows, lithography, and tribological coatings. An extensive list of applications and references can be

found in section 7 of a review paper of nanocrystalline diamond by Oliver Williams [149].

NCD films are usually grown on non-diamond substrates, which in itself is not trivial due to the high disparity between the surface energies of diamond and the most commonly used substrates, such as silicon, the low sticking coefficients of the gaseous precursors (CH_4) and competitive growth of non-diamond carbon. To overcome these issues, the substrates have to be seeded with a densely packed layer of nanodiamonds. Seeding directly onto untreated silicon results in very low nucleation densities of around 10^5 cm^{-2} [150], however a number of techniques have been developed to increase this value exponentially, close to a theoretical, measurable, maximum of approximately 10^{12} cm^{-2} [149]. Some seeding techniques are listed below:

- **Mechanical Abrasion:** Scratching of the substrate surface can form scratches, pits and an overall increase in surface area with more sites for nucleation [151]. This can be improved upon by sonication in diamond suspensions to cause 'micro-chipping' for enhanced, more uniform seed densities [152].
- **Bias-Enhanced Nucleation:** Performed *in-situ*, applying a negative bias of approx. 200 V can lead to the attraction of the positively charged gas precursors, such as CH_3^+ or H^+ species which are the predominant reagents in CVD diamond growth.
- **Seeding with diamond nano-particles:** Maximising the number of diamond particles will inevitably increase nucleation density. Therefore production of smaller nanodiamonds through milling and careful preparation of nanodiamond containing colloids through control of zeta potentials, pH levels

and concentration and use of sonication can lead to some of the highest packing densities without damaging the substrate [153].

Once the substrates are seeded, the growth may begin, however as the diamond films produced are usually very thin, the initial growth conditions are crucial. Therefore, what is known as an incubation period is needed. As growth times are generally very short for NCD films, the first few minutes, where very little diamond growth occurs, can be detrimental to the film structure. The lack of diamond growth is due to a non-complete seed coverage which generates a propensity for non-diamond growth or diffusion of carbon into the substrate. Higher methane concentrations during this period of around 5% have been shown to keep the high seeding density and to reduce the sp^2 content grown. During this growth stage a Volmer-Weber growth model is followed until coalescence [154]. Once coalesced, the growth nature transitions to a competitive columnar growth model [155]. This growth model leads to an inherent surface roughness which is dependent on film thickness. A simple schematic of the grows of NCD diamond films is shown in Figure 4.10. Further steps to the production of NCD films include the use of masking/etching

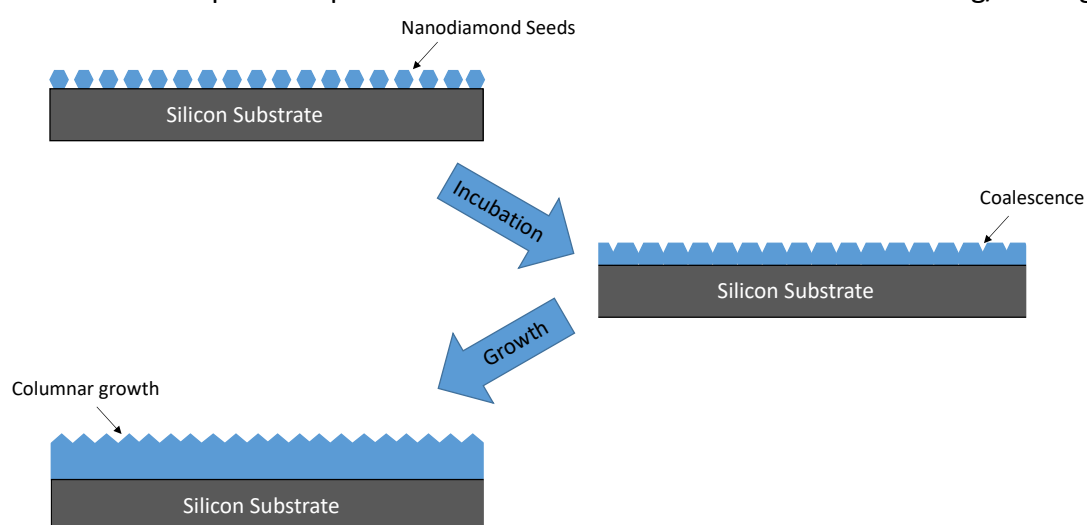


Figure 4.10: The three stages of NCD film production. Initial nucleation or seeding with nanodiamonds, individual growth of said nanodiamond seeds until coalescence, and finally, the competitive, columnar growth which follows.

of the oxide layer on silicon to create NCD structures [156], and post-growth treatments such as surface functionalisation [157] or chemical mechanical polishing which can provide rms roughness values <2 nm [158], [159].

Chapter 5 – OXYGEN TERMINATED (001) DIAMOND SURFACE

As mentioned in chapter 4, near-surface NV^- centres can strongly interact with any electronic and spin states which may be present on the diamond surface. These interactions can greatly hinder the applicability of the NV^- centre for devices which require the centre to sit within a few nanometres of the surface. As the undesirable states are more common on damaged or disordered surfaces, it is crucial that we understand how to correctly prepare the surface in order to utilise the NV centres fully [2]. Previous work has shown that the Oxygen-terminated diamond surface is a good candidate for NV-based applications. In this chapter an investigation of the oxygen terminated surfaces of a (001) diamond was performed. The oxygen species' evolution and the electronic properties, including surface photovoltage, band bending and electron affinity, of two oxygen termination methods have been studied during heating up to 1000°C and under a number of different environments, using a combination of XPS, UPS and REES. During this work an oxygen terminated surface with the highest reported positive electron affinity of 2.4 eV was produced. A discussion of errors of values quoted throughout this chapter is presented in Appendix 8.2.

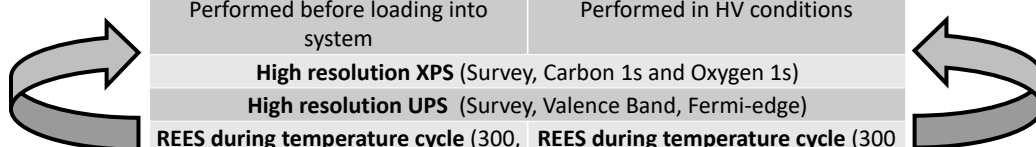
5.1 COMPARISON OF OXYGEN SPECIES FORMED BY OXIDATION TECHNIQUES

5.1.1 EXPERIMENTAL OVERVIEW

The entirety of work in this chapter was performed on a boron doped ($N_B \approx 10^{21} \text{ m}^{-3}$), CVD grown (001) single crystal diamond (approx. $7.5 \times 7.5 \times 1.5 \text{ mm}^3$) provided by Element Six Ltd. The surface was polished to a roughness of approx. 0.2 nm rms. During this work, two methods were used to produce an oxygen terminated surface. The first method involved submerging the sample in 10 ml of boiling sulphuric acid (H_2SO_4) for 10 minutes, then a further 10 mins after the addition of 0.5 g of potassium nitrate, followed by a sonication in acetone then isopropanol and dried using clean nitrogen before being loaded into the REES system. The second method was performed *in-situ*, following a heating to approximately 1000°C. The diamond was exposed to a 100 W nitric oxide (NO) plasma at a pressure of 5×10^{-5} mbar for 30 minutes, before being transferred back into the analysis chamber, as described in section 3.3.3.

Once loaded after the acid etch, XPS and UPS spectra were recorded and the sample underwent a number of heating cycles, up to 1000°C. During each cycle, REES data were recorded, and high-resolution XPS/UPS were recorded between each cycle. The sample was then treated with the aforementioned plasma treatment and again, underwent heating cycles up to 700°C with REES and high-resolution XPS/UPS taken. For clarity, Table 5.1 shows the step-by-step experimental method which was performed during this work. All the data taken in this chapter were analysed using the fitting program described in chapter 2.

Table 5.1: The experimental method used for the work in this chapter.



Acid-Etch ($\text{H}_2\text{SO}_4 + \text{KOH}$)	Oxygen Plasma Treatment (100W)
Performed before loading into system	Performed in HV conditions
High resolution XPS (Survey, Carbon 1s and Oxygen 1s)	
High resolution UPS (Survey, Valence Band, Fermi-edge)	
REES during temperature cycle (300, 600, 700, 800, and 1000 °C)	REES during temperature cycle (300 and 700 °C)

5.1.2 RESULTS

5.1.2.1 ACID-ETCHED DIAMOND SURFACE

As mentioned in section 5.1.1, two surface treatments will be discussed, starting with acid-etching. Oxygen terminated surfaces formed via acid etching have been previously reported [1],[2]. However, there are interpretation differences in the literature. Therefore, some aspects of the following results are here to test repeatability whilst at the same time, trying to be more rigorous in the analysis procedure using the newly developed fitting software and address some of these aforementioned differences.

During the investigation, survey spectra, or widescans, are taken after various temperature steps in order to monitor the surface chemistry of the diamond surface. Widescans are lower resolution scans taken over a wider range than core level scans. The widescan parameters used in the work are as follows; the energy range is from 1053.6 to -6.4 eV binding energy, in 1 eV steps. A dwell time of 0.5 s, a pass energy of 60 eV and 3 sweeps were averaged in order to provide a sufficiently high SNR. A magnesium K- α source which produces X-rays at 1253.6 eV was used for the in-house studies. Figure 5.1 shows a set of widescans at 4 stages in the experiment, as loaded and after three annealing steps, 300°C, 700°C and 1000°C. The as loaded scans are

for a clean diamond sample, with an oxygen signal indicative of around a monolayer of oxygen. In previous work, such as the calculations shown in Di Hu's thesis [160], CasaXPS would be used to fit regions on a widescan and to calculate the stoichiometry of the sample surface. In this work, the oxygen % has been calculated using both the widescans on CasaXPS and the core level scans, shown in Figure 5.1, using the MCS fitting software developed to further test its quantification ability.

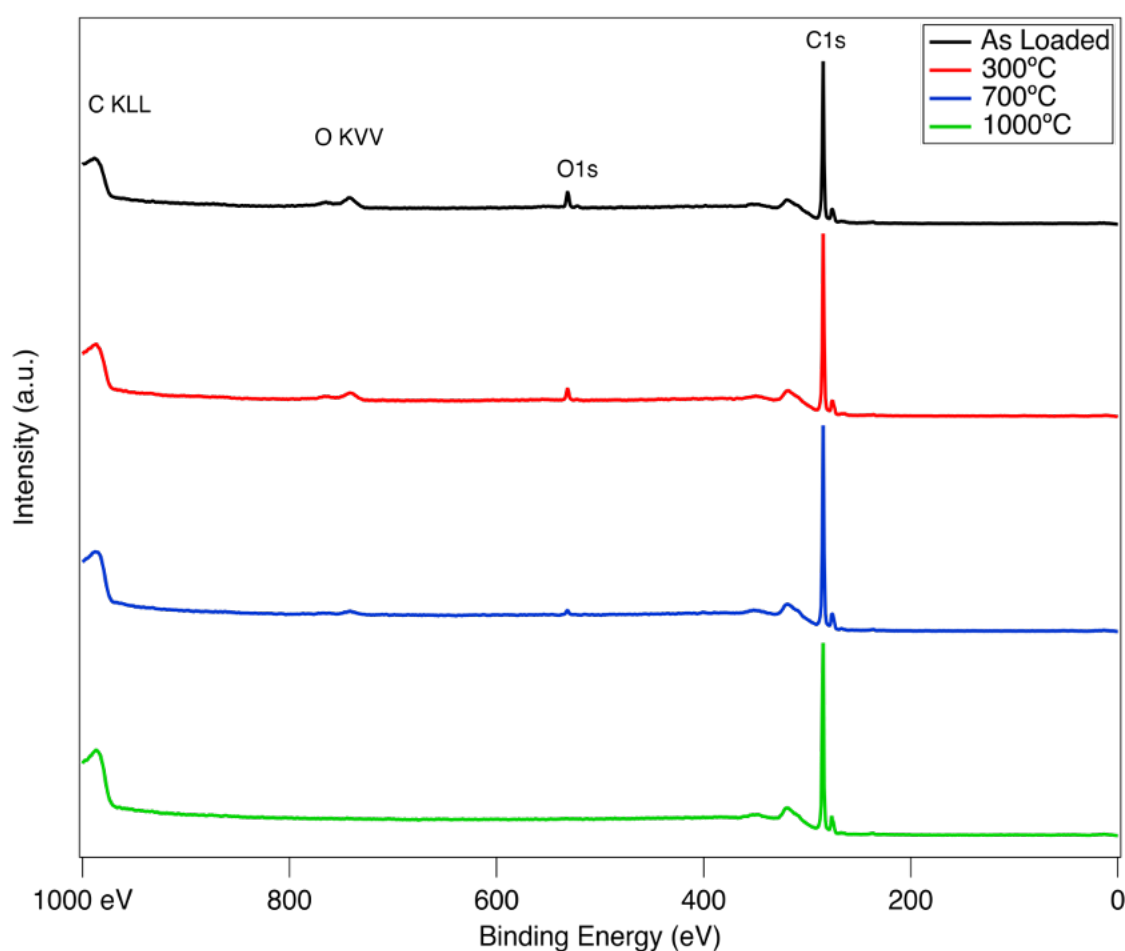


Figure 5.1: A series of widescans taken of the acid-etched (001) diamond after different heating cycles. From top to bottom the widescans are as follows: as-loaded, after 300°C, after 700°C and after 1000°C. Only three temperature steps have been chosen for illustration. The peak associated with the C1s and O1s core levels as well as the oxygen and carbon Auger peaks have been labelled.

Table 5.2: Carbon and oxygen concentration calculated from core level scans, as well as the oxygen concentrations calculated from widescans using CasaXPS, taken at different temperatures. θ_0 is the coverage of oxygen in monolayers.

Temperature (°C)	C1s(%)	O1s(%)	O1s(%) from CasaXPS	Δ O1s (%)	θ_0
Room Temp	94.6	5.4	5.1	0.3	0.99
300	96.1	3.9	3.6	0.3	0.78
700	98.2	1.8	1.3	0.5	0.28
1000	100	0.0	0.0	0.0	0.00

The results from the Igor calculations are reasonable and around the expected value for an acid-etched surface. The relative intensities can also be used to calculate the apparent oxygen overlayer thickness d , which can provide an estimation for the surface coverage of oxygen using equations 5.1 and 5.2 (shown in Table 5.2). However, higher resolution scans are required to determine the species that are present on the diamond surface.

$$\theta_0 = \frac{d}{d_0}$$

Equation 5.1

where:

$$d = \lambda \ln \left(1 + \frac{I_O \sigma_C}{I_C \sigma_O} \right)$$

Equation 5.2

where θ_0 is the coverage of oxygen (1 being a full monolayer), d_0 is the layer separation distance for (001) diamond, d is the calculated overlayer thickness, λ is the electron MFP of the C1s photoelectron, I_O and I_C are the oxygen and carbon intensities, respectively and σ_O and σ_C are the oxygen and carbon photoionisation cross-sections, respectively [161].

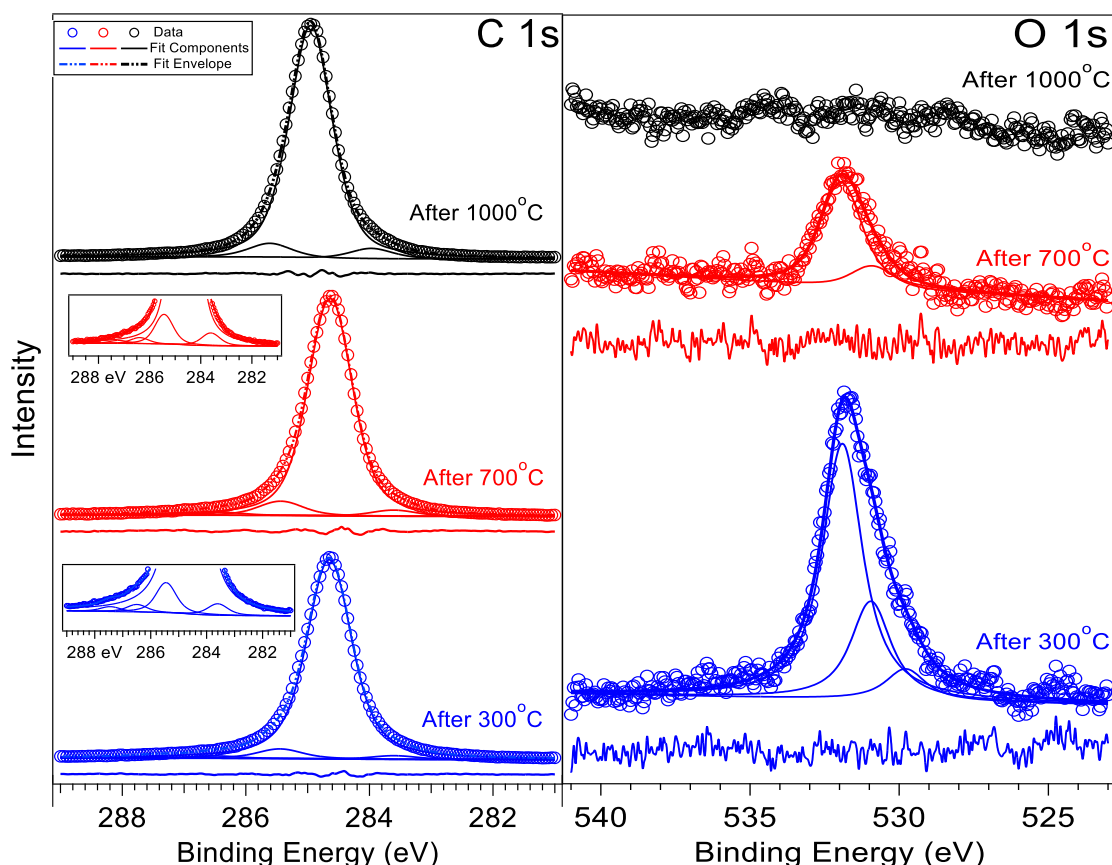


Figure 5.2: (left) A series of carbon 1s core level scans taken at different temperatures. Insets are showing the components used in fitting the core level. (right) A series of oxygen 1s core level scans taken after different temperatures. See Table 5.3 for details of the fit components. The fit residuals are shown beneath each peak.

Figure 5.2 shows a set of high resolution C1s and O1s core level scans taken after taking the sample up to 3 different temperatures, 300°C, 700°C and 1000°C from bottom to top on the Figure, respectively. The scanning parameters for the C1s spectra are as follows; the kinetic energy scan range was 958-983 eV (270.6-295.6 eV binding energy), with steps of 0.05 eV and a pass energy of 10 eV. A dwell time of 0.5 s and 30 sweeps were required in order to maximise SNR. The O1s spectra were recorded between an energy of 710 and 740 eV kinetic (513.6-543.6 eV binding) using 0.05 eV steps and a pass energy of 10 eV also. A dwell time of 0.5 s seconds and 45 sweeps were required for a reasonable SNR. Included on Figure 5.2 are the fit components, fit envelopes and the residuals for each spectrum. The data were fitted

using Voigt convolution functions with variable Gaussian and Lorentzian width contributions. The fit parameters are shown separately in Table 5.3.

The high resolution O1s spectrum at 300°C shows the presence of three oxygen species on the diamond surface at binding energies of 531.9 eV, 531 eV and 529.8 eV. These components are usually associated with ether (C-O-C), alcohol (C-OH) and ketone (C=O) groups, respectively [2]. However, some modelling suggests there can be vastly different binding energies for similar oxygen containing groups, such as oxygen bridges (C-O-C), depending on their local environment. Additionally, exact fitting can be difficult with only the three oxygen species, suggesting a plethora of overlapping oxygen species with similar, overlapping peak shapes. Because of this, fit components may be referred to by the chemical species or 'S1 - S4', as presented in Table 5.3, which refer to the ether, alcohol, ketone and sp^2 C-C bonds, respectively. At 700°C there is again a significant desorption of oxygen however the desorption rate is not the same for each oxygen species. Firstly, the ketone component at 529.8 eV has been removed completely, suggesting a more ordered surface has been formed, as ketones predominantly exist on lattice steps or restructuring of the ketone groups to the energetically favourable oxygen bridges (C-O-C).

The high resolution C1s spectra reflect the O1s spectra in the smaller components seen in the higher binding energy tail of main component. In the 300°C C1s spectrum the three higher binding energy components at 287.4 eV (S1), 286.5 eV (S2), and 285.4 eV (S3) are commonly linked to the presence of oxygen containing groups. The main component (B) lies at 284.6 eV and is the bulk C-C signal and the lowest binding energy component (S4) at 283.6 eV is thought to be sp^2 bonded carbon which may be present at the surface. The effects of heating to 700°C are not

as clear on the C1s signal as they are on the O1s signal. Although the intensity of the oxygen components was lower, the atomic percentages of the S1 and S2 components remained the same, as shown in Table 5.3. This may be due to a number of reasons; as mentioned in previous chapters, the lower detection limit of XPS is in the region of 0.1 – 2%, depending on the system studied so even detecting a measurable signal of this magnitude can be difficult. Another plausible cause is the level of hydrogen in the vacuum system. As the sample is heated, the Boralectric heater releases hydrogen with a partial pressure of $< 10^{-9}$ mbar. However, as oxygen is desorbed from the sample, surface dangling bonds are highly reactive, and the ambient hydrogen is sufficient to form hydrogen terminated areas on the diamond surface.

This can be shown further when we heat to 1000°C and we no longer have any detectable O1s signal. On the C1s peak there are still two prominent components either side of the main C-C component. These two components sit at the same energy difference from the main C-C component as the sp^2 and ether (C-O-C) components. These, along with the shift of the whole peak of around 0.4 eV to a lower binding energy, are indicative of hydrogen terminated diamond [162]. UPS and REES were used to further examine the surface termination and oxygen desorption. Other studies of the diamond surface have also theorised that multi-layer sub-surface restructuring caused by surface terminations may be attributed to a higher binding energy component close to the main C-C component [162].

Table 5.3: The function parameters used to fit the data shown in Figure 5.2. The peaks are ordered by the position and sorted from highest to lowest binding energy (left to right on graph). The FWHM given is the width of the Voigt convolution, and the widths of the Gaussian and Lorentzian peak required for the convolution are also given. Finally, the relative percentage of total area for each component is given.

Core Level	Temperature (°C)	Position (eV)	FWHM (eV)	Gaussian Width (eV)	Lorentzian Width (eV)	%
C1s	300	287.4 (S1)	0.87	0.56	0.48	0.7
		286.5 (S2)				1.1
		285.4 (S3)				4.5
		284.6 (B)				92.0
		283.6 (S4)				1.7
O1s	300	531.9	1.41	0.51	1.43	66.3
		531.0				25.5
		529.8				8.2
C1s	700	287.2 (S1)	0.86	0.64	0.36	0.6
		286.4 (S2)				1.2
		285.4 (S3)				5.9
		284.6 (B)				89.8
		283.6 (S4)				2.5
O1s	700	531.9	1.37	1.04	1.00	82.5
		530.9				17.5
C1s	1000	285.6 (S1*)	0.83	0.58	0.42	5.4
		285.0 (B)				90.5
		284.0 (S2*)				4.1

UPS spectra were taken between every heating step in order to study how the structure of valence band electrons at the surface varied with temperature. UPS was taken using the Low Angular Dispersion (LAD) analyser mode and the SPECS UVS-300 He-plasma source using the He-I plasma emission at 21.2 eV. This provides a high intensity source ideal for very surface sensitive studies. As with XPS, widescans and higher resolution UPS spectra were taken. Widescans were taken between a kinetic energy range of 7-32 eV (15 to -10 eV binding energy), at steps of 0.1 eV and a dwell time of 0.2 s. For the majority of scans a pass energy of 3 eV was used, however after 1000°C a pass energy of 1.5 eV was required to avoid saturation of the analyser CCD.

Higher resolution scans were taken of the Fermi edge on both the sample, in order to measure the valence band maximum (VBM), and on the Ta faceplate, to measure the Fermi edge for calibration. The high resolution UPS scans were taken between 22 and 32 eV with a pass energy of 3 eV and a step size of 0.01 eV; 20 sweeps were taken in order to increase the SNR and produce a reliable Fermi-edge. During measurements a -9 V bias was applied to the sample stage.

Figure 5.3a shows the normalised UPS widescans taken after heating to 300°C, 700°C and 1000°C and measured at room temperature. The inset shows an enhanced view of the VBM for the 1000°C spectrum due to the large increase in the secondary electron tail. Shown on the 300°C spectrum are the secondary electron cut-off energy (E_{cutoff}), as well as the VBM energy (E_{VBM}). These values can be used to calculate the work function (ϕ) and electron affinity (χ) of the sample using equations 5.3 and 5.4, respectively.

$$\phi = h\nu - (E_{\text{cutoff}} - E_{\text{VBM}})$$

Equation 5.3

$$\chi = \phi - E_{\text{BG}}$$

Equation 5.4

where $h\nu$ is the photon energy (21.2 eV) and E_{BG} is the bandgap of diamond, taken as 5.5 eV.

Figure 5.3b shows high resolution VBM spectra for the (001) diamond after the three temperature cycles. Marked on each spectrum is the method for calculating the VBM value. Figure 5.3c shows an example Fermi-edge measured on the Ta faceplate; the Fermi edge is fitted using equation 5.5 to calculate the Fermi level (E_{F}).

$$y = A \exp\left(\frac{(x - E_F)\Delta E}{\kappa T}\right)$$

Equation 5.5

where y is the fit data, A is the amplitude, x is the energy scale, ΔE is dimensionless broadening from the analyser, and κT is Boltzmann's constant (in eV K⁻¹) multiplied by the temperature, which accounts for thermal broadening.

During heating the secondary cut-off shifts 0.5 eV to a higher binding energy whereas the VBM shifts 0.68 eV towards the Fermi level. The increased spectrum width implies a sharp decrease in the work function indicating areas of the oxygen

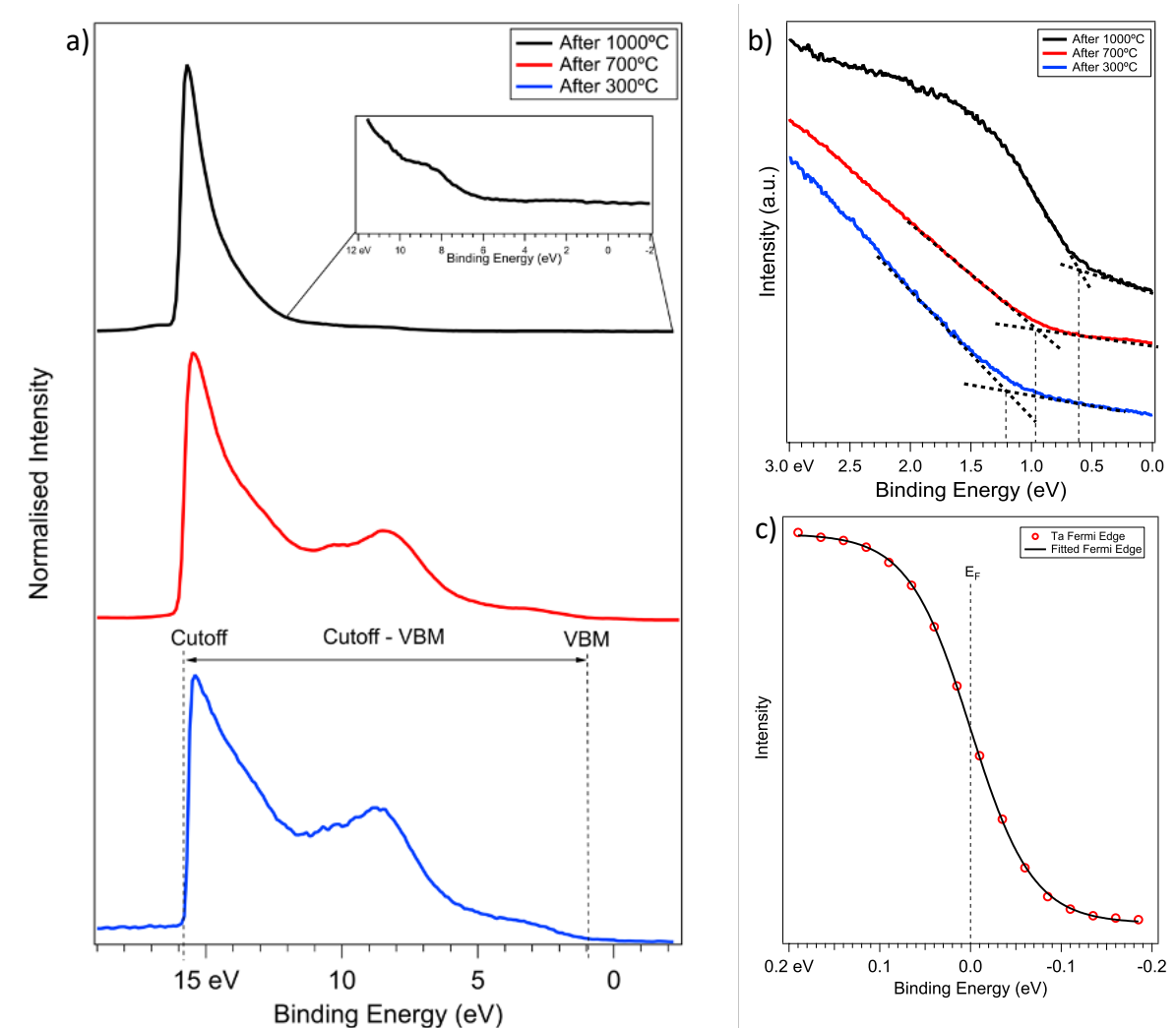


Figure 5.3: (a) Normalised UPS valence band spectra of the (001) diamond after various 300°C (blue), 700°C (red) and 1000°C (black). Marked on the 300°C spectrum are the secondary tail cut-off and the Valence Band Maximum (VBM) energies, used in calculating the work function and electron affinity. (b) higher resolution scans taken around the VBM at each stage, this can be used to obtain a more accurate VBM value. (c) an example Fermi edge taken on the tantalum faceplate and a fitted Fermi edge. This is used to calibrate 0 eV binding energy.

termination have been replaced by hydrogen termination. After 1000°C treatment the work function is still positive at 0.22 eV. This indicates areas of 2x1 surface reconstruction which can have a PEA of up to 0.8 eV [163], [164].

Table 5.4: The secondary cut-off, Valence Band Maximum and electron affinity of the (001) diamond after different temperatures.

Temperature (°C)	Secondary Cut-Off (eV)	VBM (eV)	Electron Affinity (eV)
300	15.8	1.18	1.28
700	16.2	1.17	0.87
1000	16.3	0.62	0.22

A further investigation on the acid etched surface took place at the B-07 Near Ambient Pressure XPS (NAP XPS) beamline at the Diamond Light Source at Harwell. This work utilised lower excitation photon energies to enhance the surface sensitivity by the reduction of the emitted photoelectron kinetic energy, (see section 2.1.4 for theory on the electron MFP). Spectra were recorded at room temperature, at 350°C, and under a 1 mbar H₂O atmosphere to test the oxygen termination stability. The results from this beamtime are shown in Figure 5.4. Six spectra are shown, 3 C1s core levels (left column) and 3 O1s core levels (right column). Figures 5.4a and 5.4b are the C1s and O1s core levels measured at 350°C, respectively. It is clear to see the shape of both the spectra are similar, due to similar energy difference from components to that of the home laboratory, room temperature spectra. However, the core level spectra have maxima at a binding energy approximately 0.6 eV higher. This is due to the removal of the surface photovoltage, which will be discussed in more detail in section 5.2, by the increased temperature which is consistent with data measured during real-time experiment (see Figure 5.6 for an example REES image). The fit components for all spectra are presented in Table 5.4 (C1s) and Table 5.5 (O1s). The binding energies presented are given relative to the main C1s (C-C)

component for easier comparison. Similarly, to the lab XPS, the at-temperature C1s (5.4a) core level is fitted with five components. The red component is associated with the C-C bulk diamond, the lower binding energy green component is associated with sp^2 carbon, and the higher energy blue peaks are the components most frequently associated with the oxygen surface species.

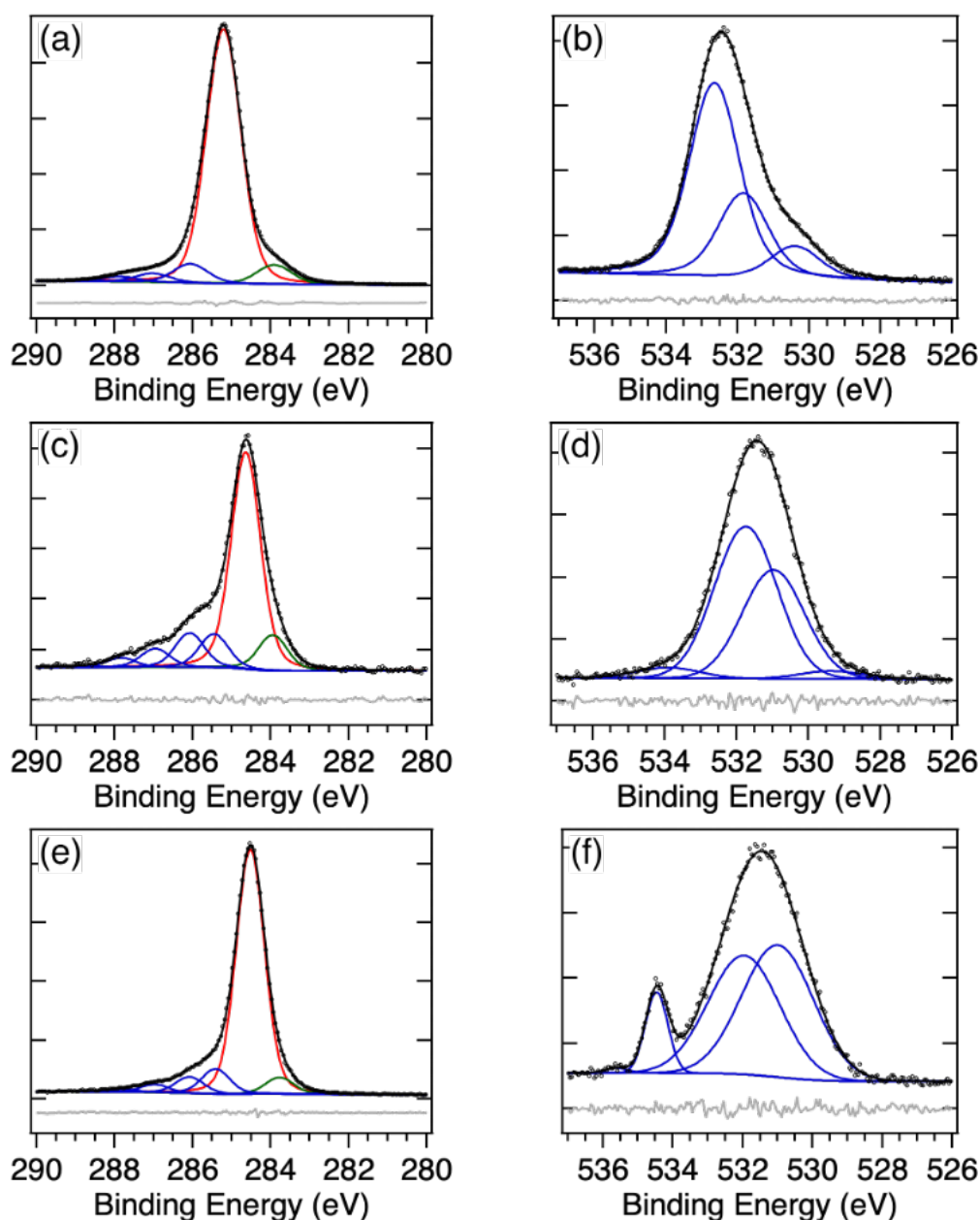


Figure 5.4: A series of C1s and O1s spectra measured using synchrotron radiation. (a) and (b) are C1s and O1s core levels measured at 347°C, respectively. (c) The surface enhanced C1s spectra measured at room temperature using a photon energy of 400 eV. (d) The O1s spectra measured at room temperature. (e) and (f) show the C1s and O1s spectra measured in a 1 mbar H₂O atmosphere. The photon energy for (a, b) and (d-f) was 800 eV. In each spectrum the raw data are shown in black, fit components shown in red, blue and green and fit residuals are shown underneath each spectra in grey.

Table 5.5: The fit parameters of the C1s core levels for the spectra shown in Figure 5.4 a, c and e. The relative binding energies with respect to the C-C component at 284.6 eV are shown along with the FWHM of the Voigt components and the area % contribution of each component.

Core Level	Condition	Parameter	C-C	Sp ² /C-H	'Sub-surface'	C-O (S1)	C-O (S2)	C-O (S3)
C1s	At Temp (5.4a)	Relative BE (eV)	0.00	-1.30	+0.85	+1.84	+2.65	N/A
		FWHM (eV)	1.06					
		% Intensity	82.2	6.0	7.2	2.8	1.8	N/A
	S-XPS (5.4c)	Relative BE (eV)	0.00	-0.69	+0.84	+1.45	+2.34	+3.22
		FWHM (eV)	0.90					
		% Intensity	62.3	10.2	9.6	9.9	5.3	2.7
	1mbar H ₂ O (5.4e)	Relative BE (eV)	0.00	-0.75	+0.87	+1.56	+2.42	+3.26
		FWHM (eV)	0.87					
		% Intensity	78.3	5.2	8.0	5.2	2.5	0.8

Table 5.6: The fit parameters of the O1s core levels for the spectra shown in Figure 5.4 b, d and f. The relative binding energies with respect to the ether (S1) component are shown along with the FWHM of the Voigt components and the area % contribution of each component.

Core Level	Condition	Parameter	Ether (S1)	Ketone (S2)	Alcohol (S3)	H ₂ O
O1s	At Temp (5.4b)	Relative BE (eV)	0.00	-0.80	-2.25	N/A
		FWHM (eV)	1.69			
		% Intensity	62.2	27.1	10.7	N/A
	In-vacuo (5.4d)	Relative BE (eV)	0.00	-0.79	-2.39	-2.15
		FWHM (eV)	2.04			
		% Intensity	54.6	38.8	2.8	3.8
	1mbar H ₂ O (5.4f)	Relative BE (eV)	0.00	-0.97	N/A	-2.5
		FWHM (eV)	2.41			
		% Intensity	43.0	47.8	N/A	9.2

A lower excitation energy, compared to the Mg anode source, of 800 eV leads to an enhanced surface sensitivity and an increased total area contribution of 17.8% from the surface components. The O1s spectrum (5.4b) is fitted with three components, similarly to lab spectra, broadly ascribed to the ether (C-O-C), alcohol (O-H), and ketone (C=O) components present, listed in order from highest to lowest binding energy, and largest to smallest area.

Figure 5.4c shows the same sample at room temperature and measured with a lower photon energy of 400 eV. The enhanced surface sensitivity shows an increase in the surface component area with respect to the main (C-C) bulk component, with the surface-based components now accounting for 37.7% of the total area. Furthermore, with the enhancement of surface components, and the complexity of oxygen species discussed previously, 4 components (shown in blue) are now required on the higher binding energy side of the main component. With the information in the fit residuals and computational modelling, it is probable even more components may be required to properly describe all bonding environments present on the surface, however reasonable limits on fit components must be set during analysis. An example of the complexity has been shown from the modelling of surface C-O-C chains where the binding energies of seemingly similar bonding structures are strongly dependant on chain length or chain termination. As well as the increase in oxygen components, changes in the relative intensities of these components reveal more information about what they are attributed too. The most notable example of this is the relative intensity change between the first higher binding energy component at 285.5 eV and the 3 components at even higher binding energies. It can be seen the adjacent component at 296.4 eV now has a higher intensity. This suggests

the 3 highest energy components are solely surface components, whereas the 285.5 eV peak may have some link to the bulk. This has been seen in previous studies of diamond surfaces where sub-surface bonding lead to a peak contribution at a slightly higher binding energy to the main C-C component [165].

The room temperature C1s core level is very similar to the laboratory experiment, however, the O1s core level, shown in Figure 5.4d shows an exaggerated O-H component at 531 eV, in comparison to the lab based spectra and a small new component around 534 eV. These differences are result of higher partial pressure of residual water vapour in the sample chamber condensing onto the surface, highlighting the impact of the measurement environment on surface sensitive techniques. The measurement environment is not as impactful at temperature due to the inability for water to condense on the hot sample surface. The photon energy for this room temperature O1s spectra was 800 eV as surface sensitivity has little effect on the O1s spectra as it is all signal from surface species regardless of photon energy. The graphs shown in Figure 5.4e and 5.4f show the oxygen terminated surface at room temperature but exposed to a 1 mbar H₂O atmosphere. Little effect is seen on the C1s showing the surface stability. However, the O1s now shows a further increase in 531 eV component, making the O-H signal the most prominent component. The new component at 534.2 eV is the gas phase water vapour signal. The water atmosphere distorts the O1s signal such that it is difficult to resolve some of the surface components, resulting in a broadening of the components.

5.1.2.2 PLASMA TREATED DIAMOND SURFACE

Following the acid etching and the subsequent heating cycles, the diamond was transferred into the *in-situ* plasma chamber, as described in chapter 4, therefore never leaving the UHV conditions and contaminating the surface. The sample was then exposed to a 100W nitric oxide (NO) microwave assisted plasma, for a total of 1 hour then transferred back into the analysis chamber where XPS, UPS and REES were taken between/during similar heating cycles.

Figure 5.5 shows XPS spectra, as well as the fit components and fit residuals, of the C1s (left) and O1s (right) core levels immediately after plasma treatment, after 300°C and after 700°C cycles. The fit parameters for the components shown are given in Table 5.7, along with the percentage for which each component contributions to the total area. As with the acid-etched surface, the atomic percentage of carbon to oxygen, as well as the monolayer coverage, were calculated using the total areas of the high resolution scans. These are shown for each stage below in Table 5.7.

As can be seen in Table 5.7, the atomic % and coverage is comparable to the same stages for the acid-etched diamond. Two main points can be discerned from the data; immediately after the plasma treatment the sample has the highest monolayer coverage recorded from all the samples so far, with just over a monolayer. The reduction to 0.85 monolayers after 300°C is unexpected, as oxygen termination should be stable up to around 400°C. Possible causes of this are; oxygen containing surface adsorbates, such as water, but with the reduction in work function seen in Table 5.9, it is hypothesised that unstable, longer-chained oxygen species (C-O_x-H) are being preferentially adsorbed/reduced in length and replaced with hydroxyl

groups. Long oxygen chains may also explain the initial monolayer coverage being greater than 1.

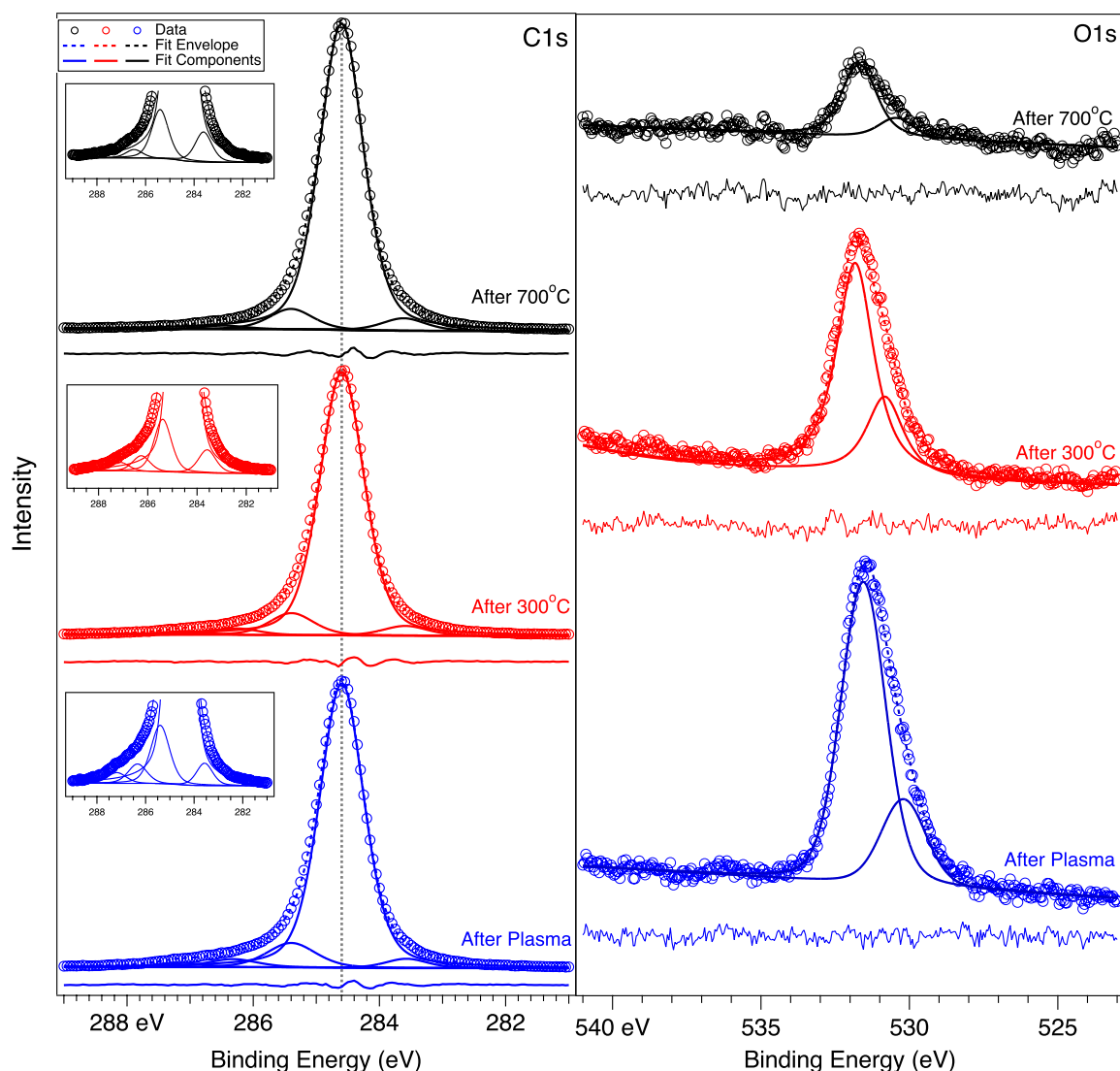


Figure 5.5: (left) A series of C1s XPS spectra of the plasma treated diamond immediately after treatment and following 300°C and 700°C anneals from bottom to top. (right) A series of O1s XPS spectra of the plasma treated diamond immediately after treatment and following 300°C and 700°C anneals from bottom to top. For details of the fit components, see Table 5.5. The fit residuals are shown below each spectrum.

Table 5.7: The atomic percentage of carbon and oxygen for the plasma treated diamond at various stages of the experiment. The monolayer coverage was also calculated for each stage.

Temperature (°C)	C1s(%)	O1s(%)	Θ_0
Room Temp	93.6	6.4	1.12
300	95.6	4.4	0.85
700	98.9	1.1	0.25

The high resolution C1s spectra in Figure 5.5 show a very similar trend to the acid-etch experiment. There are again 5 components, 3 to the left of the main bulk component (B) which are surface components, S1, S2, S3, from left to right, which again are associated with oxygen containing groups, and a fourth surface component (S4) at a slightly lower binding energy indicating the presence of sp^2 bonded carbon. The binding energies of all the C1s components are very close (within 0.2 eV) to those of the components on the acid-etched surface, however the percentage contribution of some of the oxygen containing components are significantly greater. Component S3, for example, contributes to between 7-8% of the total area, around 2% more than for the acid treated surface. This, along with the monolayer coverage results, suggests that although the oxygen coverage is similar, the functional groups are present in different amounts.

This can be corroborated by the O1s spectra. Unlike the acid-etched surface, which required 3 components, only 2 components are needed for a suitable fit. 3 peaks could be fit but did not improve the fitting criteria (Abbe's criterion/ χ -squared, see Appendix) enough to justify a third component. The two O1s components used at approximately 531.6 eV and 530.6 eV are ascribed to ether (C-O-C) and alcohol (O-H) groups, respectively. The lack of ketone groups indicates an improved surface quality as these groups are commonly associated with surface damage/roughness where there may be areas where ether bridges or alcohol groups will not 'fit'. A proposed surface consistent with this is one where ether groups form bridges and Pandey chains across the flat areas of the diamond surface and alcohol groups, or hydrogen fill in the step-edges.

Heating to 300°C shows the oxygen termination is still stable, although a slight decrease in intensity shows there would have been some surface adsorbates from the exposure to the plasma, although not a large amount. Throughout all the heating cycles up to 700°C the relative amount of oxygen species remained fairly consistent with a roughly 3:1 ether to alcohol ratio. After 700°C the O1s and C1s spectra resemble very closely the same stage from the acid-etch surface, therefore the diamond was not taken to 1000°C as it is known that the oxygen will be fully removed.

Table 5.8: The function parameters used to fit the data shown in Figure 5.6. The peaks are ordered by the position and sorted from highest to lowest binding energy (left to right on graph). The FWHM given is the width of the Voigt convolution and the widths of the Gaussian and Lorentzian peak required for the convolution are also given. Finally, the relative percentage of total area for each component is given.

Core Level	Temperature (°C)	Position (eV)	FWHM (eV)	Gaussian Width (eV)	Lorentzian Width (eV)	%
C1s	RT	287.2 (S1)	0.85	0.67	0.29	1.4
		286.5 (S2)				2.6
		285.4 (S3)				7.1
		284.6 (B)				85.9
		283.6 (S4)				2.9
O1s		531.5	1.82	1.61	0.34	78.8
		530.1				21.2
C1s	300	287.1 (S1)	0.82	0.69	0.24	1.1
		286.3 (S2)				2.1
		285.4 (S3)				7.7
		284.6 (B)				85.3
		283.6 (S4)				3.7
O1s		531.8	1.68	1.28	0.65	73.3
		530.8				26.7
C1s	700	286.4 (S1)	0.82	0.63	0.32	1.1
		285.4 (S2)				6.3
		284.6 (B)				88.6
		283.6 (S3)				4.0
O1s		531.7	1.47	1.40	0.11	76.8
		530.6				23.2

UPS was again used to probe the valence band electrons of the surface after plasma treatment. Figure 5.6(a) UPS taken immediately after plasma treatment, after 300°C and after 700°C. Also shown in Figure 5.6(b) is a comparison of the acid-etch surface and the plasma treated surface UPS spectra. As with the acid-etch data, the VBM and the secondary cut-off energies were used to calculate the surface work function and electron affinity using equations 5.3 and 5.4, shown in Table 5.9.

The widescans in Figure 5.6 show again a clear evolution of the surface from an oxygen termination, with a very prominent feature at around 3 eV binding energy following the plasma, to a partially hydrogen terminated surface showing a large secondary tail. The spectra have been normalised for clarity, but the secondary electron edge approximately doubled in intensity here. Comparing the widescans of the acid and plasma treatments, it is again seen that the oxygen coverage appears greater due to the definition of the 3 eV feature, which is mainly due to the O2p signal.

The electron affinity for the plasma treated surface was calculated to be 2.42 eV, which is the highest reported electron affinity for an oxygen terminated surface. With a 300°C degas this did reduce to 2.02 eV, but still remains a high positive electron affinity at 0.78 eV higher than the acid-etched surface after a similar degas. After 700°C the electron affinity of 0.36 eV is again very similar to the previous surface properties so after high temperature treatments the resultant surface is independent of the initial surface.

The improved surface quality and the high electron affinity are important factors when considering use for quantum technologies. A high ordering to the surface structure and the lack of defects or damage reduces the number of surface

spin states which can interact with the NV centre and reduces the noise on signals produced. A high electron affinity will reduce the charge transfer to the surface and lead to an increase in NV⁻ stability which again is ideal for quantum applications.

The oxygen desorption (and band bending, see section 5.2) was studied further during the heating cycles using REES.

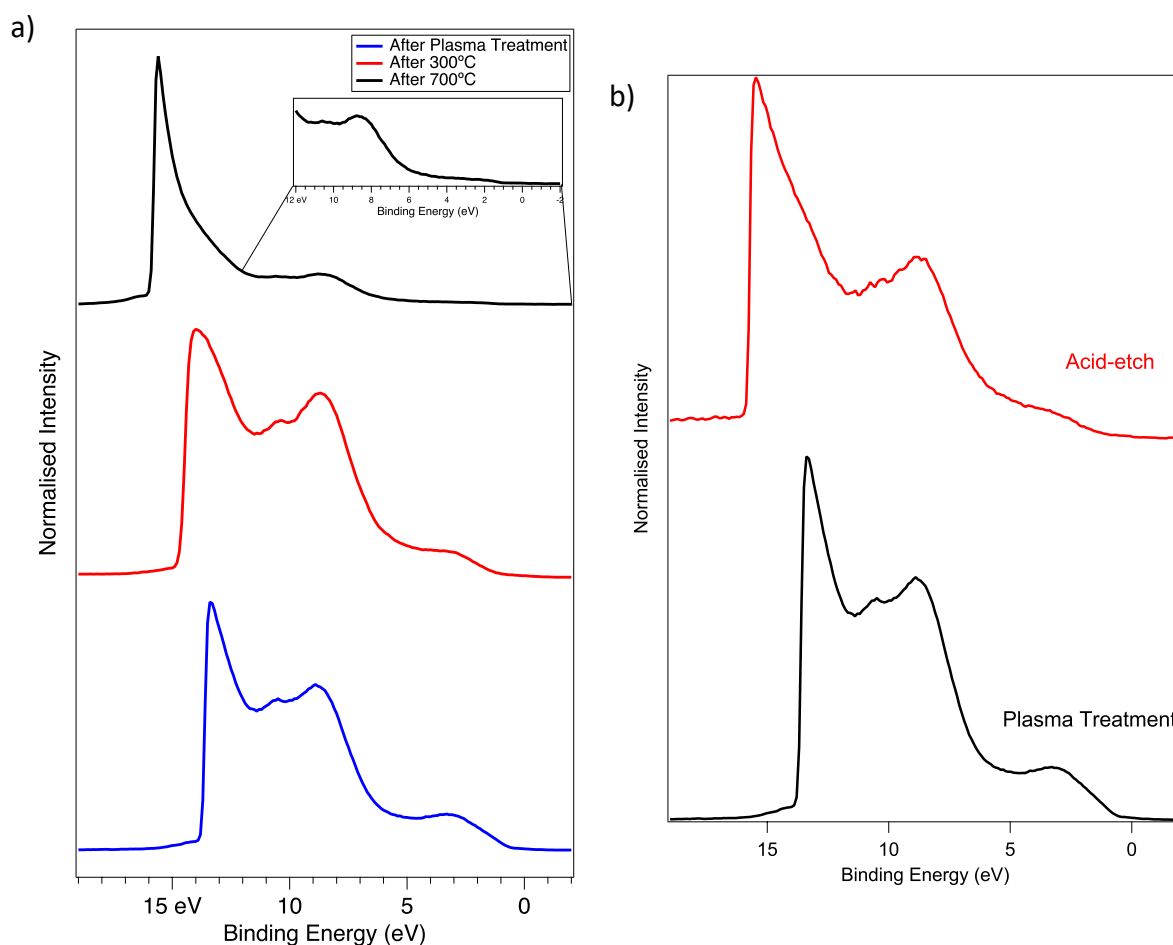


Figure 5.6: a) A series of UPS spectra taken of the plasma treated diamond surface immediately after treatment and after 300°C and 700°C from bottom to top. b) The UPS spectra for the acid-etched and the plasma treated surfaces clearly showing the large change in the secondary cut-off energy.

Table 5.9: The secondary cut-off, Valence Band Maximum (VBM) and electron affinity of the plasma treated diamond after different temperatures cycles.

Temperature (°C)	Secondary Cut-Off (eV)	VBM (eV)	Electron Affinity (eV)
RT	14.5	1.22	2.42
300	14.9	1.22	2.02
700	15.9	0.56	0.36

As described in chapter 2, REES scans involve taking multiple, snapshots in order to gain time-resolved XPS. The detector was set to 500x1 channel in order to obtain 500 data points simultaneously with a reasonable energy separation (dependant on the pass energy). In this work, C1s and O1s regions were measured each cycle, with a pass energy of 60 eV, a 2 second dwell time, and a pixel-energy ratio of 0.0168686 eV/pixel. REES data were analysed using the MCS software described in chapter 3. Both Voigt and pseudo-Voigt profiles were propagated through the large datasets, depending on the required information, and the computational difficulty.

Figure 5.7 shows the O1s areas calculated from the 300°C cycles for the acid-etch (left) and the plasma treated (right) surfaces. The arrows indicate which data points are during heating, and which are during cooling. Displayed on both graphs are the raw data (circles) and data smoothed using a boxcar smoothing method, with a box size of 20. Smoothing REES data provides much clearer trends and dramatically reduces noise, whilst keeping the time resolution.

Both datasets shown in the Figure 5.7 confirm that the oxygen species on the surface are stable up to 300°C. We can, however, see slight differences on the two surfaces. As expected, the acid-etch surface O1s signal decreases by about 10% as surface adsorbates from exposure to the atmosphere before loading into the vacuum chamber are removed from the surface. However, the O1s signal on the plasma treated surface remains fairly constant. The slight increase might also indicate a much smaller number of adsorbates on the surface, which when removed, expose the ordered surface, which generally are more sensitive to photo-ionisation.

Figure 5.8 shows REES datasets taken from the 600°C anneal of both the acid-etched (top) and plasma treated (bottom) surfaces. The temperature ramp and the O1s area are plotted together against both time and the iteration (or cycle) of the REES loop. Region 1 marked on both plots indicates the time of the ramp where the temperature increased from 500-600°C and Region 2 indicates the time held at 600°C. The ramp profiles vary because of testing of the SPECS snapshot mode during this experiment and with the development of automated current-ramping software.

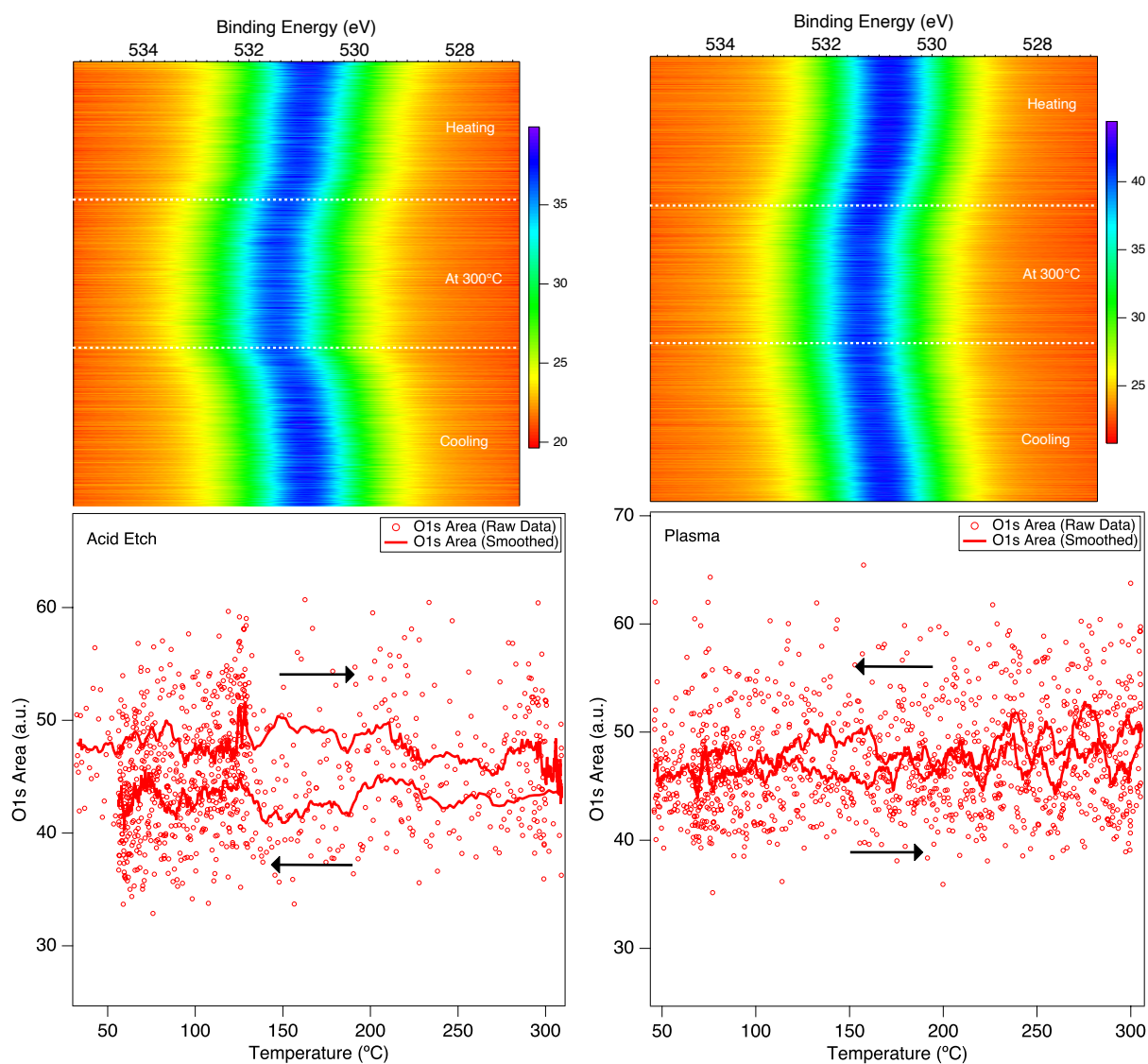


Figure 5.7: (left) O1s area calculated from a REES dataset, shown above it, during a 300°C temperature cycle on the acid-etched diamond surface. (right) O1s area calculated from the REES dataset, also shown above it, during a 300°C temperature cycle on the plasma treated diamond surface.

As shown in the high resolution spectra, there is a clear desorption of oxygen during heating to 600°C on both surfaces. However, there are noticeable differences in the desorption regimes. Most notably are the desorption rates marked by 1 and 2 in both graphs. The acid-etched surface has a higher desorption rate between 500 and 600°C, even with a lower starting signal, than the plasma treated surface. As well as this, as the acid-etched sample reached approximately 600°C a sharp, distinct change in the desorption rate was seen. Similar behaviour has been noted before in previous work on acid-etched samples. The change in rate is hypothesised to be sub-surface 'damage', caused by the strong acid treatment annealing out at the higher temperature [166]. This restructuring causes the overall surface energy to reduce and stabilise, reducing the rate at which carbon-oxygen bonds break. Sub-surface in this case is of the order of multiple atomic layers from the diamond surface. With the plasma treated surface, this shift in desorption is not seen, the typical exponential decay in desorption rate is present. This shows the plasma is much gentler surface treatment, using only a 100 W plasma on a room temperature sample. Another notable feature is the clear increase in O1s intensity on the plasma-treated surface between ~200°C and 400°C (30mins-90mins). This may be again due to non-oxygen containing adsorbates from the plasma treatment being removed and exposing the underlying surface, increasing the overall O1s intensity.

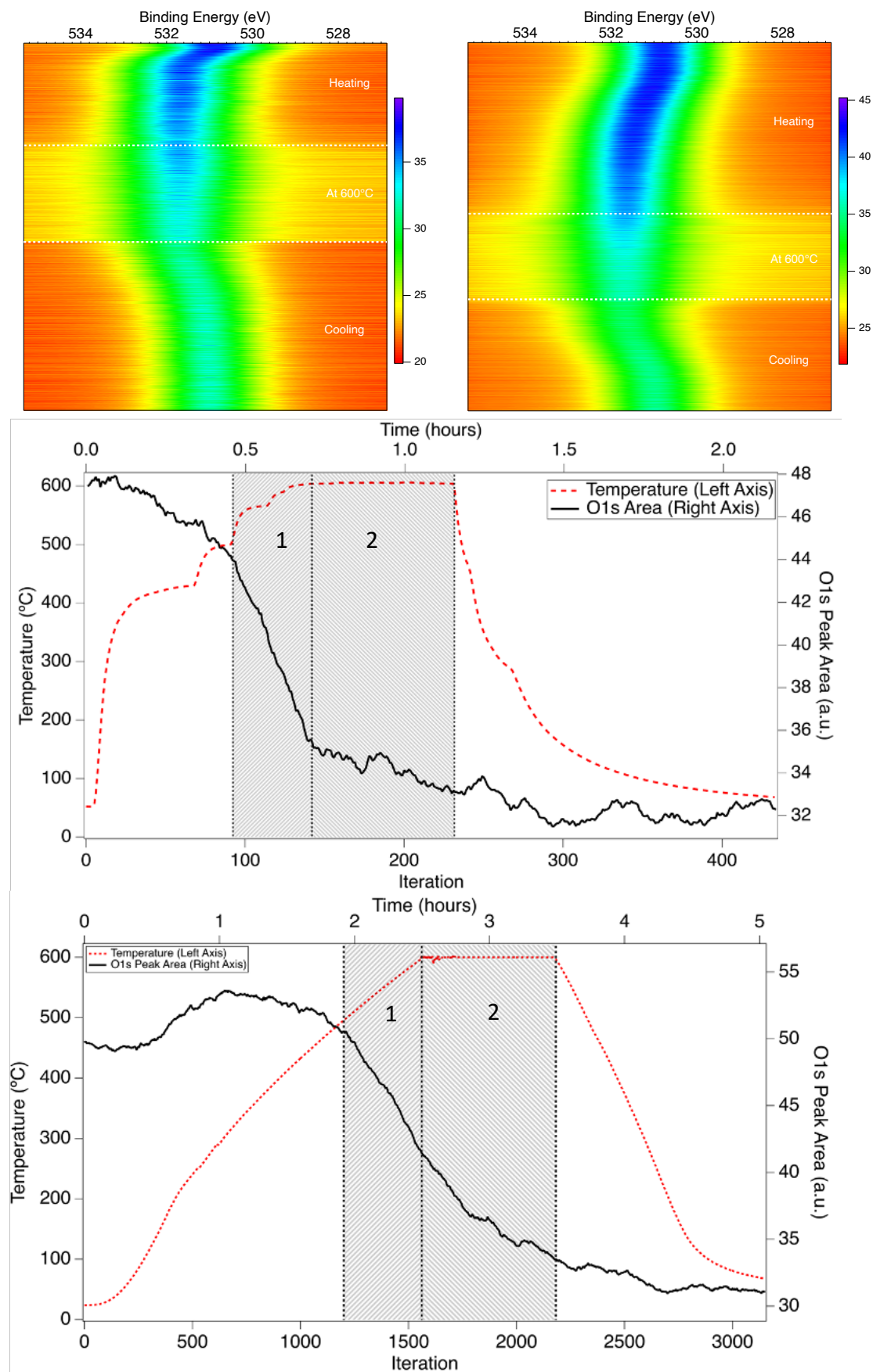


Figure 5.8: (top, left) The raw REES data from the acid-etched surface. (top, right) The raw data from the plasma treated surface. (middle) and (bottom) show the extracted O1s area from the Acid etched and plasma treated surfaces, respectively, with sample temperature (dashed-red line) on the left axes, and the O1s peak area (solid black line) on the right axes. Two regions are marked on each graph. Region 1 corresponds to the time in the experiment where the temperature is between 500-600°C and region 2 shows the time held at 600°C.

5.2 BAND DIAGRAMS AND SURFACE PHOTOVOLTAGE

With the XPS and UPS measurements presented in the previous sections some of the electronic properties of the oxygen terminated surface were studied. However, for the interpretation of certain electronic properties the band bending and surface photovoltage must be considered.

The effect of the surface photovoltage can be seen in the REES datasets given in Figure 5.7 and 5.8. The shift in binding energy of the C1s and O1s is due to a change in the surface photovoltage with temperature. This can be verified by the reversible nature of the shift, while the correspondence of the shift on both core levels suggests it must be an electronic effect, rather than a chemical effect. Furthermore, the apparent increase in binding energy with temperature, and the fact this is a p-type semiconductor, confirms it must be a surface photovoltage, rather than a traditional charging effect, which would always positively charge the surface and lead to a decrease in the measured binding energy.

Surface photovoltage is a charging effect found in semiconductors. It is brought about by the creation of electron-hole pairs in the depletion region. These are caused by radiation of sufficient energy, which leads to an accumulation of charge carriers at the sample's surface and a reduction or flattening of the surface band-bending and apparent changes in the measured binding energies. The charge carriers which accumulate at the surface are dependent on the doping of the semiconductor. In the case of boron doped diamond used in this work, as it is a p-type semiconductor, electrons are accumulated at the surface which leads to an apparent increase in the

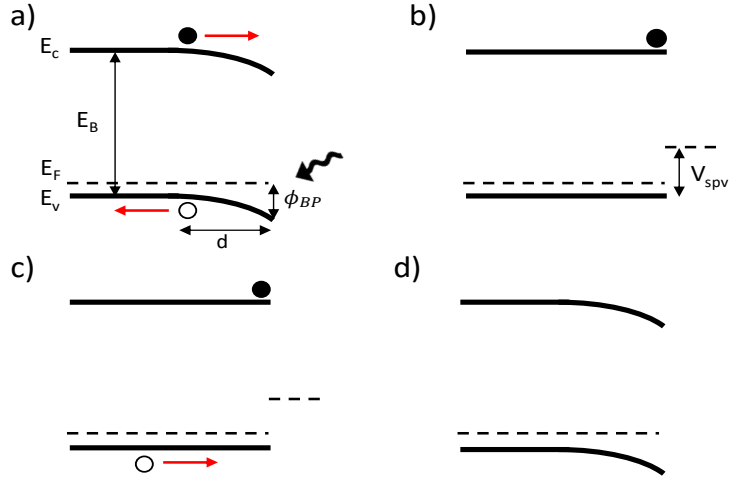


Figure 5.9: a) The band diagram of a p-type semiconductor the instant it has been exposed to excitation photons greater than the bandgap energy. b) The flattening of the bands and the generation of a surface photovoltage. c) The movement of holes toward the surface with thermal energy sufficient to overcome the potential barrier at the surface. d) The removal of the surface photovoltage and resultant downward band bending.

reported binding energies. The inverse is the case for n-type semiconductors with holes accumulating at the surface, reducing the measured binding energy. Originally modelled by Hecht [167] to explain differences in measured metal barrier heights, surface photovoltage has been measured in a number of semiconducting materials [53].

Figure 5.9a to d illustrates the 4 steps involved in surface photovoltage generation and removal with temperature. 5.9a shows the band diagram at equilibrium at room temperature, conduction band minimum (E_c), band gap (E_B), Fermi level (E_F), Valence band maximum (E_v), depletion width (d) and surface barrier potential ϕ_{BP} are all labelled. Once exposed to photons of sufficient energy (depicted by the black wavy arrow) the electron-hole pairs are generated and electrons move to the surface, and holes move to the bulk (shown by red arrows). This leads to the situation in diagram 5.9b, with the electrons sitting at the surface, flattening of the conduction and valence bands and a surface photovoltage generated (V_{spv}). This surface photovoltage is sustained provided that the thermal energy of the holes cannot overcome the generated voltage. Relatively low temperatures are usually

required to overcome this voltage and remove the surface photovoltage, leading to the band structure shown in 5.9d. However, it is sustained at room temperature in wide band-gap materials with high bulk resistances, including diamond, where this has been seen in (111) diamond with similar boron doping concentrations to the (001) sample used in this work already [16]. However, the magnitude of the sustained photovoltage is decreased as temperature is increased and this can be modelled.

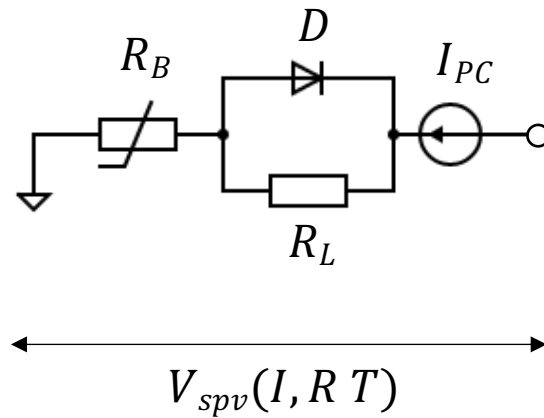


Figure 5.10: The model circuit used in the surface photovoltage model.

The described system can be modelled using the simple circuit diagram shown in Figure 5.10. Each component in the circuit diagram can be associated to some property in the physical system. A temperature dependant series resistance (R_B) models the sample's bulk, where bands are flat, and conduction should behave in an Ohmic fashion. The diamond bulk is 'connected' to the depletion width generated at the diamond-surface which is modelled by connecting the bulk resistance in series with a diode resistance (D), which is also temperature dependant. In this system the diode is a p-type Schottky diode. The opposing side of the diamond is in contact with the tantalum faceplate when mounted, thereby connecting it to ground. A current generator is added as the internally generated photocurrent (I_{PC}). The final

component is a leakage resistor (R_L) shown parallel to the diode in the Figure 5.10. Leakage current arises from electron tunnelling, electrons traps and defects or simply through conduction at the surface near the tantalum mount clips which lead to ground.

The internally generated photocurrent is proportional to the number of electron-hole pairs generated in the sample. The number of electron-hole pairs generated (N) can be estimated from the number of photons incident on the sample (Photon flux, Φ), the irradiated area, (A) and the quantum efficiency (η) by the equation

$$N = \eta \Phi_0 A$$

Equation 5.6

And the generated current in the irradiated area would be given by

$$I = qN = q\eta\Phi A$$

Equation 5.7

where q is the elementary charge, 1.6×10^{-19} C. However, further electron hole pairs are generated as the X-rays penetrate through the crystal structure. Therefore, the irradiated volume, as well as the change in photon flux due to X-ray absorption must be taken into consideration. From Beer-Lambert's law it can be stated that the photon flux Φ_{λ_x} at a depth equal to the X-ray's MFP λ_x is equivalent to

$$\Phi_{\lambda_x} = \Phi_0(e^{-1}) \approx 0.368 \Phi_0$$

Equation 5.8

where Φ_0 is the photon flux at the surface. By approximating the change in flux over any given depth x to be linear, a formula for the photon flux Φ_x can be derived such that

$$\Phi_x = \Phi_0 \left(1 - \frac{0.632}{\lambda_x}\right)x$$

Equation 5.9

Substituting Φ_x into equation. 5.7 and calculating the difference in current generated at the surface, I_0 and at a depth x , I_x the generated photocurrent between the surface and the given depth, $I_{pc}(x)$ can be calculated by

$$I_{pc}(x) = q\Delta N = I_0 - I_x = q\eta\Phi_0 A \frac{0.632}{\lambda_x} x$$

Equation 5.10

An important quantity to calculate from this is photocurrent generated in the depletion width d of the diamond sample.

$$I_d = \frac{0.63q\eta\Phi A}{\lambda_x} d = \frac{0.63q\eta\Phi A}{\lambda_x} \left(\frac{2\varepsilon_0\varepsilon_r(V_0)}{qp}\right)^{\frac{1}{2}}$$

Equation 5.11

where

$$d = \left(\frac{2\varepsilon_0\varepsilon_r(V_0)}{qp}\right)^{\frac{1}{2}}$$

Equation 5.12

ε_0 and ε_r are the permittivity of free space and relative permittivity, respectively, V_0 is the interface barrier height and p is the hole concentration. Note, this equation for the depletion width with zero current and zero applied voltage. For the (001) B-doped diamond used in this work, typical values for the depletion width are around 4.3 μm at room temperature, using a value of 1.5 V for the surface barrier height and a boron concentration of $5 \times 10^{21} \text{ m}^{-3}$, which is of the order of magnitude of the X-ray attenuation length in diamond. By equilibrating the depletion width and the X-ray

attenuation length, leading to a value of 1 for $\frac{x}{\lambda_x}$ in equation 5.11, the photocurrent generated in the depletion width can be estimated to be

$$I_{\text{pcd}} \simeq 2.3 \times 10^{-6} \text{ A}$$

Using values of 250 for η , which can be approximated by the ratio of the photon energy and bandgap $\frac{h\nu}{E_B}$, a typical photon flux for a laboratory X-ray source of 10^9 photons $\text{s}^{-1}\text{mm}^{-2}$ and a sample area of 100 mm^2 . This photocurrent is a number of orders of magnitude greater than the photoelectron current which would lead to typical charging effects and a positively charged surface. The photoelectron current I_{pe} can be estimated by the equation:

$$I_{\text{pe}} = q\eta\Phi A \frac{\lambda_e}{\lambda_x} \simeq 2 \times 10^{-9} \text{ A}$$

Equation 5.13

using a typical value of 1.5 nm for the electron MFP λ_e and a value of λ_x equal to the depletion region value (as estimated previously) as well as previously used typical values for η and Φ .

The next thing to consider is the bulk resistance's dependence on temperature. At room temperature the number of acceptors in the diamond lattice is low due to the high ionisation/activation energy E_A of boron dopants, relative to the thermal energy provided at room temperature (kT). However, by considering a p-type semiconductor to be analogous to an intrinsic semiconductor of band-gap E_A and where $E_A \gg kT$ the hole concentration can be calculated by [168]

$$p(T) = \frac{1}{4} \sqrt{N_V N_A} e^{-\frac{E_A}{2kT}}$$

Equation 5.14

where, N_V and N_A are in initial and final density of states, respectively, and kT is the Boltzmann's constant multiplied by the temperature. The low acceptor concentration leads to a high bulk resistance which as mentioned, ensures the charge is maintained at the surface by restricting charge flowing through the sample which would neutralise it. Previous work on surface photovoltage on (111) diamond at Aberystwyth University has determined a model equation for the bulk resistance on diamond in a sample with a similar dopant density. The resistance follows an Arrhenius style law in the form of

$$R_B = R_\infty e^{-\frac{E_A}{kT}} = 50 \times e^{-\frac{2087}{T}}$$

Equation 5.15

The value of 50 given for R_∞ is based on a model fitted to an experimentally measured bulk resistance. The value 2087 is equivalent to $\frac{E_A}{2k}$ assuming an acceptor activation energy of 0.38 eV. Importantly, the current in the above resistor I_R can now be calculated by

$$I_R = \frac{V}{R_\infty} e^{-\frac{E_A}{kT}} = \frac{V}{500} \times e^{-\frac{2087}{T}}$$

Equation 5.16

Furthermore, the generated photocurrent shown in equation 5.11 is temperature dependant due to the temperature dependence of the depletion width (equation 5.12), which is turn is dependent on the hole concentration (equation 5.14). Substitution of equation 5.14 into 5.12 and further substitution of 5.12 into 5.11 gives the full equation for the photocurrent generated in this system which is

$$I_{\text{xray}} \simeq \frac{0.63q\eta\Phi A}{\lambda} \left(\frac{8\epsilon_0\epsilon_r(V_0 - V_{\text{spv}})}{q\sqrt{N_V N_B} e^{-\frac{E_A}{kT}}} \right)^{\frac{1}{2}}$$

Equation 5.17

here, V_0 is the barrier height, approximated throughout this work to be 1.7 V and V_S is the surface photovoltage. In this form, although complex, all values are known constants or can be given approximate values, with the only two values to be varied in the model, the applied voltage, and the temperature. In order to avoid complex 3D data sets which formed a photocurrent surface (z-axis) dependant on voltage and temperature (x and y axis) this current was calculated for a range of voltages for a given temperature, plots of which will be shown later.

With a photocurrent model and a potential bulk resistance model, the final component to consider is diode resistance and current. The current here can be calculated using a variation on the ideal diode equation which accounts for the barrier height, as well as considering the Schottky effect brought about by the photoemission from the irradiated area. The equation for the diode current I_D is as follows

$$I_D = \underbrace{AA_R T^2 e^{-\frac{qV_0}{kT}}}_{\text{Saturation Current}} \left(e^{\frac{qV}{kT}} - 1 \right)$$

Equation 5.18

where A is the irradiated area, A_R is the relative Richardson constant, V_0 is the barrier height and V is the applied voltage. The thermionic emission current can be considered equivalent to the saturation current for an ideal diode. A leakage resistance is added to the model however, this is modelled using a simple Ohmic relationship. A typical leakage resistance value, and the value used in this model, is approximately 500 M Ω .

With equations determined for all components the model can be completed. The aim of the model is to generate the I - V characteristics of the model circuit, this

can be pictured as the current which would flow from the left to the right hand side of the circuit given in Figure 5.10. Simultaneously, the voltage dependence of the photocurrent generated, *i.e.* the current source shown in Figure 5.10, is also generated. This can be considered as the current flowing from right to left on the diagram. It can then be determined where these I - V curves intersect, is the surface photovoltage required to balance the currents and maintain the charging effect on the surface. To calculate the current in the model circuit a number of steps were taken. Firstly, the total current over the diode and leakage resistor was calculated by equation 5.18 for the diode and by Ohm's law for the leakage resistor, using the saturation current and the leakage resistance value given. From this, the voltage drop over the bulk resistance was calculated using equation 5.16. The voltage across the diode, leakage resistor and series resistance were calculated from the sum of the voltage drops over the series resistor and the 'z voltage'. This sum equals the surface photovoltage and can then be plotted against the diode current. For the I - V characteristics of the photocurrent, equation 5.17 is required only. These curves were generated for five temperatures between 300 and 600 K (approx. room temperature to 300°C) which is the temperature range in the heating cycle which shows a completely reversible binding shift in REES datasets, shown in Figure 5.7. The intersect voltage between the photocurrent and the diode circuit current is then determined for each temperature stages and this is the photovoltage generated at that given temperature.

Once the methodology was proven, the next step was to automate the process for a range of temperatures. In collaboration with Dr Tom Knight (Aberystwyth University), a python script was constructed which iteratively finds the

surface photovoltage associated with the intersection point of the two current curves for a range of given temperatures. The code utilises a bisection root finding procedure which calculates the voltage where $\Delta I_T = 0$. ΔI_T is the difference between the model circuit current and the X-ray photocurrent at a given temperature. The model is now a minimisation of equation 5.18. This is the ΔI_T as a function of the applied voltage across the diode, V . The surface photovoltage is still calculated by the sum of the series voltage and the applied voltage, given in equation 5.19. As these functions are a set of parametric equations the solution for V_{spv} can be found.

$$\begin{aligned} \Delta I_T(V) &= AA_R T^2 e^{-\frac{qV_0}{kT}} \left(e^{\frac{qV}{kT}} - 1 \right) - \frac{V}{R_L} \\ &\quad - \frac{0.63q\eta\Phi A}{\lambda} \sqrt{\left(\frac{8\varepsilon_0\varepsilon_r}{q\sqrt{N_V N_B} e^{-\frac{E_A}{kT}}} \right) \left(AA_R T^2 e^{-\frac{qV_0}{kT}} \left(e^{\frac{qV}{kT}} - 1 \right) R_s - \left(\frac{R_s}{R_L} + 1 \right) V \right)} \end{aligned}$$

Equation 5.19

$$V_{\text{spv}}(V) = V_s + V$$

Equation 5.20

In addition to solving the aforementioned equations, the software can also render the I - V curves for each temperature and stitch these together into a 'current surface' for the photocurrent and the circuit current, plotted against SPV and temperature. The surface photovoltage as a function of temperature is now the x, y values associated with the intersection of these two surfaces. A 3D render of these surfaces is shown in 5.11. With the diode current shown in blue and photocurrent shown in red. The black line is the intersection function, which is SPV vs temperature.

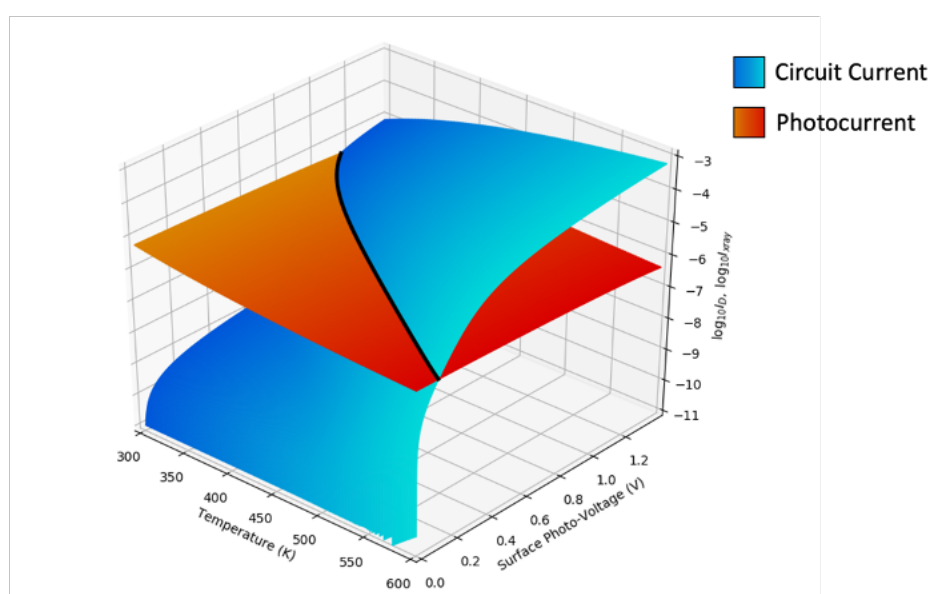


Figure 5.11: A rendering of the photocurrent and model circuit current surfaces, shown by the red and blue surfaces, respectively. The slight gradient in colour on both surfaces represents the change in temperature. The black line represents the intersection function which is the SPV vs T plot given in Figure 5.12f.

Figure 5.12 a-e show the resultant I - V curves for the model circuit (blue lines) and the generated photocurrent (red lines) for some example temperatures modelled. The dashed grey lines show the intersect voltages for each temperature also. These intersect values were then plotted against temperature, overlayed onto the C1s binding energy shift during a REES cycle shown in Figure 5.12f. As before, the peak position was extracted from a REES fit propagation. The surface photovoltage is

shifted to align to the C1s core level, however the voltage/binding energy scales are matched to each other.

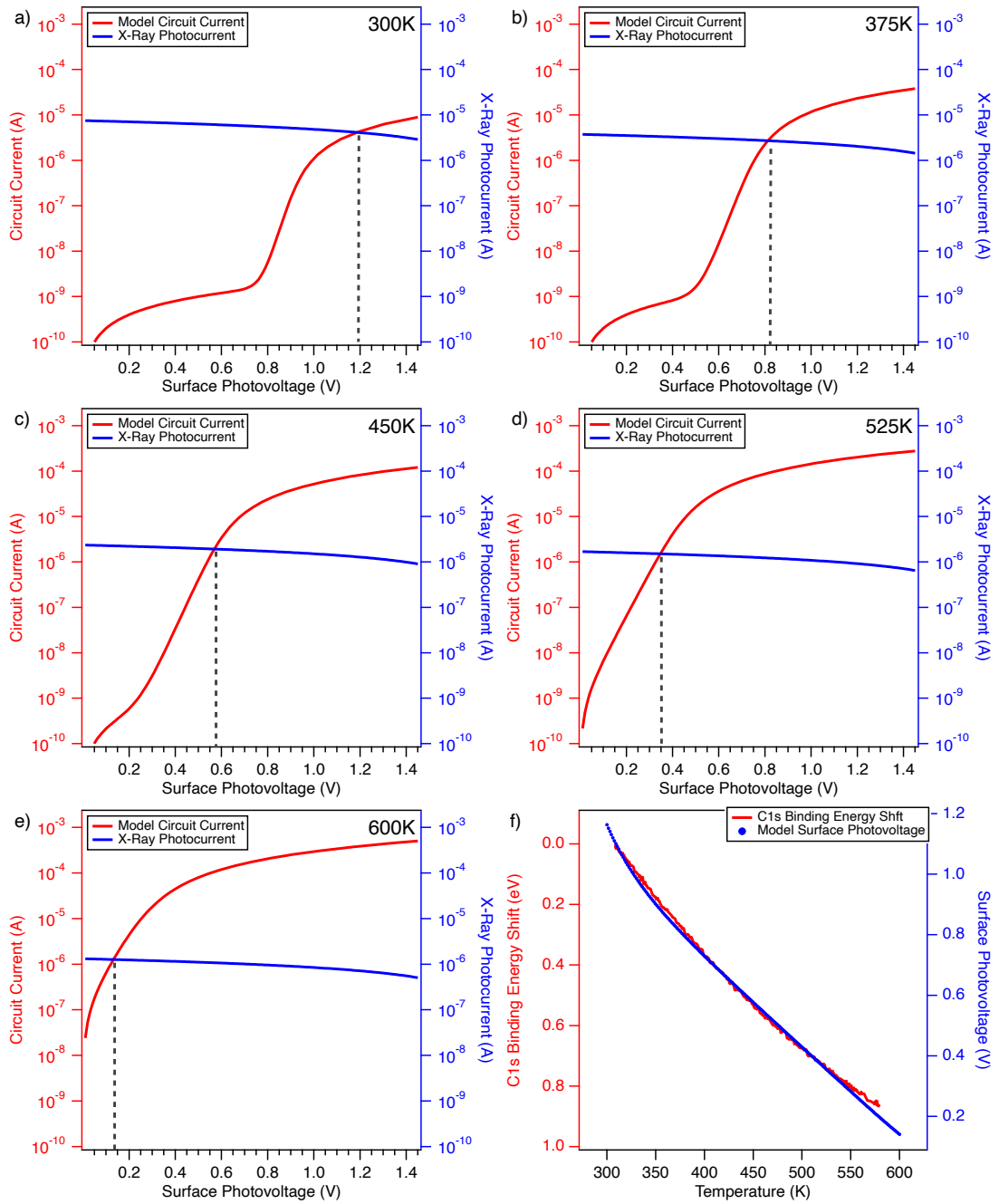


Figure 5.12: (a-e) are generated I - V curves for the photocurrent (blue lines), and the model circuit (red lines) at varying temperatures between 300 and 600 K, in 75 K steps. The dashed grey lines mark the intersection point of these curves. (f) is a plot of the intersection values against temperature (blue) overlaid on the C1s binding energy shift measured by REES during a 600 K (300°C) temperature cycle (red).

It is clear to see a significant correlation between the model surface photovoltage and the C1s binding energy. Even with a number of assumptions and

estimations made, the calculated photovoltages are within the error on the C1s binding energy measurement, considering the energy resolution for REES measurements are of the order of $\sim 1 - 1.5$ eV.

The correlation between the model and the binding energy shift indicates the importance of considering photovoltage charging effects when interpreting core level binding energies measured through photoelectron spectroscopy, especially in wide-band-gap semi-conductors, such as diamond. Frequently, when core levels of boron doped diamond are analysed, the doping is assumed to nullify charges effects. This is shown by the lack of runaway charging which can occur when measuring insulators/high band gap semiconductors using XPS. A common solution to nullify this charging effect is to use an electron flood gun, which emits relatively low energy electrons towards the sample which in essence acts as a grounding of the sample. However, it is shown here that even with boron dopants present, because the magnitude of the activation energy of the acceptor is much greater than the thermal energy provided at room temperature $k_B T$ as well as the low acceptor concentration, charging effects are still present. This is further shown by the at-temperature core level measurement in Figure 5.4a where the C-C component is at a binding energy of 285.19 eV, which is the true C1s binding energy value quoted in literature from surface photovoltage measurements on the (111) diamond [16].

With the consideration of the photovoltage, the core level scans, the UPS measurements shown, as well as the flat band C1s core level energy of 283.9 eV [16], the band diagrams for the acid etched diamond and plasma treated diamond can be determined. The band diagram for the acid etched and plasma treated diamond surfaces will be similar in nature, however the work function and surface band-

bending will be the main differences. For both cases a diamond bandgap of 5.5 eV is given and the Fermi level, which is approximately midway between the VBM and the boron acceptor level, is located at 0.18 eV above the diamond valence band maximum. The surface band-bending in each case can now be calculated by taking into account the difference between the Fermi level and the valence band maximum (measured by UPS), as well as accounting for the surface photovoltage present at the measurement temperature. The position of the VBM was measured at 1.18 eV and 1.22 eV for the acid etched and plasma treated surfaces, respectively. With a bulk Fermi level of 0.18 eV above the VBM, the surface band bending for the acid etched and plasma treated surface can be calculated to be 0.82 eV and 0.86 eV, respectively. With the work functions of both surface also known (1.28 eV for the acid etched, 2.42 eV for the plasma treated), the band diagrams can be drawn. These are shown in Figure 5.13, for the acid etched and plasma treated surfaces at room temperature (~ 300 K).

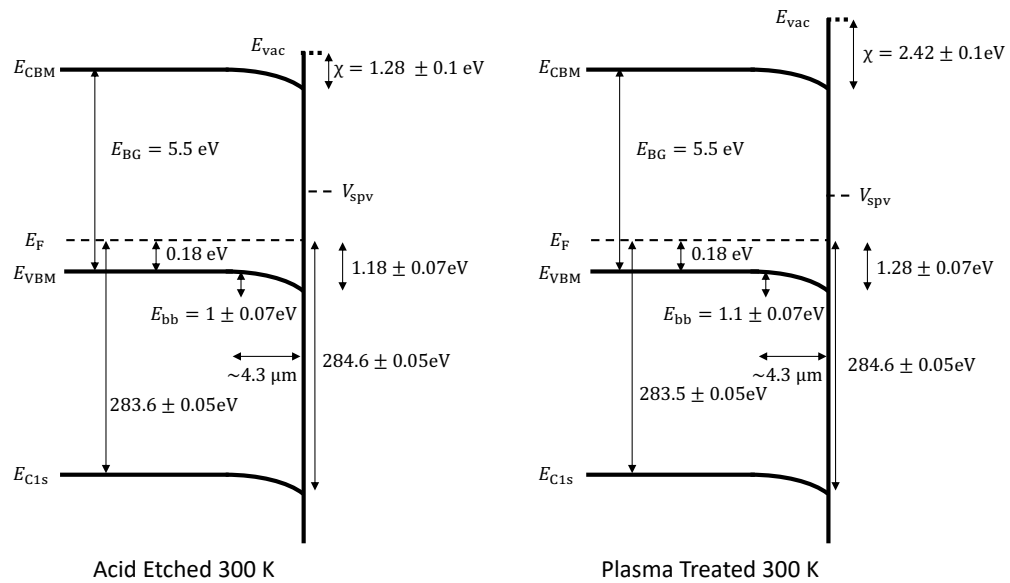


Figure 5.13: The band diagrams for the acid etched (left) and plasma treated (right) diamond surfaces at room temperature. From the model, a surface photovoltage V_{spv} of approximately 1.2 V is maintained at this temperature and is indicated on the band diagram. Errors are presented next to the given values. All values without error are quoted from literature or approximations.

Working from the top of the band diagram downwards, the values shown are E_{vac} , which is the vacuum energy. By definition this is the conduction band minimum E_{CBM} plus the electron affinity χ . E_{BG} is the bandgap, which is the difference between E_{CBM} and the valence band maximum E_{VBM} . The Fermi level is denoted by E_{F} . This is 0.18 eV above the E_{VBM} in the 'bulk' section of the diagram. The difference between E_{F} and E_{VBM} is shown by the small horizontal arrow near the diamond surface. E_{bb} is the band-bending, and corresponds to the difference between the energy separation of the Fermi level and the VBM, in the bulk and at the surface. The horizontal arrows represent the depletion width over which the band bending occurs. The values are calculated using equations 5.12 and 5.14. Two vertical arrows join the Fermi level E_{F} and the carbon 1s core level E_{C1s} . The surface energy is the measured value for the C-C bulk component taken from tables 5.3 and 5.8 for the acid and plasma treated surfaces, respectively. The bulk energy is this value minus the band bending energy. Although two values are given for the 'bulk' C1s binding energy, the difference in the values are fairly negligible due to the resolution of photoemission measurements. Not shown are the work function and ionisation energies of both samples. The work function is calculated as the difference between E_{vac} and E_{F} , whereas the ionisation energy is the difference between E_{vac} and E_{VBM} . For the acid etched surface, a work function of 5.42 eV and an ionisation energy of 6.78 eV is shown. For the plasma treated surface, due to higher electron affinity but similar band bending, a work function of 6.52 eV and an ionisation energy of 7.92 eV are exhibited.

As discussed however, there is still a significant photovoltage present at 300 K which will be suppressing the band bending. From the at temperature core level and

REES measurements, and the photovoltage model, between 300 K and 600 K the surface photovoltage is reduced by values of around 1 V. A band diagram for the diamond at 600 K is shown in Figure 5.14 which shows the true band bending of the diamond surface with values close to 2 eV for both surfaces. The depletion width at this temperature has also decreased from 4.3 μm to 0.76 μm , which is labelled but not shown to scale for clarity, indicating the difference in band bending severity in both cases.

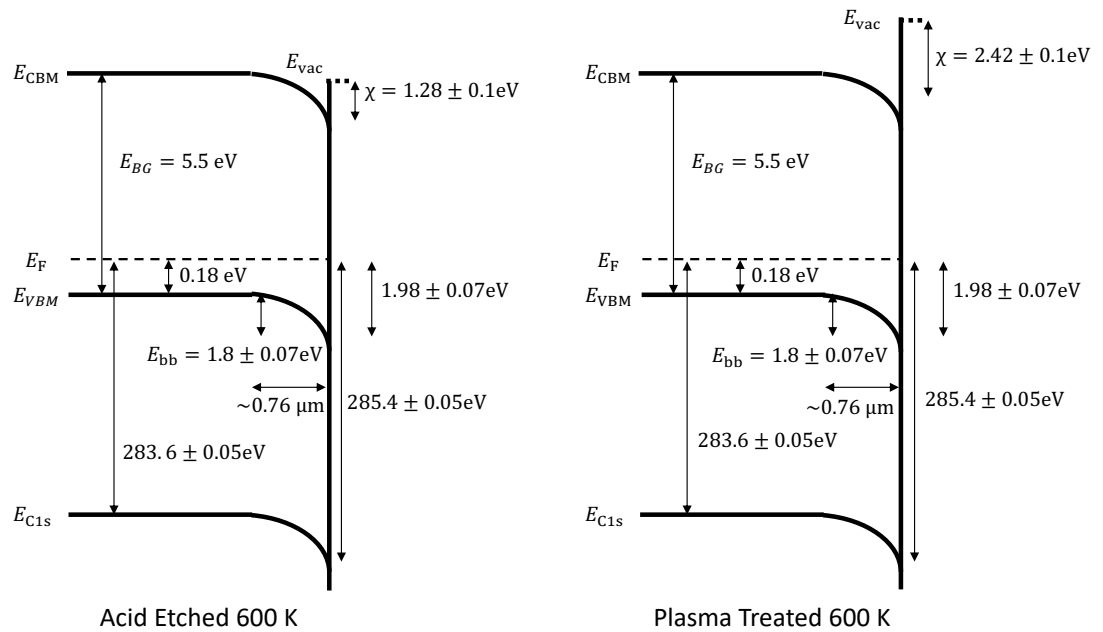


Figure 5.14: The band diagrams for the acid etched (left) and plasma treated (right) diamond surfaces at 600 K (300°C) after the removal of 1V of the sustained surface photovoltage. Errors are presented next to the given values. All values without error are quoted from literature or approximations.

5.3 FURTHER WORK

With the photovoltage model automated, it could be used to model photovoltages for other samples/conditions as values for sample or measurement dependant variables, such as X-ray flux, boron concentration and temperature can be varied easily.

More high resolution UPS and XPS measurements at low temperatures could be beneficial to determining the flat band diagram for the diamond sample. This could be possible in the OptiXS system with the low temperature stage. High temperature core level spectra could also provide further insight into the photovoltage effect. High temperature XPS is usually only measured during REES experiments and high resolution measurements are performed at room temperature in order to 'freeze' the sample in its current state during the considerably longer acquisition time. However, UPS spectra could be acquired very rapidly at a range of temperatures and could help verify the band structure changes at these temperatures. With modern day analysers, fast, high resolution core levels could be taken in a timeframe comparable to the time significant structural and chemical changes occur at the surface.

In-situ surface conductivity measurements of the oxygen terminated surface during measurement could measure the produced photocurrent and surface photovoltages experimentally to further verify the XPS measurement and the validity of the photovoltage model.

Experiments to test the reproducibility of the plasma surface shown in this chapter would be beneficial. Although the plasma treatment can produce a high quality oxygen terminated surface repeatedly, the overall coverage and electronic properties have varied with each treatment, in terms of working pressure and exposure time. Testing the effect of plasma conditions on the surface quality would help explain this.

Low Energy Electron Diffraction (LEED) measurement would provide further insight into the highly ordered nature of the plasma surface.

Chapter 6 – NITROGEN IMPLANTATION IN DIAMOND

As discussed in chapter 4, the creation and charge conversion of NV centres in diamond is an area of great interest. However, these processes aren't widely studied *in-situ*. Nitrogen implantation is one of the most popular methods of incorporating nitrogen into diamond and is instrumentally a desirable choice as it uses a piece of equipment commonly found on surface science UHV equipment, an ion source. Very low energy (<1 keV) ion sources are usually used for sputtering samples with a heavy, inert gas, such as argon, to produce a clean surface. The work presented in this chapter will be a continuation of the OptiXS section from chapter 3, with two main experiments presented. The first experiment presents successful nitrogen implantation using an ISIS 3000 ion gun into two nitrogen containing HPHT diamonds combined with *in-situ* optical measurements to further test the OptiXS system. The second experiment attempted to reproduce the nitrogen implantation on Nanocrystalline Diamond (NCD) films and combine this with the surface preparation methods presented in chapter 5 to study the effects of each stage using a combination of optical and electron based measurements. The results will be presented and limitations of the OptiXS system will be discussed, as well as suggested improvements which can be explored in future work.

6.1 EXPERIMENTAL OVERVIEW

6.1.1 THE SAMPLES

Three samples were used in this studies summarised in this chapter. Two HPHT synthesised nitrogen containing diamonds and one nanocrystalline diamond (NCD) film. The HPHT diamonds were provided in a batch from Element Six Ltd. These nitrogen containing, yellow diamonds, approximately 1 mm in diameter, and of varying morphology (from octahedral to cubic), were all first measured using photoluminescence to confirm the presence of nitrogen vacancies. The two selected were the ones showing the most intense measured signal for the NV^0 and NV^- emission lines at 575 and 637 nm, respectively, from a [111] face, and a [001] growth face. The two samples were chosen to compare the effect of implantation direction with respect to the growth planes. These were then mounted in platinum ‘top hats’ using a small lathe and jeweller’s tools. A small mounting lip was machined and depressed around the diamonds in order to secure them in place whilst keeping the desired face exposed. The platinum top hats were then mounted onto a tantalum faceplate by wrapping tantalum wire around the ‘brim’ of the top hat, and spot welded taut to the faceplate. This mounting ensured good contact between the

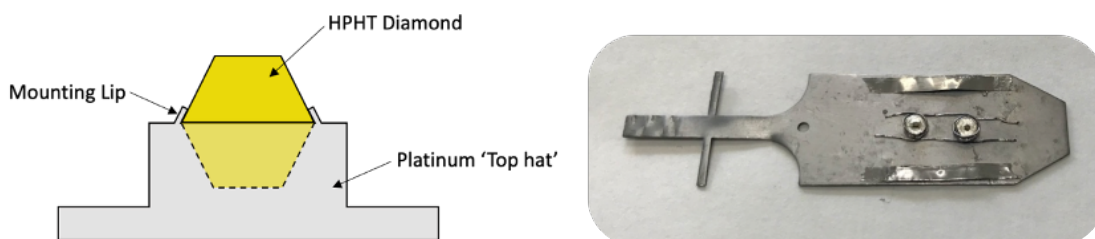


Figure 6.1: (left) The mounting configuration for a 1 mm diamond in a platinum top hat. A small ‘mounting lip’ is bent around the sample to secure it in place whilst not covering the desired face. (right) The two platinum top hats mounted on a sample faceplate. Ta wire is wrapped around the brim on the top hat and spot welded to secure it flush to the faceplate.

platinum and the tantalum faceplate for the best thermal contact between the sample and heater. Platinum was chosen for the top hat material for its relatively high melting point, chemical inertness and malleability/machinability.

The NCD film used in this work was a part of a set of four samples grown by collaborators in the Cardiff Diamond Foundry group led by Professor Oliver Williams. The films were grown on 10×10mm, 500 µm thick, silicon (100) wafers with 500 nm silicon dioxide on both sides with the front side polished to a rms roughness of <1 nm. Before growth, the samples were cleaned using the SC-1 cleaning method. This involved boiling the samples in a solution of 30% H₂O₂, NH₄OH, and deionised (DI) water in a ratio of 1:1:5 at 75°C for 10 minutes. The substrates were then submerged in DI water and placed into an ultrasonic bath for 10 minutes, followed by a spin dry at 3000 rpm for 30 seconds. As these samples were grown epitaxially on silicon, direct growth was not possible due to the difference in surface energies and sticking coefficient between diamond and silicon surfaces [159]. To overcome this issue the silicon substrates are chemically nucleated by submerging them in a 10 nm nanodiamond solution containing 0.1 g nanodiamond and 200 ml of water and sonicated for 10 minutes. This produces substrates with a seeding density greater than 10¹¹ cm⁻² (with a maximum theoretical seeding density of 10¹² cm⁻² for nanodiamond of this size). The seeded substrates were then exposed to growth conditions of 5% CH₄ and 95% H₂ (with trace amounts of argon) for the incubation period and 800°C in a Seki Technotron AX6500X microwave assisted plasma deposition reactor. After incubation the samples were grown in different methane concentrations of 2%, 3%, 4%, and 5% which can change the morphology and bonding distribution through the samples. All were characterised using Raman and

photoluminescence and one chosen for implantation. The sample in this work was the sample grown with 2% methane as it was the most ‘optically clean’. A film thickness of 4 μm was chosen, and this was monitored by *in-situ* laser interferometry and confirmed *ex-situ* by spectral reflectance measurements. Atomic Force Microscopy (AFM) measurements, shown in Figure 6.2 provided an rms roughness value of approximately 100 nm, and crystal grain sizes at the surface in the range of 0.4 – 2 μm .

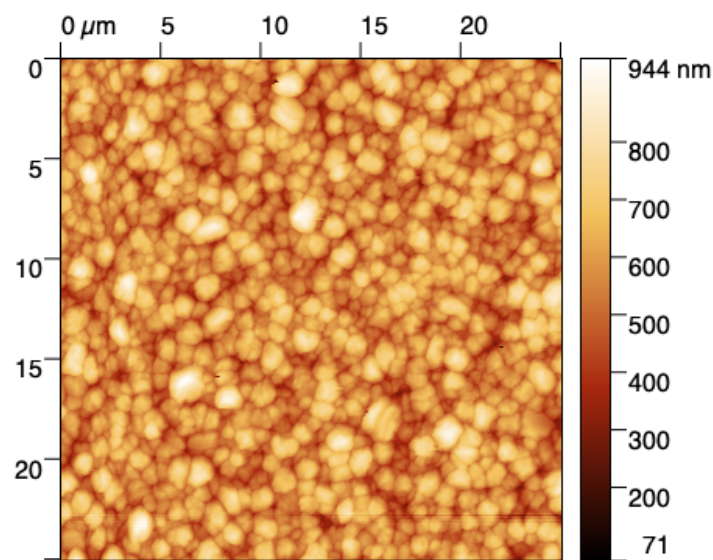


Figure 6.2: AFM measurement of the NCD film used in this study.

6.1.2 EXPERIMENTAL PROCEDURE

The first experiment used the HPHT nitrogen containing diamonds. A total of 13 diamonds were initially characterised using photoluminescence. From these, two selected crystals were mounted, acid treated, and measured again using photoluminescence. Both of these measurements were performed *ex-situ* on the Horiba LabRam Spectrometer. After the acid treatment, the (100) and (111) samples were mounted on to the tantalum faceplate and degassed to 300°C. The samples were then measured using photoluminescence before and after nitrogen

implantation at room temperature in vacuum. XPS was also attempted, but the samples were too small to measure in OptiXS, without measuring a substantial signal from the platinum holders. XPS spectra were taken of the samples in the REES system using the high magnification mode which can enable measurement of samples less than 1 mm in diameter.

Implantation was performed using the ISIS 3000 ion gun. For implantation, a filament current of 2.6 A was used to ionise nitrogen gas which was leaked into the chamber through the gun until ignition was achieved. This was usually around a pressure of 10^{-5} mbar, depending on gas purity. The current and pressure were then adjusted for an emission current of 35 mA and an accelerating voltage of 2.4 kV was used for implantation. Implantation modelling performed in the SRIM software (The Stopping and Range of Ions in Matter) predicted that nitrogen ion implantation of 2.4 keV would achieve an average implantation depth of 25 nm into the diamond sample. This implantation depth was chosen to provide near-surface implantation, whilst also ensuring surface damage is kept minimal, assuming most implantation damage is around the implantation depth. The samples were exposed to the nitrogen ion beam for a total of 60 minutes before measured again optically.

As with the HPHT samples, the four NCD samples grown were all measured *ex-situ* optically to characterise each film. The most optically 'clean' sample was chosen to be implanted. All samples were also characterised using XPS to check for sample consistency and to provide an initial characterisation. The chosen sample was mounted onto a tantalum faceplate with a section partially covered by strips of tantalum foil, which also secured the sample down. This was to provide 'before' and 'after' regions on the sample surface. Once mounted and loaded in the chamber, the

sample was measured with XPS. It was then degassed to 700°C to provide a clean sample and photoelectron measurements were repeated.

The sample was then exposed to the same implantation conditions as the previous HPHT samples, with an ion energy of 2.4 keV, an emission current of 35 mA for 60 minutes. This was then followed by a degassing, and a higher temperature 850°C annealing cycle. After annealing, the sample was exposed to a similar *in-situ* nitric oxide (NO) plasma treatment described in chapter 5. XPS measurements were repeated following each step. Optical photoluminescence measurements were taken following this procedure *ex-situ* on the Horiba LabRam.

6.2 RESULTS

6.2.1 HPHT DIAMONDS

The initial characterisation of the nitrogen containing HPHT diamonds involved taking a number of survey photoluminescence spectra in order to identify optical centres present in the diamonds. These were taken on the Horiba LabRam optical spectrometer. The excitation source for the optical measurements throughout this work was the 532 nm diode laser, described in section 3.2.3, and all optical measurements were performed at room temperature. Optical survey scans were taken between 550-900 nm which would encompass the first-order diamond Raman signal (1332 cm^{-1} , approx. 572 nm with the 532 nm source), the NV^0 signal (575 nm) and the NV^- signal (637 nm). The large measurement tail was to encompass isolated vacancies (741 nm) or other optical defects, such as a Si-V (738 nm). The survey spectra were taken with 5 second acquisition time and 2 accumulations which provided reasonable SNR and ensured cosmic ray spikes were nullified.

The samples to be mounted were selected following an area ratio analysis between the first-order diamond Raman, NV^0 and NV^- . The selected two diamonds were the samples with the highest nitrogen-vacancy signal, in comparison to the Raman signal, which each spectra were normalised to, and was assumed to be fairly consistent between samples as they are all high quality, albeit small, single crystals. Each sample was measured through a number of their crystal faces, by rotating them on the optical stage, to look for any dependence on the angle between the excitation direction (*i.e.* the polarisation of laser light), and the orientation of the nitrogen vacancies, which are always orientated along a [111] direction. Figure 6.3 shows the initial measurements of the two selected samples, as well as an image of the samples mounted in platinum, showing the (100) square face, and the (111) hexagonal face. Labelled on the spectra are the first-order diamond Raman line, neutral nitrogen-vacancy (NV^0) zero phonon line (ZPL), negatively charged nitrogen-vacancy (NV^-) ZPL and the negative NV phonon sideband (PSB). It can also be seen that other than these features the samples are fairly optically clean, with little to no optical features away from the aforementioned features, which persisted throughout this experiment.

Once mounted in platinum, these samples were acid treated to clean and oxygen terminate them. However, the oxygen termination was not possible to verify on the OptiXS system. Previous calibration measurements of the OptiXS system hemispherical analyser showed a minimum circular measurement area approximately 6 mm in diameter. These samples were close to 1 mm in diameter so were not able to be distinguished in the XPS measurements. However,

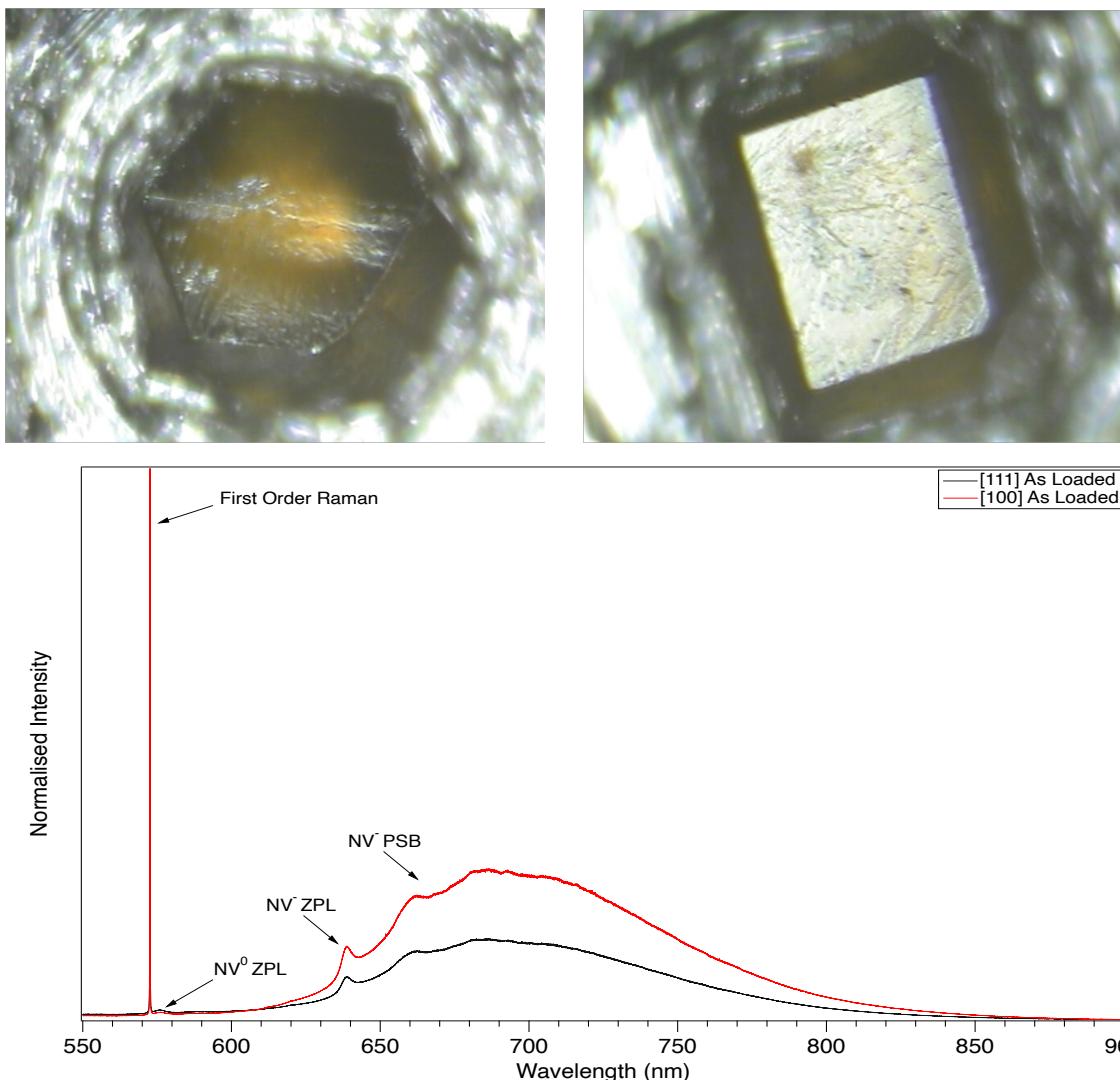


Figure 6.3: (top, left) The exposed (111) face of one of the nitrogen containing diamonds mounted in platinum and (top, right) the (100) face of a similar HPHT diamond. (bottom) The initial PL measurements from both of the samples, the (111) emission is shown in black and the (100) is shown in red.

measurements were taken on the REES system using the SPECS Phoibos100 analyser in high magnification mode. The XPS survey spectrum of the (001) diamond in Figure 6.4 shows a carbon and oxygen signal, but also a very low SNR, indicating the difficulty of measuring these samples with photoelectron spectroscopy, therefore these samples were used for optical measurement only. The scan parameters were as follows: E_B range = 53.6 – 1053.6 eV, ΔE_B = 1 eV, E_P = 100 eV, dwell time = 0.5 s and 1 accumulation.

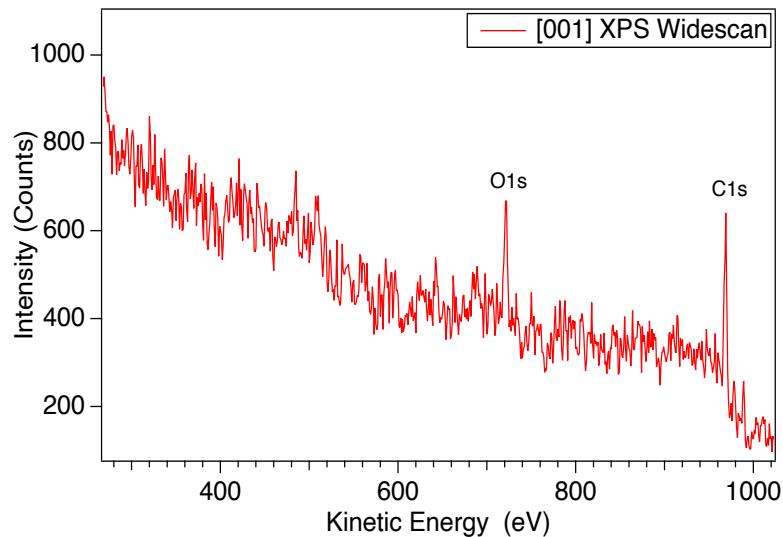


Figure 6.4: An XPS wide-scan of the [001] acid etched HPHT sample taken on REES using a high magnification mode.

Once initially characterised, the next step was to measure these samples optically again *in-situ*. The main reason for remeasuring was to characterise how the SNR varied between the optical bench and *in-situ* measurements. It was found that for a similar SNR, *in-situ* measurements required scan times at each wavelength of approximately 10 minutes (30 second acquisition time, 20 accumulations). This can be attributed to the much lower numerical aperture associated with measuring from > 30 cm from the sample, as well as light losses through optical components, fibres and alignment. Therefore, for *in-situ* measurements only static scans around the ZPLs and first-order Raman lines were taken. By using consistent scan parameters during *in-situ* measurements, statistical analysis methods, such as normalisation relative to the diamond first-order line and calculation of relative area ratios can be performed on separate static measurements. The areas of each spectral feature were determined via peak fitting using the same Voigt profiles used in the XPS analysis and the MCS program, and the areas were extracted. The NV⁻ PSB background contribution was also fitted with a Voigt profile, but with a very large FWHM,

essentially only requiring half a peak, which is mathematically similar to an exponential background.

In-situ optical measurements were taken before and after a 1 hr exposure to the nitrogen ion beam and the area ratios were compared to determine if any implantation had occurred. Figure 6.5 shows the results from this implantation run. The top row of graphs shows the [001] photoluminescence and the bottom shows the [111]. The left hand column shows the neutral NV emission peak (with the first-order Raman cropped to the shorter wavelength side) and the right hand column shows the emission from the NV⁻ centre. All spectra are normalised to the first-order diamond Raman. The red lines indicate the photoluminescence before implantation (as mounted) and the black lines show after implantation. The NV⁰ intensity scale is multiplied by 5 with respect to the NV⁻ scale for clarity. It is quite clear to see there is a substantial gain in both nitrogen-vacancy states. This increase was verified afterwards by measurements on the Horiba LabRam.

Table 6.1 shows the statistics with regards to the photoluminescence and Raman areas, as well as the ratio between the two-charge state areas and the Raman area. The ratio is given such that the relative area of the Raman is 1. From these ratios it can be seen that the population for both charge states relative to the Raman are increased significantly, however between the two samples their increase is not identical. For the (001) diamond the neutral-charge-state-area contribution is increased by 4.42 times, whereas the negative-charge-state-area ratio is only increased by a factor of 1.5. For the (111) diamond the inverse is true, with the NV⁻ area increasing by a larger magnitude of 2.5, compared to the NV⁰ state factor of

~1.6. It is unclear what is causing the differences between charge-states-area ratios between samples.

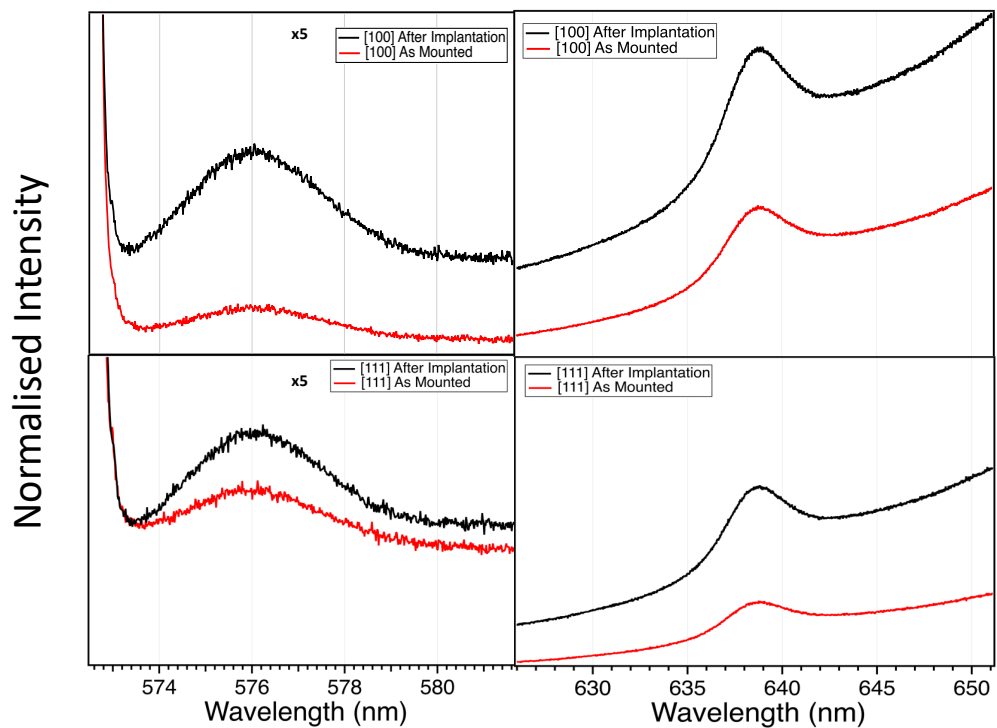


Figure 6.5: (top, left) The NV^0 photoluminescence measured *in-situ* from the (100) diamond and (top, right) the NV^- emission from the same diamond, before and after nitrogen implantation. (bottom, left) The NV^0 photoluminescence measured *in-situ* from the (111) diamond and (bottom, right) the NV^- emission from the same diamond, before and after nitrogen implantation. On all four graphs the PL before implantation is shown in red and after is shown in black.

Table 6.1: The Area analysis results from each of the spectra shown in Figure 6.4.

Sample	NV^0 Area	NV^- Area	Raman Area	$NV^0 : NV^- : \text{Raman}$
(001) Before	0.009	0.353	0.128	0.07 : 2.75 : 1
(001) After	0.043	0.602	0.142	0.31 : 4.25 : 1
(111) Before	0.023	0.182	0.143	0.16 : 1.27 : 1
(111) After	0.034	0.429	0.136	0.25 : 3.15 : 1

Changes in intensities for these optical measurements could be due to equipment based factors such as alignment, focus, laser intensity and in this case the alignment of each sample with the ion source. The background of the PSB and the area around the first-order Raman/ NV^0 peak can also introduce discrepancies and errors into the fitting. On top of this, the population increase during ion implantation should be proportional to the number of ions (or the dosage) accelerated towards the samples. In both samples the NV^- intensity area increases by a very similar

amount, approximately 0.250, which indicates there is a fixed amount of new nitrogen introduced to the sample, regardless of initial colour centre populations. Importantly, as a test for implantation in the Optics' system which can be measured *in-situ*, this can be regarded as a success, however for combined electron and optical spectroscopies, samples which can be measured by photoelectron spectroscopy are required.

6.2.2 NANOCRYSTALLINE DIAMOND FILMS

Once the nitrogen implantation was shown to be possible, the next step was to try and measure implantation in tandem with photoelectron spectroscopy and surface modification via plasma treatment. As implanting into larger single crystal samples was not a viable option, high quality, nanocrystalline diamond films grown by collaborators in the Cardiff Diamond Foundry group at Cardiff University were deemed the best option. Whilst nitrogen implantation into NCD films has been performed, it is rarely used for NV centre generation due to the relatively high sp^2 content providing a mixture of electron traps and conductive paths which lead to the neutral state being favoured. However, as a sample to test the premise of implantation, optical and electron measurements in a single system, they were thought to be ideal. This section will review the experiment and highlight the issues found, how they were rectified and summarise with future plans for similar experiments. Furthermore, with the installation of the plasma chamber onto the OptiXS system, this experiment aimed to test this also.

Four NCD films were grown with varying methane concentrations. This can affect the sp^2/sp^3 content as well as changes the overall energy in the plasma.

Because of this, each sample was measured *ex-situ* to characterise the optical properties and check for any optical defects. Survey scans for each sample were measured between 550 and 900 nm, using a 532 nm excitation source. The initial photoluminescence and Raman spectroscopy measurements are shown in Figure 6.6.

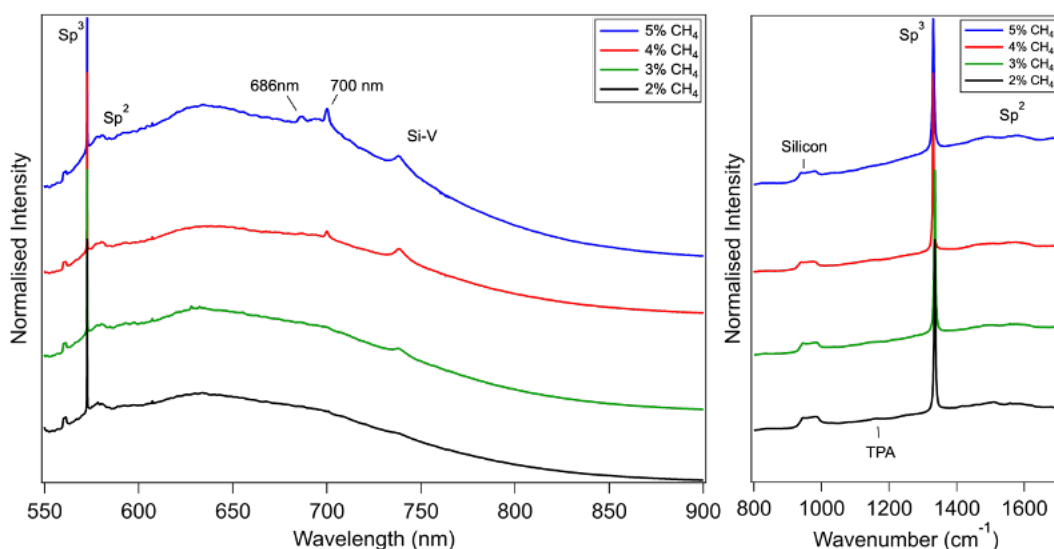


Figure 6.6: (left) The survey photoluminescence spectra for each of the four NCD films and (right) the Raman spectra centres around the diamond first-order Raman peak for each of the NCD films.

Each spectra are normalised to the first-order diamond Raman peak and offset for clarity. Most features of both the PL and Raman are typical of nanodiamond structures. The sp³ Raman signal at 1332 cm⁻¹ (573 nm), and peaks due to sp² content between 1400 and 1600 cm⁻¹ on a broad background are common features [169]. Between 950 and 1050 cm⁻¹ is a Raman feature commonly associated with silicon which is measured from the substrate, also a signal associated with *trans*-polyacetylene (TPA) is just visible around 1150 cm⁻¹ [170]. The presence of silicon vacancies in the NCD films is highly dependent on the growth conditions, suggesting at higher methane concentrations, there is a greater etching effect of the silicon substrate leading to a higher uptake of silicon into the diamond film. Growth dependent features were also measured around 686 and 700 nm, however, the

origins of these features are unclear. Each sample was also characterised by XPS, and the spectra were consistent for all four samples. The sample chosen to undergo implantation and plasma treatment was the NCD grown under 2% methane, being the most optically clean sample (shown by the black lines on Figure 6.6).

The 2% sample was first sonicated in IPA, rinsed in DI water and blow-dried with nitrogen gas. It was then mounted and loaded into OptiXS. It was not acid etched due to it being on a silicon sample. Once loaded it was measured with XPS and PL and degassed to 700°C in order to ensure as many surface contaminants as possible were removed. The film was then exposed to a similar nitrogen ion beam as the HPHT sample, of 2.4 keV N⁺ ions for 1 hour. It was then remeasured using XPS and PL. These initial *in-situ* PL measurements highlighted a number of issues. Firstly, very little sp² signal could be measured, indicating that the 4 µm sample may be too thin to be measured with the superhead optics. On top of this, and after a number of other tests, the optical fibres used were found to be leaking in a lot of light through the cladding. This, plus slight alignment issues coupling with the small aperture (100 µm input core) single mode fibre caused very large losses before detection. To resolve both these issues the output fibre was replaced with a 400 µm aperture fibre with much more sufficient cladding, and a rubber exterior. However, this was not resolved until after this work was carried out, so photoluminescence and Raman spectra taken at each stage were non-informative, therefore only XPS results will be shown.

Figure 6.7 shows the survey XPS spectra of the 2% NCD film as loaded (black line), after 700°C (red line) and after 'implantation' (blue line). The as loaded widescan is typical of a diamond like sample left in atmosphere, with a small oxygen component due to surface contaminants; this is removed almost entirely after

heating to 700°C. After implantation a significant nitrogen component becomes present around 400 eV. Quantification of the N1s and C1s areas give an elemental composition of 81% carbon and 19% nitrogen, which equates to approximately 3 monolayers. However, the expected average implantation depth was 25 nm, far beyond the reach of photoelectron spectroscopy at this energy range which suggests rather than implantation, a substantial nitride layer may have been formed. High resolution core levels were taken of the C1s and N1s core levels to probe further the N1s signal. After these were recorded and fitted, the sample was heated to determine the stability of the nitrogen on the sample surface. If adsorbed, it would simply be removed by heating, however, if chemically bonded, the nitrogen would most likely remain.

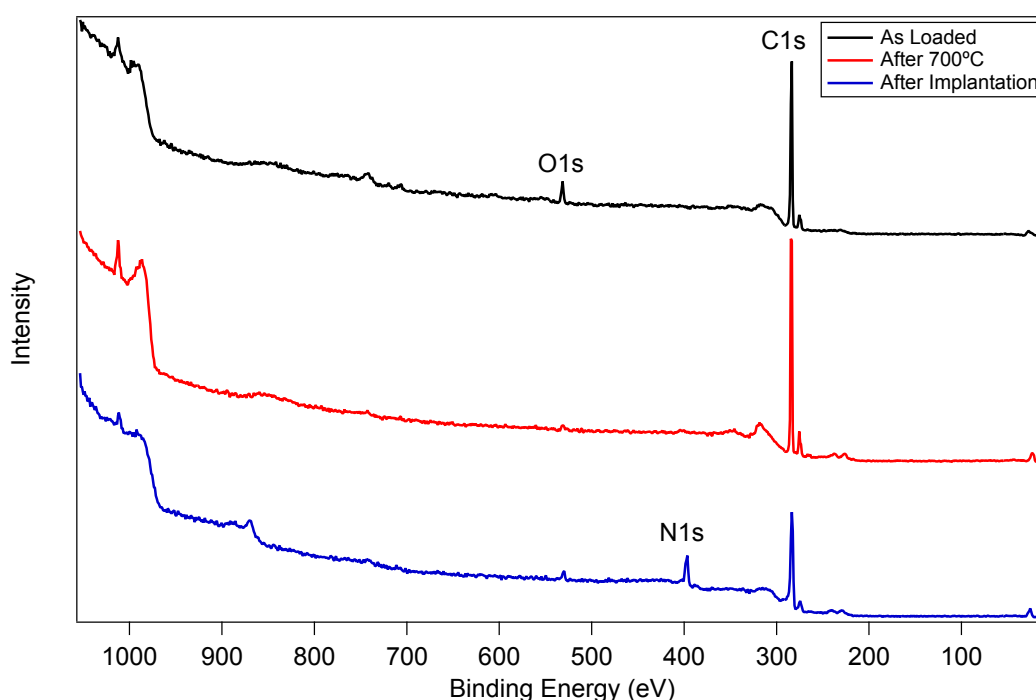


Figure 6.7: Survey XPS spectra of the NCD film as loaded (black), after heating to 700°C (red) and after nitrogen ion irradiation (blue).

High resolution C1s core levels of the NCD sample after degassing, immediately after nitrogen irradiation, and following a subsequent heating to 850°C are shown in Figure 6.8a. The N1s spectra of the irradiated sample and annealed

sample are shown in Figure 6.8b. The initial C1s core level is fit with 3 components at 284.2, 284.9 and 286.1 eV, respectively, typical of a C1s taken of diamond with a small amount of oxygen on the surface, as seen in the widescan.

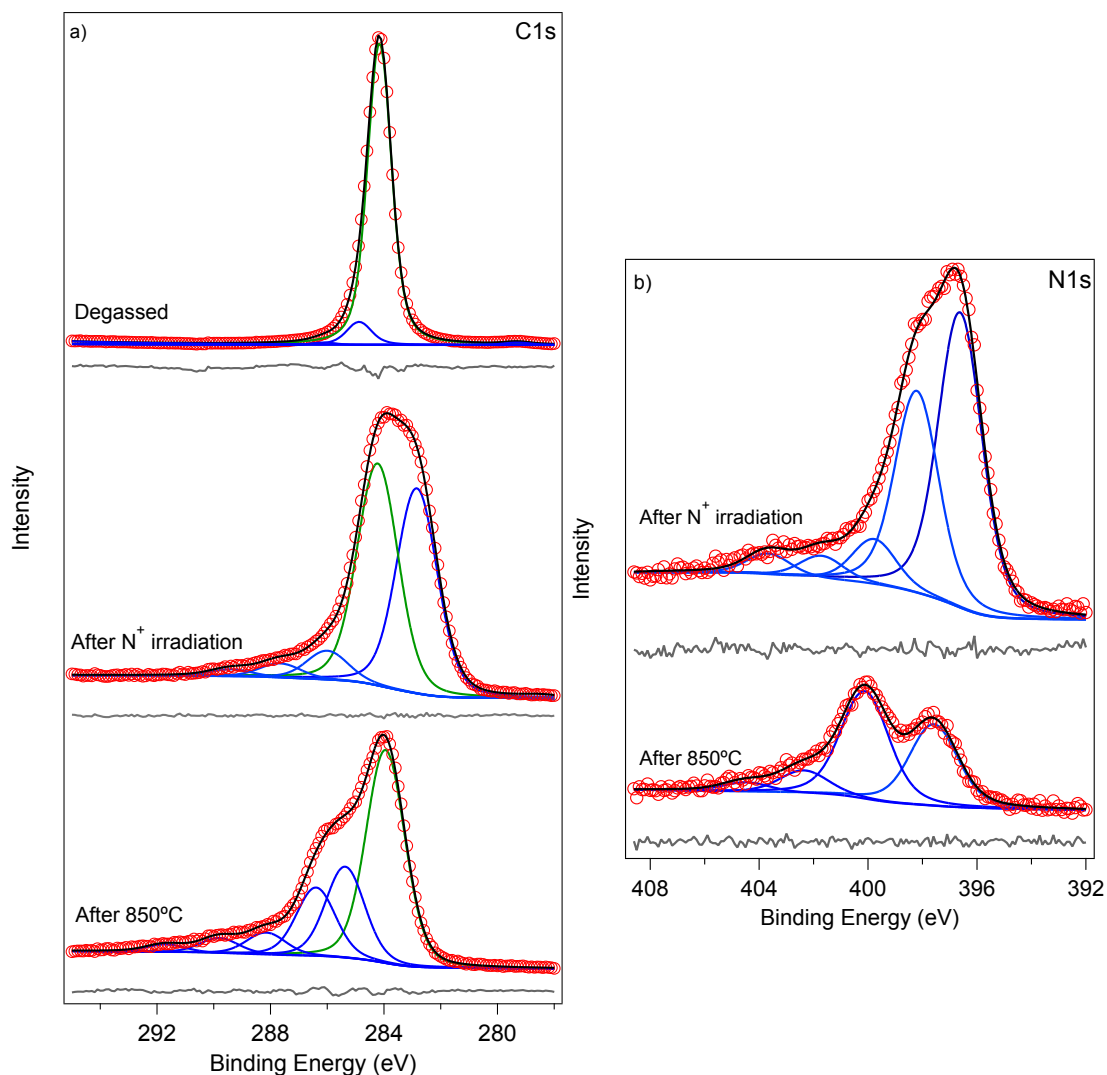


Figure 6.8: (left) The C1s high resolution core level spectra after nitrogen exposure and after an 850°C anneal. (right) the respective N1s core levels for each stage. The raw data are shown by the red circles, fit components are shown by blue/green lines and fit envelopes are shown by the black lines. The fit residuals are shown under each spectrum by the green lines.

The C1s, after nitrogen irradiation is fitted with 5 components, at 282.9, 284.2, 286.1, 287.7 and 289.4 eV, given from lowest binding energy to highest (right to left on Figure 6.8a). The FWHM of all C1s components was 1.7 eV. The component at 284.2 eV is again associated with the C-C diamond bonds (shown in green), the component at 282.9 eV indicates a large sp^2 presence following the nitrogen

exposure, and the components at 286.1 and 287.7 eV are very close to literature values for C-N and C=N termination groups [171], [172]. The two highest binding energy components can also be attributed to C-N bonding arrangements, as previous nitridation experiments on a diamond surface have shown a binding energy dependence on the number of nitrogen neighbours for each carbon atom [173]. This coupled with the various carbon-nitrogen environments which could be present in the NCD film due to crystal planes, grain boundaries, and the surface roughness could account for the extended high binding energy tail. Other factors which are difficult to take into consideration are band-bending effects which have been seen on nitrogen terminated diamond, but not nitrogen terminated graphite, because of its conductive nature.

The nitrogen 1s signal post irradiation is fitted using five components at binding energies of 396.6, 398.2, 399.7, 401.7, 403.7 eV, with a FWHM of 1.95 eV for all components. These are attributed in literature to C-N, C=N and C \equiv N species, with the higher binding energy components being most likely -N-N- species located within graphitic regions. Other suggestions for this component highlight the N1s binding energy's sensitivity to chemical environments and could be due to positively charged N⁺ ions or N₂⁺ molecules trapped within the nitride layer which has formed [173]. N1s components around 401.7 eV have also been associated with substitutional nitrogen in amorphous carbon film, as well as nitrogen doped graphene layers [174], [175], suggesting the nitrogen implantation was successful, but substantially damaged the sample.

The C1s and N1s core levels after annealing to 850°C confirm that N-termination/nitride formation has occurred, as the behaviour in certain components

mimic what is reported in the literature. The overall reduction in the N1s signal is explained by desorption of nitrogen species, the shift in the C1s to a slightly higher binding energy is seen in literature, as well as the changes in the relative areas between components. The lowest binding energy, C-N component at 286.1 eV on the C1s, and the 396.6 eV N1s component; appear to diminish much more than other components, causing a larger shoulder on the low binding energy side of the C1s core level, and an apparent splitting of the N1s core level. Current theory suggests these components are then attributed to the nitride compounds formed on the surface which when annealed would easily form volatile C_2N_2 molecules, so this component is thought to be $C\equiv N$. Interestingly, the two lowest binding energy components (282.9 and 284.2 eV) on the C1s core level, immediately after nitridation appear to coalesce after 850°C to a single component at 284.0 eV suggesting the majority of the sp^2 containing carbon is removed during heating. This, together with the nitrogen removal suggests there were regions of nitrogen containing sp^2 carbon present which may provide a basis for further study into the electronic properties of these regions.

The nitrogen terminated surface is also considered a possible candidate for use in quantum technologies based on the NV centre and some models suggest full nitrogen termination (rather than N-H) could have positive electron affinities in the region of 3.2-3.5 eV [137], [176]. With this in mind, the possibility of further studying the reproducibility and consistency of *in-situ* nitrogen termination in the OptiXS chamber for future work must be considered. With the recent improvements, real-time measurements could provide insight into the strange evolution of the peaks during annealing, as well as provide the electronic properties further if N-termination of single crystal samples was found to be possible.

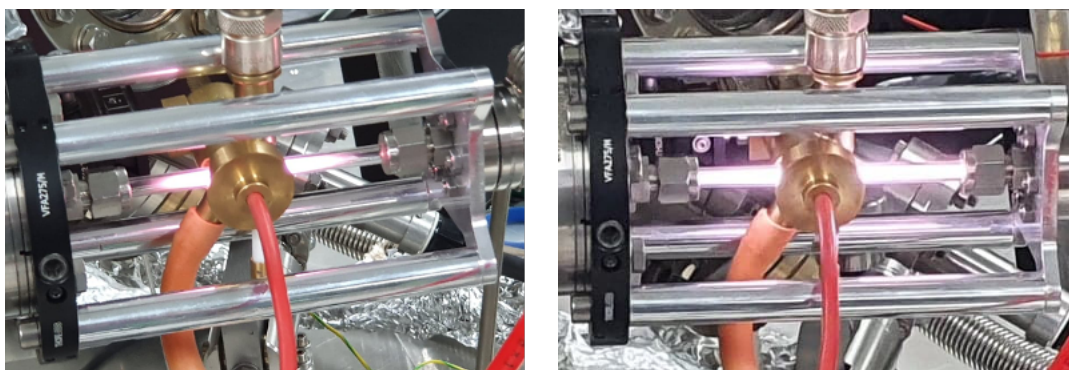


Figure 6.9: (left) An unstable plasma. Note the transparency at the ends of the capillary. This plasma would not sufficiently treat the sample. (right) A stable plasma which clearly fills the length of the glass capillary.

Post nitrogen irradiation and annealing, the plasma chamber still required testing. This would also prove more insight into the stability of the nitrogen species formed on the NCD film. The plasma chamber installed is of similar design to the plasma chamber on the REES chamber, which was also recently modified and installed. The similar design gives the possibility of interchanging the two plasma cavities, as well as possible future uses at beamlines at central facilities. The plasma treatment conditions for the NCD film treatment were as identical as possible to the conditions given in chapter 5; approximately 100 W microwave generated nitric oxide plasma through a glass cavity for approximately an hour. The ignition pressure was approximately 5×10^{-4} mbar, and this was then reduced until a stable plasma the length of the glass capillary was formed. Figure 6.9 shows an example of an ‘unstable’ plasma, where the capillary edges are clearly ‘empty’ and the stable plasma which encompasses the length of the capillary.

After plasma treatment XPS spectra were taken, this was followed by a further annealing to 700°C and final XPS measurements. The post plasma treatment and 700°C anneal are shown in Figure 6.10. Post plasma treatment, there is a substantial O1s signal, as well as an unexpected fluorine, F1s signal. However, the plasma has removed any measurable trace of nitrogen. A statistical analysis on the area

contributions of the C1s, O1s and F1s peaks show a C1s contribution of 82.3%, 9.4% area contribution from the O1s and 8.2% area contribution from the F1s. The combined contribution of O1s and F1s is 17.6%, which, is a comparable to a coverage of >2 ML. This may be due to a significant amount of adsorbed material as well as the surface roughness providing a greater surface area than a polished surface. However, there is clearly an oxidation of the NCD surface with an oxygen coverage similar to those seen in the plasma treatment in chapter 5.

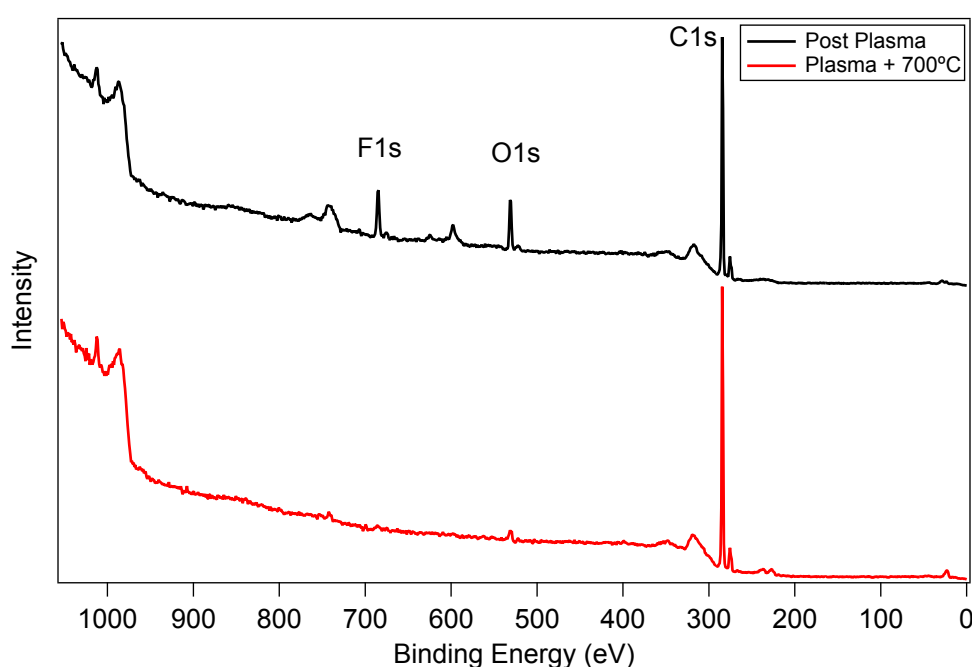


Figure 6.10: Survey spectra of the NCD films after plasma treatment (black) and following a subsequent 700°C heating cycle (red).

While the appearance of fluorine was unexpected, fluorine termination is of interest in NV centre technologies, as it provides a high positive electron affinity, similar to that of the oxygen termination, due to its high electronegativity [177], [178]. High Resolution core levels were taken of the C1s, O1s and F1s features to try to identify the bonding species present. These, along with the fit components are shown in Figure 6.11. The C1s core level was fitted with four components at 284.3, 284.8, 285.8 and 287.0 eV. The FWHM of all components are constrained to each other,

giving a FWHM for all components of 1.01 eV. The components can be attributed to C-C, C-O-C, C=O and C-F species [179], from lowest to highest binding energy respectively and confirms the apparent dual-termination of the NCD film. The component at 287 eV could be a mixture of C-OH and C-F, but C-F is more likely due to substantial F1s signal. The O1s core level was fitted using two components at 531.5 and 530.2 eV. The FWHM of these components was 2.00 eV. Only two components being required to fit the O1s core level is further evidence the chemical species

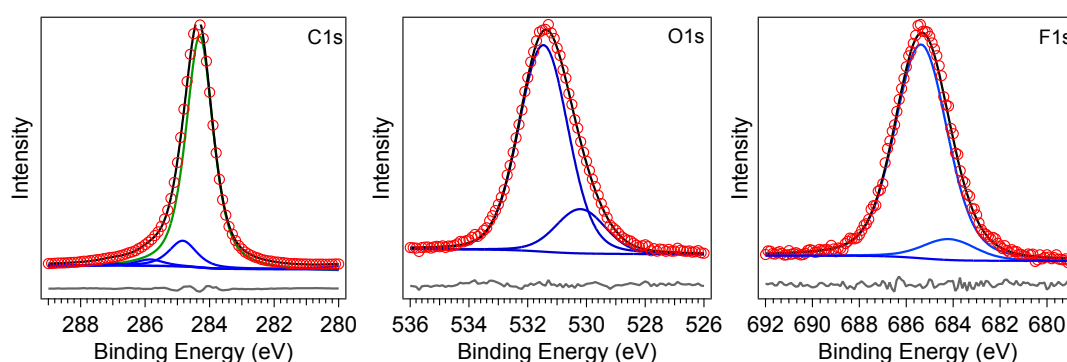


Figure 6.11: (left to right) The high resolution core level C1s, O1s and F1s spectra from the NCD film following plasma treatment. The raw data are shown by the red circles, fit components are shown by blue/green lines and fit envelopes are shown by the black lines.

present at 287 eV on the C1s core level is C-F based.

Lastly, the F1s core level is also fit with two components, at 685.3 and 684.1 eV, with FWHM values of 2.7 eV. The splitting between the two components is similar to what is seen in literature; however, the values are varied slightly. This may be due to the F1s measured in literature are most commonly on single crystal samples [178], [180], which, if doped slightly and measured at room temperature are liable to be affected by surface photovoltages which would account for the shift in binding energies seen here. Annealing of the sample to 700°C successfully reverted the NCD film back to a clean state and removed the fluorine contamination. The source of the fluorine was assumed to be from the polytetrafluoroethylene (PTFE) fittings which clamp around the glass capillary of the plasma source to create vacuum tight seal.

Tightening of the PTFE onto glass is very tricky as the glass capillary can very easily shatter. Following the detection of fluorine, the PTFE fittings were tightened and tested again for leaks using a helium leak test, which found no measurable leak. A second plasma treatment was performed to check if the fluorine contamination had been removed, however almost identical XPS spectra were found. The PTFE fittings should be far enough from the capillary end that etching of the fitting should be impossible, as is seen on the REES plasma source, so this requires further testing in future work.

Following this, the film was optically measured *ex-situ* on the Horiba LabRam bench. No detectable NV centres were found and a survey scan near identical to the untreated sample, as shown in Figure 6.6 (black line) was recorded. It is thought that the more reactive nature of the NCD films, along with the inherent as-grown surface roughness of approximately 100 nm may have provided conditions for nitrogen termination/nitride formation at the surface. Furthermore, implantation may have occurred in very shallow regions which were etched away by the plasma treatment. A repeat study of the implantation process without plasma treatment could verify this. Although some results in this study were unexpected, the processes described in this chapter may lead to further surface termination methods being possible *in-situ* in the OptiXS instrument which could pave the way to further in depth studies into these extremely useful surfaces. As well as this, limitations in the instrumentation were found. While some have already been rectified, further improvements have been discussed such as internal mirrors for better light collection for optical measurements, or fibre coupling through a flange to an *in-vacuo* objective lens. Approaching the lens to the sample would greatly increase light collection,

however longer worker distance objective lenses would still be required as to avoid shadowing effects from both incident X-rays and deposition sources.

Chapter 7 – SUMMARY

Three main developments have come from the work undertaken during this thesis. These are: the creation of the Materials Characterisation Suite software, the commissioning of the OptiXS system, and a deeper understanding of the oxygen terminated (001) diamond surface.

The development of the Materials Characterisation Suite has provided the ability to quickly and accurately fit multiple spectra with physically justified functions. It has also dramatically increased the speediness of REES analysis, as well as removed the limit to the number of cycles which can be analysed in a single fit propagation. Currently the most cycles fitted is approx. 3600 in a single fit propagation, up from the limit of 300, with a run time of approximately 5-10 minutes, depending on whether using Voigt or PseudoVoigt functions. Whilst still in development, at the time of writing the MCS has been used in 3 research groups.

The future plan for the MCS is to increase the stability of the overall program, as well as introduce analysis windows for more techniques. The research group also have a history of PhotoElectron Emission Microscopy (PEEM) analysis therefore integration of a (PEEM) panel is currently planned which can perform data slicing, image line analysis or integration of given pixels through an image stack. As well as this, a Raman spectroscopy panel which could work with Raman/photoluminescence spectra as well as 2D maps has begun development. This would find application in analysis of PL/Raman peaks as well as hyperspectral images whereby each pixel contains a spectrum. Finally, Atomic Force Microscopy (AFM) analysis is also routine in the research group, so simple image analysis functions which already exist in Igor

could be implemented for AFM analysis, resulting in a multifunctional analysis package and limiting the number of analysis programs required by future researchers.

Improvement on the analysis capabilities currently present are also planned. More tunability with regards to the range of cycles to fit for the REES analysis would be beneficial as in the current regime it can only fit from the first to last cycle or last to first. Selecting specific ranges will remove the need for slicing datasets prior to loading or reduce computation time by not having to analyse all cycles.

Chapters 3 and 6 presented the development of the OptiXS system and the first experimental results. The feasibility of *in-situ* simultaneous electron and optical measurements has been shown with the first combined measurements during iron deposition on diamond being performed. A large number of new components have also been added to the system and tested, which is far from trivial. Design of the manipulator had numerous iterations before being fully constructed as new ideas and capabilities were taken into account. The addition of the gas lines, UV source and the load lock style K-cell flange required time not only for the design and construction of the components in the immediate vicinity of the chamber, but also a near-complete overhaul to the rotary/turbomolecular pumping systems. The numerous developments have already ensured OptiXS is being used on a number of research projects, including this work, SPARC II projects and other CDT DST funded projects. However, a number of improvements can still be made.

As discussed in chapter 6, the optical capabilities are limited for thin samples, due to losses in light collection. Whilst improvements have already been made with changing the collection fibre, plans for internal mirrors or lenses which can approach

much closer to the sample are in discussion. Internal mirrors are also a candidate for improving the heating capabilities for the system. When reaching temperatures of 1100°C, the maximum of the current heating stage, a large amount of heat is lost radiatively, which is seen by a considerable heating of the chamber walls and windows. Internal mirrors are suggested as a way of reflecting the radiative losses back towards to sample area, which is predicted to improve the maximum temperature by 100°C or more.

The oxygen terminated diamond surface was thoroughly investigated in chapter 5. During this work two oxidation methods were studied and compared. XPS in the home lab as well as surface sensitive XPS and near ambient pressure XPS has revealed further insight into the chemical composition and stability of the oxygen surface. REES analysis of the oxygen surfaces during temperature cycles up to 1000°C have also been performed to investigate the desorption processes. A plasma treatment has also been performed on a (001) diamond surface and produced a positive electron affinity of 2.42 eV, the highest recorded for this type of termination. In conjunction with this work, a surface photovoltage model has been successfully developed to describe the electrical effects seen during X-ray irradiation. This model has also been developed in such a way that it may be applicable for modelling a variety of wide band gap semiconductors, such as boron nitride and can also be adapted readily to account for various photon sources, such as UV sources or synchrotrons, however this has not yet been tested.

Finally, attempts were made to measure *in-situ* nitrogen implantation effects as well as investigate the effect surface modifications have on the nitrogen-vacancy charge state distributions. Nitrogen implantation produced a nitrogen terminated

surface with some evidence of implantation present near the surface. However, the irradiated surface contained significant sp^2 content, indicating the breaking of diamond carbon bonds and the formation of complex C-N species. High temperature treatment resulted in the removal of sp^2 carbon but retained areas of nitrogen species. Etching via an oxygen plasma removed the surface C-N layer to recover an oxygen terminated surface. The surface terminations produced in this study, such as nitrogen and fluorine/oxygen co-termination, may be of interest in future studies as these are also candidates for surface terminations for NV centre applications.

Chapter 8 – APPENDIX

8.1 MCS/IGOR CURVE FITTING

8.1.1 GOODNES OF FIT

IgorPro utilises the Levenberg-Marquardt least-squares fitting algorithm, with an iterative fitting procedure, meaning the fit parameters are adjusted, and the χ^2 is calculated for each fit attempt. The algorithm then searches for a minimum in the χ^2 value, or until changes in the fit parameter have negligible effect on the χ^2 value itself. χ^2 is extensively used in the curve-fitting procedures as a goodness-of-fit parameter and is defined by:

$$\chi^2 = \sum_i \left(\frac{y - y_i}{\sigma_i} \right)^2$$

Equation 8.1

where y is a fitted value for a given point, y_i is the measured data value for the point and σ_i is an estimate of the standard deviation for y_i . On top of this, MCS implements other tools in order to help justify the resultant fits, namely the residual and reduced Abbe's criterion.

The residual R_i is the difference between the raw data and the fitting output defined as

$$R_i = S_i - M_i$$

Equation 8.2

where S_i is the i th fitted data point and M_i is the same data point from the raw data. The residual is a powerful tool in curve-fitting as it can show very clearly areas where a peak may be missing or indicate issues with the background. Common practice in peak fitting for XPS analysis is to aim for a residual with a maximum deviation of

around 1% of the total peak area. Abbe's criterion is a second goodness-of-fit parameter and is defined as

$$Abbe's\ criterion = \frac{\frac{1}{2} \sum_{i=1}^{N-1} (R_{i+1} - R_i)^2}{\sum_{i=1}^{N-1} (R_i)^2}$$

Equation 8.3

Where R_{i+1} and R_i refer to the residuals of the fit at the i th and $(i + 1)$ th data points, respectively. The Abbe criterion indicates how the residuals of a fit are distributed. Values for Abbe's criterion range between 0 and 2 with 0 indicating a constant offset between the fitting data and the raw data, 2 indicating that $R_{i+1} = -R_i$ for all cases meaning systematically anti-correlated residuals, and a value of 1 indicates random noise and a statistically distributed residual. Therefore, an ideal values for Abbe's criterion is 1. A presentation of these goodness of fit parameters are giving in [181]. Whilst the χ^2 value, Abbe's criterion, and the residual are all useful measures on the quality of the fit, complete optimisation of these values are not always meaningful, as physical justifications usually require constraints to be applied to the fit which may in turn worsen the goodness-of-fit.

8.1.2 FITTING UNCERTAINTIES

During fitting, IgorPro automatically calculates uncertainties, or standard deviations, for each fit parameter. The standard deviation values for the i th σ_i are calculated by taking the square root of the diagonal elements of the covariance matrix S , which is an output of the Levenberg-Marquardt algorithm, given by

$$\sigma_i = \sqrt{S_{ii}}$$

Equation 8.4

However, the specific values given by this calculation do not represent the physical errors, for a number of reasons:

- These values are mathematical estimations of each fitting parameter only. The fitting algorithm unaware of the physical errors on the data and has no knowledge of the true function that generated the data. That is; the algorithm assumes the provided fitting curve to be representative of that true function.
- They are strongly influenced by the number of parameters to be fit, noise levels in the data to be fit, and, in the case of peak-fitting, overlapping of peaks [182].

A further discussion about the calculation of these values, and discussions about the significance of them can be seen in [182].

8.1.3 GOOD FITTING PRACTICES

The MCS provides the ability to readily fit peaks to XPS spectra, however for meaningful results (and presentation of said results) good fitting practices must be followed. Throughout this work and the development of the MCS program, these practices were adhered to.

- **Record spectra with reasonably a reasonably high signal-to-noise ratio** – obtaining a desirable level of signal-to-noise can be crucial for deconvolution of core level components. High levels of noise can cause low intensity components to be completely undistinguishable. The level of noise which is deemed ‘reasonable’ also depends on the type of scan taken. High resolution XPS spectra require a higher SNR ratio, however REES spectra have a much lower SNR, but this is traded-off for time resolution. The core level being measured also affects the SNR as there also has to be a trade-off between

improving SNR and the length of the scan. Typical SNRs for high resolution scans and REES scans are given below.

- **Typical High Resolution SNR:** C1s SNR \approx 950, O1s SNR \approx 20
 - **Typical REES SNR:** C1s SNR \approx 35, O1s SNR \approx 3.5,
- **Choose a suitable model function:** True Voigt convolutions are physically the best representation, however with careful use a pseudo-Voigt function can be utilised. Pseudo-Voigt functions are computationally less expensive so become a better choice when fitting a large number of spectra, such as in REES experiments.
- **Reduce number of free parameters:** This can be done in two way; constrain fit parameters or reduce the total number of parameters. The number of total parameters can be minimised by only fitting physically justifiable peaks, addition of superfluous peaks may provide a 'better' fit but based on inaccurate information about the system. Statistically, the more parameters added, the greater the total uncertainty on the fit is. Constraining fit parameters helps reduce computational effort, but more importantly it provides a means to implement physical meaning to the fitting system, such as spin orbit splitting, and core-hole lifetimes (in the form of the same FWHM for all fit components).
- **Check goodness-of-fit parameters:** Utilise χ^2 , Abbe's criterion, and the residual and minimise accordingly, whilst also not wholeheartedly relying upon them.
- **Check literature:** Reference literature or any *a priori* knowledge in order to ensure fitting results are further justified.

8.2 INSTRUMENTAL ERRORS AND TYPICAL ERROR VALUES

This section will present a list of instrumental errors and estimations of them, plus typical errors values for the results quoted in this thesis. Typical error values for core level binding (kinetic) energies, FWHM, Atomic % values, Valence Band Maximum, and secondary cut-off energies will be presented.

The resolution (or peak broadening) of the HSA ΔE_{an} can be estimated by

$$\frac{\Delta E_{\text{an}}}{E_{\text{p}}} = \frac{S}{2R_0} + \frac{\alpha^2}{4}$$

Equation 8.5

Where E_{p} is the pass energy, S is the average of the entrance and exit slit width, R_0 is the nominal radius of the analyser, and α is the half angular acceptance in the dispersion direction. Table 8.1 shows the values for the pass energy, average slit width, angular acceptance and calculated resolution for the three main scan types used in this work. These values for the resolution can also be inferred as the Gaussian broadening contribution to the peak shapes.

Table 8.1: The pass energy, slit width, angular acceptance and the calculated resolution for the three photoemission methods used in this work.

Scan Type	Pass Energy (eV)	S (mm) (Average Slit Width)	α (rad)	Resolution (eV)
XPS	10	3	0.0524	0.18
REES	60	3	0.0524	1.06
UPS	3	1	0.0785	0.03

In practice the analyser broadening contribution (resolution) shouldn't directly affect the error on energy values for core level positions as the broadening should be

symmetrical, however these values have been quoted as errors in literature previously. The main source of error for core level positions would be from the energy step size used in the scan, which is 0.05 eV for high resolution XPS scans and 0.01 eV for REES scans. This would also be a source of error for FWHM values, VBM position and secondary cut-off. For REES experiments, the lower SNR as well as the coarseness of the fits used would increase the error further. The method of calculating VBM position and Secondary cut-off positions also introduce read-off, and human error. The conventional method of calculating the secondary cut-off is by taking the intersection point between linear extrapolations from the secondary electron edge, and the background. The VBM is calculated in a similar fashion, except it is the intersection point between linear extrapolations from the photoemission onset and the background level [183], [184], this is shown in Figure 5.3b. The final erroneous parameter to be discussed in the atomic % values. Errors on atomic % arise from errors on the calculated peak areas during fitting, assumptions in the relative sensitivity factors, SNR of the fitted core level, and the steadiness of the X-Ray source or electron detection. Exact quantification of the error on atomic % calculations is therefore extremely difficult, however, it is generally accepted that XPS is sensitive to chemical compositional changes of 1% [185]. Therefore, using the above justifications, errors on presented values in this work can be estimated. These values are presented in Table 8.2.

Table 8.2: Estimation of errors for quoted values used throughout this work. The errors have been quoted for values given from XPS, REES and UPS measurements. A three-fold increase in peak position and FWHM error between XPS and REES values has been given based on the higher SNR and coarser fitting procedure. A higher error for the secondary cut-off, compared to the VBM error, is attributed features beyond the secondary cut-off and the difficulty in extrapolating from the background region.

Scan Type	Parameter	Estimated Error
XPS	Peak Position (eV)	± 0.05 eV
	FWHM (eV)	± 0.1 eV
	Atomic Composition (%)	± 1 %
REES	Peak Position (eV)	± 0.15 eV
	FWHM (eV)	± 0.3 eV
	Atomic Composition (%)	± 10 %
UPS	VBM	± 0.05 eV
	Secondary Cut-off	± 0.1 eV

Chapter 9 – REFERENCES

- [1] M. W. Doherty, N. B. Manson, P. Delaney, F. Jelezko, J. Wrachtrup, and L. C. L. Hollenberg, "The nitrogen-vacancy colour centre in diamond," *Phys. Rep.*, vol. 528, no. 1, pp. 1–45, 2013.
- [2] S. Sangtawesin *et al.*, "Origins of Diamond Surface Noise Probed by Correlating Single-Spin Measurements with Surface Spectroscopy," *Phys. Rev. X*, vol. 9, no. 3, 2019.
- [3] H. Hertz, "Ueber einen Einfluss des ultravioletten Lichtes auf die electrische Entladung," *Ann. Phys.*, vol. 267, no. 8, pp. 983–1000, 1887.
- [4] A. Einstein, "On a Heuristic Point of View about the Creation and Conversion of Light," *Ann. Phys.*, vol. 17, no. 6, pp. 132–148, 1905.
- [5] S. Hufner, *Photoelectron Spectroscopy*. Springer, 2003.
- [6] S. P. Cooil, "Controlling the Epitaxial Growth of Graphene On Diamond Surfaces," *PhD Thesis, Aberystwyth Univ.*, 2014.
- [7] K. Kolasinski, *Surface Science*, Third Eidi. Wiley Books, 2013.
- [8] D. Coster and R. De L. Kronig, "New type of Auger effect and its influence on the X-ray spectrum," *Physica*, vol. 2, no. 1–12, pp. 13–24, 1935.
- [9] G. D. Mahan and E. W. Plummer, "Chapter 14 Many-body effects in photoemission," in *Handbook of Surface Science*, vol. 2, Elsevier, 2000, pp. 953–987.
- [10] R. A. Pollak, L. Ley, F. R. McFeely, S. P. Kowalczyk, and D. A. Shirley, "Characterisitic Energy Loss Structure Of Solids From X-ray Photoemission Spectra," *J. Electron Spectros. Relat. Phenomena*, vol. 3, pp. 381–398, 1974.

- [11] P. Steiner, H. Höchst, and S. Hüfner, "Analysis of the plasmon structure in XPS experiments of simple metals," *Phys. Lett. A*, vol. 61, no. 6, pp. 410–412, 1977.
- [12] B. P. Reed, "Developments in the Catalytic Graphitisation of Diamond and Silicon Carbide Surfaces," *PhD Thesis, Aberystwyth Univeristy*, 2017.
- [13] G. Wan, A. Croot, N. A. Fox, and M. Cattelan, "Empty-State Band Mapping Using Momentum-Resolved Secondary Electron Emission," *Adv. Funct. Mater.*, vol. 31, no. 4, pp. 1–6, 2021.
- [14] M. P. Seah and W. A. Dench, "Quantitative electron spectroscopy of surfaces: A standard data base for electron inelastic mean free paths in solids," *Surf. Interface Anal.*, vol. 1, no. 1, pp. 2–11, 1979.
- [15] S. P. Cooil *et al.*, "Controlling the growth of epitaxial graphene on metalized diamond (111) surface," *Appl. Phys. Lett.*, vol. 107, no. 18, p. 181603, Nov. 2015.
- [16] G. T. Williams, S. P. Cooil, O. R. Roberts, S. Evans, D. P. Langstaff, and D. A. Evans, "High temperature photoelectron emission and surface photovoltage in semiconducting diamond," *Appl. Phys. Lett.*, vol. 105, no. 6, 2014.
- [17] D. A. Evans *et al.*, "Transport and optical gaps and energy band alignment at organic-inorganic interfaces," *J. Appl. Phys.*, vol. 114, no. 12, 2013.
- [18] D. A. Evans, O. R. Roberts, A. R. Vearey-Roberts, D. P. Langstaff, D. J. Twitchen, and M. Schwitters, "Direct observation of Schottky to Ohmic transition in Al-diamond contacts using real-time photoelectron spectroscopy," *Appl. Phys. Lett.*, vol. 91, no. 13, 2007.
- [19] D. A. Evans, O. R. Roberts, A. R. Vearey-Roberts, G. T. Williams, A. C. Brieva,

- and D. P. Langstaff, "Molecular organization in organic semiconductor thin films observed in real time," *Appl. Phys. Lett.*, vol. 102, no. 2, 2013.
- [20] M. Schmid, H. P. Steinrück, and J. M. Gottfried, "A new asymmetric Pseudo-Voigt function for more efficient fitting of XPS lines," *Surf. Interface Anal.*, vol. 46, no. 8, pp. 505–511, 2014.
- [21] R. Hesse, "Product or sum: comparative tests of Voigt, and product or sum of Gaussian and Lorentzian functions in the fitting of synthetic Voigt-based X-ray photoelectron spectra," *Surf. Interface Anal.*, vol. 39, pp. 381–391, 2007.
- [22] S. Evans, "Curve synthesis and optimization procedures for X-ray photoelectron spectroscopy," *Surf. Interface Anal.*, vol. 17, no. 2, pp. 85–93, 1991.
- [23] P. Thompson, D. E. Cox, and J. B. Hastings, "Rietveld refinement of Debye–Scherrer synchrotron X-ray data from Al_2O_3 ," *J. Appl. Crystallogr.*, vol. 20, no. 2, pp. 79–83, Apr. 1987.
- [24] T. Ida, M. Ando, and H. Toraya, "Extended pseudo-Voigt function for approximating the Voigt profile," *J. Appl. Crystallogr.*, vol. 33, no. 6, pp. 1311–1316, Dec. 2000.
- [25] S. Doniach and M. Sunjic, "Many-electron singularity in X-ray photoemission and X-ray line spectra from metals," *J. Phys. C Solid State Phys.*, vol. 3, no. 2, pp. 285–291, 1970.
- [26] G. D. Mahan, "Collective excitation in X-ray spectra of metals," *Phys. Rev. B*, vol. 11, no. 12, pp. 4814–4824, 1975.
- [27] I. Kojima and M. Kurahashi, "Application of asymmetrical Gaussian/Lorentzian mixed function for X-ray photoelectron curve synthesis,"

- J. Electron Spectros. Relat. Phenomena*, vol. 42, no. 2, pp. 177–181, 1987.
- [28] D. A. Shirley, “High-resolution X-ray photoemission spectrum of the valence bands of gold,” *Phys. Rev. B*, vol. 5, no. 12, pp. 4709–4714, 1972.
- [29] A. Proctor and P. M. A. Sherwood, “Data Analysis Techniques in X-ray Photoelectron Spectroscopy,” *Anal. Chem.*, vol. 54, no. 1, pp. 13–19, 1982.
- [30] A. Herrera-Gomez, M. Bravo-Sanchez, O. Ceballos-Sanchez, and M. O. Vazquez-Lepe, “Practical methods for background subtraction in photoemission spectra,” *Surf. Interface Anal.*, vol. 46, no. 10–11, pp. 897–905, 2014.
- [31] M. H. Engelhard, D. R. Baer, A. Herrera-Gomez, and P. M. A. Sherwood, “Introductory guide to backgrounds in XPS spectra and their impact on determining peak intensities,” *J. Vac. Sci. Technol. A*, vol. 38, no. 6, p. 063203, 2020.
- [32] A. Herrera-Gomez, M. Bravo-Sanchez, F. S. Aguirre-Tostado, and M. O. Vazquez-Lepe, “The slope-background for the near-peak regimen of photoemission spectra,” *J. Electron Spectros. Relat. Phenomena*, vol. 189, pp. 76–80, 2013.
- [33] C. D. Wagner, L. E. Davis, and W. M. Riggs, “The energy dependence of the electron mean free path,” *Surf. Interface Anal.*, vol. 2, no. 2, pp. 53–55, Apr. 1980.
- [34] J. C. Ashley and C. J. Tung, “Electron inelastic mean free paths in several solids for $200 \text{ eV} \leq E \leq 10 \text{ keV}$,” *Surf. Interface Anal.*, vol. 4, no. 2, pp. 52–55, Apr. 1982.
- [35] T. Reich, V. G. Yarzhemski, and V. I. Nefedov, “Calculation of inelastic mean

- free path of photoelectrons in some solids," *J. Electron Spectros. Relat. Phenomena*, vol. 46, no. 1, pp. 255–267, 1988.
- [36] C. J. Powell, "The quest for universal curves to describe the surface sensitivity of electron spectroscopies," *J. Electron Spectros. Relat. Phenomena*, vol. 47, pp. 197–214, 1988.
- [37] H. Ebel, M. F. Ebel, P. Baldauf, and A. Jablonski, "The energy dependence of attenuation lengths in elements," *Surf. Interface Anal.*, vol. 12, no. 2, pp. 172–173, Jul. 1988.
- [38] A. Jablonski, "Universal Energy Dependence of the Inelastic Mean Free Path," *Surf. Interface Anal.*, vol. 20, pp. 317–321, 1993.
- [39] M. O. Krause and J. G. Ferreira, "K X-ray emission spectra of Mg and Al," *J. Phys. B At. Mol. Phys.*, vol. 8, no. 12, pp. 2007–2014, 1975.
- [40] R. E. Cross, "Optical Spectroscopy Instrumentation for the Characterisation of Wide Band Gap Materials," pp. 1–347, 2015.
- [41] B. Valeur and M. N. Berberan-Santos, "A Brief History of Fluorescence and Phosphorescence before the Emergence of Quantum Theory," *J. Chem. Educ.*, vol. 88, no. 6, pp. 731–738, Jun. 2011.
- [42] T. H. Gfroerer, "Photoluminescence in Analysis of Surfaces and Interfaces," *Encycl. Anal. Chem.*, pp. 9209–9231, 2006.
- [43] O. Nachtmann, *Elementary Particle Physics: Concepts and Phenomena*, 10.1007/97. Springer-Verlag Berlin Heidelberg, 1990.
- [44] R. Singh, "C. V. Raman and the Discovery of the Raman Effect," *Phys. Perspect.*, vol. 4, no. 4, pp. 399–420, 2002.
- [45] K. N. Shinde, S. J. Dhoble, H. C. Swart, and K. Park, "Phosphate Phosphors for

- Solid-State Lighting,” vol. 174, pp. 41–60, 2012.
- [46] S. A. Solin and A. K. Ramdas, “Raman spectrum of diamond,” *Phys. Rev. B*, vol. 1, no. 4, pp. 1687–1698, 1970.
- [47] J. F. O’Hanlon, “Vacuum Technology,” in *A User’s Guide to Vacuum Technology*, John Wiley & Sons, Ltd, 2004, pp. 3–8.
- [48] T. Renner *et al.*, *Quantities, Units and Symbols in Physical Chemistry*. The Royal Society of Chemistry, 2007.
- [49] F. R. Elder, R. V Langmuir, and H. C. Pollock, “Radiation from Electrons Accelerated in a Synchrotron,” *Phys. Rev.*, vol. 74, no. 1, pp. 52–56, Jul. 1948.
- [50] D. H. Bilderback, P. Elleaume, and E. Weckert, “Review of third and next generation synchrotron light sources,” *J. Phys. B At. Mol. Opt. Phys.*, vol. 38, no. 9, 2005.
- [51] J. K. Cockcroft and A. N. Fitch, “Chapter 2 Experimental Setups,” in *Powder Diffraction: Theory and Practice*, The Royal Society of Chemistry, 2008, pp. 20–57.
- [52] M. Jorge, S. Cooil, and T. Mark, “Robust p-type doping of copper oxide using nitrogen implantation,” 2017.
- [53] G. T. Williams, “Monitoring in-situ processing of solid surfaces with real-time x-ray photoelectron spectroscopy,” The University of Wales, Aberystwyth, 2011.
- [54] D. Roy, D. Tremblay, “Design of electron spectrometers,” *Rep. Prog. Phys.*, vol. 53, pp. 1621–1674, 1990.
- [55] SPECS GmbH, “Phoibos Hemispherical Analyser Series Manual (Phoibos 100, Phoibos 150),” vol. Version 2., 2006.

- [56] VSW Scientific Instruments Ltd, "HA100 Hemispherical Analyser System."
Manchester, 1980.
- [57] D. P. Langstaff and T. Chase, "A multichannel detector array with 768 pixels developed for electron spectroscopy," *Nucl. Instruments Methods Phys. Res. Sect. A Accel. Spectrometers, Detect. Assoc. Equip.*, vol. 573, no. 1, pp. 169–171, 2007.
- [58] D. P. Langstaff, A. Bushell, T. Chase, and D. A. Evans, "A fully integrated multichannel detector for electron spectroscopy," *Nucl. Instruments Methods Phys. Res. Sect. B Beam Interact. with Mater. Atoms*, vol. 238, no. 1, pp. 219–223, 2005.
- [59] X. Zhu and D. P. Langstaff, "Reduction of multiple triggering in counting detectors," *Nucl. Instruments Methods Phys. Res. Sect. A Accel. Spectrometers, Detect. Assoc. Equip.*, vol. 604, no. 1, pp. 400–403, 2009.
- [60] C. Bloomer, M. E. Newton, G. Rehm, and P. S. Salter, "A single-crystal diamond X-ray pixel detector with embedded graphitic electrodes," *J. Synchrotron Radiat.*, vol. 27, no. 3, pp. 599–607, May 2020.
- [61] S. Chauhan, N. Jain, and U. Nagaich, "Nanodiamonds with powerful ability for drug delivery and biomedical applications: Recent updates on in vivo study and patents," *J. Pharm. Anal.*, vol. 10, no. 1, pp. 1–12, 2020.
- [62] T. Ergin, N. Stenger, P. Brenner, J. B. Pendry, and M. Wegener, "Three-dimensional invisibility cloak at optical wavelengths," *Science*, vol. 328, no. 5976, pp. 337–339, Apr. 2010.
- [63] V. V Dobrovitski, G. D. Fuchs, A. L. Falk, C. Santori, and D. D. Awschalom, "Quantum Control over Single Spins in Diamond," *Annu. Rev. Condens.*

Matter Phys., vol. 4, no. 1, pp. 23–50, Mar. 2013.

- [64] L. Childress and R. Hanson, “Diamond NV centers for quantum computing and quantum networks,” *MRS Bull.*, vol. 38, no. 2, pp. 134–138, 2013.
- [65] J. R. Maze *et al.*, “Nanoscale magnetic sensing with an individual electronic spin in diamond,” *Nature*, vol. 455, no. 7213, pp. 644–647, 2008.
- [66] H. J. Mamin *et al.*, “Nanoscale Nuclear Magnetic Resonance with a Nitrogen-Vacancy Spin Sensor,” *Science (80-.)*, vol. 339, no. 6119, pp. 557–560, 2013.
- [67] M. S. Grinolds *et al.*, “Subnanometre resolution in three-dimensional magnetic resonance imaging of individual dark spins,” *Nat. Nanotechnol.*, vol. 9, no. 4, pp. 279–284, 2014.
- [68] T. Staudacher *et al.*, “Nuclear Magnetic Resonance Spectroscopy on a (5-Nanometer)³ Sample Volume,” *Science (80-.)*, vol. 339, no. 6119, pp. 561–563, 2013.
- [69] D. R. Glenn, D. B. Bucher, J. Lee, M. D. Lukin, H. Park, and R. L. Walsworth, “High-resolution magnetic resonance spectroscopy using a solid-state spin sensor,” *Nature*, vol. 555, no. 7696, pp. 351–354, 2018.
- [70] L. Rondin *et al.*, “Surface-induced charge state conversion of nitrogen-vacancy defects in nanodiamonds,” *Phys. Rev. B - Condens. Matter Mater. Phys.*, vol. 82, no. 11, pp. 1–5, 2010.
- [71] J. E. Field, *The Properties of Natural and Synthetic Diamond*. Academic Press London, 1993.
- [72] C. D. Clark, R. W. Ditchburn, H. B. Dyer, and N. F. Mott, “The absorption spectra of natural and irradiated diamonds,” *Proc. R. Soc. London. Ser. A. Math. Phys. Sci.*, vol. 234, no. 1198, pp. 363–381, 1956.

- [73] J. F. H. Custers, "Unusual phosphorescence of a diamond," *Physica*, vol. 18, no. 8, pp. 489–496, 1952.
- [74] P. Cartigny, M. Palot, E. Thomassot, and J. W. Harris, "Diamond Formation: A Stable Isotope Perspective," *Annu. Rev. Earth Planet. Sci.*, vol. 42, no. 1, pp. 699–732, May 2014.
- [75] H. P. Bovenkerk, F. P. Bundy, H. Y. Hall, H. M. Strong, and R. H. Wentorf, "Preparation of Diamond," *Nature*, vol. 184, no. 4693, pp. 1094–1098, 1959.
- [76] J. M. Zazula, "On Graphite Transformations at High Temperature and Pressure Induced By Absorption of the LHC Beam," no. LHC-Project-Note-78, Jan. 1997.
- [77] J. E. Field and C. S. J. Pickles, "Strength, fracture and friction properties of diamond," *Diam. Relat. Mater.*, vol. 5, no. 6, pp. 625–634, 1996.
- [78] J. E. Butler, Y. A. Mankelevich, A. Cheesman, J. Ma, and M. N. R. Ashfold, "Understanding the chemical vapor deposition of diamond: recent progress," *J. Phys. Condens. Matter*, vol. 21, no. 36, p. 364201, Aug. 2009.
- [79] P. W. May and Y. A. Mankelevich, "From Ultrananocrystalline Diamond to Single Crystal Diamond Growth in Hot Filament and Microwave Plasma-Enhanced CVD Reactors: a Unified Model for Growth Rates and Grain Sizes," *J. Phys. Chem. C*, vol. 112, no. 32, pp. 12432–12441, Aug. 2008.
- [80] E. K. Rideal, "The Kinetics of Chemical Change," *Nature*, vol. 146, no. 3706, pp. 603–604, 1940.
- [81] I. Langmuir, "The Adsorption of Gasea on Plane Surfaces of Glass, Mica and Platinum," *J. Am. Chem. Soc.*, vol. 40, no. 9, pp. 1361–1403, Sep. 1918.
- [82] P. W. May, J. N. Harvey, J. A. Smith, and Y. A. Mankelevich, "Reevaluation of

- the mechanism for ultrananocrystalline diamond deposition from Ar/CH₄/H₂ gas mixtures," *J. Appl. Phys.*, vol. 99, no. 10, p. 104907, May 2006.
- [83] P. K. Bachmann, D. Leers, and H. Lydtin, "Towards a general concept of diamond chemical vapour deposition," *Diam. Relat. Mater.*, vol. 1, no. 1, pp. 1–12, 1991.
- [84] J. R. Petherbridge, P. W. May, and M. N. R. Ashfold, "Modeling of the gas-phase chemistry in C–H–O gas mixtures for diamond chemical vapor deposition," *J. Appl. Phys.*, vol. 89, no. 9, pp. 5219–5223, Apr. 2001.
- [85] P. W. May and Y. A. Mankelevich, "Experiment and modeling of the deposition of ultrananocrystalline diamond films using hot filament chemical vapor deposition and Ar/CH₄/H₂ gas mixtures: A generalized mechanism for ultrananocrystalline diamond growth," *J. Appl. Phys.*, vol. 100, no. 2, p. 24301, Jul. 2006.
- [86] P. W. May, M. N. R. Ashfold, and Y. A. Mankelevich, "Microcrystalline, nanocrystalline, and ultrananocrystalline diamond chemical vapor deposition: Experiment and modeling of the factors controlling growth rate, nucleation, and crystal size," *J. Appl. Phys.*, vol. 101, no. 5, p. 53115, Mar. 2007.
- [87] T. Klein *et al.*, "Metal-insulator transition and superconductivity in boron-doped diamond," *Phys. Rev. B*, vol. 75, no. 16, p. 165313, Apr. 2007.
- [88] Z. J. Ayres, A. J. Borrill, J. C. Newland, M. E. Newton, and J. V. Macpherson, "Controlled sp² Functionalization of Boron Doped Diamond as a Route for the Fabrication of Robust and Nernstian pH Electrodes," *Anal. Chem.*, vol. 88, no. 1, pp. 974–980, 2016.
- [89] A. C. Pakpour-Tabrizi *et al.*, "The occupied electronic structure of ultrathin

- boron doped diamond,” *Nanoscale Adv.*, vol. 2, no. 3, pp. 1358–1364, 2020.
- [90] E. A. Ekimov *et al.*, “Superconductivity in diamond,” *Nature*, vol. 428, no. 6982, pp. 542–545, 2004.
- [91] G. M. Klemencic, S. Mandal, J. M. Werrell, S. R. Giblin, and O. A. Williams, “Superconductivity in planarised nanocrystalline diamond films,” *Sci. Technol. Adv. Mater.*, vol. 18, no. 1, pp. 239–244, Mar. 2017.
- [92] R. Kalish, “Doping of diamond,” *Carbon N. Y.*, vol. 37, no. 5, pp. 781–785, 1999.
- [93] M.-A. Pinault, J. Barjon, T. Kociniewski, F. Jomard, and J. Chevallier, “The n-type doping of diamond: Present status and pending questions,” *Phys. B Condens. Matter*, vol. 401–402, pp. 51–56, 2007.
- [94] E. Gheeraert *et al.*, “n-Type doping of diamond by sulfur and phosphorus,” *Diam. Relat. Mater.*, vol. 11, no. 3, pp. 289–295, 2002.
- [95] M. Nesladek, “Conventional n-type doping in diamond: state of the art and recent progress,” *Semicond. Sci. Technol.*, vol. 20, no. 2, pp. R19–R27, Jan. 2005.
- [96] Y. Katamune *et al.*, “n-Type doping of diamond by hot-filament chemical vapor deposition growth with phosphorus incorporation,” *Appl. Phys. A*, vol. 126, no. 11, p. 879, 2020.
- [97] A. Gruber, A. Dräbenstedt, C. Tietz, L. Fleury, J. Wrachtrup, and C. von Borczyskowski, “Scanning Confocal Optical Microscopy and Magnetic Resonance on Single Defect Centers,” *Science (80-.)*, vol. 276, no. 5321, pp. 2012–2014, 1997.
- [98] R. Brouri, A. Beveratos, J.-P. Poizat, and P. Grangier, “Photon antibunching in

- the fluorescence of individual color centers in diamond,” *Opt. Lett.*, vol. 25, no. 17, pp. 1294–1296, Sep. 2000.
- [99] A. Dräbenstedt *et al.*, “Low-temperature microscopy and spectroscopy on single defect centers in diamond,” *Phys. Rev. B*, vol. 60, no. 16, pp. 11503–11508, Oct. 1999.
- [100] F. Jelezko, T. Gaebel, I. Popa, A. Gruber, and J. Wrachtrup, “Observation of Coherent Oscillations in a Single Electron Spin,” *Phys. Rev. Lett.*, vol. 92, no. 7, p. 76401, Feb. 2004.
- [101] G. Davies, “Dynamic Jahn-Teller distortions at trigonal optical centres in diamond,” *J. Phys. C Solid State Phys.*, vol. 12, no. 13, pp. 2551–2566, Jul. 1979.
- [102] G. Balasubramanian *et al.*, “Nanoscale imaging magnetometry with diamond spins under ambient conditions,” *Nature*, vol. 455, no. 7213, pp. 648–651, 2008.
- [103] J. M. Taylor *et al.*, “High-sensitivity diamond magnetometer with nanoscale resolution,” *Nat. Phys.*, vol. 4, no. 10, pp. 810–816, 2008.
- [104] L. P. McGuinness *et al.*, “Quantum measurement and orientation tracking of fluorescent nanodiamonds inside living cells,” *Nature Nanotechnology*, vol. 6, no. 6, England, pp. 358–363, May-2011.
- [105] F. Dolde *et al.*, “Electric-field sensing using single diamond spins,” *Nat. Phys.*, vol. 7, no. 6, pp. 459–463, 2011.
- [106] J. H. Cole and L. C. L. Hollenberg, “Scanning quantum decoherence microscopy,” *Nanotechnology*, vol. 20, no. 49, p. 495401, Dec. 2009.
- [107] L.-S. Bouchard, V. M. Acosta, E. Bauch, and D. Budker, “Detection of the

- Meissner effect with a diamond magnetometer,” *New J. Phys.*, vol. 13, no. 2, p. 25017, Feb. 2011.
- [108] M. Howard, J. Twamley, C. Wittmann, T. Gaebel, F. Jelezko, and J. Wrachtrup, “Quantum process tomography and Linblad estimation of a solid-state qubit,” *New J. Phys.*, vol. 8, no. 3, p. 33, Mar. 2006.
- [109] G. D. Fuchs, V. V Dobrovitski, D. M. Toyli, F. J. Heremans, and D. D. Awschalom, “Gigahertz Dynamics of a Strongly Driven Single Quantum Spin,” *Science (80-.)*, vol. 326, no. 5959, pp. 1520–1522, 2009.
- [110] G. Waldherr, P. Neumann, S. F. Huelga, F. Jelezko, and J. Wrachtrup, “Violation of a Temporal Bell Inequality for Single Spins in a Diamond Defect Center,” *Phys. Rev. Lett.*, vol. 107, no. 9, p. 90401, Aug. 2011.
- [111] X.-D. Chen *et al.*, “Temperature dependent energy level shifts of nitrogen-vacancy centers in diamond,” *Appl. Phys. Lett.*, vol. 99, no. 16, p. 161903, Oct. 2011.
- [112] V. Ivády, T. Simon, J. R. Maze, I. A. Abrikosov, and A. Gali, “Pressure and temperature dependence of the zero-field splitting in the ground state of NV centers in diamond: A first-principles study,” *Phys. Rev. B*, vol. 90, no. 23, p. 235205, Dec. 2014.
- [113] D. M. Toyli, D. J. Christle, A. Alkauskas, B. B. Buckley, C. G. de Walle, and D. D. Awschalom, “Measurement and Control of Single Nitrogen-Vacancy Center Spins above 600 K,” *Phys. Rev. X*, vol. 2, no. 3, p. 31001, Jul. 2012.
- [114] H. Bernien *et al.*, “Heralded entanglement between solid-state qubits separated by 3 meters,” *Nature*, vol. 497, no. 7447, pp. 86–90, 2012.
- [115] H. Bernien, L. Childress, L. Robledo, M. Markham, D. Twitchen, and R.

- Hanson, "Two-photon quantum interference from separate nitrogen vacancy centers in diamond," *Phys. Rev. Lett.*, vol. 108, no. 4, pp. 1–5, 2012.
- [116] E. Togan *et al.*, "Quantum entanglement between an optical photon and a solid-state spin qubit," *Nature*, vol. 466, no. 7307, pp. 730–734, 2010.
- [117] J. Wrachtrup, "Schrödinger's cat is still alive," *Nat. Phys.*, vol. 5, no. 4, pp. 248–249, 2009.
- [118] P. Rabl, P. Cappellaro, M. V. G. Dutt, L. Jiang, J. R. Maze, and M. D. Lukin, "Strong magnetic coupling between an electronic spin qubit and a mechanical resonator," *Phys. Rev. B*, vol. 79, no. 4, p. 41302, Jan. 2009.
- [119] R. Alléaume *et al.*, "Experimental open-air quantum key distribution with a single-photon source," *New J. Phys.*, vol. 6, p. 92, Jul. 2004.
- [120] G. I. of A. Shingley, James, "Important optical defects in diamond and their effect on color and luminescence .," *Gems Gemol.*, vol. 49, no. 2, p. 393, 2013.
- [121] M. W. Doherty, N. B. Manson, P. Delaney, F. Jelezko, J. Wrachtrup, and L. C. L. Hollenberg, "The nitrogen-vacancy colour centre in diamond," *Phys. Rep.*, vol. 528, no. 1, pp. 1–45, 2013.
- [122] J. Harrison, M. J. Sellars, and N. B. Manson, "Optical spin polarisation of the N-V centre in diamond," *J. Lumin.*, vol. 107, no. 1, pp. 245–248, 2004.
- [123] A. Batalov *et al.*, "Low Temperature Studies of the Excited-State Structure of Negatively Charged Nitrogen-Vacancy Color Centers in Diamond," *Phys. Rev. Lett.*, vol. 102, no. 19, pp. 1–4, 2009.
- [124] X. D. Chen *et al.*, "Temperature dependent energy level shifts of nitrogen-vacancy centers in diamond," *Appl. Phys. Lett.*, vol. 99, no. 16, pp. 1–4, 2011.

- [125] J. M. Smith, S. A. Meynell, A. C. Bleszynski Jayich, and J. Meijer, "Colour centre generation in diamond for quantum technologies," *Nanophotonics*, vol. 8, no. 11, pp. 1889–1906, 2019.
- [126] I. I. Vlasov, V. G. Ralchenko, A. V. Khomich, S. V. Nistor, D. Shoemaker, and R. A. Khmel'nitskii, "Relative abundance of single and vacancy-bonded substitutional nitrogen in CVD diamond," *Phys. Status Solidi Appl. Res.*, vol. 181, no. 1, pp. 83–90, 2000.
- [127] K. Ohno *et al.*, "Engineering shallow spins in diamond with nitrogen delta-doping," *Appl. Phys. Lett.*, vol. 101, no. 8, 2012.
- [128] R. Rubinas *et al.*, "Spin properties of NV centers in high-pressure, high-temperature grown diamond," *J. Phys. Commun.*, vol. 2, no. 115003, 2018.
- [129] J. O. Orwa *et al.*, "Engineering of nitrogen-vacancy color centers in high purity diamond by ion implantation and annealing," *J. Appl. Phys.*, vol. 109, no. 8, 2011.
- [130] D. Delgado and R. Vila, "Statistical Molecular Dynamics study of displacement energies in diamond," *J. Nucl. Mater.*, vol. 419, no. 1–3, pp. 32–38, 2011.
- [131] K. Ohno *et al.*, "Three-dimensional localization of spins in diamond using ¹²C implantation," *Appl. Phys. Lett.*, vol. 105, no. 5, 2014.
- [132] Z. Huang *et al.*, "Diamond nitrogen-vacancy centers created by scanning focused helium ion beam and annealing," *Appl. Phys. Lett.*, vol. 103, no. 8, 2013.
- [133] B. K. Ofori-Okai *et al.*, "Spin properties of very shallow nitrogen vacancy defects in diamond," *Phys. Rev. B - Condens. Matter Mater. Phys.*, vol. 86, no. 8, pp. 1–5, 2012.

- [134] B. A. Myers, A. Das, M. C. Dartailh, K. Ohno, D. D. Awschalom, and A. C. Bleszynski Jayich, "Probing surface noise with depth-calibrated spins in diamond," *Phys. Rev. Lett.*, vol. 113, no. 2, pp. 1–6, 2014.
- [135] H. Yamano *et al.*, "Charge state stabilization of shallow nitrogen vacancy centers in diamond by oxygen surface modification," *Jpn. J. Appl. Phys.*, vol. 56, no. 4, 2017.
- [136] M. V. Hauf *et al.*, "Chemical control of the charge state of nitrogen-vacancy centers in diamond," *Phys. Rev. B - Condens. Matter Mater. Phys.*, vol. 83, no. 8, pp. 1–4, 2011.
- [137] S. Kawai *et al.*, "Nitrogen-Terminated Diamond Surface for Nanoscale NMR by Shallow Nitrogen-Vacancy Centers," *J. Phys. Chem. C*, vol. 123, no. 6, pp. 3594–3604, 2019.
- [138] J. Ristein, "Surface science of diamond: Familiar and amazing," *Surf. Sci.*, vol. 600, no. 18, pp. 3677–3689, 2006.
- [139] S. Cui, "Near-surface Nitrogen Vacancy Centers in Diamond," Harvard University, 2014.
- [140] J. R. & L. L. P. Strobel, M. Riedel, "Surface transfer doping of diamond," *Nature*, vol. 430, no. 6998, pp. 435–439, 2004.
- [141] J. Ristein, "Surface transfer doping of diamond," *J. Phys. D. Appl. Phys.*, vol. 39, no. 4, 2006.
- [142] D. A. Evans *et al.*, "Diamond-metal contacts: Interface barriers and real-time characterization," *J. Phys. Condens. Matter*, vol. 21, no. 36, 2009.
- [143] J. C. Zheng, X. N. Xie, A. T. S. Wee, and K. P. Loh, "Oxygen-induced surface state on diamond (100)," *Diam. Relat. Mater.*, vol. 10, no. 3–7, pp. 500–505,

2001.

- [144] K.-M. C. Fu, C. Santori, P. E. Barclay, and R. G. Beausoleil, "Conversion of neutral nitrogen-vacancy centers to negatively charged nitrogen-vacancy centers through selective oxidation," *Appl. Phys. Lett.*, vol. 96, no. 12, p. 121907, Mar. 2010.
- [145] J. Philip *et al.*, "Elastic, mechanical, and thermal properties of nanocrystalline diamond films," *J. Appl. Phys.*, vol. 93, no. 4, pp. 2164–2171, 2003.
- [146] J. E. Butler and A. V. Sumant, "The CVD of nanodiamond materials," *Chem. Vap. Depos.*, vol. 14, no. 7-8 SPEC. ISS., pp. 145–160, 2008.
- [147] T. Bautze, S. Mandal, O. A. Williams, P. Rodière, T. Meunier, and C. Bäuerle, "Superconducting nano-mechanical diamond resonators," *Carbon N. Y.*, vol. 72, pp. 100–105, 2014.
- [148] M. L. Terranova, S. Orlanducci, M. Rossi, and E. Tamburri, "Nanodiamonds for field emission: State of the art," *Nanoscale*, vol. 7, no. 12, pp. 5094–5114, 2015.
- [149] O. A. Williams, "Nanocrystalline diamond," *Diam. Relat. Mater.*, vol. 20, no. 5–6, pp. 621–640, 2011.
- [150] W. S. Yang and J. H. Je, "Effects of secondary pretreatments of substrate on the nucleation of diamond film," *J. Mater. Res.*, vol. 11, no. 7, pp. 1787–1794, 1996.
- [151] M. Daenen, O. A. Williams, J. D'Haen, K. Haenen, and M. Nesládek, "Seeding, growth and characterization of nanocrystalline diamond films on various substrates," *Phys. Status Solidi Appl. Mater. Sci.*, vol. 203, no. 12, pp. 3005–3010, 2006.

- [152] S. Iijima, Y. Aikawa, and K. Baba, "Early formation of chemical vapor deposition diamond films," *Appl. Phys. Lett.*, vol. 57, no. 25, pp. 2646–2648, 1990.
- [153] O. A. Williams, O. Douhéret, M. Daenen, K. Haenen, E. Osawa, and M. Takahashi, "Enhanced diamond nucleation on monodispersed nanocrystalline diamond," *Chem. Phys. Lett.*, vol. 445, no. 4–6, pp. 255–258, 2007.
- [154] X. Jiang, K. Schiffmann, and C. P. Klages, "Nucleation and initial growth phase of diamond thin films on (100) silicon," *Phys. Rev. B*, vol. 50, no. 12, pp. 8402–8410, 1994.
- [155] P. Smereka, X. Li, G. Russo, and D. J. Srolovitz, "Simulation of faceted film growth in three dimensions: Microstructure, morphology and texture," *Acta Mater.*, vol. 53, no. 4, pp. 1191–1204, 2005.
- [156] E. Kohn, M. Adamschik, P. Schmid, S. Ertl, and A. Flöter, "Diamond electro-mechanical micro devices - Technology and performance," *Diam. Relat. Mater.*, vol. 10, no. 9–10, pp. 1684–1691, 2001.
- [157] C. Stavis *et al.*, "Surface functionalization of thin-film diamond for highly stable and selective biological interfaces," *Proc. Natl. Acad. Sci. U. S. A.*, vol. 108, no. 3, pp. 983–988, 2011.
- [158] E. L. H. Thomas, G. W. Nelson, S. Mandal, J. S. Foord, and O. A. Williams, "Chemical mechanical polishing of thin film diamond," *Carbon N. Y.*, vol. 68, pp. 473–479, 2014.
- [159] S. Mandal *et al.*, *Novel Aspects of Diamond, Chapter 3*, vol. 121. 2019.
- [160] D. Hu, "Surface Modification and Electronic Structure Characterisation of Carbon-based and Iron-based Materials," *PhD Thesis, Aberystwyth University*,

2018.

- [161] J. M. Hill, D. G. Royce, C. S. Fadley, L. F. Wagner, and F. J. Grunthaner, "Properties of oxidized silicon as determined by angular-dependent X-ray photoelectron spectroscopy," *Chem. Phys. Lett.*, vol. 44, no. 2, pp. 225–231, 1976.
- [162] A. K. Schenk, K. J. Rietwyk, A. Tadich, A. Stacey, L. Ley, and C. I. Pakes, "High resolution core level spectroscopy of hydrogen-terminated (1 0 0) diamond," *J. Phys. Condens. Matter*, vol. 28, no. 30, 2016.
- [163] Z. Zhang, "Surface structures and electron amenities of bare and hydrogenated diamond CHOO) surfaces," *Phys. Rev. B*, vol. 51, no. 8, pp. 5291–5296, 1995.
- [164] J. Robertson and M. J. Rutter, "Band diagram of diamond and diamond-like carbon surfaces," *Diam. Relat. Mater.*, vol. 7, no. 2–5, pp. 620–625, 1998.
- [165] A. K. Schenk, K. J. Rietwyk, A. Tadich, A. Stacey, L. Ley, and C. I. Pakes, "High resolution core level spectroscopy of hydrogen-terminated (1 0 0) diamond," *J. Phys. Condens. Matter*, vol. 28, no. 30, p. 305001, Jun. 2016.
- [166] V. L. Kuznetsov, I. L. Zilberberg, Y. V. Butenko, A. L. Chuvilin, and B. Segall, "Theoretical study of the formation of closed curved graphite-like structures during annealing of diamond surface," *J. Appl. Phys.*, vol. 86, no. 2, pp. 863–870, 1999.
- [167] M. H. Hecht, "Photovoltaic effects in photoemission studies of Schottky barrier formation," *J. Vac. Sci. Technol. B Microelectron. Nanom. Struct.*, vol. 8, no. 4, p. 1018, 1990.
- [168] B. Van Zeghbroeck, "Principles of semiconductor devices," in *Colorado*

University, vol. 34, Colorado: Colorado University, 2004.

- [169] K. Ganesan, P. K. Ajikumar, S. Ilango, G. Mangamma, and S. Dhara, "Si and N - Vacancy color centers in discrete diamond nanoparticles: Raman and fluorescence spectroscopic studies," *Diam. Relat. Mater.*, vol. 92, no. December 2018, pp. 150–158, 2019.
- [170] K. Ganesan, P. K. Ajikumar, S. K. Srivastava, and P. Magudapathy, "Structural, Raman and photoluminescence studies on nanocrystalline diamond films: Effects of ammonia in feedstock," *Diam. Relat. Mater.*, vol. 106, no. March, 2020.
- [171] M. Chandran, M. Shasha, S. Michaelson, and A. Hoffman, "Nitrogen termination of single crystal (100) diamond surface by radio frequency N₂ plasma process: An in-situ x-ray photoemission spectroscopy and secondary electron emission studies," *Appl. Phys. Lett.*, vol. 107, no. 11, pp. 2–6, 2015.
- [172] M. Attrash, M. K. Kuntumalla, S. Michaelson, and A. Hoffman, "Nitrogen-terminated polycrystalline diamond surfaces by microwave chemical vapor deposition: Thermal stability, chemical states, and electronic structure," *J. Phys. Chem. C*, vol. 124, no. 10, pp. 5657–5664, 2020.
- [173] I. Kusunoki *et al.*, "XPS study of nitridation of diamond and graphite with a nitrogen ion beam," *Surf. Sci.*, vol. 492, no. 3, pp. 315–328, 2001.
- [174] R. J. Koch *et al.*, "Growth and electronic structure of nitrogen-doped graphene on Ni(111)," *Phys. Rev. B - Condens. Matter Mater. Phys.*, vol. 86, no. 7, 2012.
- [175] Y. Murata, R. Nakayama, F. Ichihara, H. Ono, C. K. Choo, and K. Tanaka, "Effects of nitrogen substitution in amorphous carbon films on electronic

- structure and surface reactivity studied with x-ray and ultra-violet photoelectron spectroscopies," *J. Appl. Phys.*, vol. 121, no. 9, 2017.
- [176] J. P. Chou, A. Retzker, and A. Gali, "Nitrogen-Terminated Diamond (111) Surface for Room-Temperature Quantum Sensing and Simulation," *Nano Lett.*, vol. 17, no. 4, pp. 2294–2298, 2017.
- [177] S. Cui and E. L. Hu, "Increased negatively charged nitrogen-vacancy centers in fluorinated diamond," *Appl. Phys. Lett.*, vol. 103, no. 5, 2013.
- [178] K. J. Rietwyk *et al.*, "Work function and electron affinity of the fluorine-terminated (100) diamond surface," *Appl. Phys. Lett.*, vol. 102, no. 9, 2013.
- [179] A. Denisenko, A. Romanyuk, C. Pietzka, J. Scharpf, and E. Kohn, "Surface structure and surface barrier characteristics of boron-doped diamond in electrolytes after CF₄ plasma treatment in RF-barrel reactor," *Diam. Relat. Mater.*, vol. 19, no. 5–6, pp. 423–427, 2010.
- [180] D. Zhao *et al.*, "Applied Surface Science Fabrication of dual-termination Schottky barrier diode by using oxygen/ fluorine-terminated diamond," *Appl. Surf. Sci.*, vol. 457, no. June, pp. 411–416, 2018.
- [181] B. Singh, R. Hesse, M. R. Linford, and B. Young, "Good Practices for XPS (and other Types of) Peak Fitting. Use Chi Squared, Use the Abbe Criterion, Show the Sum of Fit Components, Show the (Normalized) Residuals, Choose an Appropriate Background, Estimate Fit Parameter Uncertainties, Limit the Number of," *Vac. Technol. Coat.*, no. December, 2015.
- [182] R. Hesse, T. Chassé, P. Streubel, and R. Szargan, "Error estimation in peak-shape analysis of XFS core-level spectra using UNIFIT 2003: How significant are the results of peak fits?," *Surf. Interface Anal.*, vol. 36, no. 10, pp. 1373–

1383, 2004.

- [183] E. Martinez *et al.*, “Band offsets of HfO₂/GeON/Ge stacks measured by ultraviolet and soft x-ray photoelectron spectroscopies,” *Appl. Phys. Lett.*, vol. 90, no. 5, pp. 2–5, 2007.
- [184] S. Sayan, E. Garfunkel, and S. Suzer, “Soft x-ray photoemission studies of the HfO₂/SiO₂/Si system,” *Appl. Phys. Lett.*, vol. 80, no. 12, pp. 2135–2137, 2002.
- [185] A. G. Shard, “Practical guides for x-ray photoelectron spectroscopy: Quantitative XPS,” *J. Vac. Sci. Technol. A*, vol. 38, no. 4, p. 041201, 2020.